

ABSTRACT

Title of Dissertation: CHARACTERIZATION OF QUANTUM EFFICIENCY AND ROBUSTNESS OF CESIUM-BASED PHOTOCATHODES

Eric J. Montgomery, Doctor of Philosophy, 2009

Directed By: Professor & Chair, Patrick G. O'Shea
Department of Electrical and Computer Engineering

High quantum efficiency, robust photocathodes produce picosecond-pulsed, high-current electron beams for photoinjection applications like free electron lasers. In photoinjectors, a pulsed drive laser incident on the photocathode causes photoemission of short, dense bunches of electrons, which are then accelerated into a relativistic, high quality beam. Future free electron lasers demand reliable photocathodes with long-lived quantum efficiency at suitable drive laser wavelengths to maintain high current density. But faced with contamination, heating, and ion back-bombardment, the highest efficiency photocathodes find their delicate cesium-based coatings inexorably lost. In answer, the work herein presents careful, focused studies on cesium-based photocathodes, particularly motivated by the cesium dispenser photocathode. This is a novel device comprised of an efficiently photoemissive, cesium-based coating deposited onto a porous sintered tungsten substrate, beneath which is a reservoir of elemental cesium. Under controlled heating cesium diffuses from the reservoir through the porous substrate and across the surface to replace cesium lost to harsh conditions -- recently shown to significantly extend the

lifetime of cesium-coated metal cathodes. This work first reports experiments on coated metals to validate and refine an advanced theory of photoemission already finding application in beam simulation codes. Second, it describes a new theory of photoemission from much higher quantum efficiency cesium-based semiconductors and verifies its predictions with independent experiment. Third, it investigates causes of cesium loss from both coated metal and semiconductor photocathodes and reports remarkable rejuvenation of full quantum efficiency for contaminated cesium-coated surfaces, affirming the dispenser prescription of cesium resupply. And fourth, it details continued advances in cesium dispenser design with much-improved operating characteristics: lower temperature and cleaner operation. Motivated by dispenser integration with semiconductor coatings, initial fabrication of those coatings are reported on dispenser-type substrates with measurement of quantum efficiency and analysis of thermal stability. Detailed investigations are performed on dispenser substrate preparation by ion beam cleaning and on dispenser pore structure by electron microscopy and focused ion beam milling. The dissertation concludes by discussing implications of all results for the demonstration and optimization of the future high quantum efficiency cesium dispenser photocathode.

CHARACTERIZATION OF QUANTUM EFFICIENCY AND
ROBUSTNESS OF CESIUM-BASED PHOTOCATHODES

By

Eric J. Montgomery

Dissertation submitted to the Faculty of the Graduate School of the
University of Maryland, College Park, in partial fulfillment
of the requirements for the degree of
Doctor of Philosophy
2009

Advisory Committee:
Professor Patrick G. O'Shea, Chair
Professor Thomas Antonsen
Professor Richard Ellis
Professor Daniel Lathrop
Professor Wesley Lawson

© Copyright by
Eric J. Montgomery
2009

Dedication

To Alan and Carol, parents par excellence:

selfless leaders, inspirational encouragers, best friends.

Acknowledgements

I first thank my advisor and mentor, Professor Patrick O'Shea: you've been a scholar-leader sharing unflagging vision and unmistakable humor since the day I wandered into your office. I am privileged, now and always, to be your student. I am delighted to laud Dr. Kevin Jensen; passion for science and patience with students make you as valued a teacher as a theorist, and this work finds broader applicability and credibility through your insights. Dr. Don Feldman, I am humbled by your wealth of experience, freely shared, and am but one of many honored by the hospitality shown by you and Renée. Her courageous spirit continues to warm our hearts. I express great gratitude to Nathan Moody. You may never know the continued impact of our short months working together. More, you built a launch pad at IREAP and left rocket fueled and countdown running, immeasurably accelerating this effort by exemplary preparation. Continued funding comes from the Joint Technology Office (JTO) and Office of Naval Research (ONR). Additional thanks to graduate students, office-mates, and friends Peter Zhigang Pan, Chao Wu, Remington Reid, Mike Holloway, Gang Bai, Todd Firestone, Matt Virgo, and John Harris. High expectations and thanks for undergraduates Anne Balter, Chris Dunay, Jessica Leung, Noah Sennett, and Claire Stortstrom. My gratitude to Matt Paoletti, Ray Fermo, Dr. Edo Waks and all those who helped organize and give talks at the GSS. Thanks to Jay Pyle and John Barry for your expertise. Sincere thanks to Professors Antonsen, Ellis, Lathrop and Lawson for your service on my dissertation committee. And thanks beyond words for the encouragement of my dear friends at Immanuels', and most importantly, my family. We know whose success this is.

Table of Contents

Dedication	ii
Acknowledgements	iii
Table of Contents	iv
List of Tables	ix
List of Figures	x
List of Abbreviations	xiii
Chapter 1: Introduction	1
1.1 Overview	1
1.2 Motivation	1
1.2.1 Free Electron Lasers	2
1.2.2 High Brightness Photoinjectors	8
1.3 Electron Beams	9
1.3.1 Emittance	9
1.3.2 Brightness	12
1.4 Photocathode Fundamentals	14
1.4.1 Quantum Efficiency	14
1.4.2 Lifetime	17
1.4.3 Spectral Response	20
1.4.4 Temporal Response	22
1.4.5 Additional Considerations	27
1.5 Photocathode Types	29
1.5.1 Metals	29
1.5.2 Coated Metals	29
1.5.3 Positive Electron Affinity Semiconductors	30
1.5.4 Negative Electron Affinity Semiconductors	30
1.6 Comparison of Emission Mechanisms	31
1.7 Dispensers	32
Chapter 2: Historical Context	34
2.1 Electron Emission and the Photoelectric Effect	34
2.2 Photoinjection	35
2.2.1 Introduction	35
2.2.2 Types of Photoinjectors	37
2.2.3 Historical Development	39
2.3 Photocathodes for Photoinjectors	42
2.3.1 Metals	43
2.3.2 Coated Metals and Dispensers	44
2.3.3 Positive Electron Affinity Semiconductors	48
2.3.4 Negative Electron Affinity Semiconductors	48
2.4 Foundational Research at UMD	49

2.4.1 Introduction	49
2.4.2 Experimental Results.....	50
2.4.3 Theory and Simulation Results	57
Chapter 3: A Photocathode Explorer's Roadmap.....	66
3.1 Introduction	66
3.2 Expedition Roadmaps.....	67
Chapter 4: Experimental Apparatus	70
4.1 Introduction	70
4.2 Vacuum Chamber.....	70
4.2.1 Schematic	70
4.2.2 Ultrahigh Vacuum	71
4.2.3 Bakeout.....	73
4.3 Vacuum Pumps.....	74
4.3.1 Choice of Pumps	74
4.3.2 Scroll (Roughing) Pump.....	75
4.3.3 Turbopump	76
4.3.4 Ion Pumps.....	78
4.4 Vacuum Monitoring.....	81
4.4.1 Pressure Measurement.....	81
4.4.2 Residual Gas Analyzer	82
4.5 Lasers.....	83
4.5.1 Laser Diodes	83
4.5.2 Laser Specifications.....	85
4.5.3 Robotic Control	86
4.6 Cathode Flange and QE circuit	87
4.6.1 QE Measurement Circuit.....	87
4.6.2 Vacuum Chamber Feedthrough and Connections.....	87
4.6.3 Cathode Heater Power.....	89
4.6.4 Cathode-Anode Assembly.....	93
4.7 Gas Supply	95
4.7.1 Gas Species.....	95
4.7.2 Gas Tree and Valves.....	95
4.8 Film Deposition and Characterization.....	99
4.8.1 Evaporative Sources	99
4.8.2 Deposition Monitor	102
4.9 Ion Beam Cleaning.....	103
4.9.1 Saddle Field Ion Source.....	103
4.9.2 Anode Shielding and Cathode Mount Sputtering.....	107
4.10 Instrumentation Rack	108
Chapter 5: Experimental Techniques	110
5.1 Measurement Techniques.....	110
5.1.1 Pressure.....	110

5.1.2 Laser Power	110
5.1.3 Photocurrent	110
5.1.4 Coating Coverage	111
5.1.5 Cathode Temperature	111
5.1.6 Background Gas Composition.....	112
5.2 Measurement Considerations	113
5.2.1 Space Charge	113
5.2.2 Noise and Error in Measurements of Photocurrent and Laser Power	116
5.2.3 Uncertainty in Calculation of QE	120
5.3 Automation Techniques	123
5.3.1 LabVIEW introduction	123
5.3.2 QE Measurement	125
5.3.3 Code Enhancements	125
5.4 Standard Procedures	131
5.4.1 Chamber Bakeout/Pumpdown.....	131
5.4.2 Ion Beam Cleaning	133
5.4.3 Coating Deposition	135
5.4.4 Cathode Heating	136
5.4.5 Controlled Gas Exposure.....	136
5.4.6 Laboratory close-out.....	137
5.5 Precautions	137
5.5.1 Laser Safety	137
5.5.2 General UHV Cleanliness	138
5.6 Dispenser Surface Characterization Techniques	141
5.6.1 Microscopy	141
5.6.2 Focused Ion Beam Milling	143
5.7 Ion Beam Cleaning Characterization Techniques	146
5.7.1 Introduction	146
5.7.2 Surface Roughening	147
5.7.3 Surface Cleaning Effectiveness.....	150
Chapter 6: QE of Sub-monolayer Coated Metals.....	155
6.1 Theoretical Basis	155
6.1.1 Introduction	155
6.1.2 Effect of Adsorbates on Electron Emission.....	156
6.1.3 The f-factor	165
6.1.4 MFD Formulation of Quantum Efficiency	168
6.1.5 The Moments-Based Approach.....	178
6.2 Experimental Results.....	186
6.2.1 Comparison to Theory.....	186
6.2.2 Discussion of Peak QE Variation between Deposition and Desorption.....	192
Chapter 7: QE of Semiconductors.....	198
7.1 Theoretical Basis	198

7.1.1 Introduction and Contrast with Metals	198
7.1.2 Moments-Based Approach for Semiconductors	199
7.1.3 Electron Transport and Scattering	202
7.1.4 Optical Absorption	203
7.1.5 Comparison to Literature	205
7.2 Experimental Results: Cs₃Sb	205
7.2.1 Fabrication	205
7.2.2 Measured QE	206
7.2.3 Comparison to Theory	209
7.3 Experimental Results: Na₂KSb(Cs)	210
7.3.1 Fabrication	210
7.3.2 Measured QE	211
Chapter 8: Cesium Loss and Recesiatio	214
8.1 Introduction	214
8.2 Cesium Loss Mechanisms	214
8.2.1 Evaporation	215
8.2.2 Back-bombardment	216
8.2.3 Contamination	216
8.2.4 Dissociation	217
8.3 Cesi ated metals	219
8.3.1 Heating	219
8.3.2 Contamination and Recesiatio	220
8.4 Semiconductors	229
8.4.1 Heating	229
8.4.2 Survey of Alkali Antimonide Temperature Stability	231
Chapter 9: Cesium Dispenser Photocathode	233
9.1 Design and Fabrication	233
9.1.1 Introduction	233
9.1.2 Canister	234
9.1.3 Sintered Tungsten	236
9.1.4 Cesium Reservoir Materials	237
9.2 Installation and Activation	239
9.2.1 Cathode mount	239
9.2.2 Activation	239
9.3 Rejuvenation	243
9.4 In-situ Cs-Sb Fabrication on Dispenser	244
9.5 Dispenser Comparison and Discussion	246
9.5.1 Comparison	246
9.5.2 Discussion of Future Design Directions	247
Chapter 10: Conclusion and Outlook	249
10.1 Summary of Work	249
10.1.1 Cesium-Coated Metal Photocathodes	249

10.1.2 Cesium-Based Semiconductor Photocathodes	251
10.1.3 Cesium Loss and Recesiation Studies	252
10.1.4 Cesium Dispenser Photocathode Development.....	253
10.2 Future Directions	254
10.2.1 High QE Semiconductor Contamination and Recesiation	254
10.2.2 High QE Semiconductor Rejuvenation	255
10.2.3 Theory of Cesium Diffusion and Evaporation in Dispensers.....	255
10.2.4 Alternate Dispenser Diffusion Barrier Designs.....	256
10.2.5 Alternate Dispenser Reservoir Designs.....	256
10.2.6 Enhanced Experimental Capabilities.....	257
10.3 Closing Thoughts	259
References	258
Appendix A: Material Parameters.....	266

List of Tables

Table 1.1: Typical peak QE values	16
Table 1.2: Photocathode Typical Temporal Response.....	24
Table 4.1: Vacuum chamber specifications.....	73
Table 4.2: Ion pumping speeds for common gases relative to water vapor	79
Table 4.3: Laser specifications	85
Table 4.4: Steady-state heater power versus cathode temperature: raw data.....	90
Table 4.5: Heater power calculation constants.....	92
Table 4.6: Valve/Pump states during normal operating modes	99
Table 5.1: Calculation of relative uncertainty in QE for all laser wavelengths	121
Table 5.2: LabVIEW QE measurement process summary	125
Table 5.3: Highlighted LabVIEW code modifications and upgrades	126
Table 7.1: Trialkali fabrication steps.....	212
Table 9.1: Comparison of Cesium Dispenser Cathodes.....	246

List of Figures

Figure 1.1: Schematic of an FEL wiggler	4
Figure 1.2: QE vs Lifetime of Operational Photocathodes	18
Figure 1.3: 1P28 (Cs-Sb) PMT, Hamamatsu	21
Figure 1.4: R464 (K-Cs-Sb) PMT, Hamamatsu.....	21
Figure 1.5: R2557 (Na-K-Sb) PMT, Hamamatsu	21
Figure 1.6: Emission barriers: thermionic, metal, and semiconductor (to scale, zero applied field)	32
Figure 1.7: Reservoir Type Dispenser Cathode, cross-section	33
Figure 2.1: Transition from thermionic to photo-injection	37
Figure 2.2: Historical Development of Dispenser Cathodes as Thermionic Sources	46
Figure 4.1: Experimental Chamber, original design by N. Moody.....	71
Figure 4.2: Turbopump station with scroll roughing pump	77
Figure 4.3: Turbopump manifold with pressure gauges and electromechanical valve	78
Figure 4.4: Stanford Research Systems RGA 200	83
Figure 4.5: Diode lasers	84
Figure 4.6: Lasers on translational mounts with thermopile power meter for auto-calibration..	86
Figure 4.7: QE circuit diagram.....	87
Figure 4.8: Cathode electrical feedthrough	88
Figure 4.9: Isolated low-noise anode-cathode voltage supply	89
Figure 4.10: Variac (variable AC transformer) for cathode heater power control.....	90
Figure 4.11: Heater power vs cathode temperature and fit to radiative/conductive cooling.....	91
Figure 4.12: Cathode and anode, side view	93
Figure 4.13: Cathode and anode showing standoffs and electrical	94
Figure 4.14: Silver cathode mount	94
Figure 4.15: Initial gas supply schematic.....	96
Figure 4.16: Upgraded gas supply schematic with valve codes.....	96
Figure 4.17: Detail of gas supply tree and valves	97
Figure 4.18: Detail of miniature regulator and interchangeable lab bottle	97
Figure 4.19: Cesium sources, SAES St-101.....	100
Figure 4.20: Alkali sources, Alvatec: (left) flange assembly, (right) source detail.....	101
Figure 4.21: Entire 8" flange assembly: alkalis, left; antimony, right.....	101
Figure 4.22: Quartz crystal exchange in deposition monitor, face with new installed and used crystal (left), rear view and spring mount (right).....	102
Figure 4.23: Deposition monitor above anode-cathode assembly inside vacuum chamber	102
Figure 4.24: Saddle field ion gun detail, showing beam exit.....	104
Figure 4.25: Ion gun and adjustable mount with argon fine leak valve	104
Figure 4.26: Ion beam alignment scans.....	106

Figure 4.27: (left) Anode showing ion beam cleaned area after multiple antimony depositions, (center) Cathode-facing side of anode showing copper sputtering and discoloration of exposed, heated, oxidized surface	107
Figure 4.28: New dispenser, left, versus used dispenser, right, showing faint copper sputtering on outer top rim edge	107
Figure 4.29: Equipment rack with power supplies, instruments, and LabVIEW computer control	109
Figure 5.1: RGA filament, thoriated tungsten	112
Figure 5.2: RGA scan and background gas analysis	113
Figure 5.3: Space-charge-limited current from high QE Cs ₃ Sb cathode.....	115
Figure 5.4: QE vs applied field, Cs ₃ Sb	116
Figure 5.5: Data set for photocurrent noise (10 hour lifetime measurement, Cs:W).....	121
Figure 5.6: Photocurrent noise by laser wavelength, first hour of previous figure	122
Figure 5.7: GPIB stacking cable connectors	124
Figure 5.8: Sample case structure on block diagram, for QE plot settings	127
Figure 5.9: Detail of block diagram, showing initialization of reference nodes	128
Figure 5.10: Detail of block diagram, showing data acquisition and file write	129
Figure 5.11: LabVIEW interface with multialkali fabrication.....	130
Figure 5.12: Laser safety housing	138
Figure 5.13: Dust-minimized workspace	140
Figure 5.14: Optical microscopy of sintered tungsten surface, 70% dense, 1500 magnification.....	141
Figure 5.15: E-beam microscopy of sintered tungsten, 70% dense	142
Figure 5.16: E-beam microscopy of sintered tungsten after peroxide etch: (left) surface-normal viewing angle, (right) glancing viewing angle showing roughness of etched surface.....	143
Figure 5.17: E-beam microscopy of initial ion beam milling	144
Figure 5.18: Continuation of milling in previous figure	144
Figure 5.19: Gradual extension of pore-adjacent milled profile	145
Figure 5.20: Crystal-face dependent sputtering and surface roughening of sintered tungsten	148
Figure 5.21: "The Hamburger." Micro-protrusion as shadow mask during ion cleaning	150
Figure 5.22: Ion beam cleaning vs anneal cleaning of tungsten, cesiated after cleaning.....	151
Figure 5.23: QE vs ion beam cleaning duration, Cs:Ag.....	152
Figure 5.24: Coverage vs ion dose, Cs:Ag.....	152
Figure 6.1: GL theory: work function of cesium on tungsten.....	165
Figure 6.2: Cs:W study of f	166
Figure 6.3: K:W study of f	166
Figure 6.4: Na:W study of f	167
Figure 6.5: Theory vs experiment: cesium on sintered tungsten.....	189
Figure 6.6: Theory vs experiment: potassium on sintered tungsten.....	189
Figure 6.7: Theory vs experiment: sodium on sintered tungsten	190
Figure 6.8: Theory vs experiment: potassium on silver	190
Figure 6.9: Peak QE discrepancy: deposition vs desorption, Cs:W.....	192
Figure 6.10: Cs:W, hypothetical 100% uniform coverage, hard sphere model (to scale)	193

Figure 6.11: Cs:W, hypothetical 50% uniform coverage, hard sphere model (to scale)	193
Figure 6.12: Cs:W, hypothetical 50% random coverage, hard sphere model (to scale)	194
Figure 7.1: Cs ₃ Sb optical parameters	204
Figure 7.2: Theory vs Literature Data: QE of Cs ₃ Sb.....	205
Figure 7.3: QE during fabrication of Cs ₃ Sb	206
Figure 7.4: QE vs temperature during fabrication and cooling.....	208
Figure 7.5: QE of Cs ₃ Sb, experimental results vs predictive theory	209
Figure 7.6: QE during fabrication of Na ₂ KSb(Cs)	213
Figure 8.1: Dissociation Energies and Temperatures for Alkali Antimonides	218
Figure 8.2: Cs:W deposition (100 °C).....	219
Figure 8.3: Cs:W evaporation	220
Figure 8.4: Contamination and recession procedure (QE vs time).....	222
Figure 8.5: Recession of Cs:Ag after CO ₂ contamination	222
Figure 8.6: Recession of Cs:Ag after O ₂ contamination	223
Figure 8.7: Recession of Cs:Ag after N ₂ O contamination	224
Figure 8.8: QE of Cs:Ag vs Langmuirs of exposure to CO ₂	225
Figure 8.9: QE of Cs:Ag vs Langmuirs of exposure to O ₂	226
Figure 8.10: QE of Cs:Ag vs Langmuirs of exposure to N ₂ O	226
Figure 8.11: QE of Cs:Ag vs deposition, pre- and post-CO ₂ contamination.....	227
Figure 8.12: QE of Cs:Ag vs deposition, pre- and post-O ₂ contamination	228
Figure 8.13: QE of Cs:Ag vs deposition, pre- and post-N ₂ O contamination	228
Figure 8.14: Initial cooling and stability of Cs-Sb cathode formed in-situ on dispenser.....	229
Figure 8.15: Re-heating and irreversible QE loss of Cs-Sb cathode despite active dispenser..	230
Figure 8.16: Vapor Pressures of Alkalis over Selected Antimonides	232
Figure 9.1: Commercial dispenser (thermionic cathode).....	233
Figure 9.2: Prototype dispenser from UMD.....	234
Figure 9.3: First cesium dispenser cell.....	235
Figure 9.4: Dispenser in copper clamp.....	236
Figure 9.5: Custom Cs:Bi reservoir cartridge from Alvatec: (left) indium seal, (right) rear seal...	238
Figure 9.6: Cs:Bi reservoir cartridge and cathode for scale.....	238
Figure 9.7: Cathode mounted behind annular anode.....	239
Figure 9.8: Activation of 2nd gen. cathode with Alvatec Cs:Bi reservoir	240
Figure 9.9: Pressure and temperature of 2nd gen. cathode activation.....	241
Figure 9.10: Vacuum RGA analysis during activation of 2nd gen. cathode vs Cs Alvasource	242
Figure 9.11: Rejuvenation of 2nd gen. cathode with 60% dense 20-mil thick tungsten disc ...	243
Figure 9.12: Dispensed-cesium Cs ₃ Sb fabrication attempt	245

List of Abbreviations

AC	Alternating Current
APLE	Average Power Laser Experiment
BCC	Body-Centered Cubic
CW	Continuous Wave
DC	Direct Current
DPSS	Diode-Pumped Solid State (laser)
ECV	Electromechanical Valve
FCC	Face-Centered Cubic
FEL	Free Electron Laser
FWHM	Full-Width Half-Maximum
GL	Gyftopoulos-Levine
GPIB	General Purpose Interface Bus
IR	Infrared
IREAP	Institute for Research in Electronics and Applied Physics, UMD
LANL	Los Alamos National Laboratory
LCLS	Linac Coherent Light Source (Stanford)
MFD	Modified Fowler-Dubridge
NCRF	Normal Conducting Radio Frequency
NEA	Negative Electron Affinity
NPS	Naval Postgraduate School

NPT	National Pipe and Thread (fitting)
NRL	Naval Research Laboratory
OD	Optical Density
PEA	Positive Electron Affinity
PITZ	Photo-Injector Test Facility at DESY in Zeuthen
PMT	Photomultiplier Tube
QE	Quantum Efficiency
RF	Radio Frequency
RGA	Residual Gas Analyzer
SRF	Superconducting Radio Frequency
SS	Stainless Steel
TEC	Thermo-Electric Cooler (Peltier cooler)
UHV	Ultra-High Vacuum
UMD	University of Maryland, College Park
UPS	Uninterruptible Power Supply
UV	Ultraviolet
YAG	Yttrium-Aluminum-Garnet ($\text{Y}_3\text{Al}_5\text{O}_{12}$)
YLF	Yttrium-Lithium-Fluoride (LiYF_4)

Chapter 1: Introduction

1.1 Overview

Opening the subject of cesium-based photocathodes, it will be appropriate to provide motivation for the research herein reported. The story shall then trace backwards through increasing levels of detail towards the photocathode itself, moving into a summary of the fundamentals of photocathode performance.

1.2 Motivation

Let us begin with the end in mind. Diverse applications spanning a wide range of topics, from ship-based missile defense via directed energy, to imaging of time-resolved nanoscale molecular dynamics, are driving the development of the free electron laser (FEL) as a light source, and which we are about to introduce in Section 1.2.1. The FEL in turn, in order to produce a high quality optical beam, must be provided a high quality relativistic electron beam. This, too, shall be made more clear shortly. The source of choice for this beam is a particle accelerator driven by a high brightness photoinjector, which shall be introduced in Section 1.2.2. These can be very large devices, on the scale of tens of meters to kilometers in length. Our focus now turns to the electron beam itself, in Section 1.3, where we define what we mean by a "high quality" electron beam required from the photoinjector. The photoinjector itself gets its name from the location where the story begins, and where the electrons are born into the vacuum of the accelerating structure: the photocathode. So, from a massive machine we have traced our way back to a small, centimeter-scale device, which emits electrons via the photoelectric effect when triggered by an

incident drive laser pulse striking the photoemissive surface. Next, from this centimeter-scale device, we further shrink our scale of investigation in Section 1.4 as we introduce the fundamental operational concepts relating to photocathodes, most of which are rooted in physics occurring on the nanoscale. The important classes of photocathodes will be introduced in Section 1.5. We wrap up our introduction with a look in Section 1.7 at a proposed answer to an as-yet-unmet challenge in photocathode technology posed by the demands of high power FELs: the cesium dispenser photocathode. That challenge, the fundamental motivation for this research, was summed up by the National Academy of Sciences in 2009 in these words: "Drive-laser-switched photocathodes are the likely electron source for megawatt-class free-electron lasers. Photocathodes have been used in accelerator applications for more than 2 decades; however, they have not reached the level of performance in terms of quantum efficiency and robustness that will likely be required for a reliable megawatt-class free-electron laser." [3]

1.2.1 Free Electron Lasers

Free electron lasers stand unique among sources of coherent radiation; they can be designed to emit anywhere within a wide range of wavelengths from infrared to hard x-rays, they exhibit excellent optical beam quality, and they have the potential to achieve average power higher than any competing laser technology within certain wavelength windows. Their "tunability" (or more precisely, their design flexibility in emission wavelengths) and their beam quality enable broad applications in medicine and science, while their average power promise has drawn intense interest from the defense community.

This introductory sub-section will summarize the basic principles of free electron lasers which lead to the above mentioned qualities. The next sub-section will briefly introduce how photocathodes, and more broadly, high-brightness photoinjectors, serve as both an enabling and limiting technological frontier motivating the research contained in this dissertation.

A brief word of historical introduction is warranted. Free electron lasers, or FELs, owe their genesis to the work of several early pioneers working independently: of Hans Motz, who proposed the wiggler magnet configuration in 1951 and later demonstrated (incoherent) millimeter and nanometer radiation; of Robert Phillips, whose comparatively low-beam-energy "ubitron" in the late 1970s resembled an FEL while relying on space-charge waves to produce long-wavelength centimeter to millimeter radiation; and most notably of John Madey, who in 1970 proposed the concept and name of "free electron laser" and in 1976 demonstrated laser gain, following that demonstration in 1977 with an FEL in the optical resonator configuration exhibiting 3.5 micron coherent emission. By 1983, three additional FELs had been demonstrated: the first in Orsay, France, in the visible; the second in Stanford, California, in the near infrared; and the third in Los Alamos, New Mexico, in the mid-infrared. Rapid development has continued [1].

The characteristics of FELs which are listed above (tunability, beam quality, and average power potential) will now be addressed in turn using fundamental theory and examples of the state-of-the-art thus far achieved.

Tunable (design wavelength selectable) pulses of light from FELs find diverse applications. In medicine, laser surgery can be performed much more cleanly using 1-6 micron short

pulses. In physics, ultrafast spectroscopy demands ultrashort-pulse, extreme ultraviolet radiation. Fast, tunable ultraviolet sources are of great interest to chemists studying chemical dynamics. Biologists can study protein structure with x-ray radiation. Propagation of high-power beams in real world (particularly maritime) environments is aided by using infrared wavelengths which are least absorbed or scattered.

In all these cases, the design tunability of an FEL results from the electron-wiggler interaction where the electron beam is caused to radiate. The basic concept of the wiggler is shown in Figure 1.1: Schematic of an FEL wiggler. A set of permanent magnets is arranged in pairs as shown, where a wiggler period is the distance from a magnet pair to the next identical pair (in this simplified illustration, every other pair, but for example in the widely used Halbach configuration, every fourth pair). The alternating direction of the magnetic field causes the relativistic electron beam to oscillate (to "wobble") transversely to both the direction of propagation and the

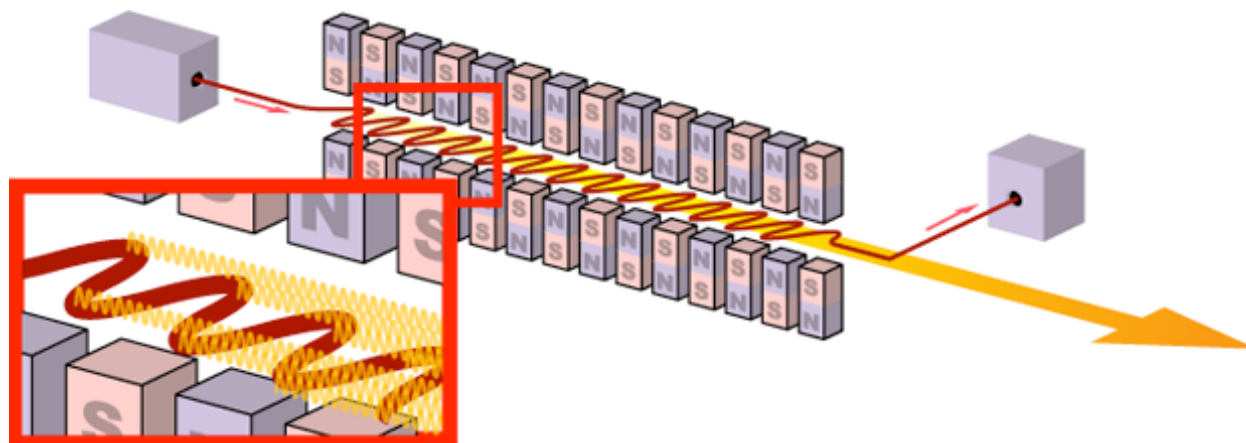


Figure 1.1: Schematic of an FEL wiggler

direction of the magnetic field. During each bend of the beam, synchrotron radiation is emitted. This can add coherently and constructively with the radiation from previous bends as long as the matching condition is obeyed (here generalized for off-axis radiation - for on-axis the third term in parentheses goes to zero):

$$(1.1) \quad \lambda = \frac{\lambda_w}{2\gamma^2} \left(1 + \frac{K^2}{2} + \gamma^2 \theta^2 \right)$$

where λ is the radiation wavelength in the lab frame, λ_w is the wiggler period in the lab frame, γ is the relativistic factor for the electron beam, θ is the emission angle of the radiation being considered, and K is the so-called "wiggler parameter" given by

$$(1.2) \quad K = \frac{e}{2\pi m_0 c} \lambda_w B_0$$

with B_0 the magnetic field strength at the center of the wiggler, e the fundamental electric charge, m_0 the electron mass, and c the speed of light. In practical units,

$$(1.3) \quad K = 933.73 \lambda_w [\mu\text{m}] B_0 [\text{T}]$$

The larger the wiggler parameter, the stronger the electron-wiggler interaction. The formula can also be interpreted as the number of wiggler wavelengths in the circumference of a cyclotron oscillation.

Two pedagogical notes are made here. This discussion uses K , whereas an older convention found in some texts [2] is to use the rms wiggler parameter $a_w = K/\sqrt{2}$. Additionally, throughout this work the term "wiggler" shall be interpreted to generally mean the alternately poled permanent magnet section of the FEL, regardless of the strength of the wiggler parameter. This is convenient for brevity, although it glosses over the oft-drawn distinction between strongly oscillatory devices, "wigglers", with $K \gg 1$ and in which the electron beam is non-overlapping with the cones of emitted synchrotron radiation from each bend, and less strongly oscillatory devices, "undulators", with $K \lesssim 1$ and in which there is full overlap of the electron beam with the cones of emitted synchrotron radiation, which leads undulators to exhibit interference effects not seen in more strongly oscillatory devices.

The matching condition ensures that in the beam frame, the optical phase front, traveling at c , slips ahead of the electron beam, traveling just slightly less than c , by exactly one wavelength for every wiggler period. The wiggler period is reduced in the beam frame by the Lorentz contraction factor γ , and the additional factor of $1/2\gamma$ corrects the radiated wavelength for relativistic Doppler shift from the beam frame to the lab frame.

Since γ is given by the beam energy relative to the electron rest mass mc^2 by $E = (\gamma - 1)mc^2$, we can determine for a given beam energy and desired output wavelength what wiggler period and magnetic field strength we should design. Conversely, when a wiggler has been built and installed, the emission wavelength may be tuned operationally by adjusting either

beam energy (γ) or magnetic field strength (B_0 , hence K , typically by adjusting the wiggler with a gradual widening or narrowing of the gap between magnet pairs). Practically speaking, FELs produce light from infrared to hard x-ray, with wiggler periods tending to be of the order of cm, wiggler parameters about unity, and beam energies from hundreds of MeV to tens of GeV.

Having determined the parameters which may be varied to tune the radiation wavelength of an FEL, either in design or in operation, the discussion now turns to brightness. Brightness is expressed in units of power per unit area per unit solid angle. A related measure is brilliance (or spectral brightness), which is brightness per percent spectral bandwidth (See Section 1.3.2). High brightness sources are desirable for scientific applications because of their high beam quality. Achievable brightness is less amenable to simple analytic expression than is tunability, due to the wide variety of possible FEL designs and the many factors which can affect power and beam quality. A modern example of a high-brightness FEL is the Linac Coherent Light Source, or LCLS, built at Stanford University. With a peak brilliance approaching 10^{33} photons per second per square mm per square mrad per 0.1% bandwidth, it exceeds previous third-generation synchrotron sources in brilliance by nearly ten orders of magnitude.

High power, related to brightness, may be divided into two categories: high average power and high peak power. The former finds interest at IR wavelengths from the defense community and from the power-beaming community, and at UV wavelengths from the lithography community. The latter is well suited to high-density physics studies using x-ray radiation and to laser machining using near-IR radiation. FELs can achieve very high power compared to conventional laser sources because the radiation is produced from the electron beam in a vacuum. Therefore

there are none of the material breakdown concerns of a solid-state or gas laser. In addition, the output optical power is proportional to the power of the electron beam itself, which can be quite significant in large accelerators. At the time of this writing, the high-average-power record for an FEL was held by Jefferson Lab with 14.3 kW in the IR. Further power increases can be expected towards hundred-kilowatt machines and more, as technological challenges are overcome. The 2009 National Research Council report on high-power free-electron laser technology [3] stated the two "tall poles" in the high-power FEL "tent", the two top technological challenges to overcome in the quest for higher average power, were high power mirror coatings and robust, efficient photocathodes.

1.2.2 High Brightness Photoinjectors

Since the FEL undulator interaction requires good overlap of the electron beam and the radiated photon beam, a very high brightness electron beam is required (see Section 1.3.2), and this becomes more stringent with shorter FEL design wavelength. Thus state-of-the-art high peak brightness photoinjectors with very tightly focused beams are those found in the shortest wavelength devices in operation: the hard x-ray FELs. And the technological frontier for photoinjection is also being pushed by those researching high average power FELs, which likewise require a high brightness photoinjector, in this case one exhibiting particularly high average current while maintaining beam quality. In both instances of high brightness, the choice of photocathode and drive laser appropriate to the application is challenging: hard x-ray FELs tend to be designed with metal cathodes (SLAC uses copper), whereas the QE of such cathodes is simply too low for

the high average power FEL designs, and the search for improved photocathodes there is ongoing.

1.3 Electron Beams

Two figures of merit are of paramount importance in the production and use of electron beams (or more generally, charged particle beams) in accelerators and hence in FELs: emittance and brightness. These are of such importance to the field of photoinjection that they will be introduced and briefly discussed in dedicated sections in this chapter. By no means is an attempt made at an in-depth derivation or analysis; in fact, excellent treatments of the subject are found in the literature, notably Reiser's canonical text [4], and in a more specialized and cathode-specific discussion, in Jensen's book on electron emission physics [5]. Rather than rederive what has been done, let us here consider a simple yet practical view of the meaning of these widely used terms and of their reporting and use.

1.3.1 Emittance

Emittance of an electron beam (or more generally a charged particle beam), at its simplest, incorporates the ideas of beam size and beam angular spread. If a beam could somehow be produced in which all electrons travelled along the same vector, indefinitely, this would be a zero emittance beam. Low emittance beams of electrons are essentially small diameter, well collimated beams, and as might be guessed, are desirable due to good preservation of the electron beam

quality during propagation through the accelerator and FEL, and as a result to strong interaction at the undulator itself. An equivalent conceptual understanding identifies the emittance of the beam as related to the volume of the beam in transverse four-dimensional trace space, where each electron has a given x and y position and momentum, and the aggregation of all electrons in the beam define an x and y size of the beam and its x and y momentum distributions (normalized to the longitudinal momentum, hence the term trace space rather than phase space), which in turn define how small the beam is and how well collimated.

Emittance can be quoted in several flavors, and in fact has an unfortunately bewildering array of forms in the literature. Let us start with the simplest case. In one dimension (say, x , representing one transverse axis of the beam), the trace space is 2D (x and $x' = dv_x/dv_z$), the ideal beam fills an ellipse, and the area of that ellipse divided by π is the emittance of the ideal beam:

$$(1.4) \varepsilon = \frac{1}{\pi} \iint dx dx'$$

This is the total emittance of the ideal beam, and is thus seen to have units of length, since x' is unitless. As an aside, Liouville's theorem can be applied (conservation of phase space area) and total emittance can be recognized as a conserved quantity.

However, since real beams are not ideal, a much more common representation in practice than total emittance is the rms emittance, obtained from moments of the (nonideal) beam distribution in trace space via:

$$(1.5) \varepsilon_{\text{rms}} = \left(\langle x^2 \rangle \langle x'^2 \rangle - \langle x x' \rangle^2 \right)^{1/2}$$

where the notation of taking a moment of a power of x or x' is defined as usual, here shown for the first moment of x :

$$(1.6) \langle x \rangle = \iint x n(x, x') dx dx'$$

with n being the 2D beam distribution, which more generally would represent the projection of the full 4D representation on to the x - x' space. Rms emittance is conserved under linear forces. Growth of rms emittance can occur with nonlinear forces, causing a twisting of the phase space ellipse into a larger, more complex shape.

Since under relativistic acceleration the beam will transform, it is common to define a normalized rms emittance which is constant under acceleration:

$$(1.7) \varepsilon_{n, \text{rms}} = \beta \gamma \varepsilon_{\text{rms}}$$

where the relativistic factors are quickly identified. A further variation sometimes quoted is effective normalized rms emittance

$$(1.8) \varepsilon_n = 4 \varepsilon_{n, \text{rms}}$$

which in fact scales the rms emittance so as to correspond to the total emittance of a uniform beam.

To complicate matters still more, the units of emittance vary widely from author to author, with some using mm-mrad, some using nm-rad, some using microns (which are still units of length and interchangeable with mm-mrad, but have the disadvantage of not explicitly direct-

ing attention to angular divergence) and still others using π -mm-mrad (which to the untrained eye can artificially reduce the emittance quoted since, to compare to units of mm-mrad, the numeric value must then be multiplied by π).

A related concept to that of transverse emittance of the whole beam (the calculation of which generally includes every particle in a given bunch projected onto the transverse trace space) is slice emittance, which, as the name suggests, makes several transverse slices down the length of the beam and projects the emittance from each onto transverse trace space separately. This concept is often discussed in support of the emittance compensation technique -- further details are a subject of beam dynamics in injectors and as such are beyond the scope of this investigation, but may be found in, for instance, Refs. [6; 7].

1.3.2 Brightness

Brightness of an electron beam, at its simplest, incorporates the ideas of beam current, transverse size, and collimation; in short, brightness expresses the total beam current achieved for a given emittance. Brightness is critical when specifying electron beams for FELs, since the average power radiated by the FEL will be limited by the average power of the electron beam (which is proportional to the current) and by its brightness. Such a limitation comes from the requisite good overlap of the electron beam with the optical mode in the FEL in order to achieve high gain. It is here that photocathodes, as part of the larger context of photoinjectors, truly shine: the brightness obtainable from these electron sources is unparalleled.

A simple formulaic representation for average brightness, assuming an ideal uniform hyperellipsoidal trace space distribution, is derivable as

$$(1.9) B = \frac{2I}{\pi^2 \epsilon_x \epsilon_y}$$

which is a function of the beam current and the x and y emittances, whereas average normalized brightness (which is constant under relativistic acceleration in the same way as normalized emittance) is then

$$(1.10) B_n = \frac{B}{(\beta\gamma)^2} = \frac{2I}{\pi^2 \epsilon_n^2}$$

where for simplicity radial symmetry has been assumed. The caveat here is important: real beams are not uniform and are certainly not hyperellipsoidal in trace space. However, the preceding formula is a useful starting point for further discussions because for any real beam one could imagine an equivalent uniform beam with the same rms volume in trace space.

The performance of the Boeing APLE, the first high duty factor photoinjector (25%), which was operated in the early 1990s, was reported at 35 milliamps average current with an effective rms emittance of 10 pi mm-mrad, at a beam energy of 5 MeV, such that the average brightness was 7.2 uA/mm²•mrad² [8].

One should not confuse average beam brightness (which is calculated from average beam current) with peak beam brightness (which is calculated from peak current within a single electron bunch), nor should one confuse beam brightness with a related quantity from the field of ac-

celerator-based light sources: spectral brightness (photons per second per unit solid angle per 0.1% spectral bandwidth). Spectral brightness is also known as brilliance, often used to characterize synchrotron light sources or FELs, which, like beam brightness, comes in the average and peak varieties.

1.4 Photocathode Fundamentals

We here discuss several of the more commonly used figures of merit and operational considerations for photocathodes. This is by no means an exhaustive discussion but highlights critical factors to be analyzed when selecting a photocathode for a photoinjection application. In order of discussion, these factors are: quantum efficiency (QE), lifetime (of QE), spectral response, temporal response, damage threshold, and energy spread.

1.4.1 Quantum Efficiency

Quantum efficiency is defined as the ratio of emitted electrons to incident photons; that is, the fraction (or percentage) of incoming photons which result in a photoemitted electron. The above definition of QE necessarily ignores such nonlinear emission mechanisms such as two-photon effects, which do not play a significant role even at the highest generally used photocathode irradiance levels of a few hundred watts per square centimeter. It likewise assumes the generation of a single photoexcited electron per photon, again a reasonable assumption for the photon energies of interest, although some indications of multiple photoexcitations from very high energy photons have been reported [9]. What QE does include is the optical characteristics of the

cathode (reflectance, transmittance, absorption, penetration depth), the electron transport characteristics of the cathode (scattering mechanisms, mean free path/relaxation time), and the surface energy barrier characteristics of the cathode (for metals, work function; for semiconductors, electron affinity and band structure; in all cases, applied field, temperature, and surface coatings). QE as stated also assumes that the emission is not space-charge limited (see the discussion in Section 5.2.1 on the Child-Langmuir law) -- in other words, that photocurrent is linear with optical intensity in every respect. It is important to note that QE is a *number ratio* of electrons to photons and as such is unitless; it is not the related ratio of *electric current density to optical irradiance*, a ratio of Coulombs to Joules. In the latter case, the ratio depends on the energy of the photon; for example, given the same QE at two wavelengths, the shorter wavelength (and hence higher energy) photons would require a higher number of microJoules per pulse to produce a bunch containing the same charge (and hence same number of electrons).

QE relates to the electric current density and the optical irradiance via the optical wavelength and Planck's constant, the speed of light, and the electron charge:

$$(1.11) QE = \frac{hc}{q\lambda} \frac{J_\lambda}{I_\lambda}$$

and can be determined experimentally by measuring the incident laser power and the resulting emission current, assuming the laser spot size is smaller than the cathode and the temporal response of the cathode is instantaneous, such that the emitted electron pulse follows the incident laser pulse exactly (this is not true for real cathode materials as discussed in Section 1.4.4, but

will not be apparent in the QE measurements reported later since they are made using CW lasers). Thus a given cathode and drive laser, in practice, produce a given photocurrent. In convenient units this photocurrent can be expressed as approximately

$$(1.12) i_{\lambda}(\text{mA}) = \frac{\lambda(\mu\text{m})}{124} P_{\lambda}(\text{mW}) \text{QE}(\%)$$

A related photoinjector example is that at the doubled Nd:YAG drive laser wavelength of 532 nm, with 2% QE, a 1 nC bunch requires roughly a $0.117 \mu\text{J}$ laser pulse. Some photocathode

Cathode material	$\lambda(\text{nm})$	QE (%)	type	drive laser at given λ
Cs ₃ Sb	527	4	semiconductor	2nd harmonic Nd:YLF
Cs ₂ Te	263	13	semiconductor	4th harmonic Nd:YLF
K ₂ CsSb	527	8	semiconductor	2nd harmonic Nd:YLF
Na ₂ KSb	532	4	semiconductor	2nd harmonic Nd:YAG
Na ₂ KSb(Cs)	532	10	semiconductor	2nd harmonic Nd:YAG
Mg	266	6×10^{-4}	metal	4th harmonic Nd:YAG
Cu	266	1.4×10^{-4}	metal	4th harmonic Nd:YAG
Ba	337	0.08	alkaline earth	N ₂
(Cs)W	375	0.11	coated metal	at UMD teststand, GaN diode
(Cs)GaAs	532	5	NEA	2nd harmonic Nd:YAG

Table 1.1: Typical peak QE values

QEs representative of those used in photoinjectors are tabulated in Table 1.1: Typical peak QE values. Note that QE tends to be low for metals and high for semiconductors. At its heart this difference can be attributed to better electron transport in semiconductors, as will be discussed later.

1.4.2 Lifetime

The lifetime of a photocathode -- that is, how long the QE lasts -- is a less well-defined concept than QE. Why is this the case? Firstly, the lifetime can be expressed under different operating conditions. Some photocathode lifetimes are quoted under storage, some under intermittent use, some under continuous duty, etc. Secondly, the lifetime is a function of many environmental and operational variables. The variables of importance depend on the cathode in question. Among these variables include vacuum pressure, partial pressure of any contaminating gases (particularly oxidizers), presence of ions and subsequent back-bombardment in DC vs RF photoinjectors, cathode heating, possible surface coating evaporation, drive laser induced material changes, etc.

Nevertheless, it is critical in practice to have a cathode which has good lifetime for the application at hand. The necessary lifetime will of course depend on that application but in almost any case longer is better. However, there is a trade-off with QE such that cathodes exhibiting good QE tend to have low lifetime, whereas low QE cathodes are very robust. This trade-off is illustrated in Figure 1.2: QE vs Lifetime of Operational Photocathodes.

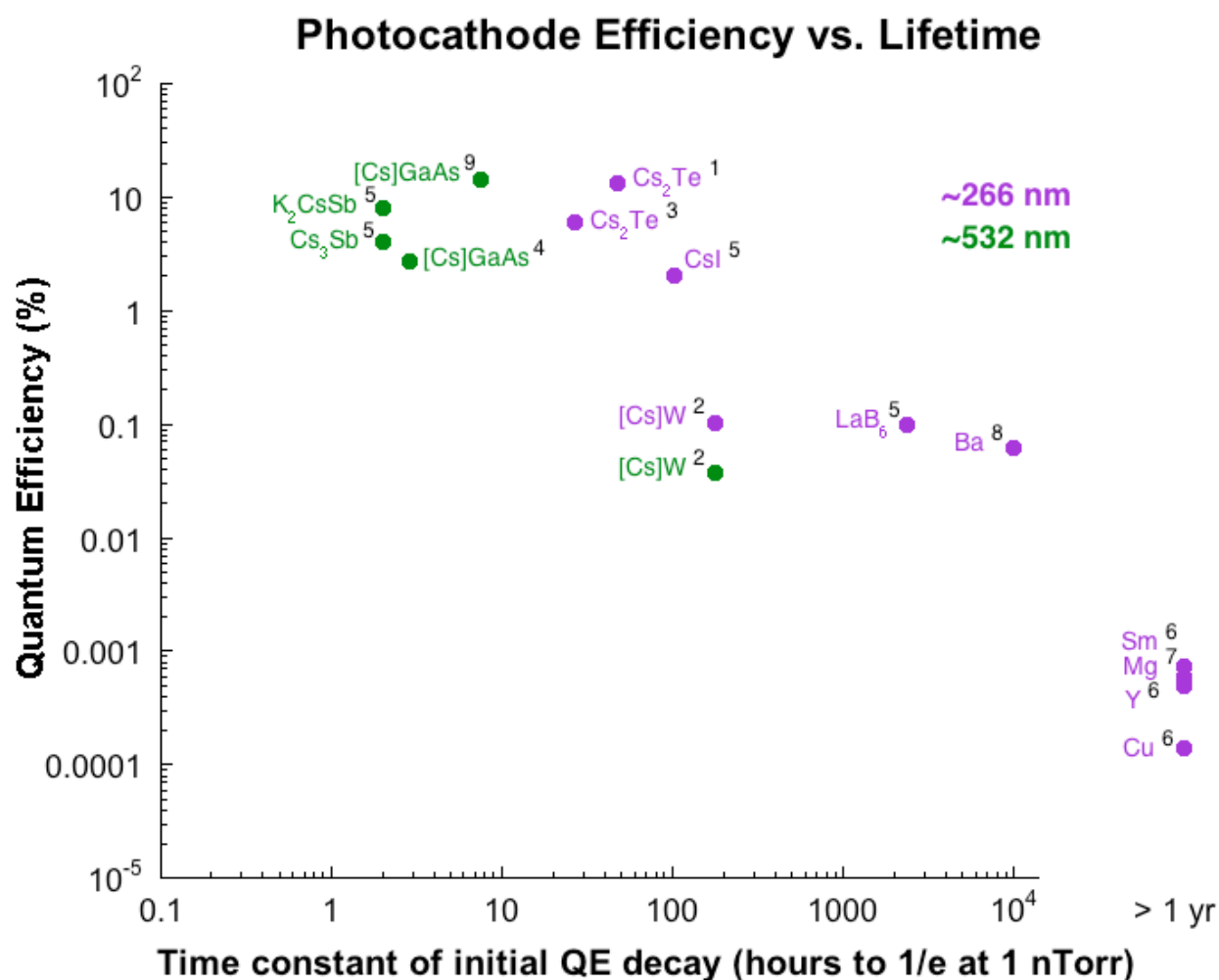


Figure 1.2: QE vs Lifetime of Operational Photocathodes

The references for the data are as follows: (1): Ref. [10]; (2): Ref. [11]; (3): Ref. [12]; (4): Ref. [13]; (5): Ref. [14]; (6): Ref. [15]; (7): Ref. [16]; (8): Ref. [17]; (9): Ref. [18]. Note that Cs:W was tested at a UV wavelength of 375 nm, not the 4th harmonic YLF/YAG of the other UV photocathodes. The QE at 266 nm would be quite a bit higher: the theory of Chapter 6 predicts it is approaching the percent level. Note also that the lifetime of the bialkali cited was in the Boeing

APLE photoinjector, which was known to have significant problems with water vapor contamination. The expected lifetime in more typical vacuum conditions would be higher.

In the figure we see clearly that the metal cathodes on the far right exhibit extended lifetime whereas their QE is abysmal. The semiconductors achieve remarkable QE, but such QE is achieved in part through delicate surface coatings which result in sensitivity to vacuum conditions.

Some care is needed in reading the graph. The horizontal axis does not directly report lifetime in a given case. This is because different machines run under widely varying operating conditions. Making the broad first-order assumption that the dominant lifetime decay mechanism is vacuum contamination which in turn is linear with background pressure, the lifetime data has been normalized to an operating pressure of 1×10^{-9} Torr. For example, if the reported lifetime were 1000 hours at 1×10^{-11} Torr, the lifetime shown above would be reduced from the reported value by a factor of 100, corresponding to an expected 100-fold increase in contamination rate at 1×10^{-9} Torr over what that cathode would have actually experienced at 1×10^{-11} Torr.

Clearly, the assumption here is not strictly valid, since contaminant partial pressure is not linear with total pressure, and since many cathodes have other limiting mechanisms on lifetime. The case of Cs:GaAs comes to mind, where extracted charge is a commonly quoted figure for cathode life, rather than time, since Cs:GaAs is typically used in DC photoinjectors where back-bombardment by ions is what destroys the cathode QE over time. Nevertheless, in this case the operating pressures are so low as to render contamination negligible, allowing the back-bom-

bardment to dominate, and at much higher nanoTorr levels the lifetime would indeed be contamination-limited.

A final note is that certain types of cathodes do not have to be replaced fully when the QE decays below a certain level. Again taking the case of Cs:GaAs, a recesiation process is commonly used to restore some of the QE of a given cathode, which can be pulled from the chamber for the process (or merely retracted into the cathode assembly, as at Jefferson Lab) and later reinserted while remaining under vacuum. Other types of cathodes (dispenser and reservoir cathodes) can be periodically or continuously rejuvenated in-situ under heating. They normally find application as thermionic sources, though this dissertation treats them in detail as potential photocathodes. See Section 1.7 in this chapter for an introduction.

1.4.3 Spectral Response

Clearly, the wavelength of the drive laser will affect the performance of the photocathode. Let us contrast the behavior of the metals and coated metals with the semiconductor photocathodes. Metals and coated metals, as derived in Chapter 6, have a QE which varies quadratically with the photon energy less the work function, at least in the visible to near-UV range where useful drive lasers are available. In contrast to metals, semiconductors such as the alkali antimonides are the same materials as used in the photomultiplier tube (PMT) industry and, as such, exhibit similar spectral response. For the photoinjector application and unlike PMTs, the key is to obtain good QE at the specific drive laser wavelength of choice, and the overall spectral response is not critical. Nevertheless it is instructive to view a selection of typical PMT response

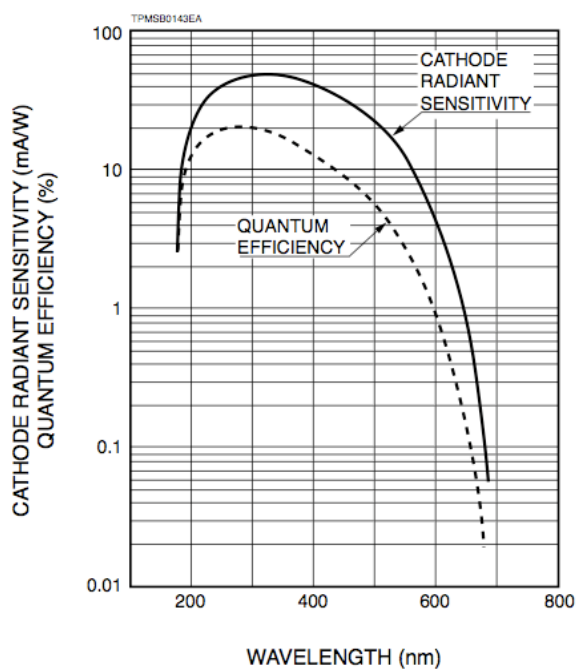


Figure 1.3: 1P28 (Cs-Sb) PMT, Hamamatsu

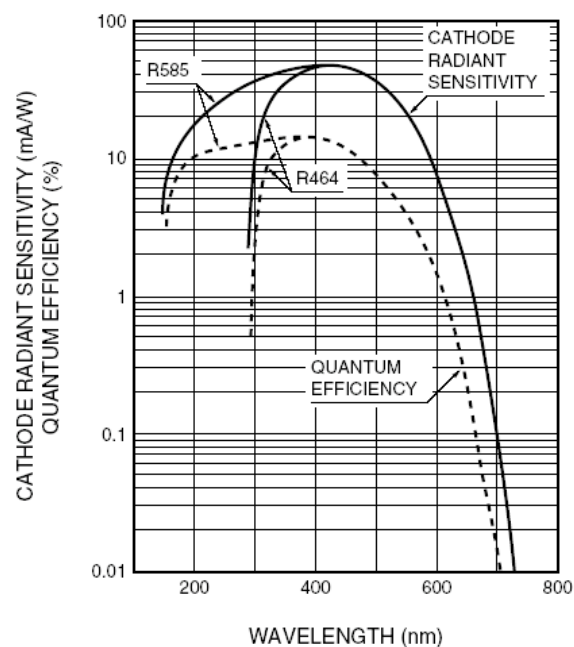


Figure 1.4: R464 (K-Cs-Sb) PMT, Hamamatsu

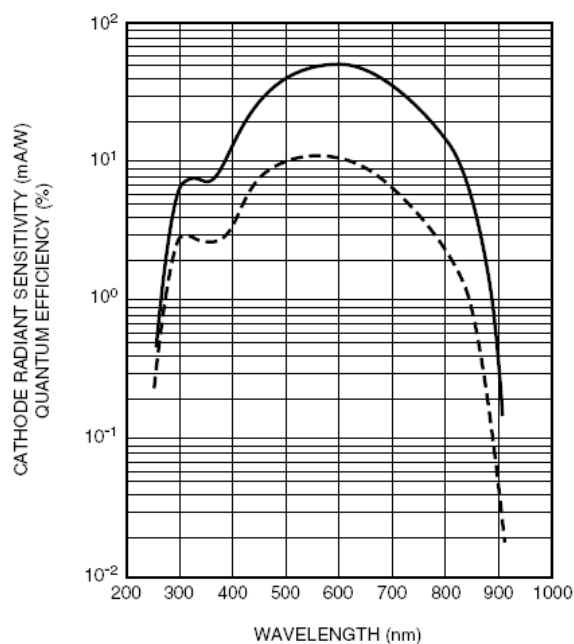


Figure 1.5: R2557 (Na-K-Sb) PMT, Hamamatsu

curves from industry. Fig. 1.3 illustrates the response of cesium antimonide. Fig. 1.4 illustrates the bialkali cesium potassium antimonide. And Fig. 1.5 illustrates the bialkali sodium potassium antimonide. Notice the sharp onset of photoemission at lower photon energy. When a photon's energy exceeds the bandgap it is capable of photoexciting electrons. Also unlike metals QE does not improve indefinitely as photon energy is increased; in part this is explained since when the photon energy exceeds approximately twice the bandgap of the semiconductor, the photoexcited electrons have enough energy that when halved through elastic scattering with valence electrons, the final state is still allowed (is above the bandgap). Therefore significant numbers of final electron-electron scattering states become available and the electron transport properties of the material degrade.

1.4.4 Temporal Response

Given a short enough laser pulse, the resulting photoemission will not be able to follow that pulse due to the finite emission time of electrons from the material, and the electron bunch will be smeared out in time compared to the original optical drive laser pulse. This finite electron emission time is dominated by the optical penetration depth and electron escape depth in the material. Cathodes with long optical penetration depth and long electron escape depth (semiconductors) exhibit longer response times, simply due to the finite time required for the electrons to transport to the surface for emission. In addition, some electrons will also be excited near the surface and emitted quickly, hence the smearing out of the temporal pulse shape and not merely a delay time in emission. Cathodes with short optical penetration depth and optical escape depth

(metals) only see photoemission from a region very near the surface, and thus are prompt emitters.

Optical penetration depths vary significantly, but in metals tend to be on the order of tens of nanometers, and in semiconductors on the order of a hundred nanometers. Electron escape depths in metals are similarly short, since the relaxation time characteristic of scattering in a metal is a few femtoseconds and for a 1 eV electron a distance of 1 nanometer is travelled in 2 femtoseconds; thus electrons escape from tens of nanometers deep within the metal. Electron escape depths in semiconductors are longer due a number of factors. There is reduced electron-electron scattering, such that the relaxation times in semiconductors are longer than in metals for the energy ranges of interest (eV). There is also a higher possibility of multiple scattering events before emission since each electron-phonon scattering event does not necessarily reduce the electron energy below that required for photoemission. As a result, a photoexcited electron near the surface but initially directed unfavorably may actually travel a convoluted path as it undergoes several electron-phonon interactions before eventually reaching the surface and being emitted. This is good for QE, since such electrons would have been lost in a typical metal, but not so good for response time. As the most extreme example of good electron transport in semiconductors consider the highly regular lattice structure and exquisite purity of III-V crystals like GaAs grown for the semiconductor industry. Such crystals have a minimum of lattice defect sites, layer interfaces, or other inhomogeneities in the crystal structure and so exhibit excellent transport properties. This leads, however, to extended response times compared to the film-deposited anti-

monides and tellurides, which means high purity crystals are not necessarily ideal for photoinjection applications.

Table 1.2: Photocathode Typical Temporal Response shows the typical behavior of photocathodes used in photoinjectors. Note that an RF photoinjector will require a more prompt emitter than a DC photoinjector, because in an RF photoinjector the field is only appropriate for acceleration across a few degrees of phase of the RF field, and for typical RF klystron frequencies of, say, 700 MHz (L band, used currently at the Los Alamos NCRF high average power photoinjector) or 2856 MHz (S band, used currently at the SLAC LCLS x-ray light source), this equates to an electron bunch length of a few picoseconds, requiring an emitter prompt on the picosecond timescale.

Cathode	Optical Penetration Depth @ λ (nm)	Escape Depth / Mean Free Path (nm)	Dominant Scattering Process	Response Time
Cu	~13 @ 263	~1	electron-electron	<<ps
K2CsSb	~60 @ 532	~30	electron-phonon	~1ps
Cs3Sb	~100 @ 532 ~20 @ 375	~30	electron-phonon	~1ps
Cs2Te	~12 @ 254	-	electron-phonon	~3ps
(Cs)GaAs	~1000 @ 532	~1000	electron-phonon	~40 ps ~10ps with 150nm epilayer

Table 1.2: Photocathode Typical Temporal Response

These values are approximate; a word regarding their origin or estimation is warranted. Response times are well known in general and have been reported for the materials in question by Moody, for instance [19]. Optical penetration depth is wavelength-dependent, and where not available directly (e.g., Cs₃Sb which is found in Sommer [20]), it can be calculated from the imaginary component of the index of refraction via $\delta = \lambda/4\pi k$. Electron escape depth is a more hairy beast, but to first order can be approximated by the mean free path. This approximation assumes escape from a narrow cone of trajectories and that a single scattering event will preclude emission, so it is a good approximation for metals and less good for semiconductors. Considering the cathode types in turn, copper has been well-studied and both the optical penetration depth [21] and the relaxation times have been reported. From the relaxation time the mean free path may be inferred if the energy of the electron is known. For copper, the electron energy has been obtained by taking the photon energy of the drive laser at 263 nanometers (4.66 eV), subtracting the work function (4.5 eV) lowered by a reasonable operational field via the Schottky effect (1 MV/m lowering it by 0.04 eV), which leaves a 0.2 eV electron. This then propagates at 5.9 km/s which means in a typical 5 femtosecond relaxation time, the mean free path is very approximately 1 nm. For the antimonides, while exact values in the literature can be hard to come by (for good reason, considering the variation in fabrication procedures, layer inhomogeneity, various doping levels, etc.), the similar structure and behavior of this class allows us to lump them together in terms of typical absorption and transport parameters. As confirmation of this, consider that optical penetration depths for the bialkali cesium potassium antimonide [22] compare very favorably with those reported for cesium antimonide [23]. In addition, mean free paths reported

for S-20 (trialkali) cathodes [22] are identical to those calculated by Jensen for cesium antimonide. For the case of cesium telluride which does not, unlike the antimonides, respond in the visible, the optical constants have been measured [24] from which the optical penetration depth can be calculated. The mean free path or escape depth was not available. Lastly, for cesiated gallium arsenide, the material has been well studied at the DC photoinjector-driven FEL at Thomas Jefferson National Accelerator Facility, which first lased in 1998 [25], and by others looking to that material as a candidate for future electron guns [26].

Interpretation of the approximate values given in Table 1.2 is straightforward; metals exhibit short escape depths as photoexcited electrons rapidly thermalize through a multitude of electron-electron scattering events in the highly populated conduction band, and so many photoexcited electrons are too deep to ever be emitted and are lost, reducing QE (which is already low due to high reflectivity). Antimonides exhibit deeper optical penetration but also deeper electron escape depths. Combined with better optical absorption and lower reflectivity in the first place, this bodes well for QE but increases response time to the picosecond level. Highly pure and regular crystalline structures such as GaAs are even better at electron transport but do not respond at the picosecond level and in fact the NEA characteristic of the cesiated gallium arsenide plays against it from a response time perspective, because electrons continue to dribble out of the semiconductor at very low energy after long transport times and many scattering events, since there is no barrier to cut off the emission at a threshold energy above the bandgap.

A point which is perhaps counterintuitive at first is that ultrashort response times, as are found in metals, can be equally as undesirable as long response times. This is a result of the non-

ideal temporal structure of a high power drive laser pulse itself. No laser pulse is perfect and a given pulse tends to exhibit fluctuations in power throughout. This noise results in part from the nonlinear frequency-doubling process typically used for photocathode drive lasers such as Nd:YAG or Nd:YLF, which takes any initial power fluctuations on the fundamental and amplifies them to the n th power at the n th harmonic. If the cathode is prompt enough to track these extremely fast fluctuations and superimpose them on the electron bunch, a bunch with longitudinally varying charge results. Such a bunch undergoes adverse interactions further down the accelerator and in the FEL, increasing emittance of the beam or radiating at undesired wavelengths. SLAC LCLS has described such a "microbunching instability" in detail and in fact has had to compensate for it with a laser heater technique. All in all, a cathode with a response time on the order of a picosecond is the "Goldilocks" emitter for RF photoinjection applications: not too fast, not too slow, but just right.

1.4.5 Additional Considerations

Other considerations come into play when analyzing photocathodes, though they may have less of a role in determining the appropriate photocathode choice for a given system. One such consideration is optical damage threshold. High intensity lasers result in fast heating of the surface, and especially for heat-sensitive coated surfaces or low thermal conductivity materials under high duty factor, this can potentially result in damage, either simply through localized overheating (and coating evaporation), or, at higher intensities still, through actual surface processing and plasma formation. Typical drive lasers do not develop such dangerous intensities,

making this effect a less critical one. Another consideration is transverse energy spread of the emitted electron bunch. This affects beam quality delivered to the accelerator, and is a function of the surface energy barrier of the photocathode. An electron, in order to be photoemitted, must have a momentum component perpendicular to the surface equivalent to a kinetic energy exceeding the barrier at the surface (assuming low field, then for metals, the work function, and for semiconductors, the bandgap plus the electron affinity). However, an electron traveling at some azimuthal angle with respect to the surface normal may still satisfy this condition while retaining a nonzero surface-parallel momentum component. This transverse momentum, upon emission, and over the entire population of emitted electrons (which are emitted over the allowed range of azimuthal angles, and some of which have had their energy modified through one or multiple scattering events before emission), results in a transverse energy spread. However, since photoinjectors utilize photons of a few eV at most, the transverse energy spread resulting will be on the order of an eV as well. After acceleration to relativistic energies this is not a critical consideration in most cases, at least not until one is concerned with the so-called thermal emittance of the cathode which arises from the aforementioned nonzero transverse momenta. One may say, why not consider longitudinal energy spread as well? At relativistic beam energies the beam is effectively "frozen" longitudinally and therefore this too is not a serious matter as long as initial acceleration to such energies is rapid and space charge forces within the electron bunch do not have time to detrimentally affect it.

1.5 Photocathode Types

Photocathodes fall broadly into four classes of materials, each with unique emission properties stemming from optical absorption, electron transport, and emission barrier characteristics. These classes are: metallic, coated metallic, semiconductor, and negative electron affinity (NEA) cathodes -- essentially coated semiconductors.

1.5.1 Metals

Metallic photocathodes are exemplified by the cathode material being an elemental metal, such as copper, magnesium, lead, niobium, etc. Some cathodes are more suitable for room temperature operation (Cu, Mg) while others are preferred in superconducting cavities (Pb, Nb). Metal cathodes exhibit low QE up to four or five orders of magnitude below that of the best semiconductor photocathodes, extremely long lifetime of months or years even under harsh operating conditions, poor or nonexistent visible response but improving into the UV, and very prompt emission on the sub-picosecond scale. Metals are not only used as photoemitters but as field emitters in the form of sharp tips or of arrays of such tips.

1.5.2 Coated Metals

Coated metals improve the QE of metal photocathodes by adding a low work function coating to the surface. Coated metals exhibit low but reasonable QE on the order of a tenth of a percent, shorter lifetime than metals due to the sensitivity of the coating to contamination, evapo-

ration, or damage, improved visible response, and similarly prompt emission. Examples include cesiated tungsten and cesiated silver, both of which are discussed in this work. More commonly such cathodes are not used as photocathodes but rather as thermionic sources: consider barium, scandate, or M-type dispenser cathodes. While the coatings on these cathodes may not last long unrejuvenated, they are being continuously replenished in situ by a subsurface reservoir of the work function lowering material. This dispenser concept will be detailed later and its application to photocathodes is the thrust of this work.

1.5.3 Positive Electron Affinity Semiconductors

Semiconductors have excellent QEs and in fact hold the record for the highest QEs ever achieved, on the order of 50% in some vacuum tube devices. This is obtained at significant cost: lifetime is severely reduced (in some cases to days and in others, mere hours). Spectral response is good across the visible, generally peaking somewhere between the green and the near UV, and falling off rather quickly in the red to infrared on the one hand, and in the UV on the other. Semiconductors are not nearly as prompt emitters as metals, but for those which can be fabricated as thin coatings, reasonable promptness on the picosecond scale can be achieved readily.

1.5.4 Negative Electron Affinity Semiconductors

When coated with a low work function material, it is possible in some specialized cases to reduce the electron affinity of the semiconductor to below the bottom of the conduction band (hence the term negative electron affinity, or NEA), such that any photoexcited electron will

have sufficient energy to be emitted. Effectively there is no emission barrier in such cathodes. The classic example is cesiated gallium arsenide, which is also attractive as a spin-polarized electron beam source when grown on a gallium arsenide phosphate substrate [27]. Other III-V semiconductors can also be NEA. QE can be very good, more than 5% with a green drive laser for cesiated gallium arsenide. Lifetime is extraordinarily sensitive to vacuum conditions, and with incredible effort (i.e., picoTorr type vacuum) such cathodes can last for days or weeks of operation [28], but almost exclusively are limited therefore to superconducting photoinjectors with their excellent vacuum capabilities. Spectral response is similar to the other semiconductors and like them can utilize a green drive laser. Temporal response can be poorer, primarily due to the thickness of the crystals used and the time it takes electrons to trickle out after being photoexcited.

1.6 Comparison of Emission Mechanisms

The photoemission process involves excitation of an electron by a photon, transport of that electron to the surface, and emission over the energy barrier. In Fig. 1.6 are contrasted the emission mechanisms of the thermionic dispenser cathode with the metal and semiconductor photocathodes. The dispenser uses a metal substrate with a low work function coating like barium, and at elevated temperature (~ 1000 °C) significant populations of electrons in the Maxwell-Boltzmann thermal tail are excited above the vacuum level and emitted. The room-temperature uncoated metal's work function requires much higher energy photons for photoemission than the semiconductor where only the band gap and electron affinity must be overcome.

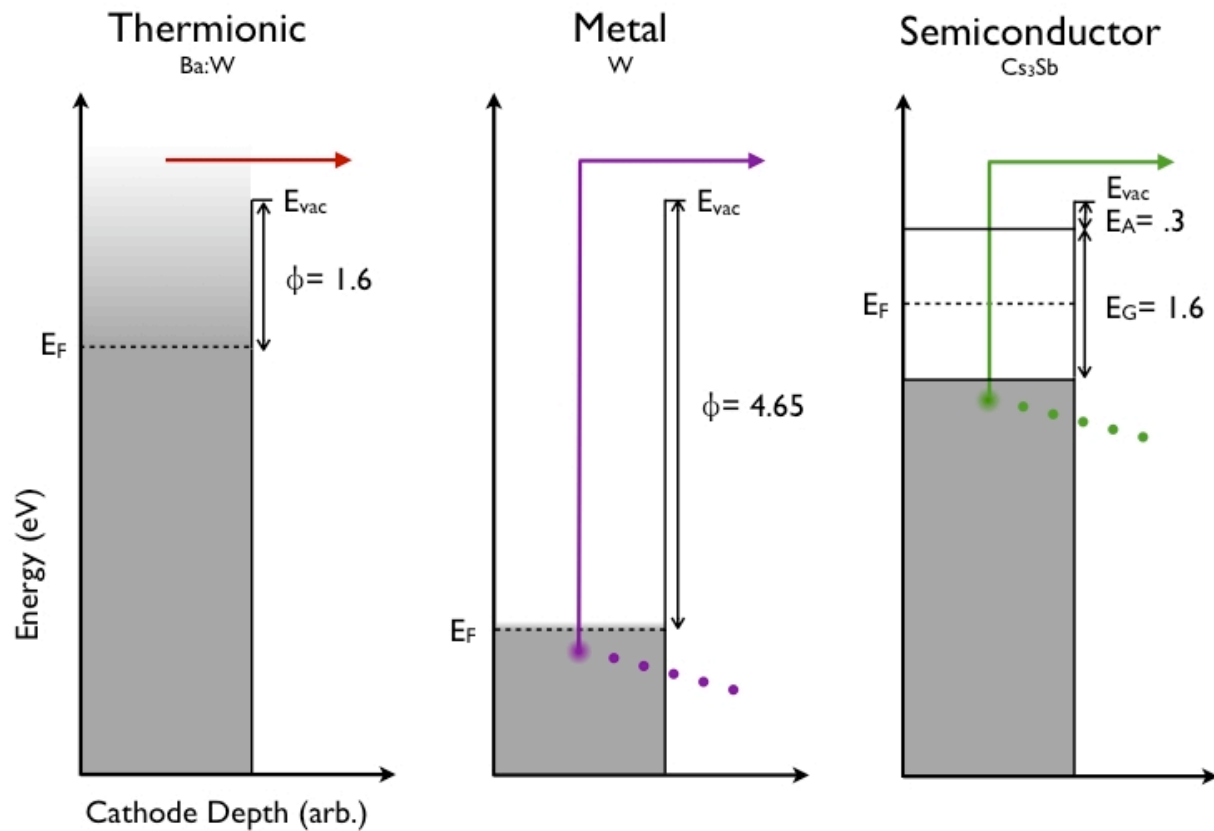


Figure 1.6: Emission barriers: thermionic, metal, and semiconductor (to scale, zero applied field)

In metals, the conduction band (populated to the Fermi energy at zero temperature) overlaps the valence band. In semiconductors, the band gap separates the conduction and valence bands, with tremendously reduced electron-electron scattering.

1.7 Dispensers

Since a metal with a low work function coating has much improved electron emission characteristics over the bare, uncoated metal, cathodes of this sort have long been studied. But

these coatings are susceptible to evaporation or damage, and as such, the invention of the dispenser cathode was a significant advance. In this cathode, a porous metal matrix forms the cathode surface. Either impregnated within the matrix or in a reservoir beneath the porous surface is a work function lowering material. Under heating this material continuously rejuvenates the surface layer by diffusion. A dispenser of the reservoir type designed and used at UMD is shown in cross-section in Figure 1.7. Note the source of free cesium contained within the reservoir, ready for activation under initial heating which will melt the indium seal and allow the Cs:Bi intermetallic compound to sublime cesium into the reservoir, which in turn will allow that cesium to diffuse to the surface, forming a low work function, improved quantum efficiency partial monolayer coating.

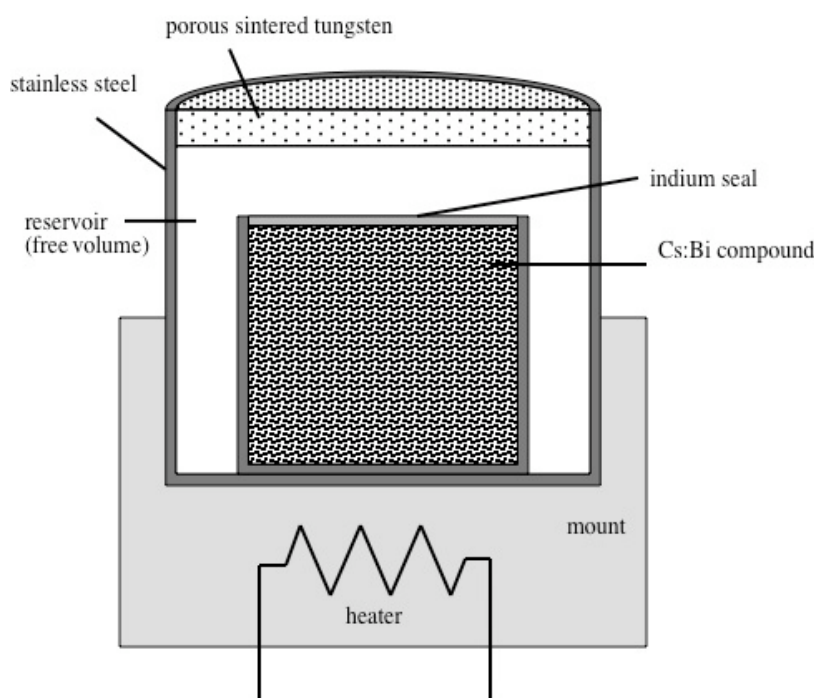


Figure 1.7: Reservoir Type Dispenser Cathode, cross-section

Chapter 2: Historical Context

2.1 Electron Emission and the Photoelectric Effect

Electron emission, as a fundamental process in nature, was observed (Nollet, 1749; Morgan, 1785; Hittorf, 1858; Crookes, 1878) and even patented (Edison, 1884) years before it was understood. The first observation of electron emission which was definitively identified as such was by J. J. Thompson in 1897, whose "cathode rays" were shown to be beams of negatively charged particles. Thompson also made the first charge-to-mass ratio measurement of the electron and studied the effect of electric and magnetic fields on electron beams.

The history of photoemission began in 1885 when Heinrich Hertz, experimenting with generation and detection of the newly discovered radio waves, observed that ultraviolet radiation from the arcing in the generator, when incident on the cathode in the detector, caused a measurable increase in current. Hertz had discovered the photoelectric effect [29]. Philipp von Lenard's subsequent experiments, published in 1900, revealed a puzzling problem: a threshold wavelength for photoemission existed for any material [30]. Einstein correctly explained this threshold as a quantum effect [31], for which he subsequently received the 1921 Nobel Prize.

Thus, by 1905, the identification of the electron and photon and their interaction through the photoelectric effect was complete. But fundamental identification did not entail an understanding at the nanoscale: the details of photoemission at the nanoscale would take decades to develop. For example, work function as a macroscopic concept was introduced by Kelvin and

later Richardson around the turn of the twentieth century, but its lowering through the dipole interaction of a cesium layer [32; 33], is of more recent vintage.

Much of the motivation for these studies would wait for the discovery of practical photocathodes. Throughout the twentieth century, the discovery of new and improved photocathodes would continue albeit at an erratic pace. Photocathode development itself found a large driver early on in the photomultiplier tube (PMT) industry. More recently, additional impetus for development of photocathode technology has come from the particle accelerator community and in particular the demands of high brightness photoinjectors.

2.2 Photoinjection

2.2.1 Introduction

Early designers of high brightness injectors found challenges with the existing thermionic cathode technology. A quick comparison of the peak brightness achievable from a thermionic versus a photocathode source is instructive. Refer to Eq. (1.10) and note that the proportionality to peak current is linear, and assume similar beam divergence. Since a thermionic cathode is not generally operated with best lifetime at current densities of much more than 1 A/cm^2 (although with much reduced lifetime current densities in excess of $10\text{-}100 \text{ A/cm}^2$), and since a photocathode can achieve peak currents on the order of 100 amps from a 10-millimeter-square drive laser spot, one can estimate to first order a possible gain of two orders of magnitude in peak brightness from the use of a photocathode: an order of magnitude from the higher current, and another from

the smaller beam size (and hence smaller emittance). An additional advantage is the critical ability to quickly switch the electron source on the picosecond time scale thereby creating a bunch already of the appropriate length for RF linac acceleration, and obviating the need for later bunch compression techniques which may be detrimental to emittance. Laser-switched photocathodes make this possible; with thermionic sources the emission was either continuous or the switching was electrically gated and severely limited by the switching speed of the high voltage electronics. The development of injectors, from thermionic machines requiring bunch compression after the cathode [34], to photoinjectors capable of much lower emittance and producing picosecond

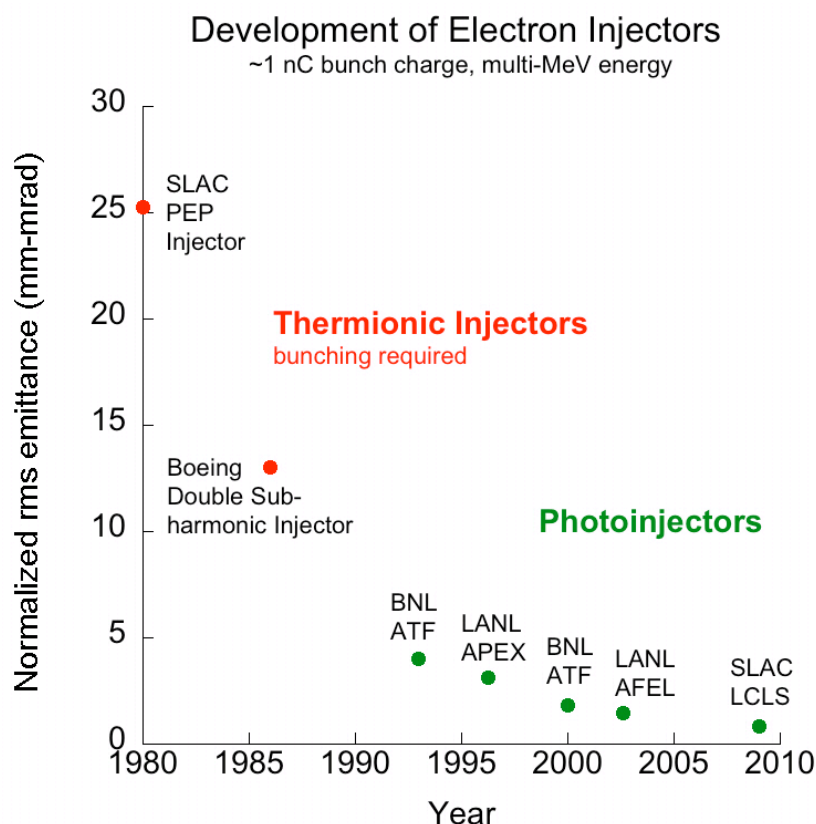


Figure 2.1: Transition from thermionic to photo-injection

electron bunches without compression, is shown in Fig. 2.1, adapted and updated from Ref. [35].

2.2.2 Types of Photoinjectors

A photoinjector is simple in concept: a photocathode emits electrons when triggered by a drive laser pulse, and the electrons are quickly accelerated to relativistic energies by a strong electric field. Variation in the types of photoinjectors for FELs simply results from different approaches to the method of generating the accelerating field, and variation in the types of photocathodes in use stems from the constraints or advantages of the photoinjector using it, as well as beam requirements from the FEL.

The applied field may be radio frequency (RF) or direct current (DC), and the RF linear accelerator (linac) accelerating structure into which the beam is injected may be normal conducting or superconducting. Thus three main categories of photoinjectors, or guns (as in "electron guns") emerge: normal conducting RF (NCRF), superconducting RF (SRF), and DC. These shall be briefly introduced in turn. Each category is pushed to achieve the highest possible accelerating gradient: high gradient means shorter beamline to attain a given beam energy, and also has the advantage of quickly accelerating a bunch of electrons into the relativistic regime where internal repulsive forces of the beam are less problematic to maintaining beam quality.

RF photoinjectors use an RF cavity (frequencies of order 1 GHz are most common for high current operation though photoinjectors have been built and tested from 144 MHz to 17 GHz) in order to produce the high fields required to accelerate the electrons. Short bunches of

electrons are required since only a few degrees of phase of the RF field is suitable for acceleration which preserves good beam quality. These bunches are produced at exactly the right moment by synchronizing the photocathode drive laser with the RF klystrons to inject the electron bunch at optimum phase. A solenoid near the cathode provides focusing and allows emittance compensation to further improve beam quality. RF photoinjectors offer much higher gradient operation than DC guns. In general, the higher the RF frequency, the higher the gradient which can be achieved: the SPARC-X 2.856 GHz (S-band) photoinjector has 120 MV/m peak [36] and 25 MV/m accelerating gradients, patterned off of the very similar LCLS at SLAC.

NCRF guns in particular are the first and most common type of photoinjector. They involve high power RF with high ohmic losses in the cavity walls and a great deal of heating. Active cooling of the walls via complex, high-flow-rate cooling channels is essential to preserve structural integrity and field quality, but still the electric field gradients achievable are limited in part by the heating of the walls. This is ameliorated by operating in pulsed mode (less than 100% duty cycle, where 100% would be defined as every RF cycle being loaded with an electron bunch) so that overall heating is reduced, and in pulsed mode NCRF guns have exhibited the highest operational accelerating gradients of any photoinjection technology. Whereas pulsed mode guns can achieve peak accelerating gradients in excess of 100 MV/m, CW operation is heating-limited to about 10 MV/m [37].

SRF guns can achieve high field in CW operation because they have low losses to RF heating, with peak accelerating fields of order 20 MV/m demonstrated at the only currently operational SRF photoinjector, at Rossendorf, Germany [38]. Future designs are expected to reach 50

MV/m. But SRF guns have their own challenges because they operate in the superconducting regime, specifically with the liquid helium plants associated with maintaining large superconducting linacs at 2 K. The extremely high Q (narrow resonance) niobium cavities are also an engineering challenge. Nevertheless, high duty factor/high gradient is a compelling combination that drives development and has led to planned construction of several devices worldwide.

DC guns were first used with thermionic injection, not photoinjection. But whereas with thermionic cathodes the field had to be gated to switch the beam, a laser-switched photocathode allows for a steady DC field. DC gradients are limited by the breakdown of the dielectric (usually ceramic) insulators used to separate the high voltage components. Jefferson Lab, for instance, operates in the 350 kV range with about 4 MV/m at the cathode. The lower gradient means lower bunch charge is used in general compared to what is possible with RF photoinjectors. DC guns also tend to be larger than RF devices to allow larger high voltage standoffs.

2.2.3 Historical Development

NCRF Photoinjectors

The RF photoinjector was first introduced at Los Alamos National Laboratory (LANL) in 1985 [39] in support of efforts to develop a high power free electron laser. Emittance compensation was first used to produce higher quality electron beams from RF photoinjectors in 1989 [6] at the LANL HIBAF machine based on earlier observations of unexpectedly low emittances downstream from the cathode, and has since become a widespread technique to achieve low rms emittance in space-charge dominated beams. It has the happy effect of reducing the required ac-

celerating gradients to preserve good beam emittance which in turn reduces ohmic heating in a normal conducting RF (NCRF) gun. The AFEL at LANL was built using lessons learned from HIBAF and achieved 1.6 mm-mrad emittance at 1 nC bunch charge and up to 20 MeV, with a duty factor of 0.01% [40]. LANL demonstrated first lasing of photoinjector-driven FELs in the infrared [41] and later in the ultraviolet [42]. Meanwhile, Boeing had built a high duty factor NCRF gun as part of the Average Power Laser Experiment (APLE) in 1992. The performance of the Boeing APLE high duty factor photoinjector (25%), with a 35 mA (average) beam current at 5 MeV had somewhat higher emittance of 5-10 mm-mrad, but high bunch charge of 1-10 nC. Modern high-average-current NCRF photoinjectors are currently under development or design at Los Alamos, BESSY in Berlin, and Thomas Jefferson National Accelerator Facility [40]. Among lower duty factor machines, the highest bunch charge photoinjector in the world is at Argonne National Laboratory's AWA facility [43]. This machine delivers up to 160 nC bunches with 8 MeV energy, and routinely produces 60 nC bunches with 7 ps bunch length for a peak current of about 10 kA. This gun uses a magnesium cathode with a 248 nm drive laser and a QE of 0.014%.

SRF Photoinjectors

Since in NCRF injectors the improvement of high accelerating gradient simultaneously with high duty factor leads to unacceptable heating of the structure via RF ohmic losses, superconducting RF (SRF) accelerators are of interest for photoinjection. A photocathode was first used in an SRF cavity in 1988 at the University of Wuppertal. Cesium antimonide cathodes used

there lived several days in the excellent vacuum of the SRF cavity but at cryogenic temperatures had QE of at best 5% [44]. A purpose-built SRF gun was first operated with a photocathode at Forschungszentrum Dresden Rossendorf in 2002 [45], using Cs₂Te. The cathode had surprisingly low QE at cryogenic temperatures of at best 0.25% at 266 nm, and due to this and to limitations of the drive laser, 20 pC bunch charge was the most achieved, though at a 22 MV/m accelerating gradient with 0.9 MeV beam energy resulting. New designs at Rossendorf [46] allow emittance compensation to be used with SRF cavities and are expected to attain 1 mm-mrad emittance with much higher 2.5 nC bunch charge. Now under construction here in the U.S. is an SRF injector at Brookhaven National Laboratory, designed to demonstrate high average current operation.

DC Photoinjectors

A DC photoinjector with a GaAs photocathode producing a polarized electron beam was introduced at the Stanford Linear Accelerator Complex (SLAC) in 1977. The DC photoinjector was first built and operated as a driver for a superconducting linac and FEL at Jefferson Laboratory in 1996 and has continued to undergo development [13]. It used from the outset an NEA cesiated gallium arsenide photocathode with 5% QE at 532 nm [47]. It is the world's highest-average-brightness photoinjector in operation [37]. The machine is used to drive an infrared FEL which currently holds the world record for average power from an FEL, 14.3 kW at 1.6 microns.

Candidate photocathodes for NCRF, SRF, and DC photoinjectors continue to be an active, ongoing area of research and development. Continued interest, especially in the high aver-

age power photoinjector regime, is in attaining simultaneously both improved cathode lifetime and excellent quantum efficiency.

2.3 Photocathodes for Photoinjectors

Since we have introduced four photocathode types in the introductory chapter (metallic, coated metallic, semiconductor, and NEA), we shall review the history and utility of each type in photoinjection applications. We shall emphasize in the discussion of coated metals the overlapping category of dispenser cathodes used as photocathodes. As these cathodes are introduced, it is important to bear in mind the advice of the National Research Council's Committee on a Scientific Assessment of FEL Technology for Naval Applications: "Photocathodes have been used in accelerator applications for more than 2 decades; however, they have not reached the level of performance in terms of quantum efficiency and robustness that will likely be required for a megawatt-class free electron laser." [3].

The ideal photocathode for a high-current (1 A average, 1 kA peak) photoinjector can be sketched. This hypothetical cathode should have an excellent QE of more than 10% so that the average current requirement can be achieved with existing drive laser technology. High QE in the green would additionally enable the drive laser, typically Nd:YAG or Nd:YLF, to use frequency doubling, rather than the more power-fluctuation-prone pulses associated with frequency tripling or quadrupling. The cathode should be resistant to QE degradation in all forms: RF or laser heating, ion bombardment, contamination. The lifetime should enable reliable operation without the need for frequent change-out of the cathode, so more than 100 hours is desirable

and the longer the better. High fields of perhaps 50 MV/m will be seen by the cathode and it must be able to maintain performance these conditions: dark current from field emission must be minimized. (Small nanoprotrusions with low work function become strong field emitters under extreme fields.) The particular material in question must also be able to achieve the kind of current densities required (hundreds of amps per square centimeter) in order to achieve such high average currents in a small beam. It should have picosecond response time in order to create short pulses for the RF linac yet average out sub-picosecond power fluctuations on the drive laser. No photocathode currently exists combining all these characteristics, and the selection of a photocathode for a particular application involves trade-offs among all points, while research continues to probe possible new technologies. Such is the focus, indeed, of this work.

2.3.1 Metals

Metal photocathodes are extremely robust but with their deplorable QE have limited applicability to high average current operation. Nevertheless their use is widespread where high average current is not an overriding design goal. The Linac Coherent Light Source (LCLS) at Stanford, which recently demonstrated the world's first lasing at 1.5 Ångströms, uses a copper cathode. A powerful drive laser produces up to one nanocoulomb per bunch, though the operational bunch charge tends to be less than half that for emittance reasons. But the repetition rate is extremely low and so the average current is likewise low at LCLS. Among other metals, Brookhaven National Laboratory has demonstrated the use of samarium as a metal photocathode as well as magnesium [15]. Yttrium, oddly enough, is the record-holder in terms of highest cur-

rent density achieved from a photocathode [48]. Superconducting guns have investigated niobium [49] and lead [50] because of the simplicity of having a photoemitter which is also a superconductive metal, so that the back wall of the SRF cavity doubles as the cathode.

2.3.2 Coated Metals and Dispensers

The early pioneering work on coated metals (cesiated tungsten being of peculiar interest to this work, for which the seminal reference is Taylor and Langmuir's in 1933 [51]) and their emission characteristics, combined with the massive impetus during and post- World War II with the ensuing effort to develop powerful microwave sources for radar systems, led to the development of the core technologies required for high power RF sources [5]. Of these, one was the dispenser cathode, first introduced as a reservoir type by Phillips Corporation in the 1940s, with impregnated versions appearing the next decade, further advances to M-type (Os and Ru coated) dispensers in the 1960s, and controlled porosity dispensers beginning in the mid-1970s (developed by L. Falce and others at NRL, Varian, and Hughes, and featuring uniform emission, reduced Ba evaporation, and increased lifetime). In all these instances, the dispenser was used as a thermionic cathode, not a photocathode -- the requirements for extremely high quality, low emittance beams from the accelerator and FEL community which motivated the development of the photocathode, were and are not as pressing a factor in microwave sources using thermionic dispensers; these have rather been concerned with obtaining high current densities while maintaining operational reliability.

Dispensers are of course not the only thermionic source; tungsten (W) and lanthanum hexaboride (LaB_6) have a long history of use as thermionic electron emitters. Among dispensers themselves, there are various flavors: the basic sintered tungsten dispenser (using alkali or alkaline earth metals to activate the tungsten surface), the thoriated tungsten cathode (or filament, as found in the residual gas analyzer in the apparatus described in this work), the oxide dispenser cathodes (converting alkaline earth carbonates to alkaline oxides for emission at somewhat more modest temperatures), the alloy dispenser cathodes, and the scandate cathodes. A general historical overview, adapted from Ref. [52], is shown in Figure 2.2.

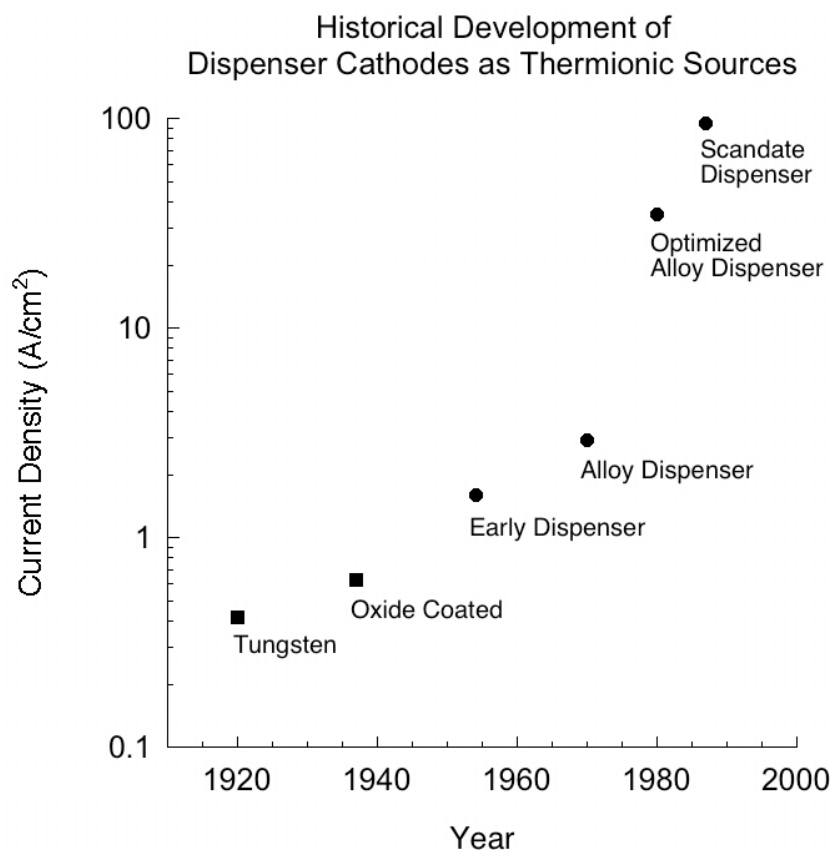


Figure 2.2: Historical Development of Dispenser Cathodes as Thermionic Sources

Of course, the higher the operating current density from a given thermionic source, the hotter it must run to maintain that, and so the shorter the dispenser lifetime. One would not expect good lifetime, for instance, from continuously running a thermionic dispenser at 100 A/cm^2 . As a thermionic source, the dispenser cathode finds application in a dizzying array of technologies, including cathode ray tube displays, klystrons in radar and electronic warfare systems, satellite communication transmitters, magnetrons in kitchen microwaves, and of course particle accelerators, in the latter case not only sometimes as beam sources but also as components in the klystrons feeding RF to linac accelerating cavities.

The direct application of thermionic-type dispensers to photoinjection has been limited. CANDELA at Orsay in France has reported on the installation and operation of a calcium aluminum carbonate dispenser utilizing a porous tungsten matrix, illuminated by a frequency-tripled Ti:sapphire laser, in their S-band gun [53]. This dispenser has a QE of 0.1% and is rejuvenated periodically. Some tests have been performed at Argonne National Laboratory's Ballistic Bunch Compression (BBC) gun with M-type thermionic dispensers in a photoinjection configuration, with excellent results [54]. And at the University of Maryland (UMD), as is detailed in Section 2.4.2, tests of several types of dispensers as photocathodes were performed although not in a photoinjection configuration [55; 56].

Most if not all of the dispensers discussed above used some species of alkaline earth metal as the actively diffusing low work function coating. The thrust of this work is to introduce and detail the research at the University of Maryland in the development and characterization of alkali-based coated photoemissive surfaces for dispenser photocathode applications, particularly

cesium-based cathodes, in contrast to the alkaline earths historically used. Maryland is not alone in this effort: other implementations of cesium dispensers for photoinjection have been studied at, for instance, Los Alamos National Laboratory [57]. Cesium offers lower temperature operation than the alkaline earths, and with the smallest electronegativity of any non-radioactive element on the periodic table, its work function lowering abilities are impressive.

2.3.3 Positive Electron Affinity Semiconductors

Semiconductor cathodes offer unsurpassed QE, but for all their importance, the development of semiconductor photocathode technology has come in irregular steps -- and for the early discoveries truly involved more art than science [58]. The first of these fortuitous discoveries was the S1 (silver-oxygen-cesium) photocathode in 1929 by Koller [59] and Campbell [60]. Searches for better photocathodes with better quantum efficiency or spectral response were confounded by a lack of understanding of photoemission physics, and became exercises in trial and error. While the first semiconductor photocathode, cesium antimonide, was found in 1936 [61], it would not be until 1955 that the first multi-alkali antimonide was discovered [62]. The continued development of semiconductor photocathodes has often been one punctuated more by luck than guiding insight [58]. At present the most discussed PEA semiconductor cathodes in the photoinjection community are those already demonstrated in operating guns: cesium telluride (with UV drive lasers) and the alkali antimonide family (with UV or green drive lasers).

2.3.4 Negative Electron Affinity Semiconductors

NEA cathodes became some of the first photocathodes to be developed on a strictly scientific footing [58]. They are commonly, though not exclusively III-V semiconductors, and most famously cesiated gallium arsenide, which is capable of spin-polarized electron emission if so desired, are used in the highest power superconducting DC FELs [13], but their sensitivity to vacuum conditions precludes operation in the harsher environment of NCRF photoinjectors.

2.4 Foundational Research at UMD

2.4.1 Introduction

Understanding and demonstrating reliable, high-brightness electron emission from new or refined cathodes has in large part been motivated by the demands of next-generation free electron lasers (FELs). Here at the University of Maryland, in collaboration with Dr. Kevin Jensen of the Naval Research Laboratory, a concerted effort has been made for the past five years to develop the essential physics and engineering of suitable cathodes for these next-generation FELs. Some of that work is reported in later chapters, but this summary is meant to place that work in the proper context.

In 2001, shortly after Dr. Patrick O'Shea was appointed professor to the Electrical and Computer Engineering department at Maryland and joined the Institute for Research in Electronics and Applied Physics (IREAP, formerly the Institute for Plasma Research), he published a re-

view article in Science magazine with co-author Dr. Henry Freund [1] on the development of FEL technology up until that time.

"The development of linac-based FELs with both higher power and shorter wavelength was delayed by technological issues. In particular, the electron brightness was the principal limiting factor. The essential breakthrough was the development of laser-switched photocathode electron sources (photoinjectors) to replace thermionic cathodes, improving the electron beam brightness in rf linacs by two orders of magnitude."

Research at Maryland under O'Shea's direction has focused since that time on photocathodes and their application to high-brightness electron injection, with funding provided under the Joint Technology Office and the Office of Naval Research. The past five years (2003-2008) have seen significant advances in our experimental capabilities, in our demonstrations of new photocathode concepts, in our predictive modeling of photoemission, and in our application of that theory to beam simulation codes.

In the following pages is a summary of our research publications through that time period: eighteen journal articles and twenty-three conference publications. For clarity of reading, they are broadly categorized into (1) experimental results and (2) theory and simulation results. Experimental results were conducted serially and are presented chronologically. Theoretical and simulation results were sometimes conducted in parallel, and so are organized topically, reverting to the chronological narrative within those topics. Overall, there naturally follows a logical

progression from first principles through subsequent refinements to our most current understandings of the processes involved.

The intent is to provide a historical walkthrough of the content and context of this research, and to highlight critical breakthroughs in each case so as to direct the interested reader to the appropriate publications discussing them.

2.4.2 Experimental Results

2003

Photocathode research at the University of Maryland under O'Shea's leadership, from the very beginning, centered on the dispenser cathode concept as a means of extending photocathode life. Dispenser cathodes can continuously or periodically bring fresh low-work-function material to the surface of the cathode, replenishing lost material and rejuvenating quantum efficiency (QE). This in-situ rejuvenation makes dispensers an attractive candidate for long-lived, robust, efficient photocathodes. Early work at UMD by Dr. Don Feldman and graduate student Matt Virgo used existing Scandate dispenser cathodes, as reported in Ref. [56], and looked at nonlinear photoelectric emission when using an infrared drive laser. Scandate cathodes use a porous tungsten matrix impregnated with scandium and barium oxides, as well as calcium aluminate. Under heating scandium and barium diffuse to the surface and lower the workfunction to between 1.5 and 2.0 eV. The UMD tests used a 4.5 ns pulsewidth Nd:YAG drive laser while varying the electric field at the cathode between 0 and 2.5 MV/m. The second, third, and fourth harmonics (532,

355, and 266 nm) exhibited normal single photon emission in direct proportion to laser intensity and independent of applied field up to 2 MV/m. At the fundamental of 1064 nm, unlike single-photon emission, the photocurrent was found to be a strong function of both the initial lattice temperature and the applied electric field as well as the laser intensity. It was immediately noted that the photon energy of 1.17 eV was not sufficient to overcome the workfunction barrier, nor were there appreciable numbers of electrons in the thermal distribution with high enough energy to be photoemitted. However, laser heating of the free electron gas in the metal not only shifted the thermal distribution to higher energies, but it also explained the nonlinearities in photoemission. Future work at UMD, particularly in collaboration with Dr. Kevin Jensen of NRL in the development of theory to support predictive simulations, would keep firmly in mind the importance of including the time-dependent effect of laser heating on photoemission.

2004

In 2004 [63], the UMD group reported on a continued comparison of experiment to theory, now using three types of dispenser cathodes: B type, scandate, and M type. B type cathodes consisted of a sintered tungsten matrix impregnated with barium calcium aluminate, scandate cathodes of the same matrix but using scandium and barium oxides, and M type of a thin osmium coating on an otherwise B type cathode. Quantum efficiencies were measured for the second through fourth harmonics of a Nd:YAG laser (532, 355, and 266 nm). Even for the third harmonic the QE did not exceed 0.08% for scandate and 0.26% for M-type cathodes.

The explanation of QE for these three dispenser cathode types was given in a theoretical model of time-dependent photoemission, but that model contained certain inadequacies, and the interested reader should refer rather to the more recent works published since that time by Jensen et al. Nevertheless, the 2004 application of a physics-rich photoemission code as a predictive estimator of performance was an important step forward.

2005

By 2005 the initial investment in studying photoemission from standard off-the-shelf dispenser cathodes, which until that time had been primarily operated for thermionic emission, had paid off with a validated, predictive, time-dependent model of QE for commercial dispenser cathodes as a function of laser pulse width, laser power, applied field, and temperature.

Therefore the decision was made to fabricate custom dispenser cathodes specifically with photoemission in mind. The Cs:W system was chosen for this purpose: tungsten, because it was readily available in porous sintered form and was proven technology in thermionic dispenser cathodes, and cesium, because it lowered workfunction more than any other elemental coating and had been well-studied on tungsten since Langmuir's seminal work in the 1930s.

In preparation for the first tests of a cesium dispenser, an understanding of cesiation of metal surfaces was sought. Graduate student Nathan Moody conducted experiments to carefully evaporate cesium from external sources onto clean metal substrates (solid tungsten and silver discs) while measuring QE, thereby obtaining an empirical relation between QE and amount of cesium supplied to the surface by the evaporative sources. This empirical relation was then com-

pared to predictive theory (Gyftopoulos-Levine) developed by Jensen which related QE to percent-monolayer coverage of cesium. As first reported at the 2005 Particle Accelerator Conference [64], agreement between experiment and theory was notable and confirmed that both arms of the research program were on the right track. Moody did note, however, that the method of cleaning the metal substrates prior to cesium deposition by a heat anneal followed by an argon plasma discharge cleaning did not appear to leave an atomically clean surface, particularly in the case of silver, which could not be annealed above 600°C without risking evaporating silver and coating the vacuum chamber and viewports. Future work would rectify this difficulty.

Later that summer, in the proceedings of the 2005 Free Electron Laser Conference [65], Moody described the design of the prototype cesium dispenser photocathode. A cesium reservoir was sealed inside a cylindrical steel cell, with one of the cylinder's end faces being a disk of 60% dense sintered tungsten. The reservoir material was a 5:1 ratio of titanium to cesium chromate powders, which when heated to about 600°C, would react to produce titanium chromate (a solid remaining in the reservoir) and free cesium. The cesium could then diffuse to the surface to replace lost cesium and rejuvenate QE. This design would soon undergo testing in the UMD Photocathode Research Laboratory, building on the understanding of the QE of cesiated metals already achieved. Critically, peak QE as a function of cesium coverage occurred at a defined fraction of a monolayer and thus could be used as a relative indicator of the amount of cesium remaining on the surface. Measurement of peak QE, therefore, would be a crucial diagnostic in the dispenser photocathode tests because it allowed estimation of remaining surface cesium given changes in quantum efficiency.

2006

In 2006 these experimental results were published in peer-reviewed form, along with detailed theoretical calculations and comparisons, in Ref. [66]. Additional experiments on cesium-coated silver and tungsten surfaces, and comparison to initial theoretical models of quantum efficiency as a function of surface coverage, were presented in Ref. [67].

Also in 2006, at that year's Free Electron Laser Conference, Moody, Feldman, Montgomery, et al. reported significant experimental progress towards low workfunction controlled porosity dispenser photocathodes [68]. The prototype dispenser described in 2005 (now with 70% dense sintered tungsten) was tested in two modes of operation: continuous rejuvenation (constant elevated temperature) and periodic rejuvenation (operation at room temperature with brief periods of elevated temperature for rejuvenation). In both modes the rejuvenation temperature for this cesium based dispenser was dramatically lower than the early tests of commercial barium-based dispenser cathodes: no more than 160-180°C in continuous mode, compared to more than 1000°C for barium dispensers.

In addition, a new method of surface cleaning was introduced: argon ion beam cleaning. This replaced the problematic anneal and plasma discharge processes used in prior work, with two major advantages. First, the ion beam treatment produced an atomically cleaner surface. Second, the time required to ion clean was much less than that required to anneal and plasma discharge clean. In concert, these advantages allowed a faster pace of experiments while providing

better data with which to confirm dispenser operation and validate Jensen's model of QE versus coverage.

Initial activation of the dispenser (reaction of cesium chromate with titanium in the reservoir, freeing atomic cesium to diffuse to the surface) was successful, and subsequent gentle heating produced a peak QE equal to that obtained via external evaporation of cesium. This strongly implied a uniform surface coverage of cesium for the dispenser, but which could be achieved via in situ rejuvenation of cesium rather than merely via deposition from external evaporative sources. Subsequent operation under continuous rejuvenation mode resulted in constant replenishment of the cesium layer, extending 1/e lifetime of QE from 5.2 days for a recesiated but room temperature tungsten surface, to an astonishing 47 days for the same surface under continuous rejuvenation. In both cases the decrease in QE was attributed to a combination of desorption and ion backbombardment from the applied DC voltage. The overall performance of the prototype cesium dispenser photocathode suggested that it could serve as a temperature-controlled dispensing platform on which a variety of high QE cesium-based photocathodes could be built.

2007

Following Moody's graduation with the Ph.D. in Electrical Engineering in 2006, he published the results of the cesium dispenser photocathode tests in Applied Physics Letters [11]. This paper compared the experimental data with an updated theoretical model which included a moments-based approach to electron emission probability and a refined model of the temperature

and energy dependent electron scattering terms, and in addition to the theory being free of adjustable parameters, the agreement with experiment was 30% or better.

Then-graduate student Eric Montgomery, building on Moody's work, reported at the 2007 Particle Accelerator Conference the first high QE results from UMD [69]. A cesium-antimony (Cs-Sb) cathode with an initial 100 Å thick Sb layer was fabricated with a QE of 11% at 375 nm. Heating and cooling tests showed that above about 50°C, the Cs-Sb cathode began to lose QE. Comparing this with the higher operating temperatures of the dispenser photocathode at 150°C or more, it was proposed that both a more temperature-stable semiconductor and a lower dispenser operational point were desirable. To this end, Montgomery reported testing of a second-generation dispenser with a minimum operation temperature of 120 °C and an activation temperature of 270 °C, achieved by using a thinner porous tungsten disc and a different reservoir material. While still falling short of stable operation with Cs-Sb, this dispenser showed the operating temperature could be adjusted significantly, justifying the dual focus on optimization of dispenser design and fabrication of more temperature-stable semiconductors.

2008

A more comprehensive analysis of the results obtained in the second-generation dispenser and of the fabrication and temperature stability of cesium antimonide was published by Montgomery et al. in Ref. [70]. This paper additionally discussed the diffusion of cesium in a dispenser utilizing a porous substrate and progress on modeling of such a system for future optimization of controlled porosity dispenser photocathodes.

2.4.3 Theory and Simulation Results

In parallel with experimental efforts by the UMD Photocathode Research Laboratory, Dr. Kevin Jensen began developing theoretical models in 2002 to improve our ability to model, understand, and simulate electron emission in real world applications. Close collaboration between theory and experiment continued to be emphasized throughout the program.

Because several theoretical models for various processes inherent to electron emission were developed more or less concurrently, the results of theory and simulation are here presented topically, and chronologically within those topics, rather than forcing the narrative to strictly follow a timeline as was done for the experimental results discussed in the prior section.

Thermal-Field Emission Model

Field emission and thermal emission obey well-known equations (the Fowler-Nordheim and Richardson-Laue-Dushman equations, respectively) which have similar form. There is a need, however, to handle not only cases of electron emission at elevated temperature or high field, but elevated temperature *and* high field. In fact, intermediate field and temperature ranges do not allow the pure field or pure thermal approximation and require a combined approach. In Ref. [71] the first effort towards a generalized thermal-field model for electron sources was made. The focus was the emission barrier models (the extension to photoemission discussed later was also via the barrier approximation, significant because it treats the low work function, high

field regime). Of course the general thermal-field theory was required to asymptotically limit to the Richardson and Fowler-Nordheim equations. A convenient dimensionless ratio was introduced to compare the thermal and field scales such that the theory scaled from completely field-dominated to completely thermally-dominated conditions. Validation of these thermal-field emission models were done using the numerical evaluation of an exact tunneling probability based on the no-image charge barrier. The analysis was considerably extended and clarified in a subsequent publication, Ref. [72]. In this reference was described a continued reliance on a numerical approach for solutions - this was computationally expensive for beam simulation code implementation of the theory. Therefore the theory was definitively modified and updated in Ref. [21]. Here an analytic model replaced the numerical approach. Included was a leading order theory suitable for use in PIC (particle-in-cell) and beam simulation codes (versions of which have been incorporated). Analytic thermal-field functions of electron emission rather than separate calculations of thermal and field emission eliminates the need for numerical integration and significantly reduces execution time and overhead, thereby enabling faster and more accurate computation of the local current density from electron emission. Perhaps most beneficially, the faster evaluation enabled consideration of detailed multidimensional cathode structures where multiple evaluations of current density would be required.

Thermal-Field-Photoemission Model

With a thermal-field framework in hand, based on emission barrier models, the extension of the generalized theory to include photoemission required that the effect of the lowered work function of a photocathode be incorporated into the emission barrier. The model needed to treat the thermal excitation of the initial distribution of electrons being photoemitted. In addition, a photoemission model suitable for dispenser cathode emission modeling needed to treat the case of a surface only partially covered with a low work function coating. This introduces local nonuniformity of the work function and of the emitted current density. In 2003 [73] a time-dependent thermal photoemission model was reported. Salient features of this model included consideration of laser heating of the electron gas and heating-induced excitations of the background lattice (phonons). The theory obtained quantitative agreement [56; 63] with measurements of extracted charge from a scandate dispenser photocathode fields from 0 to 2.5 MV/m, laser intensities from 12 to 22 mJ in 4.5 ns pulses, laser wavelengths at the fundamental and 2nd, 3rd, and 4th harmonics of a Nd:YAG laser, varying quantum efficiency and varying temperature. But because heating of the electron gas impacted thermal-field emission as well as photoemission, the theory was extended to treat emission from laser heated metal needles using a numerical (rather than analytical) model of the emission current [74]. Importantly, this led to a consideration of the combined treatment of low workfunction, high fields, photoexcitation, and other effects where the incident electron energy was near the barrier maximum, but additionally to a consideration of multidimensional emitters (such as field emission arrays) and the statistical nature of such arrays under the heading of the general thermal-field-photo model.

The electron transmission probability in the emission model had initially used a classical, analytical image charge model. The quality of the approximations and of the resulting equations of electron emission [75] was investigated using a transmission coefficient and a steady-state (early) version of the Wigner function, or quantum distribution function, approach. While for field emission the classical and quantum methods were comparable and verified the approximations made in obtaining the analytic method, of further interest was the ability of the Wigner approach over the image charge method to model the dipole layer thought to occur on a surface with a low work function coating. The Wigner approach was revisited and refined to this end in a subsequent work, detailing how surface coatings reduced the emission barrier [67].

When incorporating photoemission there are unique considerations separate from those made for either the thermal or field emission cases. First, the surfaces may be partially covered with a work function lowering coating and any theory must support such partial coverage. Second, new material parameters are introduced (such as work function, optical reflectance, and optical absorption depth). Third, the theory resulting must support extension to operating conditions and harsh vacuum environments typically found in present and future high power rf photoinjectors. These ideas are detailed by Jensen in Ref. [66] along with comparison to experimental results collected by Moody and Montgomery. In this work, Jensen retained a marked emphasis on predicting QE without the use of adjustable parameters - e.g., using physical constants and literature-reported material parameters to the exclusion of any fitting. (As will be discussed in Section 6.1.3, this work did assume an f -factor of unity which is now understood to be incorrect when comparing to experiment -- and the variation of f could be cynically considered the use of

a fitting factor, although a tightly constrained one.) In order to achieve the goal of extension to operating conditions in high power photoinjectors, the theory included a robust temperature and time-dependent model. Specifically, temperature was modelled as a function of laser heating including heat diffusion and transfer of the absorbed drive laser power to the electrons and then via scattering to the lattice. The local time-dependent temperature then impacted photoemission via scattering (electron transport to the surface). The resulting emission probability was then affected by the scattering undergone during transport and by the initial electron gas temperature. The new material parameters relating to optics were included as wavelength-dependent reflectance and optical penetration depth. The work function was varied with partial-monolayer coverage via a hard-sphere Gyftopoulos-Levine type theory.

This detailed model was used for prediction of the QE of bare metals, cesium-coated metals, and various commercially available dispenser cathodes. It is capable of investigating temperature evolution of electron emission even when the various processes involved (gun duty cycle, cathode heating, laser pulse absorption, electron transport scattering, emission barrier tunneling) occur over time scales from seconds (machine operation scale), to nanoseconds (adjacent pulses in drive laser pulsetrain), to picoseconds (individual laser pulse duration), to femtoseconds (scattering). All this was achieved with a minimum of unknown factors, because of the emphasis on avoiding adjustable parameters, drilling down to the basic underlying physics.

It describes the relation of the scattering rates to the heat transport and ultimately to the QE. And finally, it relates the work function variation due to Cs surface coverage non-uniformity to the emission probability. The theory performed exceptionally well by comparison not only

to measurements of QE in the literature, but also to our experiments measuring the QE of cesiated surfaces and dispenser cathodes.

Moments-based Approach

At the conclusion of Ref. [66] Jensen observed that the most important modifications yet to be made to the general thermal-field-photoemission theory would be in the electron transport and emission terms of the QE formulation. For the former (transport) term, what was needed was a proper quantum mechanical treatment of the scattering terms (particularly electron-electron and acoustic phonon) and the dependence of those terms on the initial temperature and energy of the photoexcited electrons, thus more fully describing the transport attenuation factor that strongly affects the QE. For the latter (emission) term, what was needed was not the formerly one-dimensional emission equations that had formed the basis of the general thermal-field and photoemission models discussed in the earlier theory, but a higher-order model incorporating more than just the electronic momentum normal to the emitting surface. In Ref. [21], Jensen addressed both the transport and emission terms, the first providing an important change to the scattering factors, and the second developing a Moments-based approach to QE calculation (based on integrals of the electronic momentum) that resulted in very good agreement with both bare metals and with partially cesiated surfaces.

Application to Emittance and Semiconductor Photoemission

The new Moments-based approach (so-called, but of course also including the previously described scattering factor contributions as well) was applied quickly to the problem of emittance of a photocathode. The theoretical intrinsic emittance was calculated and described using the Moments-based approach in Ref. [76] and later corrected slightly to include the photon energy in the transverse momentum component by Dowell and Schmerge in Ref. [77].

A further extension of the theory made possible by the Moments-based approach was the treatment of cesium antimonide semiconductor photocathode materials (with an eye to other semiconductors as well, on the prerequisite that certain material parameters are reported in the literature). However, because the reflectivity and laser penetration depth parameters are not always readily available for any given semiconductor, particularly in the wavelength range of interest (as was the case for the 375 nm response of Cs_3Sb in this work), the extension to semiconductor QE and emittance required co-development of an analytical model of a generic semiconductor [23] to obtain the dielectric constants of interest in order to calculate those optical parameters and to obtain the effective mass where literature is ambiguous or nonexistent (as was again the case for Cs_3Sb). An analytical model has the added benefit of avoiding catastrophes where one parameter might be updated based on new experimental data but other, dependent parameters might be inadvertently left unchanged.

The course of theoretical development in photoemission thus spans a wide range of photocathode technologies, from bare metals, to low workfunction coated surfaces, to semiconduc-

tors. More recently [78] it was further shown that Spicer's earlier, well known semi-empirical three-step model (which relies on experimental QE data and fitting parameters), in fact follows the same form as these newly developed, fundamentally physics-based models of photoemission. This is important as the models continue to move from descriptive to predictive applicability.

Application to Field Emission in Accelerators

Also recently, the thermal-field portion of the General Thermal-Field-Photoemission theory was applied to the problem of Dark Current (generally due to or accompanied by field emission in accelerator structures). Specifically, the nature of the surface required to give rise to such emission was investigated. Combined with advances in geometrical models of emitter sites, the theory treated breakdown and Nottingham heating in accelerators [79].

Conference Publications

The announcement of many of the theoretical results described above were at specialized conferences and were contained in their conference proceedings, in particular, the *Particle Accelerator Conference* [55; 64; 69; 80-83], the *International Vacuum Electronics Conference* [84-88], the *Free Electron Laser Conference* [65; 68; 89-91], the *International Vacuum Nanoelectronics Conference* [92; 93], and the *Directed Energy Symposium* [94-97]. In a number of these conferences, results of the application of the theoretical emission models to beam simula-

tion codes (particularly the PIC code MICHELLE) [82; 83; 87; 88; 96] and the simulation of surface coating diffusion and evaporation [70] were presented.

Chapter 3: A Photocathode Explorer's Roadmap

3.1 Introduction

In the long and colorful history of photocathode discovery and development a recurring challenge has been the scarcity of predictive, fundamentally physics-based theoretical models of quantum efficiency. Without such a guide, much early work in photocathode research became, in the spirit of the alchemists of old, an exercise in trial and error [58]. Such an inefficient approach is not suitable for rapid technological progress. The continued scientific advancement of the state of the art in photocathode performance hinges upon the combined efforts of theorists mapping the unknown lands which lie ahead and experimentalists then venturing into that new territory, map in hand. Thus, in this work these two common themes run through all such expeditions: to research basic science underlying cesium dispenser cathode development, and, in the pursuit of that knowledge, to advance fundamental predictive theory for photocathodes.

This work follows a logical and systematic progression of ideas in the form of four "expeditions" into the science of cesium-based photocathodes. These forays into the unknown are intended to both inform and be informed by theoretical support. Expeditions I and II, the quantum efficiency of cesium-coated metal and cesium-based semiconductor photocathodes respectively, stand alongside well-developed theory which comes from the UMD-NRL collaborative effort. Both theory and experiment will be detailed. In contrast, Expedition III, cesium loss and recession studies, while fundamentally building on literature going back to the 1930s, is intended to inform and support future theoretical work on the diffusion and evaporation of cesium in cesium-based coatings. Such work finds its eventual application in Expedition IV, cesium dis-

penser photocathode development, which is very much a groundbreaking effort and is at present wholly experimental in content -- but the careful optimization of which will rely on the physics-based knowledge obtained from the previous three tasks.

In the following section will be detailed each Expedition and the goals and approach for the work to be reported in subsequent chapters.

3.2 Expedition Roadmaps

Expedition I: Cesium-Coated Metal Photocathodes

Chapter 6 will discuss the physics of photoemission from metal cathodes and the impact on the emission barrier seen with the application of sub-monolayer coatings of cesium (and other alkali) metals. Topics include photon absorption, electron transport and scattering, and the emission barrier. The emphasis will be on the prediction of QE, particularly as a function of sub-monolayer coverage of the alkali coatings. Experiments with alkali coatings on tungsten and silver substrates will be reported. The goals of this work are to refine existing models of coated-metal QE by expanding the body of data to include other alkali coatings, and this is done by including both potassium and sodium experimental data in the comparison to theory. As will be discussed, the theory contains a specific coverage-related factor whose importance to the comparison to experiment had been overlooked. The use of the new alkali data reveals the proper comparison techniques and paves the way for a more broadly applicable predictive theory of the QE of sub-monolayer coated metals.

Expedition II: Cesium-Based Semiconductor Photocathodes

Chapter 7 will take some of the concepts in modeling photoemission of metals introduced in Chapter 6 and apply them to the photoemission of semiconductors. Again optical absorption, electron transport and scattering and the emission barrier will be topics of great interest. However, the scattering mechanisms will be different as will be the details of the emission barrier. A comparison to data in the literature will be given for the representative case of cesium antimonide. Experiments to be reported will be the fabrication and QE testing of both cesium antimonide and cesium sodium potassium antimonide. The goals of this section are twofold: to compare to and validate theoretical models, and to determine the suitability of semiconductor photocathode materials for dispenser operation in high average power photoinjectors -- simultaneously exhibiting good quantum efficiency at green wavelengths and good thermal stability for operation on the surface of a heated dispenser.

Expedition III: Cesium Loss and Recession Studies

In Chapter 8 will be opened the topics of the mechanisms of cesium loss, the resulting deleterious impact on QE, and the potential for recession of such cathodes. The overarching goals of this section are: firstly, to support the underlying principle of the cesium dispenser, that cesium loss results in QE loss and shorter-lived photocathodes; secondly, to better understand the mechanisms by which that can occur, both for coated metals and semiconductors; and thirdly, to demonstrate that the resupply of cesium to a coated surface which has been contaminated in fact

restores QE. The sum total of these investigations will provide a firm footing for the discussions of dispenser photocathodes to come in the following chapter.

Expedition IV: Cesium Dispenser Photocathode Development

Chapter 9 will conclude the reporting of experimental results with a comparison of the cesium dispenser technology introduced by Moody to a second generation dispenser. The performance characterization will include activation and operation of the devices and the resulting QE. The goals of this section are to show that the dispenser design is flexible, to show that progress has been made in creating a range of possible operating temperatures and improved cleaner operation, and to probe the interaction of an operating dispenser with high QE semiconductor cathode materials deposited on its surface. This chapter will conclude with an eye to future research directions for cesium dispenser photocathode development.

Like any good explorer, we dare not undertake an expedition without the necessary tools in hand and the knowledge of how to properly use them. Such is the content of the next two chapters.

Chapter 4: Experimental Apparatus

4.1 Introduction

The measurement of the quantum efficiency of a photocathode is quite simple in concept: determine the photocurrent which results from a given incident laser power, and convert using the electric charge and photon energy to a ratio of emitted electrons to incident photons. The experimental details, however, are not trivial, and care is essential in order to ensure repeatability and in order to allow the most accurate comparison to theoretical models. Ultrahigh vacuum (UHV) operation is essential. Power-stabilized mW-class narrow-linewidth light sources are needed. Low noise circuitry is utilized. Fine control of gas supply rates is important. Sub-Ångström resolution film thickness measurements are required. Ion beam cleaning ensures an atomically clean substrate. And automation of experimental procedures and data acquisition is incorporated under computer control using LabVIEW wherever possible.

4.2 Vacuum Chamber

4.2.1 Schematic

The quantum efficiency, lifetime, and recesiation of photocathodes is performed in the vacuum chamber shown in Fig. 4.1. The chamber itself is a 6-way stainless steel cross with 8" Con-Flat flanges. The cathode mount extends horizontally from the cathode feedthrough to the center of the chamber, where the cathode faces the lasers, ion gun, and evaporative sources of antimony and alkali metals.

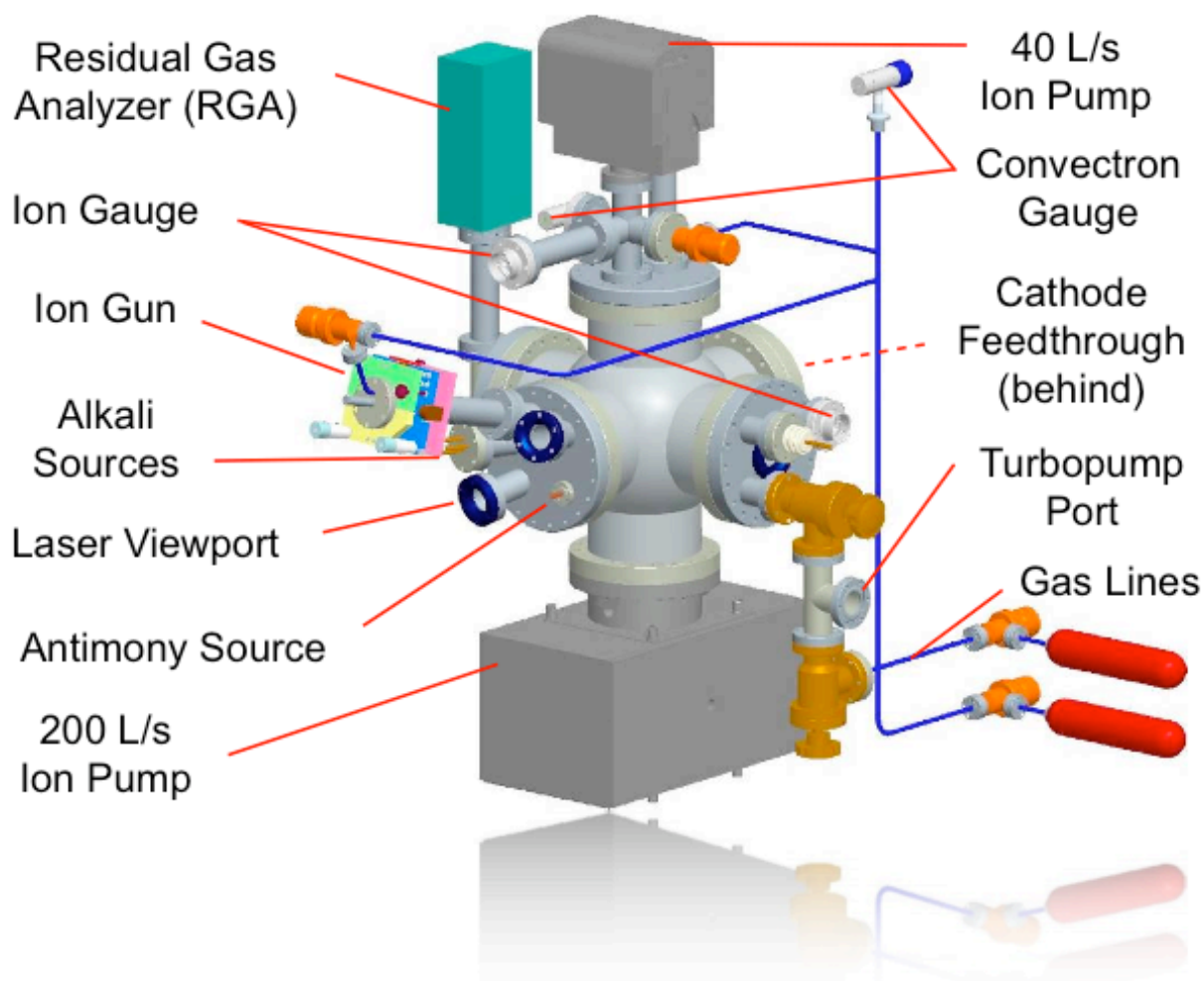


Figure 4.1: Experimental Chamber, original design by N. Moody

4.2.2 Ultrahigh Vacuum

A experimental challenge is attaining and maintaining ultrahigh vacuum of up to 1×10^{-10} Torr (where 760 Torr is one atmosphere). Such vacuum is necessary to limit contamination by the background gas during experiments. For an ideal gas the rule of thumb from the Langmuir unit is that one monolayer's worth of gas impacts a surface in one second at 1×10^{-6} Torr. Thus if

the background gas were to have a sticking coefficient of 100%, it would take roughly 20 minutes at 1×10^{-9} Torr to fully coat the surface. Such an extreme is not the case, and in fact the majority of the background gas in the properly baked-out apparatus does not strongly affect lifetime of photocathodes (H_2 , Ar, N_2), but it is still imperative to maintain sufficiently high vacuum to allow experiments of several hours to be conducted without major contaminant-induced surface changes. Thus nanoTorr or better base pressures and partial pressures for reactive gases (CO , O_2 , CO_2 , H_2O) of order 1×10^{-11} Torr are targeted.

Background gas loads are from several possible sources: real leaks from the outside atmosphere, virtual leaks from trapped volumes in low-conductance cavities such as standard screw threads or from defective welds, material sources like alkali sources or anything with substantial vapor pressure, and outgassing of all vacuum components, either by desorption from the surface or, for hydrogen, by diffusion from the bulk. A helium tank to spray the light, easily diffused gas near suspect areas and a leak-checker or RGA can be used to locate the position of any real leaks in the system - severe leaks will reveal themselves via an atmospheric signature in the RGA spectrum of nitrogen, oxygen, and water vapor. Leaks are minimized by the use of only UHV-qualified components and by careful inspection of the knife-edges on Con-Flat flanges during removal or installation, as well as careful cleaning of the copper gaskets which are used when mating the flanges.

As it pertains to the vacuum chamber for this experiment, a good deal of the gas load which determines the base operating pressure in a leak-tested system is determined by the outgassing and diffusion from the metal walls of the chamber. Electropolishing was performed on

the chamber when it was initially ordered in order to minimize this outgassing by eliminating micro-protrusions and reducing surface roughness. Electropolishing also inhibits oxidation of the stainless steel which would normally occur at about 300 °C -- and such temperatures are routinely approached immediately adjoining the heaters during a bakeout process.

The chamber is as initially configured in volume and surface area, though important upgrades of instrumentation and capabilities have been performed. Specifications are:

Construction of main chamber	Electropolished 304 stainless steel
Standard Con-Flat flanges	8" (chamber), 6" (cathode), 2.75" (instrumentation and valves), 1.33" (ion gun gas, Sb source)
Total internal volume	12.1 L
Total internal surface area	15,200 cm ²
Ion pumps internal surface area	2,900 cm ²
Dimensions (LxHxW)	89.5 x 97.0 x 74.0 cm

Table 4.1: Vacuum chamber specifications

4.2.3 Bakeout

After atmospheric exposure (such as change-out of alkali sources, cathode replacement, quartz crystal replacement or ion gun repair) it is necessary to raise the temperature of the entire apparatus to increase the rate of desorption of contaminants like water vapor from the walls of the chamber. This process is termed bakeout and the procedures are discussed in Section 5.4.1. It is following the bakeout process that the gas load is sufficiently reduced that nanoTorr pressures are achieved. The bakeout temperatures are controlled by the flow of current through so-called

heater tapes: resistive wire woven through a coarse fiberglass weave into a strip typically 1/2" to 1" wide and 1 to 6' long. Bakeout cannot be initiated until the volume of gas has been pumped away so that oxidation of the internals of the chamber is not problematic.

Following a bakeout the evacuation of the vacuum system has reached the third of four limiting fundamental factors on gas load. Initially pressure is limited by the volume of gas present, and that is pumped away prior to the bake. The bake then removes much of the adsorbed surface gases, which is the second limiting factor on vacuum. The third limiting factor is diffusion of gas (mainly hydrogen) from the bulk of the metal chamber walls to the surface and into the vacuum. This limit extends to the bottom of the UHV range at 1×10^{-12} Torr. XHV vacuum systems below 1×10^{-12} Torr begin to see effects from permeation, where gas actually slowly penetrates through the walls into the chamber. This limit is not reached in the experiments reported here.

4.3 Vacuum Pumps

4.3.1 Choice of Pumps

It is not enough to have low gas load to achieve UHV; high pumping speed is also necessary. A single pumping technology cannot span the entire 13 order of magnitude pressure range from 760 torr to 1×10^{-10} Torr in these experiments. Three stages are used in the chosen apparatus. A roughing pump is first used to reach about 1 Torr. This pump is a scroll pump with the feature that it is "dry" --i.e., very clean and does not introduce pump oil into the system like rotary

vane or piston pumps. Secondly, a turbopump with blades rotating at 1000 Hz is connected to the roughing pump, and stages the vacuum under 1×10^{-6} Torr. Its base pressure is of order 1×10^{-8} Torr with a fully baked-out chamber, but the pumping speed is reduced at lower pressure and so it takes a long time to get there. In practice it is used to get the chamber pressure below 1×10^{-7} Torr. Finally, two ion pumps are used to further reduce the pressure to or below 1×10^{-9} Torr. The turbopump is isolated from the chamber at this point because the ion pumps are fully capable of maintaining the vacuum at this level, save in isolated high-gas-load cases such as the argon release during activation of a Cs:Bi source.

4.3.2 Scroll (Roughing) Pump

A simple dry scroll pump is integrated with the turbopump to create a "turbopumping station" - this is conveniently wheeled for transfer from lab to lab if needed. The scroll pump is controlled by the same microcontroller as the turbopump and the two work as a single unit in practice, though if desired the turbopump may be set to the "off" state and the scroll pump used exclusively. This is advisable only if it is known that an extended period of pumping will be done in the high pressure regime, because the roughing pump is dirty compared to the rest of the system even though it is oil-free, and if operated directly on the chamber below a few Torr, backstreaming of contaminants can be a problem.

4.3.3 Turbopump

A turbomolecular pump, more commonly referred to as a turbopump or simply a turbo, uses a stack of counter-rotating vanes with speeds of about 1000 Hz on magnetic bearings in order to create uni-directional molecular flow of gas. Tolerances are very tight and so shock to the pump when it is spun up should be avoided. This includes the sudden release of high pressure gas into the vanes. The results of such an incident can be catastrophic: the housing is designed expressly to contain the shrapnel resulting. The turbopump has a remarkable range from 1 Torr down to 1×10^{-8} Torr. Modern turbopumps are very reliable and can go for years of continuous operation without needing servicing.

Turbopumps have a pumping speed which depends on the gas species. The heavier the atom or molecule, the more effective the vanes are at enforcing uni-directional flow. Hydrogen, as the lightest gas, has a very poor pumping speed.

The turbopumping station is shown in Fig. 4.2. The scroll pump is on the lower right, the microcontroller on the lower left, and the turbopump behind the fan in left-center. The manifold at the top is to allow pressure measurement and integration of an electrically actuated, normally-closed UHV valve so that the chamber is isolated in the event of power failure.



Figure 4.2: Turbopump station with scroll roughing pump

The manifold itself is detailed in Fig. 4.3. At the left is the port leading to the turbopumping vanes. The four-way cross connects to a Convectron pressure gauge at the top and an ion gauge at the bottom, which monitor pressure from atmosphere to 1×10^{-4} Torr, and from 1×10^{-5} to 1×10^{-10} Torr, respectively. On the right is the electromechanical valve which is powered by a 24V supply and is only open when energized. If power is lost for any reason, the valve immediately closes to form a UHV seal. At the top is seen the flexible electroformed bellows leading to the vacuum chamber. It should be noted that the more convoluted the path, the more the pumping speed is reduced in the molecular flow regime (1×10^{-6} Torr and below). This state is termed "conductance-limited." If the full pumping speed of the turbopump were desired, a direct connection to the large 6" flange would be advisable to avoid the conductance limit.



Figure 4.3: Turbopump manifold with pressure gauges and electromechanical valve

4.3.4 Ion Pumps

The ion pumps have the unique feature of the complete absence of moving parts. Inside the box-like pump housing are two assemblies, the anode and cathode, made from a stainless steel multicell structure (reminiscent of honeycomb) and a flat titanium plate or pair of plates, respectively. The two assemblies are separated by high voltage, typically 5-6 kV. Ion pumps work by the principle of a Penning cell: a uniform magnetic field is applied from a permanent magnet perpendicular to the plates, causing electrons emitted by the cathode to spiral around the magnetic field lines on their way to the anode. This increased path length makes collisions of the electrons with background gas more likely. Collisions ionize the gas, and each ion is then accelerated by the electric field into the titanium cathode at high energy. Gas is pumped by three methods:

reaction with the titanium (chemisorption), implantation in the titanium or burial beneath sputtered titanium on the cathode or cathode-facing surfaces (physisorption), and diffusion into the titanium (for hydrogen). All processes occur simultaneously and continuously. Sputtering continually reveals a fresh layer of titanium for reaction while covering over other implanted ions or covering adsorbed ions on cathode-facing surfaces.

The effectiveness of ion pumps, like turbopumps, is very dependent on gas species. Hydrogen is pumped differently because accelerated hydrogen ions are low enough mass that they do not sputter the titanium efficiently. Instead, hydrogen diffuses into the bulk of the cathode - this process is efficient and can pump hydrogen well - a distinct advantage over the turbopump. In most cases the hydrogen gas load is high enough, however, that it remains the dominant species at UHV even with the use of ion pumps. Noble gases are poorly pumped at low pressure because they do not react with the titanium and so the rate is sputtering-dependent which in turn is pressure-dependent. Pumping speeds relative to water vapor for the diode and noble diode pump designs are shown in Table 4.2 adapted from Ref. [98].

Gas	H ₂	He	CH ₄	H ₂ O	N ₂	O ₂	Ar	CO ₂
Mass (amu)	2	4	16	18	28	32	40	44
Diode	220%	2%	90%	100%	85%	70%	5%	100%
Noble Diode	160%	15%	90%	100%	85%	70%	20%	100%

Table 4.2: Ion pumping speeds for common gases relative to water vapor

Argon (and by association other inert gases) are commonly associated with the "argon instability" in diode ion pumps where covered, sputtered-over argon atoms on the anode can be suddenly released, ionized, and accelerated into the cathode, causing more sputtering, uncovering more argon in a cascading effect, with a sudden increase in pressure. The pump becomes a source of argon until the instability passes and if pumping in isolation can result in periodically spaced spikes in pressure. This can be avoided by limiting the argon which the pump is forced to deal with, or by selection of a design of the pump which uses good geometries non-conducive to the instability (e.g., the star-cell/triode or noble diode designs). Even when argon is not a problem, however, initial pump behavior following turn-on after a bake-out can involve substantial outgassing which introduces the opportunity for cascading, uncontrolled ionization and discharge from cathode to anode. This is controlled by turning on the pumps with the turbopump also in operation to remove excess gas.

Two ion pumps are installed on the chamber: a 40 L/s pump at the top and a 200 L/s pump at the bottom. The dual pumps provide redundancy and also a more even pumping profile across the chamber. Both pumps' high voltage power supplies are connected to a battery-powered uninterruptible power supply (UPS) so that UHV is maintained even in the event of a power failure. This can be maintained for hours since, despite the high voltage of the pumps, the current used is extremely low. Ion current measured by the pumps is also indicative of the pressure of the chamber just as in an ion gauge, so the two pumps also function as two additional pressure monitors for the system.

4.4 Vacuum Monitoring

4.4.1 Pressure Measurement

Two types of pressure gauges are used on the vacuum system. The range from atmospheric pressure to 1×10^{-4} Torr is covered by Convector gauges. These gauges measure the degree by which convective cooling affects the power required to maintain the temperature of a heated filament. This is a function of the properties of the gas present. Calibration is done with nitrogen, so any other gas will clearly have a convective cooling effect different from that done with the calibration. This is most evident in the case of argon where the pressure of a Convector gauge reads thirty times lower than the true pressure because the convective cooling from argon is much less than that from nitrogen (the mass of an argon atom is heavier and thus there are fewer collisions with the filament at a given temperature). A backfill of argon has reached atmospheric pressure of 760 Torr when a nitrogen-calibrated Convector gauge reads only 24 Torr. The second type of gauge is the Bayard-Alpert ion gauge which covers the range from 1×10^{-5} Torr to 1×10^{-10} Torr. The ion gauge uses a thermionic filament to emit an electron beam which ionizes background gas, and then the ion current is measured, from which the pressure of the system can be deduced.

Convector gauges are relatively maintenance free. They do need to be mounted horizontally so that the convection can occur in the same orientation as the internal design of the gauge. Ion gauges suffer from initially high outgassing of the hot filament following pumpdown after at-

mospheric exposure, which leads to erroneously high pressure readings, particularly immediately following turn-on of the gauge. The Granville-Phillips model 307 gauge controllers are equipped with a "degas" functionality which temporarily ramps the filament current in order to speed the outgassing process and ready the gauge for use. The use of degas and the operation of the gauges at pressures over 1×10^{-5} Torr should be avoided long-term since this is detrimental to the life of the filament. The gauge controllers will automatically shut off the gauges to protect the filament at pressures over 1×10^{-4} Torr.

4.4.2 Residual Gas Analyzer

The residual gas analyzer, or RGA, uses a thoriated tungsten filament to ionize background gas, which is then accelerated by high voltage. The operation is similar to a mass spectrometer which would send the ions through a bending magnet. The mass of the ion (the gas species) determines the gyromagnetic radius in the magnetic field and thus the ion current as a function of position would give the mass spectrum of the background gas pressure. In practice a more compact device can be built using the same principle but a combination of RF and DC fields. The Stanford Research Systems RGA 200 (Fig. 4.4) is the device installed on the test chamber and uses a quadrupole mass filter to select which mass can pass through the combination of RF and DC fields to reach a sensitive electrometer. Software automates this process and allows the user to immediately analyze the spectrum to identify relative percentages of which gas species are present. In addition, the height of any given spectral peak is a current which indicates the partial pressure of that gas species. The RGA electrometer is sensitive to ion currents equiva-

lent to 1×10^{-10} Torr partial pressures. The RGA filament is, like the ion gauges, limited in life and should never be used above total pressures of 1×10^{-4} Torr.

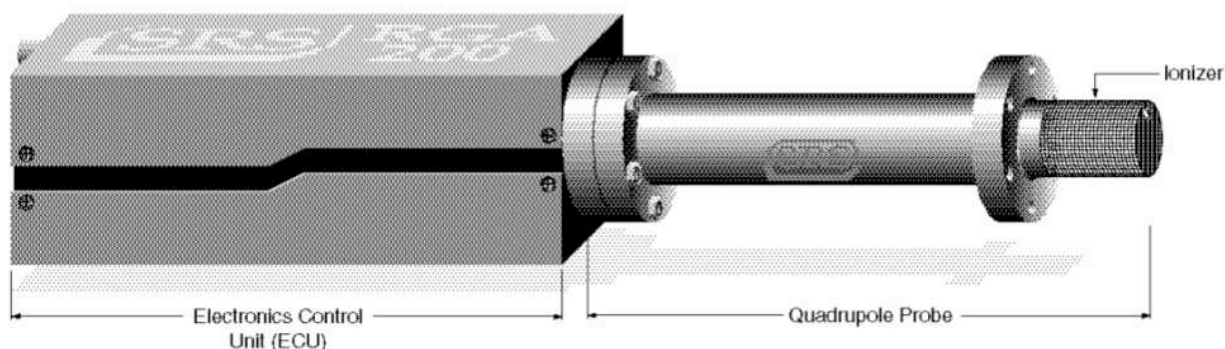


Figure 4.4: Stanford Research Systems RGA 200

4.5 Lasers

4.5.1 Laser Diodes

The measurement of extremely low quantum efficiencies such as those exhibited by metals at zero or low cesium coverage requires sources intense enough to produce measurable photocurrent. With the 486 Keithley picoammeter, resolution in the low noise QE circuit of photocurrent was of order 10 picoamperes. Using Eq. 1.12 and assuming a QE of 0.01% and a wavelength of half a micron, a source of 2.5 mW is required to achieve signal-to-noise in photocurrent of 100 (photocurrent of 1 μA). These power levels are not available in narrow-linewidth incoherent sources such as mercury lamps filtered by monochromators. Incoherent sources also suffer from lack of collimation which can make intensity on the cathode a difficult measurement. Commercially available tunable lasers satisfy the requirement but are costly. A compromise was reached in Moody's design of the test chamber at Maryland with the selection

of five laser diodes at five different wavelengths. The diodes chosen spanned the visible range and into the near-infrared and near-ultraviolet. The shortest wavelength commercially available diode was purchased for the measurement of QE in the UV: a gallium nitride diode at 375 nm. Diode lasers have compact form factors and modest power requirements and can output tens of mW of optical power. Diodes can be purchased in power-stabilized packages with built-in thermoelectric coolers which allow <1% peak-to-peak power fluctuations over 8 hours.

The green laser shown in Fig. 4.5 is not a diode directly outputting green light. Instead, in order to obtain the 532 nm wavelength, a diode-pumped solid-state (DPSS) laser was installed. This laser uses a GaAs diode at 808 nm to pump a Nd:YAG crystal which achieves population inversion and lases at 1064 nm. The output is frequency-doubled in a nonlinear KTiOPO₄ crystal to obtain 532 nm, power-stabilized to <5% peak-to-peak fluctuations over 8 hours.

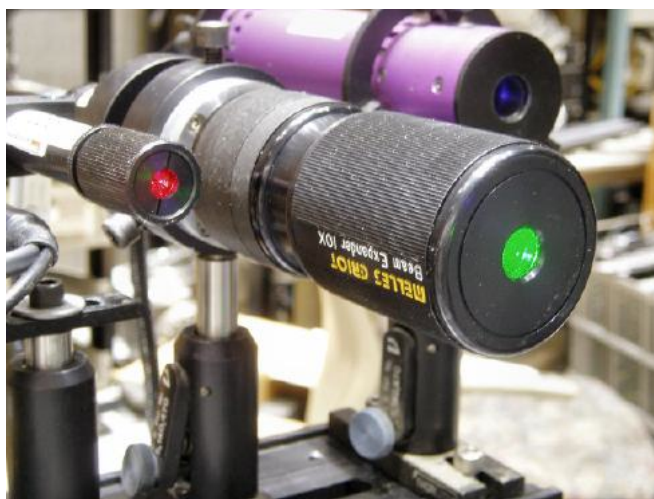


Figure 4.5: Diode lasers

4.5.2 Laser Specifications

Laser power for all five lasers used is in the 5-15 mW range. Beams are collimated and are circular or (in the case of the InGaN and GaN edge-emitting diodes for blue and UV) elliptical. Spot sizes are 1-3 mm radius in order to avoid unwanted heating effects or space charge limited emission resulting from too tight a spot and too high an intensity. Table 4.3 gives the lasing wavelength and corresponding photon energy, color and nominal power from the laser, where the nominal power is that specified by the manufacturer. Power output does slowly fall over hundreds of hours of use as the diode ages and is re-calibrated as needed in the course of experiments. The power after four years of intermittent use (measured June 2009) is also shown - the 375 nm GaN diode has the shortest lifetime. The current and voltage of each laser specified as well as the linewidth and power stability achieved by the diode/DPSS.

λ (nm)	E_{photon} (eV)	color	P_{nominal} (mW)	P_{4_years} (mW)	voltage (V)	current (mA)	$\Delta\lambda$ (nm)	stability (%)
808	1.53	IR	12.5	13.3	5.0	80	<10	<2
655	1.89	red	10.0	8.7	5.0	85	<10	<2
532	2.33	green	5.0	4.5	3.0	300	<0.1	<5
405	3.06	blue	5.0	5.3	6.5	500	<20	<1
375	3.31	UV	8.0	3.3	6.5	500	<10	<1

Table 4.3: Laser specifications

4.5.3 Robotic Control

The five lasers are mounted on a translational stage actuated by a linear motor (the LMA-400 by Aerotech Corp.) under LabVIEW computer control. The motion of the motor (speed, acceleration, drift, etc.) was tuned to match the loaded mass of the laser assembly when mounted on the translational stage. The lasers take 200 ms to move to each new commanded position and the encoded linear motor mount has positioning repeatable to 100 nm resolution, more than sufficient to ensure the same region of the cathode is illuminated with each new cycle through the lasers. The rigid optical mounts are aligned by hand to place each laser spot on the center of the cathode, and the spot position is viewed either with wavelength-appropriate laser goggles or with a video camera to ensure eye safety. A temporarily mounted iris on the viewport during alignment ensures the beam path is collinear for all lasers, which enables positioning of the thermopile power meter for automated LabVIEW calibration of laser power as desired.



Figure 4.6: Lasers on translational mounts with thermopile power meter for auto-calibration

4.6 Cathode Flange and QE circuit

4.6.1 QE Measurement Circuit

In order to push the signal-to-noise of the photocurrent as high as possible thereby enabling measurements of very low QE with reliability and repeatability, the noise in the QE measurement circuit must be minimized. This is done in two ways. First, the voltage applied between anode and cathode is isolated from the rest of the circuitry in the lab. Second, the coax cable running from voltage supply and picoammeter to anode and cathode feedthroughs is triax with the outer braid grounded to minimize noise pickup. The circuit is shown in Fig. 4.7.

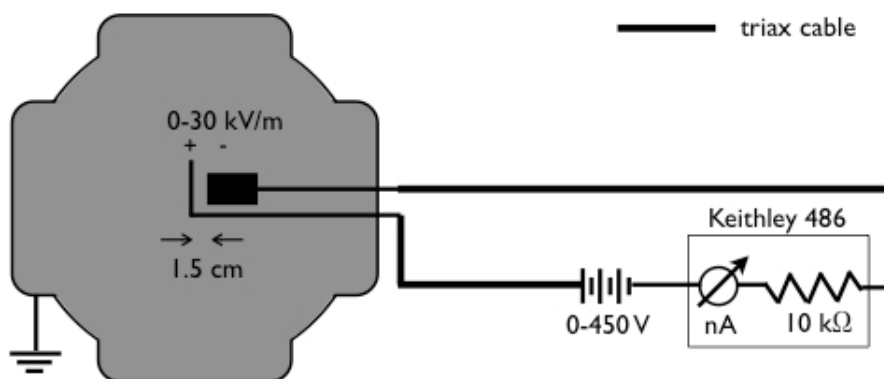


Figure 4.7: QE circuit diagram

4.6.2 Vacuum Chamber Feedthrough and Connections

The UHV electrical feedthrough for the cathode flange has five electrically isolated terminals shown in Fig. 4.8: two for the thermocouple plug (top), one for the anode (lower left), one

for the cathode (lower center), and one for AC power to the cathode heater (lower right). The anode connection doubles as ground for the AC heater power.

Under ion cleaning the connections are changed: a grounded thermocouple plug is used, the heater and QE circuit are disconnected, and a separate ammeter is connected to the anode and the cathode respectively, allowing independent measurement and data acquisition for ion current collected by both anode and cathode. The cathode is biased -90V with a 10-cell battery pack between the cathode and the ammeter to preferentially direct ion current to the cathode.



Figure 4.8: Cathode electrical feedthrough

The isolated 450 V supply for the QE circuit (originally 286 V with Moody's design) is likewise a stack of 9 V batteries in series with pickoff connections to allow a range of voltages to be se-

lected as the operating point. The low photocurrents drawn during operation guarantee the batteries will not be depleted within the lifetime of the experiment, but reasonable care must be taken to shut off the voltage when clipping leads to the feedthroughs, lest crossed wires short the battery pack and cause rapid discharging and overheating with risk of leakage.



Figure 4.9: Isolated low-noise anode-cathode voltage supply

4.6.3 Cathode Heater Power

The AC power to the cathode heater is provided by a variable AC transformer (variac). The output of the 110 V variac is sent through a stepdown transformer to supply approximately 0~10 volts AC to the heater coil. During operation the heater draws a few watts of power. The power draw can be measured at several steady-state temperatures (shown in Table 4.4) and the results bear some discussion.



Figure 4.10: Variac (variable AC transformer) for cathode heater power control

Power (W)	5	8	12	23
Temperature (°C)	200	300	400	600

Table 4.4: Steady-state heater power versus cathode temperature: raw data

The heater power versus equilibrium (steady-state) temperature, following an analysis developed in discussions with K. Jensen, is plotted in Fig. 4.11 and the fit to a Stefan-Boltzmann radiation law with a conductive heat loss term is shown. Constants of the system used in obtaining the fit are given in Table 4.5. The cathode assembly under UHV is shown to be dominated at operational temperature by conductive cooling down the cathode stem.

The equation fitted is a steady-state power equation based on the Stefan-Boltzmann radiation law with a conductive term dependent on the temperature gradient down the cathode stem:

$$(4.1) P = \varepsilon(T) A \sigma (T^4 - T_0^4) + \kappa A_{\text{stem}} dT/dx$$

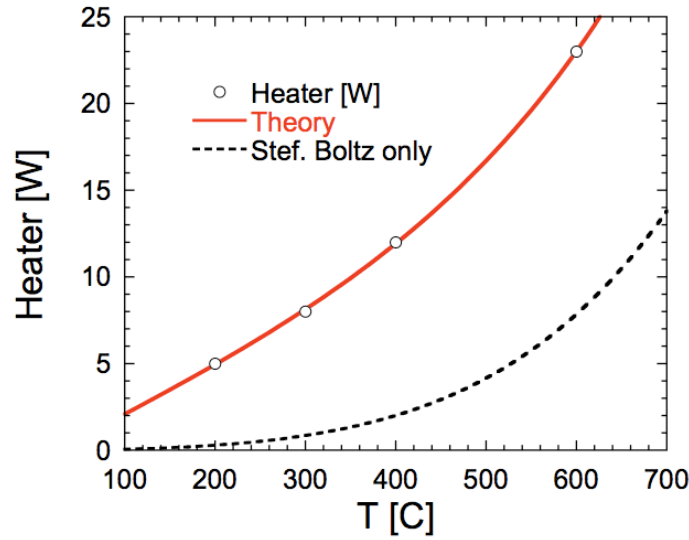


Figure 4.11: Heater power vs cathode temperature and fit to radiative/conductive cooling

where A is the surface area of the cathode and cathode mount, and A_{stem} is the average cross-sectional area of the conductive cooling path over the distance x down the cathode stem. The temperature dependence of the emissivity is taken to be [99; 100]:

$$(4.2) \varepsilon(T) = \frac{8}{3\omega_p} (A_{ee} T^2 + B_{ep} T)$$

where A_{ee} is a term in the relaxation time of copper from electron-electron scattering and B_{ep} is from electron-phonon scattering. The thermal gradient used for the conductive term is linear:

$$(4.3) dT/dx = g_1 (T - g_2 T_0)$$

So the equation fitted in explicit dependence on temperature and with fitting parameters f, g is:

$$(4.4) P = f \frac{8}{3\omega_p} (A_{ee} T^2 + B_{ep} T) A \sigma (T^4 - T_0^4) + g_1 (T - g_2 T_0)$$

where f accounts for emissivity not being that of single-crystal copper, g_1 accounts for the slope of the temperature gradient based on the thermal conductivity of the cathode stem, its length, and its cross-sectional area, and g_2 accounts for the difference from ambient room temperature of the heat sink (the chamber wall).

ω_p (Cu)	1.64×10^{16} 1/s	A (cathode + mount)	20.48 cm^2
A_{ee} (Cu)	4.045×10^7 1/s•K ²	T_0 (ambient)	300 K
B_{ep} (Cu)	1.86×10^{11} 1/s•K	f	3.74
σ (S-B constant)	5.67×10^{-12} W/cm ² •K ⁴	g_1	0.0263 W/K
κ (Cu)	4.01 W/cm•K	g_2	0.986

Table 4.5: Heater power calculation constants

The fitting constants may be interpreted as follows. The emissivity is significantly larger than for pure crystalline copper (as would be expected from machined copper) and/or the radiating area is larger than estimated (such as the heater housing). From g_2 the heat sink (chamber wall) is at room temperature. From g_1 the effective cross-sectional cathode stem area divided by the length of the cathode stem (assuming thermal conductivity of copper) is 0.0066 cm corresponding to an average cross-sectional area of about 7 mm²: since half of the stem is stainless steel as shown in Fig. 4.13 with a thermal conductivity of 1/25 that of copper, this is not at all

unreasonable. Overall it is shown that despite the small stem, the conductive cooling dominates at dispenser operating temperatures and we begin to see contributions from radiative cooling at dispenser activation temperatures. At anneal-cleaning temperatures radiative cooling would dominate.

4.6.4 Cathode-Anode Assembly

The anode and cathode are mounted as shown in Figs. 4.12 and 4.13. The annular anode allows collection of photocurrent while permitting laser light and the ion beam to strike the cathode. It serves a dual purpose as a shadow mask for the rest of the cathode assembly to protect it from the effects of ion beam sputtering and from conductive metal deposition on the insulators, which would lead to higher dark current in the QE measurements.



Figure 4.12: Cathode and anode, side view

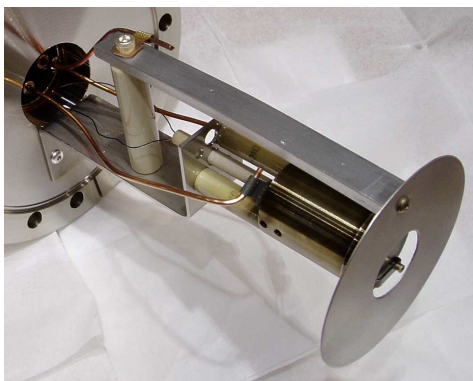


Figure 4.13: Cathode and anode showing standoffs and electrical



Figure 4.14: Silver cathode mount

If a silver or tungsten disc cathode is to be used, the copper dispenser clamp is replaced with the direct mount to the heater body as shown in Fig. 4.14. The anode stem is reduced in length to preserve the anode-cathode separation distance in this case.

4.7 Gas Supply

4.7.1 Gas Species

Multiple species of gas are required for various experimental procedures and cathode test processes. There are five primary gas species discussed in this work, although use of additional species is easily enabled via exchange of the lab bottle connected to the gas tree. Those species are as follows:

- Argon (Ar), seven 9's pure, for use during ion bombardment cleaning of the cathode
- Nitrogen (N_2), seven 9's pure, for purge or backfill prior to breaking vacuum
- Oxygen (O_2), nitrous oxide (N_2O), and carbon dioxide (CO_2), as oxidizing contaminants for cathode contamination and QE lifetime testing

Previous experiments in this experimental chamber with hydrogen as an ion bombardment species (as has been reported by Dowell in Ref. [101]), or for Paschen discharge cleaning, proved unsatisfactory due to an adverse weakening of the springs holding the quartz crystal of the deposition monitor in place under prolonged exposure to hydrogen. Therefore that gas was not used during the course of the experiments reported here.

4.7.2 Gas Tree and Valves

Early experiments in this work used the gas tree as designed, and later work involved a significant revision to the design in order to supply multiple gas species for contamination tests. The initial system schematic is shown in Fig. 4.15. Note that a single line feeds both the fine leak

valves on the chamber. The upgraded system schematic is shown in Fig. 4.16. Here two separate lines have been used to allow one to be dedicated to high purity argon for the ion cleaning and the other to be dedicated to contamination testing via the leak valve at the top of the chamber.

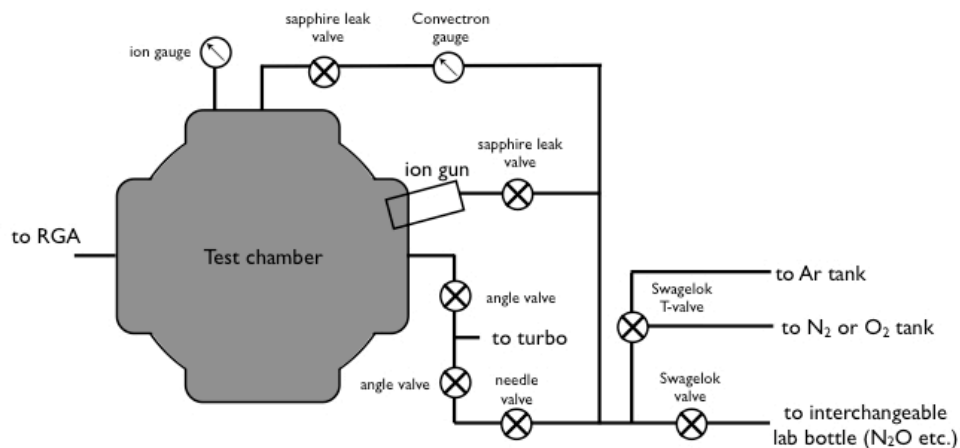


Figure 4.15: Initial gas supply schematic

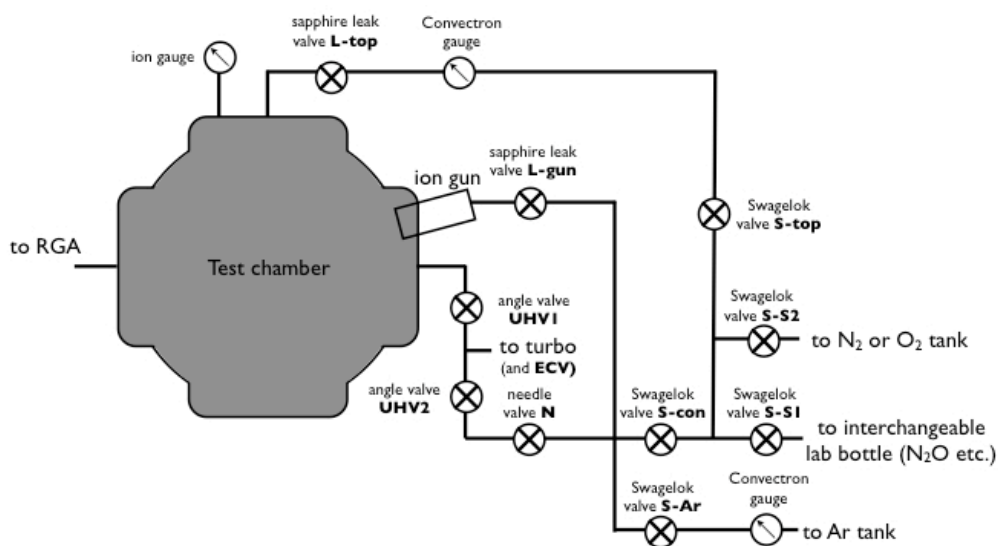


Figure 4.16: Upgraded gas supply schematic with valve codes



Figure 4.17: Detail of gas supply tree and valves



Figure 4.18: Detail of miniature regulator and interchangeable lab bottle

The goal in laying out the upgraded multi-gas supply system was in assuring that the entire tree of gas lines may be evacuated by the roughing pump while allowing clean supply of argon to the ion gun and alternate supply of selected gases to the main chamber leak valve. The prior capability to glow discharge clean the chamber had not been used since commissioning and

was deemed unnecessary. This allowed removal of an electromechanical valve which, although conveniently GPIB relay-controlled, had exhibited leaks through the 1/4" NPT fitting threads.

Retaining all other capabilities while enabling the new multi-gas supply involved three steps. First, the 1/4" SS tubing leading to both sapphire seat fine leak valves was separated into two dedicated lines. Second, the two lines were connected via a manual valve which would be opened in the event of roughing the second line along with the first. Third, the gas input to the second line was modified via a second regulator and valve to allow a small lab bottle of gas to be installed on the frame of the experimental table.

Referring to the valve codes given in Fig. 4.16, the following table illustrates the open/closed positions of the various valves in the tree in order to operate in each of the eight normal operating modes. Those eight modes are: A) normal operation during QE measurement, B) turbopumping of the chamber, C) roughing of the argon line, D) roughing of the entire tree, E) argon leak during ion clean, F) dry nitrogen purge of the chamber, G) gas species 1 leak, H) gas species 2 leak. An open valve is designated by O, a closed valve by X, and a dash where it is not relevant for the operating mode.

Mode C, roughing of the argon line, can be performed simultaneously with mode A, normal operation during QE measurement. This was useful when the sapphire leak valve developed a slow leak even when closed due to wear and possible cracking of the sapphire seat, and it was important to minimize the amount of argon entering the chamber and pumped by the ion pumps.

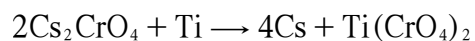
Mode	ECV	UHV1	UHV2	L-Gun	L-Top	N	S-Con	S-Top	S-Ar	S-S1	S-S2
A	X	X	X	X	X	-	-	-	-	-	-
B	O	O	X	X	X	-	-	-	-	-	-
C	O	X	O	X	X	O	X	-	-	-	-
D	O	X	O	X	X	O	O	O	X	X	X
E	O	O	X	O	X	O	X	-	O	-	-
F	X	O	O	X	X	O	X	-	O	-	-
G	O	X	X	X	O	-	X	O	-	O	X
H	O	X	X	X	O	-	X	O	-	X	O

Table 4.6: Valve/Pump states during normal operating modes

4.8 Film Deposition and Characterization

4.8.1 Evaporative Sources

Sources used for the initial dispenser tests under Moody and shortly thereafter were cesium evaporative sources from SAES. They combine cesium chromate and titanium with the proprietary St-101 getter compound (with reduction agents zirconium 84% and aluminum 16%) to achieve a cleaner release. The reaction of the chromate at high temperature follows the reaction



in which each cesium atom gains an electron and each titanium atom loses four. Cesium vapor is released at about 6 A of current when the source is new. Over the life of the source that must be increased to maintain evaporation rate, up to approximately 10 A as the last cesium is released. Generally the sources should be changed at 7-8 A for good rate control: about 10 heat cycles.

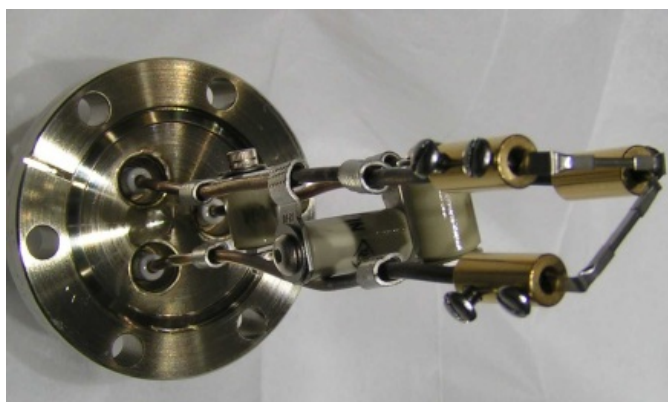


Figure 4.19: Cesium sources, SAES St-101

The SAES sources were not without problems. RGA scans of the background gas during cesium deposition revealed worrisome levels of water vapor, carbon monoxide, and carbon dioxide in the chamber which could negatively impact cathode QE. The sources also were inconsistent; roughly 15% of the sources installed failed to activate or produce any cesium at all. For these reasons a new kind of source was procured from Alvatec.

The Alvatec sources (advertised under the Alvasource trade name), like the SAES sources, are available not only with cesium but with a wide range of materials including the alkali earth metals Cs, Na, and K. In preparation for using all three in multialkali antimonide fabrication it was necessary to also increase the number of sources on the flange from two to four (three plus a spare Cs source). The sources and flange upgrade are detailed in Fig. 4.20.

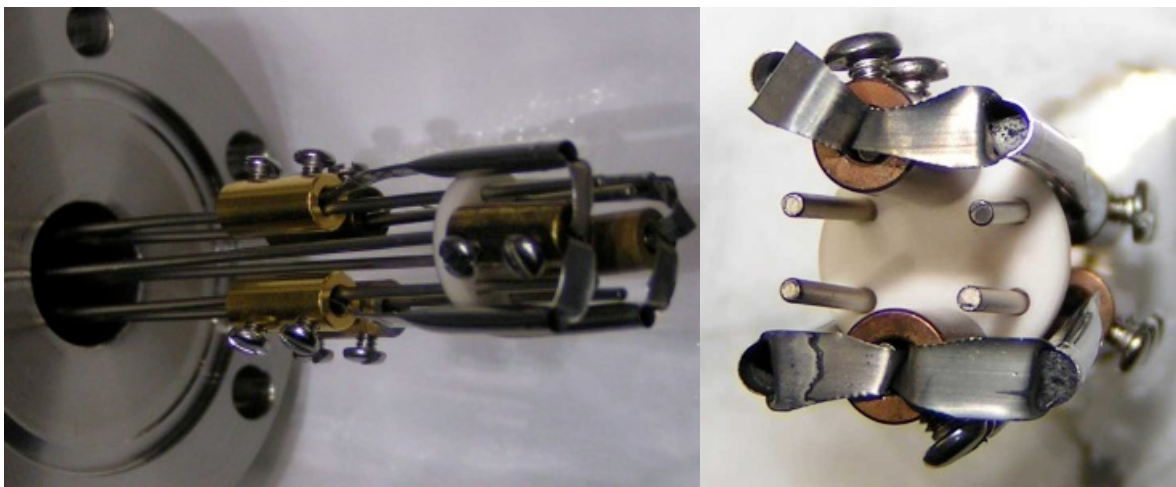


Figure 4.20: Alkali sources, Alvatec: (left) flange assembly, (right) source detail

The antimony source is mounted on the inside face of the 8" flange containing the sources and the laser viewport and ion gun, as shown in Fig. 4.21. It must achieve much higher temperatures than the alkali sources: antimony melts at 631 °C. The source is a steel tube with crimped and welded ends and an exit hole facing the cathode. Antimony pellets are loaded into the hole to replenish the source. A high current DC supply provides the 40-45 amps needed to run the antimony evaporation. A metal shield prevents unwanted radiative heating of other sources.



Figure 4.21: Entire 8" flange assembly: alkalis, left; antimony, right

4.8.2 Deposition Monitor

Deposition is measured via a quartz crystal microbalance deposition monitor. The quartz crystal is mounted in-plane and above the cathode facing all the evaporative sources. Any material deposited on the cathode is likewise deposited on the deposition monitor crystal. The crystal and mount are shown during a replacement process in Fig. 4.22. The installed configuration in reference to the cathode-anode assembly is seen in Fig. 4.23.

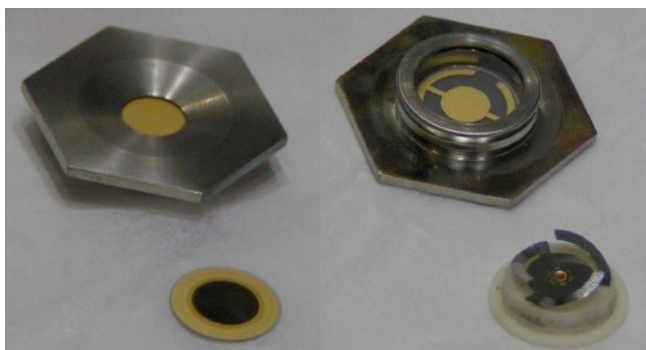


Figure 4.22: Quartz crystal exchange in deposition monitor, face with new installed and used crystal (left), rear view and spring mount (right)



Figure 4.23: Deposition monitor above anode-cathode assembly inside vacuum chamber

Note the three lines coming into the monitor from above: two for water cooling, one for electrical. The crystal must be water cooled in order to maintain a constant temperature. A Swiftech MCP350 pump (350 L/hr, 13' head) is used to circulate the anti-algae-treated water through Tygon tubing and a fan-cooled radiator from a CPU overclocking kit. Active cooling was deemed unnecessarily complicated and it proved sufficient to use the passively radiative system to maintain a stable monitor reading next to a hot, active dispenser cathode.

The principle of operation of the deposition monitor is straightforward. The initial resonance frequency of a freshly installed quartz crystal is 6 MHz. This frequency is reduced with additional mass deposited on the crystal, and by measuring the frequency shift, the added mass may be ascertained. Then using standard densities available for evaporated metal films, mass is converted within the Inficon XTM/2 controller to film thickness (Ångströms) which is displayed with 1 Å precision and recorded by LabVIEW with 0.1 Å precision. The film thickness so recorded is approximately, but not exactly, what is deposited on the cathode. But the sources have a wide enough evaporation angular distribution that the approximation is a good one.

4.9 Ion Beam Cleaning

4.9.1 Saddle Field Ion Source

Removal of deposited films and a return to a (reproducibly) atomically clean substrate condition for the next series of experiments is enabled by use of the Microbeam-7 saddle field ion source from AtomTech. High purity research grade argon is supplied via the 1.33" Con-Flat



Figure 4.24: Saddle field ion gun detail, showing beam exit



Figure 4.25: Ion gun and adjustable mount with argon fine leak valve

flange, and a 10 kV supply enables acceleration of the ionized argon atoms. Full control of beam current and energy is possible. The operation of the gun is not fully efficient and an energy corresponding to about 85% of the applied field is achieved. Thus for the 6.4-6.5 keV argon ions standard in these experiments, the applied voltage was about 7.5 kV.

Distance to the cathode is about 15 centimeters. The beam exiting the gun is not collimated, so it has spread to cover nearly the entire anode surface by the time it reaches the cathode. In order to improve the fraction of ion current actually reaching the cathode, it is negatively biased 90V below ground during ion cleaning to preferentially attract argon ions to the cathode rather than the anode.

Argon is supplied via a sapphire-seat precision leak valve. This enables the pressure of argon inside the gun to be adjusted in order to cause the plasma to "strike" (where the density of atoms is such that the ionization of one causes it to be accelerated and ionize more in a cascading effect) and a beam to be created. The gun must not be over-pressured or a "wide mode" beam will be created which is detrimental to the life of the gun and is ineffective at providing high ion current to the cathode for cleaning.

Periodic refurbishing is needed since internal parts are slowly eroded by the passing of the beam and sputtered material is slowly deposited on insulator surfaces. The latter situation is signaled when initial turn-on of the high voltage results in a high current draw from the power supply even before the argon has been supplied. Such a condition indicates a short circuit in the gun. The gun can be removed from the chamber and disassembled and the parts replaced. This was performed once during the course of experiments in this work. Since that time more than 110 Coulombs of beam have been supplied without the need for additional refurbishing.

The ion gun beam has a line-of-sight propagation at a 13° angle to cathode-surface-normal. In case alignment is not ideal, the gun port is mounted on a manually adjustable microme-

ter-actuated bellows with $\pm 20^\circ$ freedom in the horizontal and vertical directions. If the cathode has been changed out with one of differing dimensions it will be necessary to perform an alignment of the ion beam to maximize the current on the cathode. The results of such an alignment are shown in Fig. using a -90V bias on the cathode. The peak cathode current achieved here was 1.4 mA with a FWHM range of 0.26 inches and 0.28 inches for the right and left micrometers, respectively. Compare this to operation without the -90V bias. The peak cathode current achieved in such a case is just 0.45 mA , nearly a third that with the bias, and the FWHM is a range of 0.14 inches on both micrometers. Clearly the bias strongly attracts the beam, for the only way to explain the wide FWHM of the biased test is that the beam follows the field lines toward the cathode even when pointed significantly off-center. The difference in peak current is an indication of the focusing of the beam: with a biased ion current 3.1 times larger, the beam is reduced in size by biasing by roughly the square root of 3.1 , about 56% of its initial diameter.

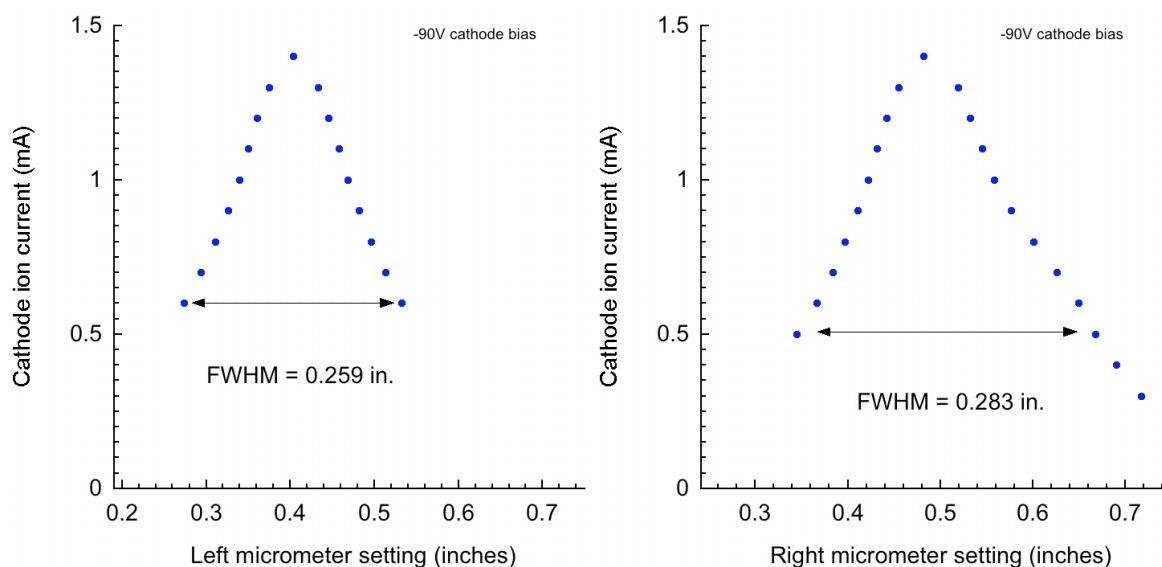


Figure 4.26: Ion beam alignment scans

4.9.2 Anode Shielding and Cathode Mount Sputtering

As the ion beam is operated, it will not only sputter the cathode but any exposed surface in the beam path. The copper dispenser mount sputters onto the back of the anode as shown in Fig. 4.27. The beam also leaves a circle on the anode face where all deposits have been removed. When the dispenser is removed the outer edge of the lip around the tungsten face shows additional copper sputtering deposits - see Fig. 4.28. Critically, there is no direct line-of-sight from sputtered areas to the cathode face.

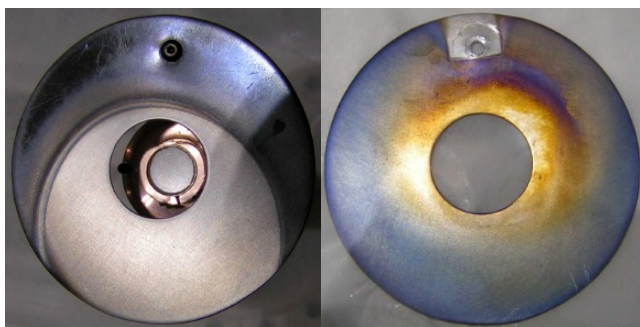


Figure 4.27: (left) Anode showing ion beam cleaned area after multiple antimony depositions, (center) Cathode-facing side of anode showing copper sputtering and discoloration of exposed, heated, oxidized surface



Figure 4.28: New dispenser, left, versus used dispenser, right, showing faint copper sputtering on outer top rim edge

4.10 Instrumentation Rack

Instruments rack-mounted near the vacuum chamber for experimental measurement and control are viewed in Fig. 4.29. From top to bottom row by row, and left to right in each row, they are as follows.

- Atomtech 800 series ion gun power supply, 10 kV
- Digitel SPC 40 L/s ion pump controller, Amrel PPS-2016 (alkali source current supply)
- HP 59306A GPIB-controlled relay actuator, SRS SR630 thermocouple monitor
- Digitel MPC 200 L/s ion pump controller
- Granville-Phillips 307 and 330 ionization gauge controllers
- Amrel PPS-2016 (2, alkali source current supplies)
- Keithley 286 picoammeter, Inficon XTM/2 deposition monitor controller
- PC running LabVIEW affording automation and control of all GPIB-capable devices
- scratch-built housing for water pump, radiator, and QE circuit voltage supplies
- HP 6681A 0-6V, 0-580A DC power supply (antimony source current supply)

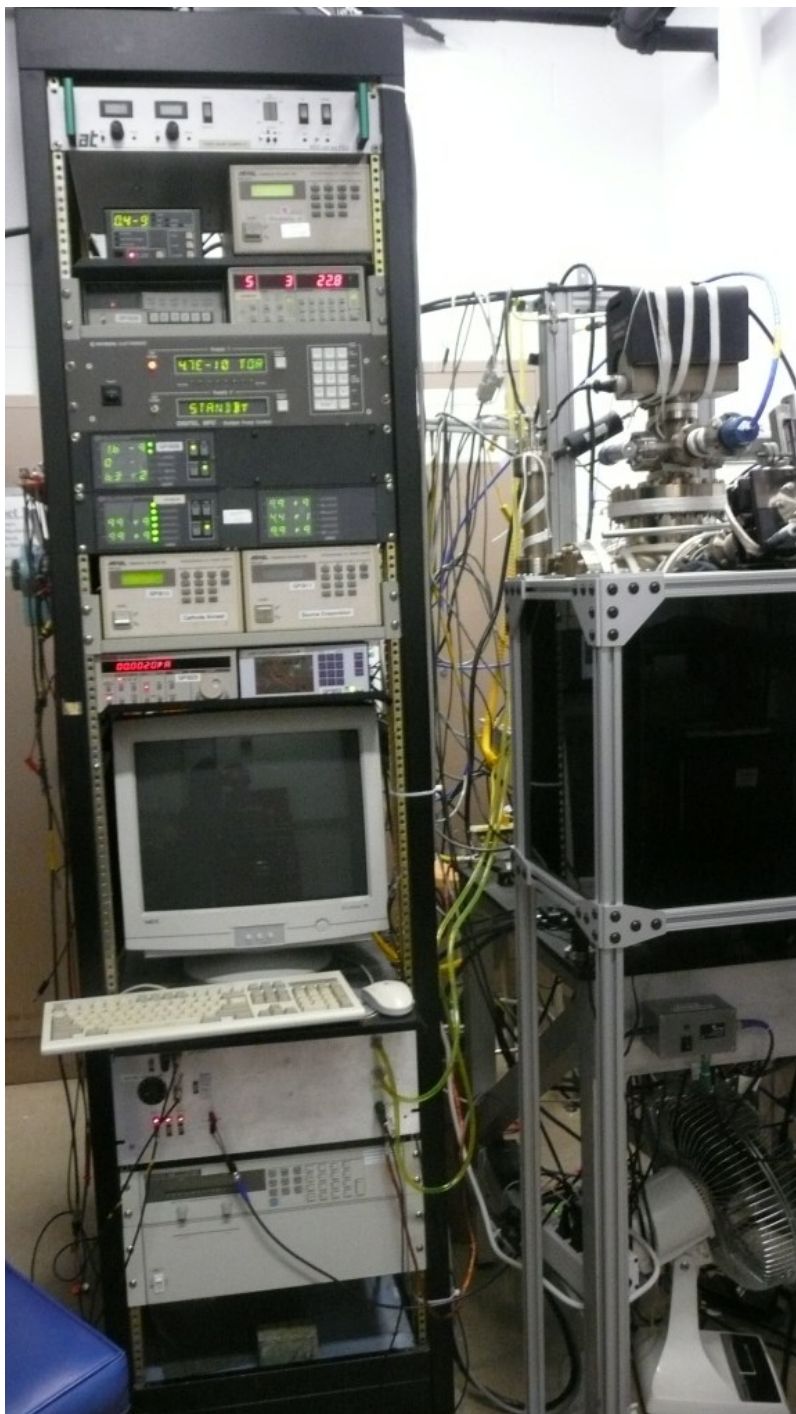


Figure 4.29: Equipment rack with power supplies, instruments, and LabVIEW computer control

Chapter 5: Experimental Techniques

5.1 Measurement Techniques

5.1.1 Pressure

Pressure was monitored using ion gauges and, at higher pressures such as during ion cleaning, nitrogen backfill, or atmospheric exposure, Convectron gauges. As mentioned previously, Convectron gauges read 30x low for argon since they are calibrated for nitrogen. Both ion gauges and Convectron gauges were read by the Granville-Phillips controllers which were in turn connected to the GPIB network and read by LabVIEW.

5.1.2 Laser Power

Laser power was measured either by hand, using alignment of the lasers with the thermopile detector (and appropriate safety precautions as in Section 5.5.1) or by automated LabVIEW control with the thermopile detector mounted inside the laser safety housing and the lasers commanded to position in turn. A multiplicative factor of 0.93 was applied to all laser power measurements to account for viewport transmittance so the laser power used in the QE calculations was laser power incident on the cathode, as distinguished from that exiting the diode.

5.1.3 Photocurrent

Photocurrent was measured using the Keithley picoammeter. The ammeter has the ability to measure from the picoamp range all the way to 2.3 milliamps. This range is covered by five

sets of internal circuitry which each have a different dynamic range, the highest ending at 2.3 milliamps, the next at 230 microamps, and so on. Switching between circuits is automatic but can result in momentary open-circuit conditions with unphysical currents reported. LabVIEW watches for and removes such data.

5.1.4 Coating Coverage

Coverage was measured by the Inficon deposition monitor. The various evaporants were all assigned a "film number" which has the preset values needed for the XTM/2 controller to convert from the frequency shift of the quartz crystal to a thickness reading in Ångströms. Film numbers are assigned as: 1, Cs; 2, Sb; 3, K; and 4, Na. The monitor was also re-zeroed at the beginning of an experimental run. Finally, it should be noted that the crystal and monitor do not account for evaporative losses from the sensor, so in theory the cumulative deposition totals could have been slightly under-reported depending on the volatility of the evaporant. In all cases here, the monitor reading was stable within Å/hr after deposition of material indicating such is not a great concern.

5.1.5 Cathode Temperature

Cathode temperature was measured by a K-type thermocouple in the molybdenum body of the button heater. It does not measure cathode surface temperature directly. Thermal conductivity and reasonably slow temperature changes are assumed to result in small thermal gradients so the thermocouple reading can reasonably be inferred to indicate actual surface temperature.

5.1.6 Background Gas Composition

Background gas composition was measured using the SRS RGA-200. The "200" indicates a maximum 200 amu in mass scans. For the built-in software analysis package to work properly in determining relative percent composition of the gases in the chamber, a range of 1-58 amu must be selected. The filament was turned on only when doing a scan or an initial outgassing (post-bake) to preserve life of the filament. The filament can be replaced (shown in Fig. 5.1) but is an extremely delicate, almost surgical operation which also involves atmospheric exposure to the chamber. It is inconvenient and difficult and should be avoided by not abusing the filament. A sample RGA scan and analysis readout are shown in Fig. 5.2 from a mixed contaminant test.



Figure 5.1: RGA filament, thoriated tungsten

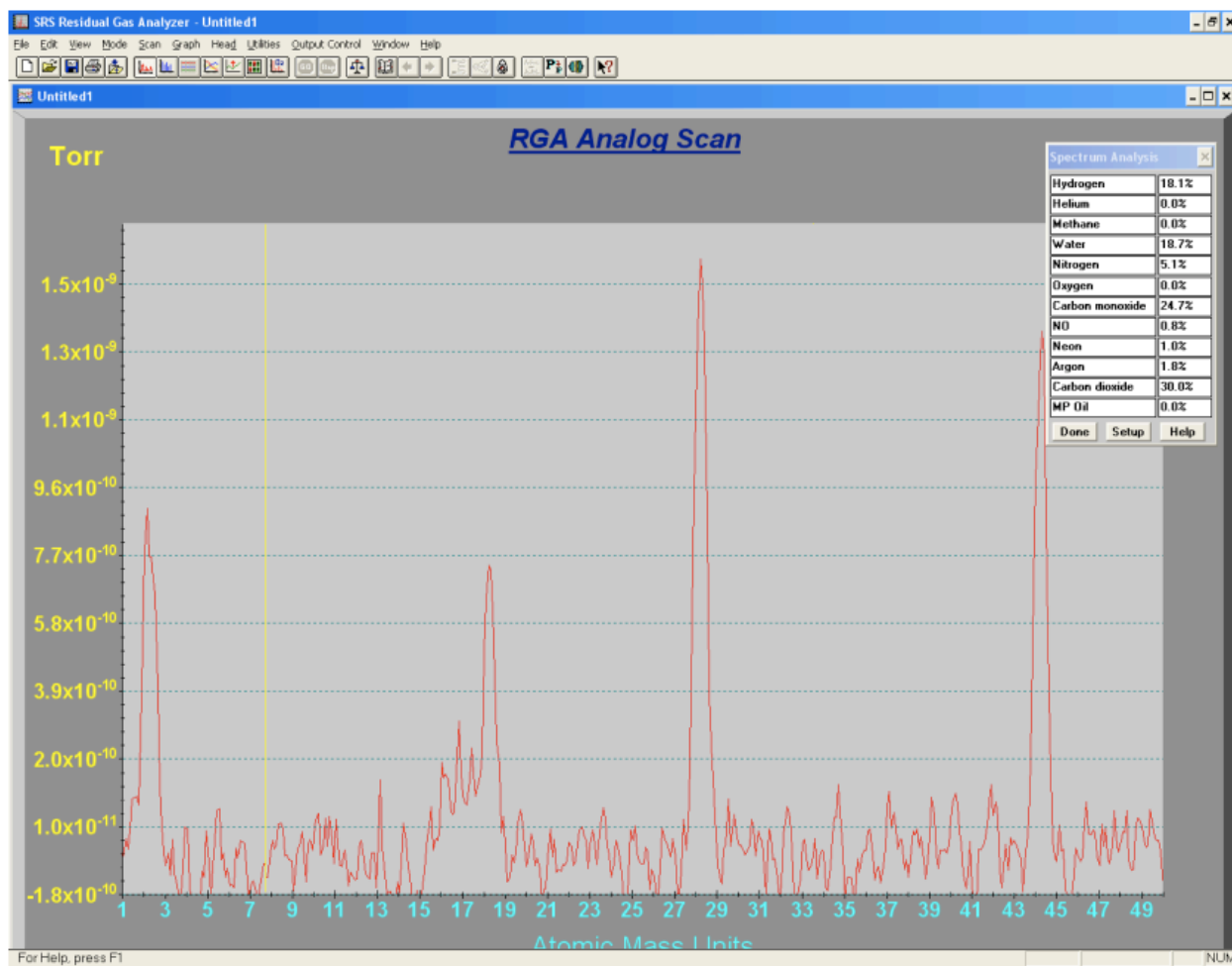


Figure 5.2: RGA scan and background gas analysis

5.2 Measurement Considerations

5.2.1 Space Charge

If the anode-cathode voltage is not high enough, the extraction of sufficient photocurrent will shield the anode from the cathode and result in a fictitiously low measurement of QE. This is

known as the space charge limit and is characterized by the Child-Langmuir law, which gives the maximum current extractable for a given voltage:

$$(5.1) J_{\max} = \frac{1}{9\pi d^2} \sqrt{\frac{q}{mc^2}} V^{3/2}$$

where d is the cathode-anode separation and V is the applied voltage.

The experimental anode-cathode distance is about 2 cm. With the lower QE cesiated metal experiments the existing apparatus was sufficient to apply an anode-cathode voltage of 180V and not see space-charge effects in the extracted current. Calculating the Child-Langmuir limited current from a 4 millimeter square cathode (corresponding to the approximate size of the laser spot) one obtains 1.2 mA for the space-charge-limited average current. Typical photocurrents in the cesiated metal experiments using drive lasers of a few mW were of order 1 uA, much less than this limit.

However, when working with higher QE semiconductors it was necessary to revisit this problem. When varying the voltage, if the emission is not space-charge-limited, the photocurrent will stay constant. In Fig. 5.3 this is shown, plotting extracted current versus voltage to the 3/2 power so as to show the Child-Langmuir behavior at low voltage. The material under test in this data was a cesium antimonide cathode driven by a 6.2 mW 375 nm diode laser at 11% QE. The maximum applied voltage was 180 V.

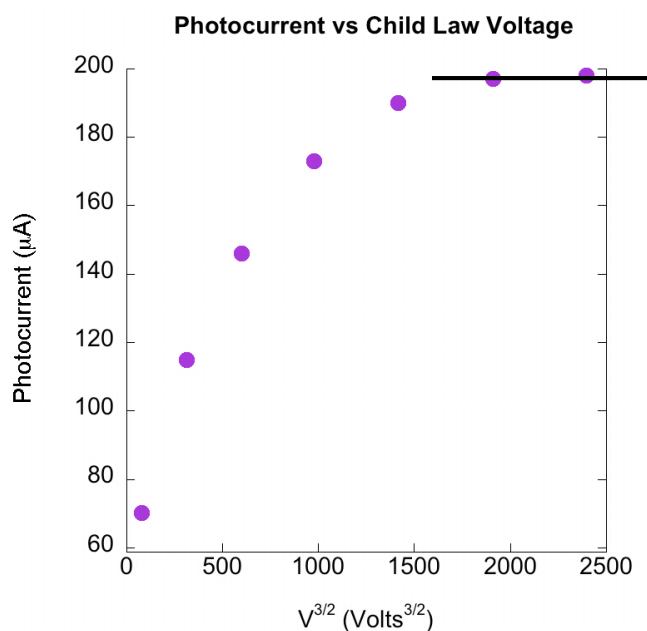


Figure 5.3: Space-charge-limited current from high QE Cs_3Sb cathode

The early behavior at low voltage sees significant space-charge effects. The late behavior shows the photocurrent has leveled off versus voltage, indicating the photocurrent is no longer limited and must be linear with drive laser intensity.

To ensure the space-charge limit was avoided, the isolated voltage supply was increased to a maximum 450V -- approximately 30 kV/m at the cathode. Photocurrent versus applied field is shown in Fig. 5.4 for three Cs_3Sb cathodes of varying thickness. Note the change in the vertical scale between each of the plots due to the reduced QE of the thinner cathodes. The initial Sb layer thicknesses of 6, 15, and 40 Å correspond to estimated total cesium antimonide thicknesses of (using the x5.9 rule from Ref. [102]) 35.4, 88.5, and 236 Å respectively. (Compare this to the

optical penetration depth at 375 nm of 200 Å and it is clear that thinner cathode QE should indeed be less than ideal.)

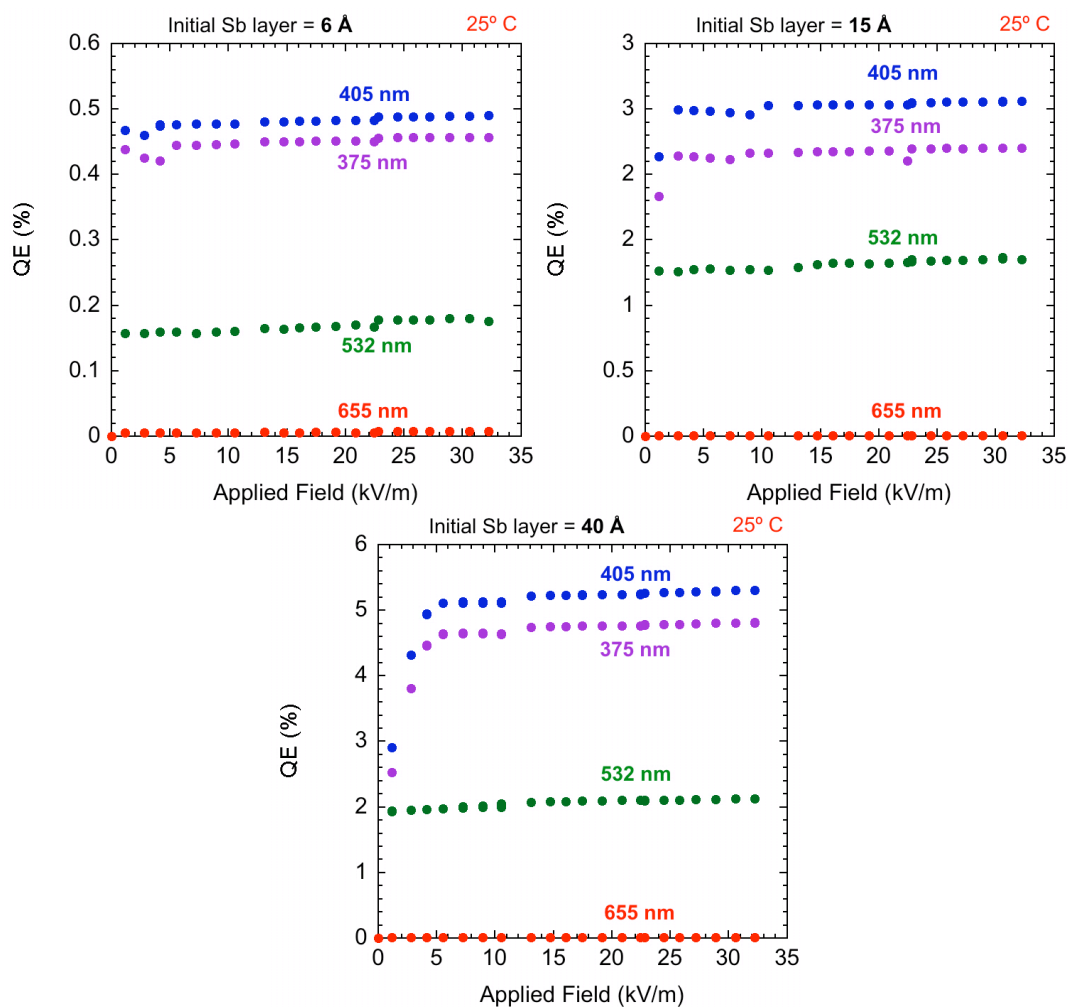


Figure 5.4: QE vs applied field, Cs_3Sb

5.2.2 Noise and Error in Measurements of Photocurrent and Laser Power

Noise is seen in this experiment as the so-called "dark current" present even when the cathode is not illuminated. The current is measured in the closed circuit and varies depending on

the picoammeter setting. With the dynamic range set to a 23 μA maximum (as is the case for some cesiated metal QE measurements, which are those with the lowest photocurrents and hence the most sensitivity to noise) the dark current is an average 0.4 nA. Compared to the photocurrents at the 0.11% QE maximum of cesiated tungsten, which measure just over 2 μA , it is seen that the signal-to-noise in the experiment is quite satisfactory. This situation only improves with the higher QE, hence higher photocurrent, alkali antimonides.

Error in the experiment comes from both random and systematic sources. The possible sources of systematic errors are discussed first with the steps taken to minimize them. In the measurement of QE there are only two experimentally determined quantities: laser power and photocurrent. Each of these two has its own unique considerations regarding systematic errors.

Laser power is measured using the PM3Q thermopile detector. A thermopile detector is a stack of thermocouples in series to produce a higher total voltage, and the response is directly proportional to the thermal power in the laser beam. As such it is DC coupled and suitable for CW laser measurement, as in this work, or for average power measurements of pulsed beams. Thermopile detectors are low impedance devices with low sensitivity to noise in the associated circuitry, but they are of course quite thermally sensitive, so they cannot be mounted in an environment of fluctuating temperature or external heat sources other than the laser beam. Using one's hand to hold the detector steady in the beam path, for instance, results in systematic error and erroneous readings. Another source of systematic error in the measurement of laser power is failure to account for the transmittance of the quartz viewport. A clean viewport has a flat transmittance across the full spectrum of lasers used in this work of 93% (3.5% reflectance at the win-

dow inner and outer surface), but care must be taken not to allow the viewport to become coated with thin films which will change the reflectance of the inside surface. This was observed once following the anneal of a silver cathode, where the temperature of the cathode resulted in a not insignificant vapor pressure of silver, enough to coat the viewport with a semitransparent film of silver deposits. Under normal operation or even under annealing of tungsten with its much lower vapor pressures, this is not a problem. If it does occur the viewport must be removed and cleaned.

Systematic error in the measurement of photocurrent is more subtle. As previously discussed in Section 5.2.1, space charge effects are real and deceptive, and if the measurements are operated with low enough anode-cathode voltage and high enough photocurrent to enter the space charge regime, the photocurrent and apparent QE will be artificially depressed. A second source of extraneous photocurrent, this time causing it to appear higher than normal, is the possibility of photoemission from other surfaces besides the cathode in the chamber. The energy of the UV and blue lasers in particular (3.31 and 3.06 eV, respectively) are not higher than the workfunction of most bare metals (compare tungsten at 4.65 eV, silver at 4.26 eV, copper at 4.65 eV, and molybdenum - the cathode heater casing - at 4.37 eV). However, when coated with work function lowering cesium as a result of either direct deposits from the wide spray of the evaporative sources or secondary deposits from migrating cesium, such metals can and will become photoemissive at the laser wavelengths in question. Cesium-coated tungsten, for example, has a work function minimum of 1.3 eV. For this reason the laser spots are focused narrowly on the cathode and avoid illumination of other nearby surfaces. An extremely subtle source of dark current and

hence systematic error in the photocurrent is the operation of ion gauges. Ion gauges use a hot filament as previously described to thermionically emit electrons which then ionize the background gas for measurement. These hot filaments can produce ballistically traveling ions which, if line-of-sight exists between ion gauge and cathode, actually contribute to the dark current. Characteristically this is a pressure-dependent dark current. In early experiments Moody observed 10 nA dark currents from this source. The effect was eliminated by moving ion gauges to sites in the chamber without line of sight to the cathode and anode assembly. Finally, significant systematic error can be encountered if operating unknowingly at elevated temperatures where thermionic emission is non-negligible. If thermionic emission is not recognized and all current is attributed to the photoelectric effect, the resulting QE calculation will have inflated values. For this reason the LabVIEW code includes the ability to measure current from the cathode un-illuminated in addition to measuring the current for each wavelength of laser. The un-illuminated current is the sum of dark current and thermionic emission, and at higher temperatures may be considered entirely thermionic since it is not difficult during experiments like dispenser activation to elevate the cathode temperature to the point where thermionic emission dominates not only dark current, but even photocurrent (see Figure 9.8: Activation of 2nd gen. cathode with Alvatec Cs:Bi reservoir, for an example at temperatures in excess of 300 °C).

Random error in the measurement of laser power can come from the fluctuation of temperature of the diodes, but this is so well-controlled by the fans and thermoelectric coolers (TECs) of the lasers that the power stability is better than 5% over 8 hours for the 532 nm DPSS laser and better than 2% for all other lasers. Random error in the measurement of photocurrent

can come from the noise pick-up of the long, 10' cables between the batteries and ammeter and the anode and cathode. By using triaxial cable and grounding the outer braid this is minimized.

5.2.3 Uncertainty in Calculation of QE

The dependence of QE on laser wavelength, on laser power (cathode-incident, which includes viewport transmittance) and on the resulting photocurrent is restated:

$$(5.2) QE = \frac{hc}{q\lambda} \frac{I}{P_\lambda}$$

where the equation is the same as Eq. (1.11) but the total laser power P_λ and photocurrent I have replaced the optical irradiance and current density, under the assumption that the entire laser spot illuminates a region smaller than or equal to the cathode size. Laser wavelength is not measured directly in the lab, but is rather reported upon delivery by the manufacturer; nevertheless it is a measured quantity. Since the three measured quantities are uncorrelated, the uncertainty in QE is the sum in quadrature of the relative uncertainties of the variables, obtained via:

$$(5.3) \Delta QE = QE \sqrt{\left(\frac{\Delta \lambda}{\lambda}\right)^2 + \left(\frac{\Delta P_\lambda}{P_\lambda}\right)^2 + \left(\frac{\Delta I}{I}\right)^2}$$

where of course Δ denotes uncertainty. The preceding formula presumes a Gaussian statistical distribution about the mean of a given measurement x with standard deviation Δx .

Relative uncertainties for the lasers are given with reference to Table 4.3, where the power stability gives the relative uncertainty in optical power directly and the relative uncertainty in

wavelength is a quick ratio of the appropriate two columns in the table. The results of the calculation of QE uncertainty are performed here to demonstrate upper-bound uncertainties for all data sets which follow. The data set used to obtain typical photocurrent relative uncertainty at peak QE of cesiated tungsten is shown in Figs. 5.5 and 5.6. The uncertainty in laser power and wavelength dominates, so all QE data sets share error bars of +/- 2.5% to 5%.

Laser (nm)	$\frac{\Delta\lambda}{\lambda}$	$\frac{\Delta P_\lambda}{P_\lambda}$	$\frac{\Delta I}{I}$	$\frac{\Delta QE}{QE}$
808	.0124	.02	.009	.0252
655	.0153	.02	.001	.0252
532	.000188	.05	.001	.0500
405	.0494	.01	.0004	.0504
375	.0267	.01	.0005	.0285

Table 5.1: Calculation of relative uncertainty in QE for all laser wavelengths

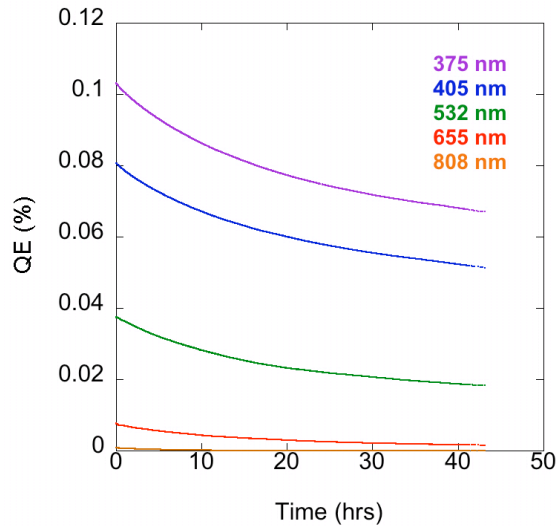


Figure 5.5: Data set for photocurrent noise (10 hour lifetime measurement, Cs:W)

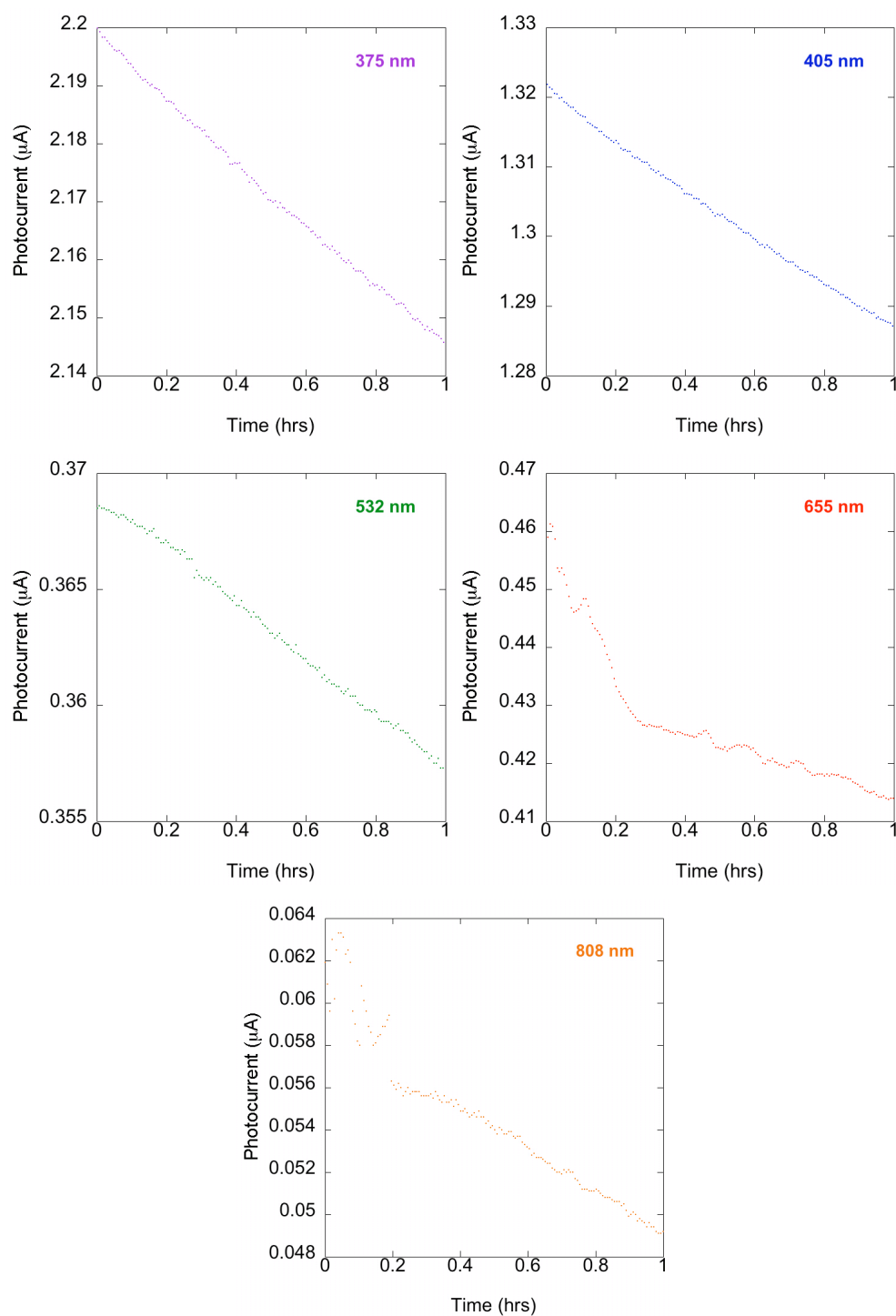


Figure 5.6: Photocurrent noise by laser wavelength, first hour of previous figure

5.3 Automation Techniques

5.3.1 LabVIEW introduction

LabVIEW (a pseudo-acronym for Laboratory Virtual Instrumentation Engineering Workbench) is a commercially available, widely used graphical programming interface for the control and automation of processes and for the acquisition and display of data. LabVIEW contains two environments for each user-written program: the front panel, a window containing all displays and controls, and the block diagram, a window containing all variables, formulas, commands, programmatic structures like for loops or if statements, calls of subroutines, etc. The front panel has the appearance of a dashboard or instrument panel, while the block diagram is similar in appearance to a circuit diagram.

Each program, with front panel and block diagram together, is called a virtual instrument or VI. Programming of a VI begins with the placement of controls or indicators on the front panel, which automatically show up as variables which can be written to or read from in the block diagram. Connections, logical operations, programmatic structures, etc. are then placed and routed in the block diagram to achieve the desired outcome. A VI may also call other VIs, which are termed sub-VIs in the same sense as subroutines. For reliability, ease of development, and quick debugging in this work, modular programming was used, with separate experimental functions programmed in separate VIs. This is particularly useful if a function will be used more than once in the process of any experiment; the same sub-VI can then be called every time.

The interface of the LabVIEW software with the instrumentation which controls the experiment is done via the general purpose interface bus (GPIB) standard, IEEE 488.1, originally developed by Hewlett-Packard in the late 1960s under the HP-IB trade name. GPIB is a parallel data bus with handshaking, with a maximum data transfer speed of 8 MB/s. The handshake is necessary due to the wide variety of devices which use GPIB, and is the initial communication between the controller and device where the two agree on a common state and optimal data transfer speeds, etc., before proceeding with reads or writes. For this work, a GPIB expansion card uses the PCI slot of the computer. The card contains a GPIB stacking connector port to run standard GPIB cable from the computer to the devices. The 24-pin stacking connectors (shown in Fig. 5.7) allow cables to be daisy-chained or connected in a star configuration from a common central hub, as is done in this apparatus. A maximum 20 meters of cable can be used from the controller card to any device on the network. Under GPIB, the computer uses a standard format to query and command each device, though the command syntax is device- or manufacturer-specific. A VI is written to control each device with the appropriate command syntax included. These VIs are then called by the main program to command or query each instrument.

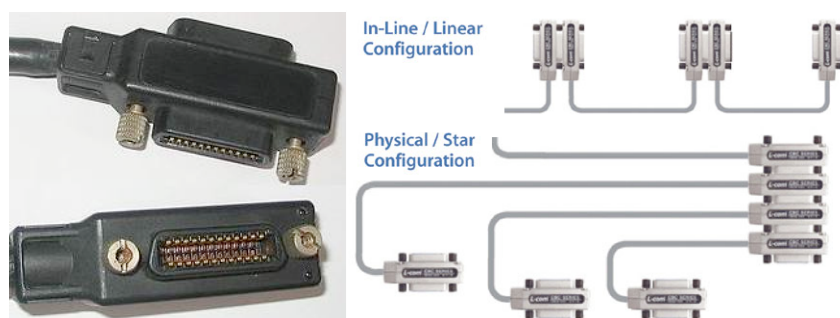


Figure 5.7: GPIB stacking cable connectors

5.3.2 QE Measurement

Automation of QE measurement proceeds via LabVIEW software in the following steps:

Initialization <ul style="list-style-type: none"> - Re-home linear motor (gives encoder a defined reference point) - Open and write header information to data file - Open and initialize variables - Define states of front panel charts and displays
While Loop (loop until stopped by user command, by timer, or by various errors) <ul style="list-style-type: none"> - Review front panel for modifications to laser sequence - Command next laser in turn to illuminate the cathode - Acquire all data (photocurrent, calculated QE, pressure, coverage, temperature, etc.) - Update plots - Command instruments with updated settings (heaters, current sources, etc.) - Write all data to next row in file
Close <ul style="list-style-type: none"> - If triggered by a stop condition, print front panel and close file

Table 5.2: LabVIEW QE measurement process summary

5.3.3 Code Enhancements

Existing code at the start of the work presented herein was written by N. Moody and is detailed in Ref. [19]. Numerous enhancements to the capabilities and operation of the code were programmed over the course of experiments, with highlights summarized in Table 5.3.

- Massive rewrite to "call by reference" for all variables (rather than "call by value"). Reduces memory use, cleans up block diagram, and allows simpler debugging.
- Plot QE not as one line of all laser wavelengths, but as a separate line for each laser. Much clearer plots are obtained, though two full cycles are needed before each wavelength has two data points and can begin plotting a line. Current is plotted point by point immediately.
- Automate laser calibration using thermopile power meter at the start of every experiment, if needed. Updates QE calculation directly and includes 93% transmittance of viewport.
- "Overnight mode": allows long experimental runs like QE lifetime measurements to use longer laser cycle periods so that the blue and UV diodes may be turned off while the other lasers are in use. Reduces duty cycle of the limited-life InGaN and GaN diodes by half or more.
- Allow optional measurement of "dark" cathode current, which for a hot cathode is the thermionic current. (Commands the robot to move all lasers away from the viewport.)
- Enable "thermionic correction" where thermionic current is subtracted from photocurrent during hot cathode operation so QE reported is not artificially inflated. Does ignore photo-thermal interactions, a good first-order approximation.
- Compute and display QE vs coverage plots live and on screen
- Allow marking of QE vs time plot at key points in experiment for later reference
- Display maximum QE numerically as well as graphically
- Record cathode temperature and pressure vs time plots on front panel
- Enable zeroing of any plot at any time
- Write operator name, date, time, filename, and column headers to data file
- Automate front panel chart printing after end of experiment for use in lab notebooks
- Enable instant screenshots at any time, saved to data folder
- Automate selection of appropriate film constants on deposition monitor when changing from one evaporation source to another
- Eliminate data artifacts (e.g., erroneously high photocurrents when Keithley 286 switches circuits to shift dynamic range, glitching pressure monitors, etc.)
- End experiment in the following cases: overpressure/poor vacuum, target coverage, *target QE*, target experimental run time, user command
- Detailed commenting

Table 5.3: Highlighted LabVIEW code modifications and upgrades

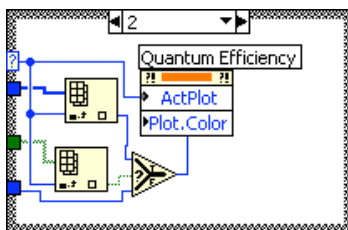


Figure 5.8: Sample case structure on block diagram, for QE plot settings

A sample case structure from the block diagram is shown in full in Fig. 5.8. A portion of the block diagram for the main program, EiM_v2_Dispenser.vi, is shown in Fig. 5.9 (the full diagram is too large to display with legibility), emphasizing the vast number of inputs and outputs which the call-by-reference scheme organizes and initializes. Each variable may then be searchably tracked in every location that calls it by reference -- much easier for debugging or modification than trying to trace clustered wiring diagrams to track down which data set is used where. In Fig. 5.10 the same program is detailed but in another, later part of the main while loop in the block diagram. The data acquisition and file write commands are shown. The front panel of the main program is shown in Fig. 5.11. Programmatic controls are at top left, cathode heater controls top center, laser controls just below that, and deposition controls at the bottom. A trialkali (cesium sodium potassium antimonide) fabrication has just been completed. The vertical yellow lines on the QE vs time plot are markers showing when depositions from the various sources were begun. The QE vs coverage plot is meaningless for this experiment though for a coated metal it would show the familiar Gyftopoulos-Levine-like behavior with a peak in QE between one-half and two-thirds coverage. The pressure, temperature, photocurrent, and coverage plots versus time have been cleared in preparation for a new experimental run.



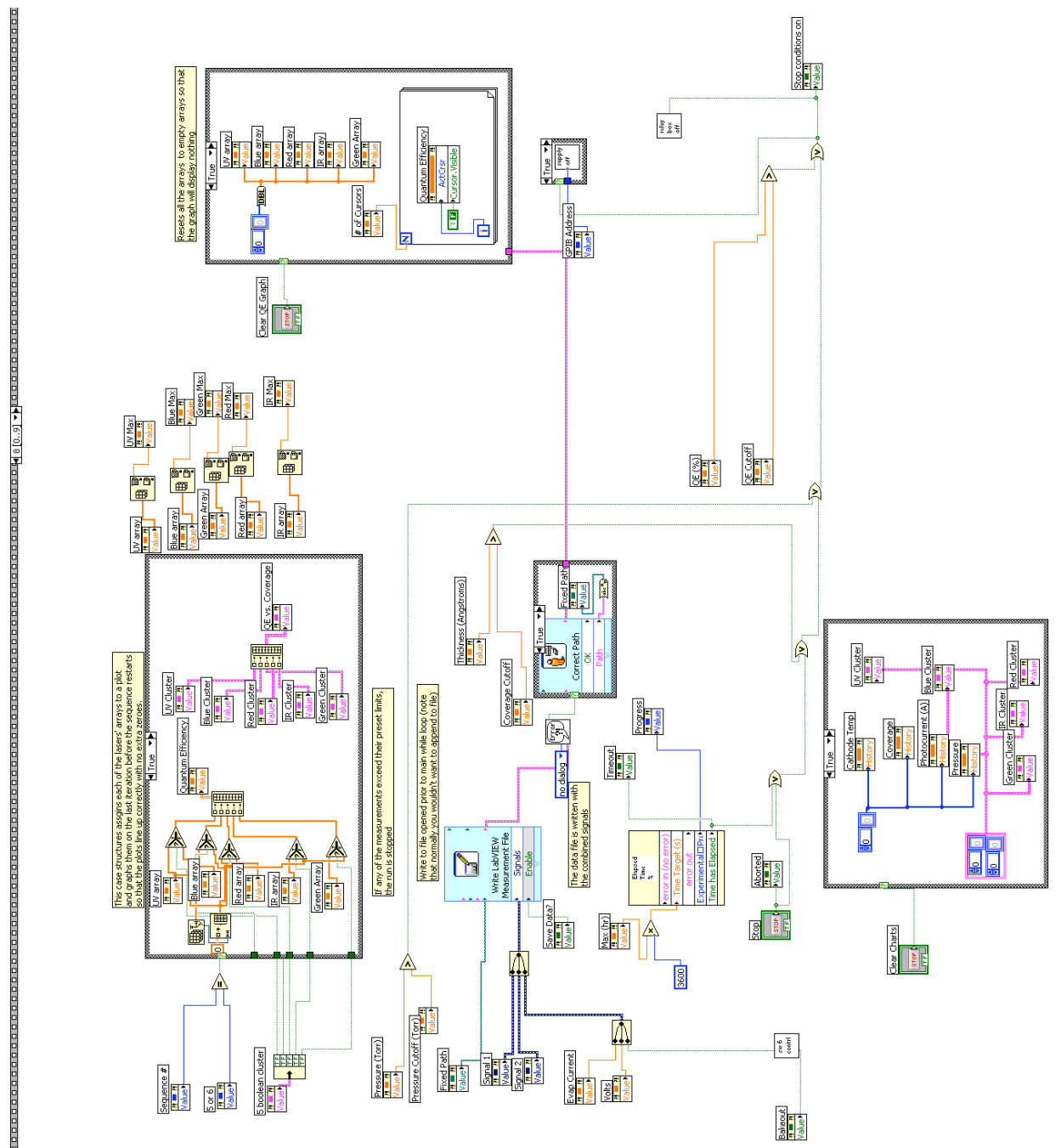


Figure 5.10: Detail of block diagram, showing data acquisition and file write

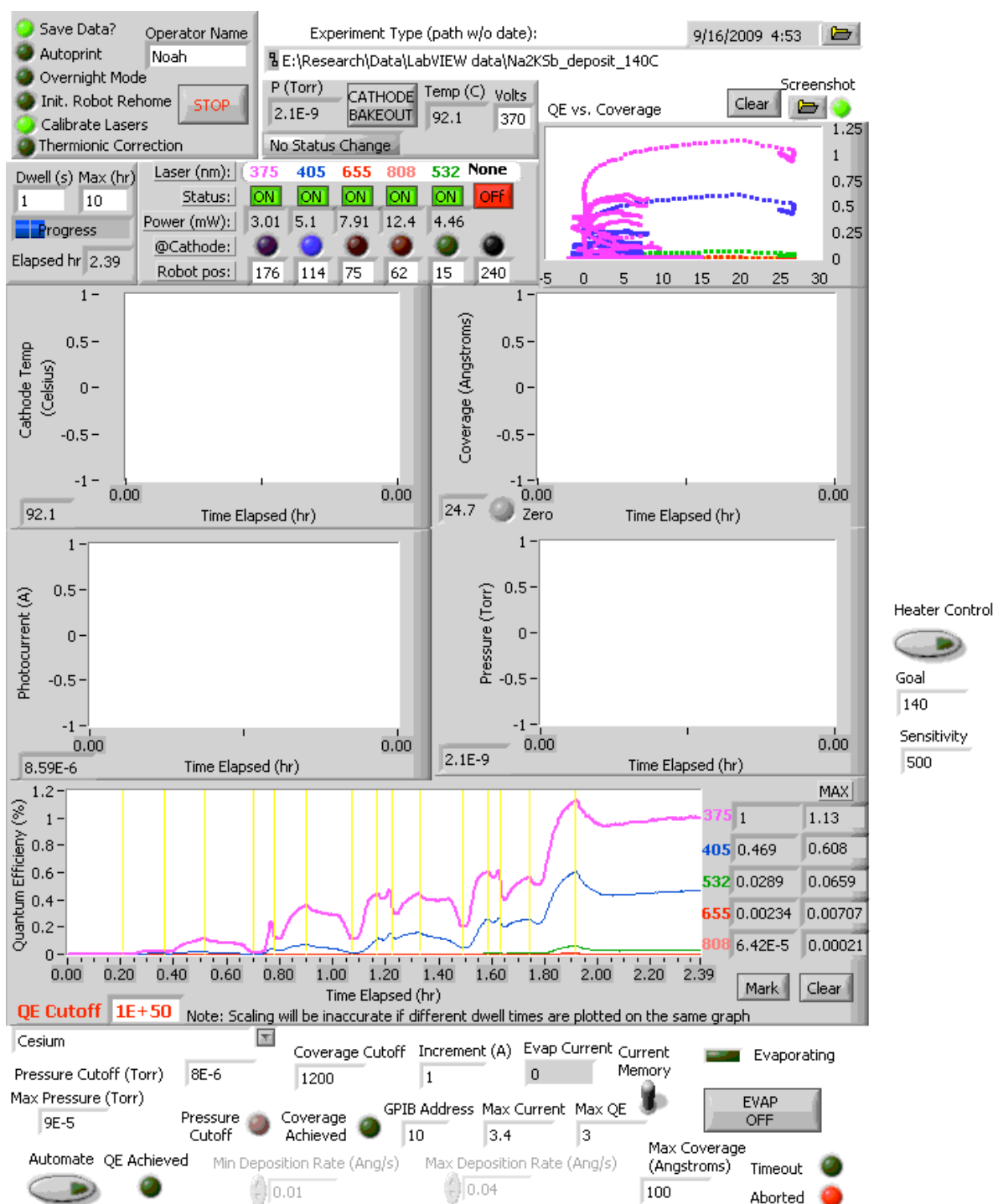


Figure 5.11: LabVIEW interface with multi-alkali fabrication

5.4 Standard Procedures

5.4.1 Chamber Bakeout/Pumpdown

The length of time the chamber is exposed to atmospheric contamination and at what humidity largely determines the time required to bake out the vacuum system. In all cases a bake-out was considered complete when the pressure under turbopumping at the elevated bake temperature is below 5×10^{-7} Torr. This could be attained in a few hours with proper care (example: removing a 2.75" Con-Flat flange with the system overpressured with N_2 , and replacing a blank plate immediately while working with the flange). With a full chamber opening, a bake of at least 24 hours was needed. With new components, two or three days may be required.

When the ion pumps are first turned on, it is advisable to leave the turbopump actively pumping on the chamber for a few minutes. Post-bake this is important to allow the ion pumps to outgas. Also, the initial turn-on can be done at slightly higher than usual voltage in the ion pump if there has been significant argon pumping by the ion pump. The problem with argon and the noble gases in general is that they are non-reactive with the titanium walls of the ion pump and do not adsorb well, so the only way they can be removed from circulation is by being buried by sputtered titanium. If or when a pocket of argon gas so trapped is uncovered by additional sputtering, a cascading release of more of the trapped argon can occur - almost as if the pump burped argon. It can be helpful to force this to occur via elevated operating voltage, when the turbopump is still pumping on the chamber, so that the excess argon may be removed from the system

entirely. With new pumps or systems where argon has not been pumped over the long term by the ion pumps, this should not be necessary.

Local bakeout temperatures anywhere on the apparatus were not allowed to exceed the temperature limits of the components. Heater tapes can easily approach local temperatures of 300 °C, so two examples of where heater tape was not used under any circumstances were across viewports (the solder will melt) or around bellows (the welds will develop leaks under stress). Most of the UHV stainless steel components are bakeable to 450 °C. Likewise the system was inspected before bakeout to ensure all heat-sensitive components had been either removed (like the RGA head and video camera), or disconnected (like the Tygon tubing for water circulation through the deposition monitor, which was tightly clamped and pinched closed on both the supply and return lines before disconnection because of the 7' head of water above the pump), or at least not in contact with the heater tape (like any plastic-insulated wires and cables). If increased bakeout temperature was desired the entire chamber was wrapped in an aluminum foil thermal blanket, with foil tape to join the edges of each sheet; cathode temperatures of order 200 °C are reached without the thermal blanket and of order 300 °C with it. Monitoring of hot spots with multiple thermocouple positions was employed when using thermal blankets, particularly near components with lower bakeout limits.

One of the keys to successful experiments is anticipating failure mechanisms and building fail-safes into the operation of the apparatus. (An example is the UPS backup for the ion pumps during power outages.) With regard to bakeouts which, under standard procedure, run overnight without supervision, the effect of a power outage could be problematic. If an outage

occurred, shutting down the turbopump and heaters, backflow of gas through the stationary turbopump vanes would occur into the still-hot chamber, increasing the risk of oxidation of components or increased contamination rather than the intended reduced outgassing. For this reason all bakeout heaters were run through power relays (Furman MP-20) which have a momentary-off feature. If power is lost, the relay reverts to the off state until signaled manually to turn on again. This prevents the heaters from operating on an un-pumped chamber after an outage. Secondly, an electromechanical valve (ECV) was installed on the turbopumping station with a normally-closed state. When powered, it opens to allow pumping. By likewise routing power to the ECV through the momentary power relays, any loss of power immediately isolates the chamber from the pumps to prevent backflow contamination, and the valve does not re-open until the user arrives to reset the system state. One downside is that readily available ECVs are not high-conductance (they have small bore sizes) and so the pumping speed of the turbo station is limited by the valve. Under normal use of the turbo in this work this is not critical since base pressures are achieved with ion- and not turbo-pumping. There is a slightly increased pump-down time after an ion clean, still short vs experimental durations.

5.4.2 Ion Beam Cleaning

The ion beam cleaning procedure involves more manual tasks than most because so much of the equipment or tasks are not GPIB/LabVIEW controllable. It was performed in 6 stages: pumping and gas preparation, electrical preparation, initialization, cleaning, pumpdown, and reconnection.

The gas lines of the tree, if not filled with pure argon, were turbopumped for half an hour and then flushed with argon three times. The turbopump was isolated from the tree. The lines were then overpressured with pure argon (so any leaks in the swagelok connections, never designed as high vacuum components, were outward not inward). With the turbopump isolated and the pressure at 1×10^{-8} Torr, the valve to the UHV chamber could be safely opened. Ion pumps were turned off.

All unnecessary equipment was turned off -- grounding issues with the ion gun HV supply had been problematic, causing erratic operation of the Ethernet link to the motor robot and of the GPIB-controlled relay box for laser power, and though proper grounding was subsequently installed, it was deemed safest to err on the side of caution. The QE circuit voltage was turned off and the circuit disconnected. Ammeters were connected to measure cathode and anode ion current. The thermocouple plug was grounded to bleed off ion current. The cathode was biased -90V. Prior to leaking argon in to the gun the ion gauges were turned off.

The LabVIEW program "ion_cleaning_dose_and_current_monitor.vi" was initialized. The ion gun HV supply was turned on, checked for short-circuit current, and then adjusted as desired. Standard 7.5 kV settings were maintained with currents of a few microamps.

The plasma in the gun was "struck" by gradually increasing the argon leak rate using precision leak valve L-gun. The beam was run to the desired dose (standard was 40 minutes, 1.6×10^{17} ions). Ion current tended to drop slowly over the first ten minutes as the gun internals

heated and pressure equilibrated. The cleaning was stopped by closing the argon valve, turning off the high voltage, and stopping the LabVIEW acquisition.

Pumpdown was performed using the turbopump since the ion pumps were not designed for pumping large amounts of noble gases. Base pressure of at least 5×10^{-7} was reached before turning on ion pumping and isolating the turbopump again. The -90V bias was turned off, QE circuit reconnected, ammeter reset for photocurrent (microamps) not ion current (milliamps), and power restored to any devices powered down. Prior to QE measurement the robot was re-homed and the laser alignment checked.

5.4.3 Coating Deposition

An ion beam cleaning was performed before coating the cathode. Then the QE program was initialized. The deposition monitor was re-zeroed if needed. In the main QE program under the "Evaporation Module" the evaporation of the chosen alkali was initiated, entering an appropriate current (starting at 3A for a fresh Alvasource and incrementing by 0.1 A if needed; 6A for a used source was not unusual). If depositing antimony, the current was entered directly on the supply, ramping in 1A increments towards 43 A over about ten minutes assuming the source had already been outgassed. When desired thickness or QE was approached the source was turned off. The antimony source tended to deposit 2-3 Å additional material as it cooled from 43 Amps. The alkali sources were much more responsive, with 0.1-0.3 Å of additional deposition.

5.4.4 Cathode Heating

In the active QE program the cathode heater button was toggled to turn on the heater relay. AC heater power was measured using a clamp-on ammeter and standard voltmeter at the leads at the feedthrough. Power was controlled manually on the variac, with marked dial locations corresponding to equilibrium temperatures attained at that setting to aid in the process. The step-down transformer at the top rear of the equipment rack has a toggle switch; that was always in the on state for power to be applied to the cathode. The variac was adjusted as necessary over the course of minutes or hours to achieve the desired temperature profiles for the experiment.

5.4.5 Controlled Gas Exposure

The QE program was initialized and run throughout. Before introducing contaminant gas, the ion pumps were turned off and turbopumping begun on the chamber. The LabVIEW program (which integrated pressure over time to obtain Langmuirs of exposure) was zeroed and initialized. To start the gas leak into the chamber, the knob on the precision leak valve L-top was turned one full rotation, then slowly beyond that until the pressure in the chamber reached the target between 1×10^{-7} and 1×10^{-6} Torr. Before the end of the measurement an RGA scan was run to determine background gas composition. This allowed conversion from total Langmuirs of exposure to contaminant Langmuirs of exposure via the partial pressure of the oxidizing gas present. The filament was turned off after the scan. The leak valve was closed when the target depreciation was reached. A recesiation was usually performed afterward.

5.4.6 Laboratory close-out

Before leaving the lab the equipment was always placed in a safe state. All lasers were powered off, at the laser head or at the power supply, particularly the blue and UV lasers with their shorter life. All high voltage and high current supplies (QE circuit HV supply, ion gun HV supply, antimony current source) were powered off if not in use. The turbopump and electro-mechanical valve were off if not in use, on if pumping down the gas tree or chamber or during a bakeout. The RGA filament was checked to be off so as not to burn it out inadvertently.

5.5 Precautions

5.5.1 Laser Safety

The diode and DPSS lasers used in this work are Class 3B: they fall in the wavelength range of 315 nm to near-IR, between 5 mW and 500 mW. Protective eyewear was required in the lab when performing alignments. The uninitiated might expect one pair of laser goggles, but such a pair would be opaque if it truly protected at all wavelengths. Two pair are required for full-spectrum protection: the Thorlabs LG3 is orange in color and protects from 190-532 nm (the UV, blue, and green lasers) with OD 7+, and the Thorlabs LG4 is blue in color and protects from 190-400, 633, and 662-835 nm (the UV, green, red, and IR lasers) with OD 5+. (OD, or optical density, refers to the orders of magnitude by which intensity at a given wavelength is reduced.)

For everyday operations it was inconvenient to wear goggles continuously and to stock enough for all persons in the lab, so a laser safety housing (Fig. 5.12) is used which encloses the lasers and translational mount. Black laser fabric hangs from the experiment side and small hoods of the same fabric cover the beam path to the viewports. A video camera pointed through the upper viewport allows monitoring of the laser spot position on the cathode: the camera's GaAs sensor is able to detect the full range of wavelengths.

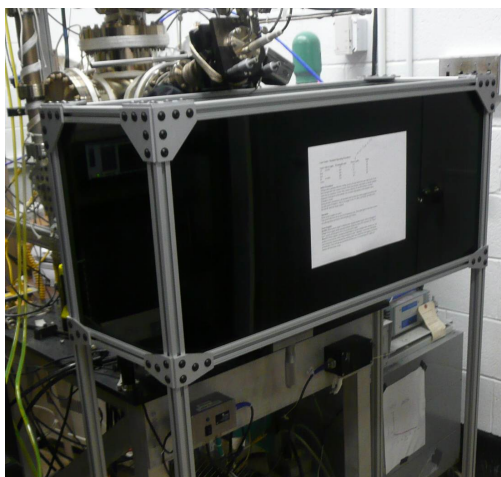


Figure 5.12: Laser safety housing

5.5.2 General UHV Cleanliness

Proper procedures are essential to ensure the UHV surfaces are not unnecessarily contaminated during handling. Particularly the oils found in human fingerprints can result in significantly increased outgassing and release of carbon-based compounds in the vacuum chamber and were strenuously avoided.

Powder-free latex gloves were required at all times, and were only used to handle clean surfaces. Gloving was done without touching the outside of either glove with an ungloved hand. After gloving, hands were kept out of lint-producing pockets and out of hair, face, etc. If while using gloves the wearer touched un-cleaned surfaces, the gloves were changed for a fresh pair before returning to work with the UHV components. This often led to regloving several times during an operation, and it was found useful to have two people, one gloved and one ungloved to handle both clean and dirty tasks.

The clean-surfaces-only rule required that as a result, all tools, bottles, etc. be wiped down with an ethanol wipe to remove oils and dust before the final gloving and UHV work, so that they could be handled by the worker throughout the process. Kimwipes, the trade name for low-dust absorbent tissues, were used for the ethanol cleaning. They are white, so any dirt or oil removed shows as a dark stain on the wipe. A surface was not sufficiently cleaned in the ethanol stage until the wipe came away white every time.

A low dust environment was essential. Short of working in a clean room, the following precautions were helpful. The work area was not in a high foot traffic area and was away from any active air ducts since cycling of the HVAC system stirs up dust which has collected near the outlets. The work area was prepared as in Fig. 5.13 by first covering all surfaces on which would be laid UHV components with aluminum foil (oil-free, "dry anneal A" foil is preferred but not always available), and by using wipes or foil to temporarily cover any components which were not currently being worked on so that dust is not allowed to settle. All tools and materials were

cleaned and laid out in advance. Tools which contain cadmium or lead or were painted were not used.

Storage under proper conditions was important. Parts which were intended for long-term storage were wrapped in aluminum foil, and moisture-sensitive materials such as unused evaporation sources were stored in a desiccator - a glass sealed jar, with desiccants in the base, which minimizes humidity during storage. Commonly used desiccants are deliquescent salts like calcium chloride or other hygroscopic materials like calcium sulfate and silica gel. The desiccants usually have a colored saturation indicator in them, often cobalt chloride (CoCl_2). Anhydrous cobalt chloride is blue, turns purple when it bonds with two water molecules, and then pink under further hydration and saturation. The desiccants were changed before they had reached their absorption capacity and replaced with fresh ones; the periodicity with which this is needed depends on humidity and how often the desiccator is opened and may be months or years. Most used desiccants can be recycled if desired by oven drying.

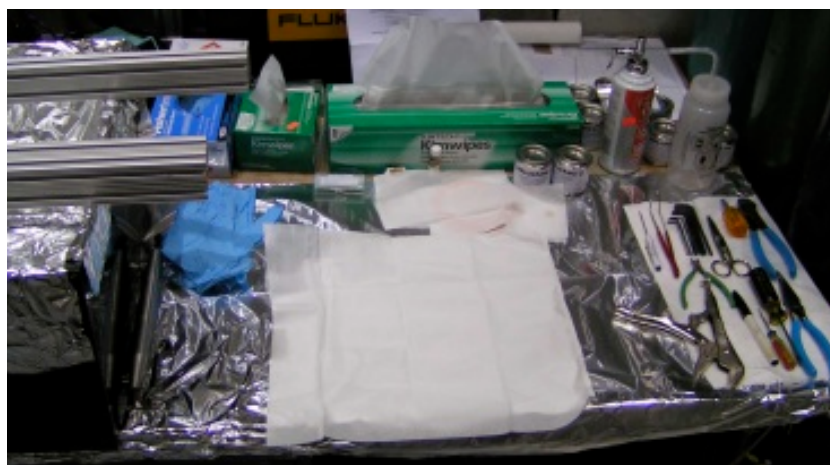


Figure 5.13: Dust-minimized workspace

5.6 Dispenser Surface Characterization Techniques

5.6.1 Microscopy

In order to characterize the sintered tungsten used in the cesium dispenser photocathode, two microscopy techniques were used. Optical microscopy was first performed to get a quick and general look at the surface, and to use depth of field to determine surface roughness. Then electron microscopy was performed to characterize the grains and pores in sintered tungsten in much finer detail.

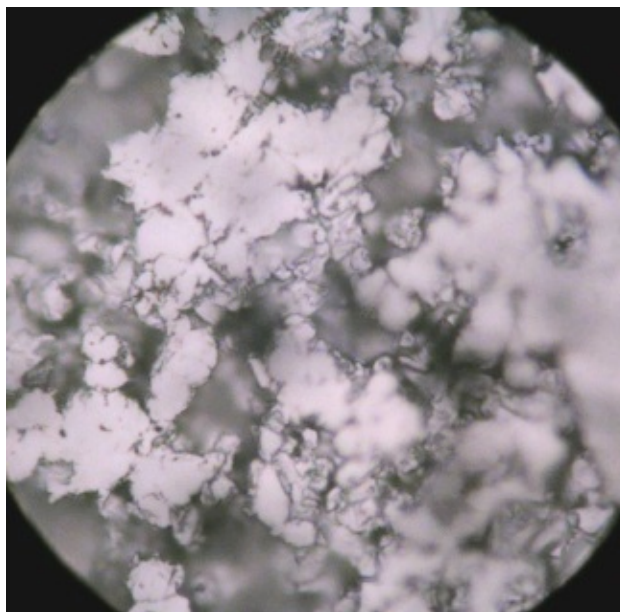


Figure 5.14: Optical microscopy of sintered tungsten surface, 70% dense, 1500 magnification

In the optical microscope photo shown in Fig. 5.14, many 1-10 micron size grains of tungsten are visible in random orientations. A length scale is not available but the picture may be compared to electron micrographs where such a scale is displayed. The depth of field in this case, based on the optics used, is also approximately one micron, and so the surface roughness is in-

ferred to have height variation of that order as well since some areas of the surface are slightly out of focus beyond the depth of field.

Electron microscopy was then performed to quantify and further detail the observations made. The 1-10 micron grain size is shown with the 10 micron length scale in Fig. 5.15. Note the small sub-micron size pore located almost dead-center.

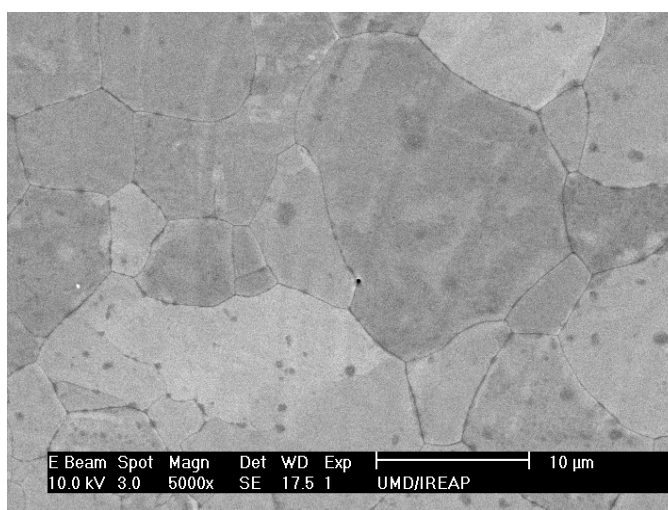


Figure 5.15: E-beam microscopy of sintered tungsten, 70% dense

This, the rear face of the cathode, also shows faint concentric ring-like striations from mechanical polishing (e.g., a buffing pad on a drill press) which are not found on the front face. The polishing on the back surface would not have been finished with the same fine grit as the front in order to meet spec. Another observation is that the cathode is pore-sparse, possibly as a result of over-polishing and filling in existing pores. The cathode was specified as 70% dense by the manufacturer, Spectra-Mat, but initial imagery does not appear to support this claim. This pore sparsity was not observed on the more carefully polished front face. This cathode (D02) and

in fact its twin (D03) failed to activate and dispense cesium, whereas an otherwise identical cathode but from a different polishing batch (D01) activated properly. To investigate the porosity further the D02 cathode was placed in a 30% dilute hydrogen peroxide etching solution for one hour. Following this process, the cathode was again placed under the electron microscope. The results are shown in Fig. 5.16 for the back face of the cathode. Many pores have been opened up or exposed, and the claim of 70% density appears valid. It was evidently the surface only which had a sparsity of pores. This further emphasizes the need for care in the polishing process.

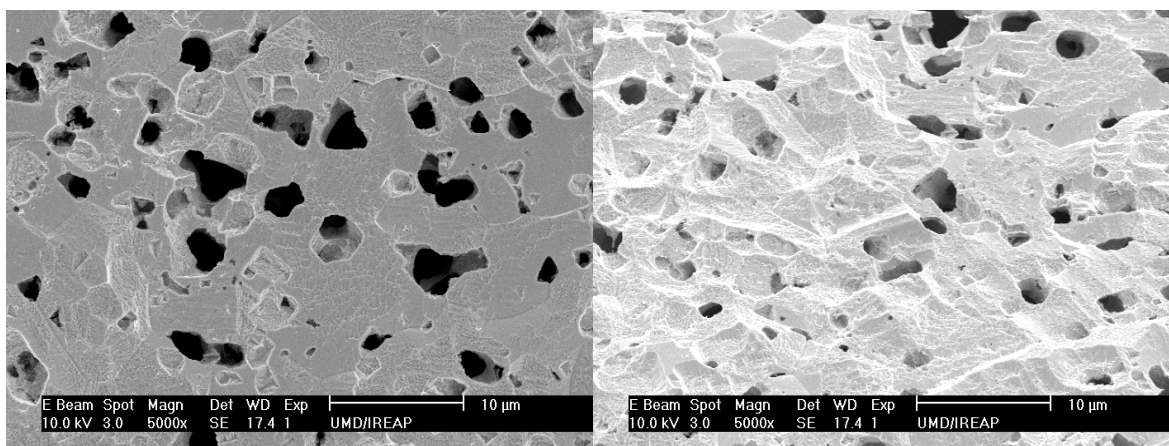


Figure 5.16: E-beam microscopy of sintered tungsten after peroxide etch: (left) surface-normal viewing angle, (right) glancing viewing angle showing roughness of etched surface

5.6.2 Focused Ion Beam Milling

Following the electron microscopy, the pores themselves were investigated using focused ion beam (FIB) milling. An electron microscope obtains imagery while a tiny, pico-amp beam of gallium atoms sputters away a very controllable region of the surface. As illustrated in Fig. 5.17,

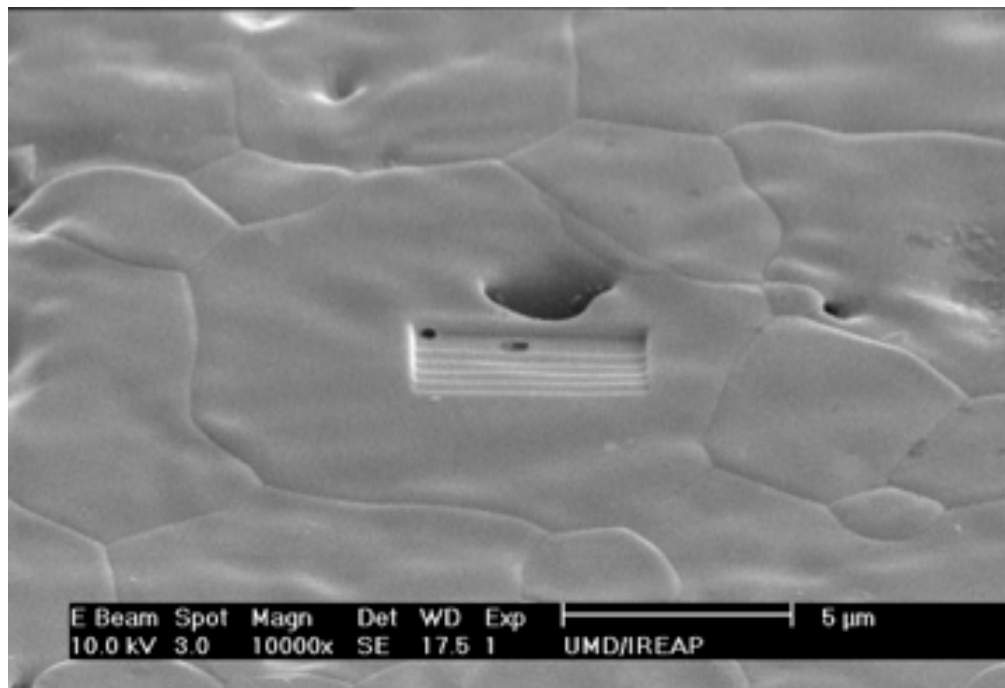


Figure 5.17: E-beam microscopy of initial ion beam milling

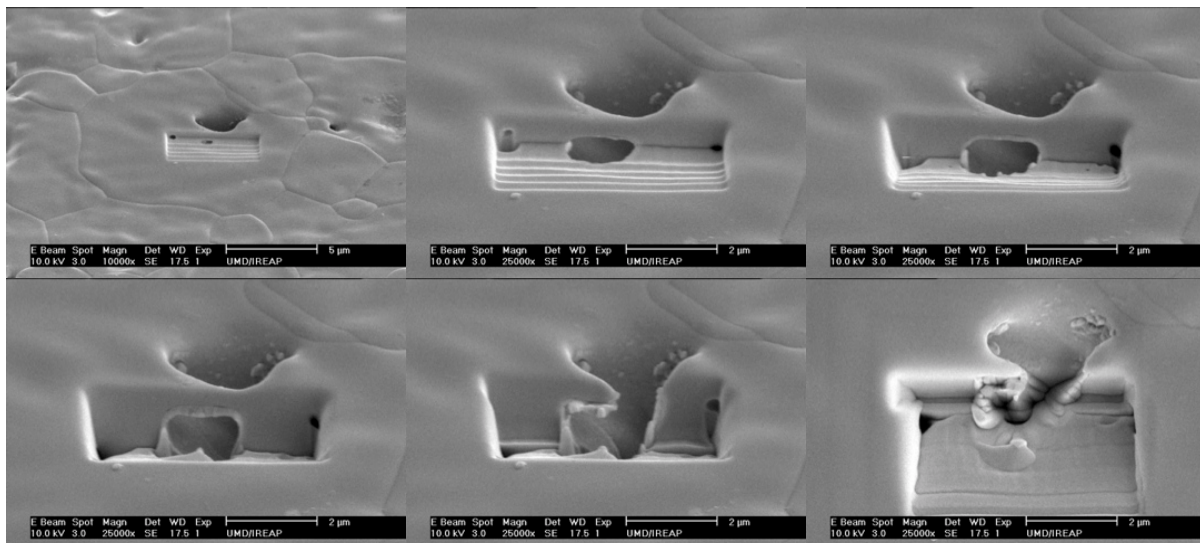


Figure 5.18: Continuation of milling in previous figure

focused ion beam (FIB) milling was used to probe the subsurface structure of the pores seen on the cathode surface. The gallium ion beam at 10 keV was used to mill away tungsten in a five micron square area while taking electron microscopy imagery of the sintered tungsten surface in order to probe pore structure. In Fig. 5.17 the detail of an initial milling sequence is shown, and in Fig. 5.18 the continued series is illustrated. The scale of the first image is five microns, and of the remaining images, two microns. The last image is a steeper viewing angle to give perspective and shows a subsurface grain boundary running left to right near the far edge of the milled region, not evident in the initial image prior to milling. The pore in question is shown to be highly irregular in shape, to angle strongly beneath the grain in which it is found, to end at a subsurface grain boundary, and to fail to intersect with two nearby subsurface pores in free space but to indirectly connect with them via grain boundary walls.

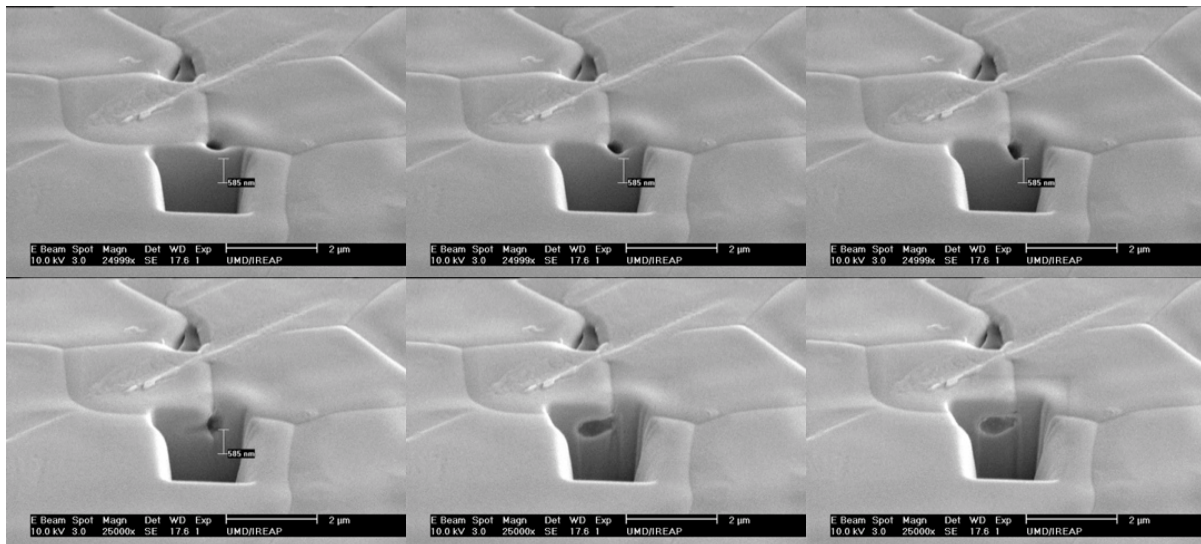


Figure 5.19: Gradual extension of pore-adjacent milled profile

Due to the deposition of excess milled tungsten in the pore which obscured otherwise interesting areas in Fig. 5.18, a different technique was developed. The milled region was deeply processed adjacent to, but not intersecting, another pore. The region was gradually extended towards the top of the imagery in Fig. 5.19, such that the pore was gradually exposed in sub-surface detail without unwanted deposition of metal within the pore itself. In this case also, the pore appears to end without a free-volume connection to other pores, only one grain width beneath the surface.

The conclusions of this investigation are: first, visible pores on the surface are not indicative of pore channel continuity on the 10-micron scale; second, pore density on the surface may be reduced due to polishing effects; third, pore direction is random and pore location is not always at grain intersections; fourth, pore size at the surface may grossly overestimate the pore dimensions subsurface; fifth, individual pore free-volume continuity is highly unlikely to be maintained through a 40-mil (1 mm) thick sintered substrate; and therefore sixth, cesium diffusion along grain boundaries as well as through pores is proposed as the mechanism by which is obtained the observed uniform coverage of cesium in dispenser QE tests.

5.7 Ion Beam Cleaning Characterization Techniques

5.7.1 Introduction

Characterization of the ion beam cleaning and its effects on the substrate was very important because the process preceded every QE experiment in this work. The studies reported here

had two primary goals: determine whether the beam induces surface roughening and of what order, and determine the effectiveness of ion cleaning from a dose perspective to quantify the amount needed to remove a monolayer coating completely from the surface.

5.7.2 Surface Roughening

Minimal indications of crystal-face dependent sputtering rates leading to roughening on the sub-micron scale were found during argon ion cleaning of sintered tungsten at 6.5 keV. Shown in Fig. 5.20, from work done in collaboration with A. Balter [103], is scanning electron microscopy (SEM) and focused ion beam (FIB) imagery of the sintered tungsten surface. Four images are presented, moving counter-clockwise from the upper left. Image A is an FIB image; the secondary emission from the FIB which forms the image varies with crystal face, so darker and lighter grains correspond to random orientation with different crystal faces in view. Image A compares directly to image B, taken via SEM, as seen by the corner feature in the lower right. Grain correlation is highlighted to aid identification. It is known that the crystal orientation affects sputtering yield, and the image A corresponds to before an ion clean while B is post-cleaning: little change is seen in the macroscopic appearance of the grains, so if any variation in sputtering rate occurred from grain to grain, it is not obvious in this imagery. Images C and D, while not at identical positions or magnifications (scales of 2 and 1 microns respectively), show typical grain appearance before (C) and after (D) ion cleaning. There is visible a small increase in apparent surface roughness, but this may be due to different imagery locations.

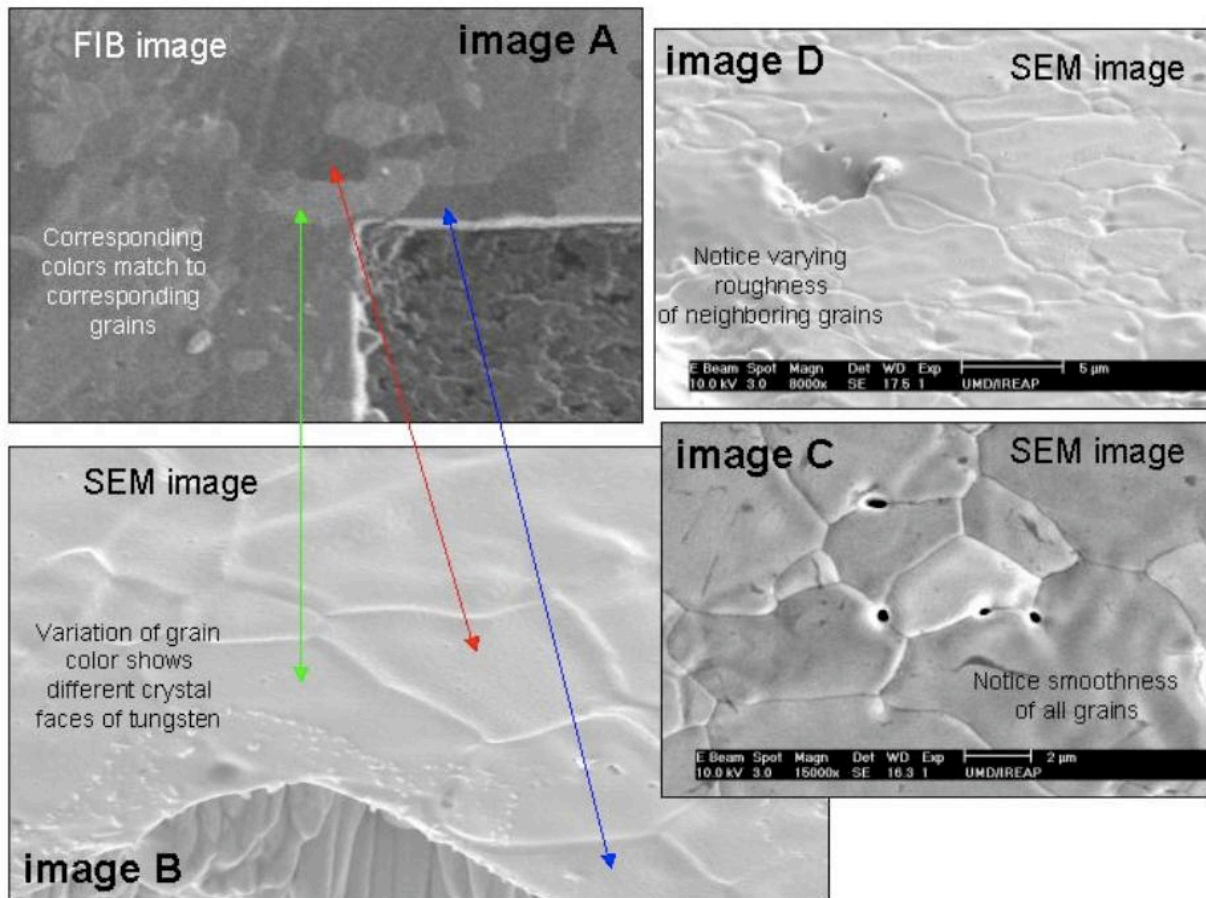


Figure 5.20: Crystal-face dependent sputtering and surface roughening of sintered tungsten

Following the acquisition of the imagery above, simulation was performed using the commercial ion implantation program SRIM[®], and with the appropriate parameters for a 6.5 keV argon ion beam impacting tungsten the average ion penetration depth in 60% dense sintered tungsten was estimated at 4.8 nanometers. This is still less than the average grain size by nearly three orders of magnitude; any processing of varying rates must occur at the sub-micron scale, so surface roughening grain-to-grain in a single cleaning must be minimal. Even over extended pro-

cessing of multiple grain depths, the random grain orientation would tend to average out the crystal face dependent sputter yield effect.

Further insight comes from a 2-micron micro-protrusion, facetiously named "The Hamburger", which was discovered during microscopy and which had acted as a shadow mask for a small semi-circular region of the surface during ion cleaning. Thus a side-by-side comparison of pre- and post-ion cleaning surface structure on a scale much smaller than the grain size is enabled. This imagery is shown with 2 micron and 1 micron scale size in Fig. 5.21. It is indicative that there may be increased grain smoothness at the 100 nm scale after processing, within the single crystal face of one grain. Interestingly, a very close look at the shadowed region shows that there are in fact two nearly-overlapping regions of semi-circular shape: this comes from a slight realignment of the ion beam during processing of the cathode and confirms that the observed feature is indeed shadow masking from the ion beam cleaning. Perhaps most importantly, it is clear that there is indeed measurable sputtering of the substrate tungsten atoms during ion cleaning, but this processing rate appears to be even, at least within the bounds of a single grain.

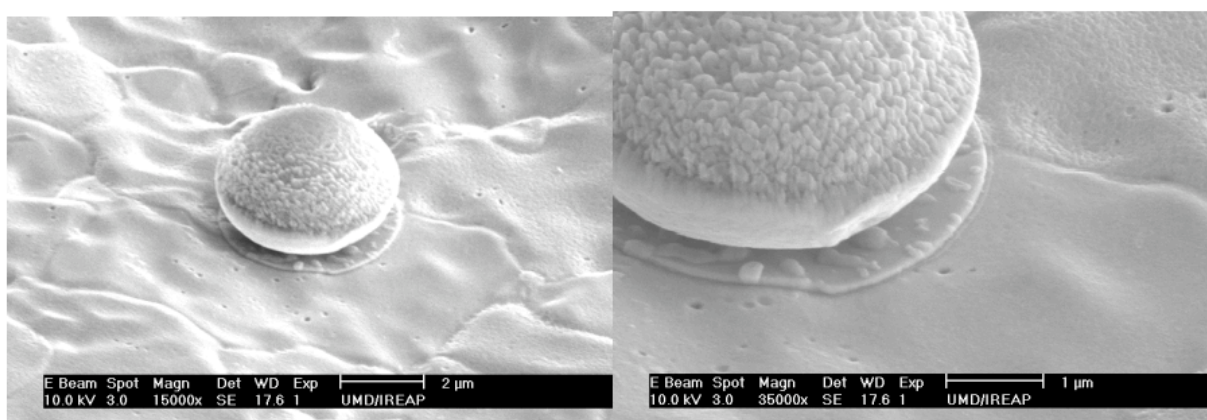


Figure 5.21: "The Hamburger." Micro-protrusion as shadow mask during ion cleaning

5.7.3 Surface Cleaning Effectiveness

As has been discussed by Moody, 6.5 keV argon ion beam cleaning yields significant (factor of 2) improvements in peak QE from cesiated tungsten substrates compared to anneal-cleaning of identical cathodes of 650 °C for thirteen hours, as displayed in Fig. 5.22, adapted from Ref. [19]. Similar results are seen for cesiated silver substrates where the peak QE improvement of 6.5 keV argon ion beam cleaning over anneal cleaning was an even more impressive factor of 3 [104].

Since ion cleaning has such a beneficial impact on the atomic cleanliness of the cathode prior to cesiation, it is used in preference to anneal cleaning in most cases. (Annealing may still be beneficial when removing antimony if the anneal exceeds the melting point of antimony -- workable in the case of a tungsten substrate, but inadvisable for silver which would itself begin to evaporate). Therefore it was important to characterize how long a cleaning should last. When

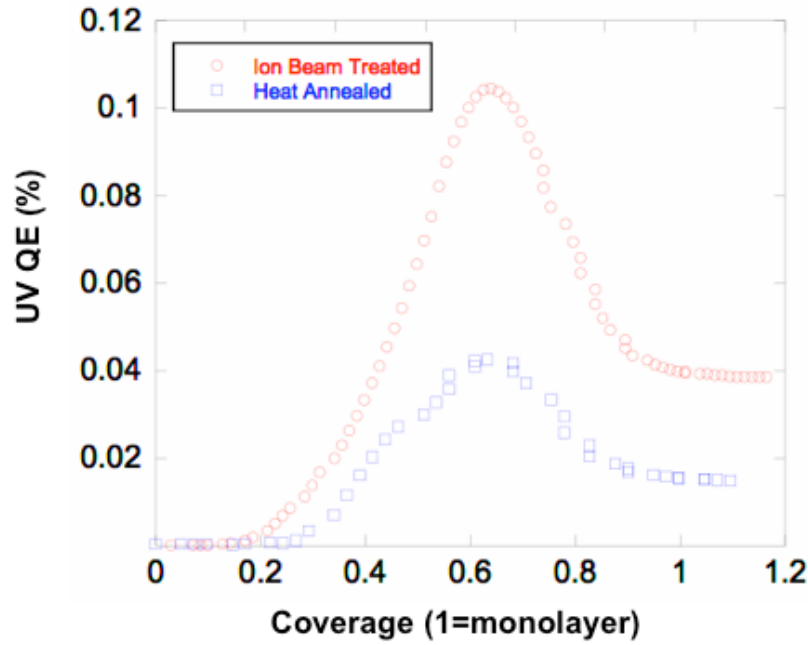


Figure 5.22: Ion beam cleaning vs anneal cleaning of tungsten, cesiated after cleaning

experimenting with cesiated silver substrates, an analysis of a variable duration ion beam cleaning's effect on QE was performed [105]. The results are shown in Figs. 5.23 and 5.24 for a 1 mm radius laser spot at 375 nm on a 1 inch diameter silver cathode with a 6.5 keV Ar ion beam. The latter figure simply takes the thickness of cesium and converts it to coverage (% monolayer) according to the GL theory peak for Cs:Ag of 53.6% scaled by the equation $\theta = (x - x_0)[53.6/(x_{\text{peak}} - x_0)]$ where x_0 was the initial Cs thickness (nominally zero, but in practice not precisely, due to drift of tenths of an Ångström on the deposition monitor prior to deposition) and x_{peak} was the thickness at the peak QE. The time axis is converted to dose (number of ions) via the ion beam current integrated throughout the cleaning procedure. A monolayer of cesium is, as would be expected, cleaned off the surface very quickly. Almost no cesium re-

mains after one minute. Continued cleaning may be beneficial for removing other, more strongly adsorbed contaminants, or in the case of reactive metals after atmospheric exposure, for removing an oxide or sulfide (tarnished) layer to expose a fresh substrate surface.

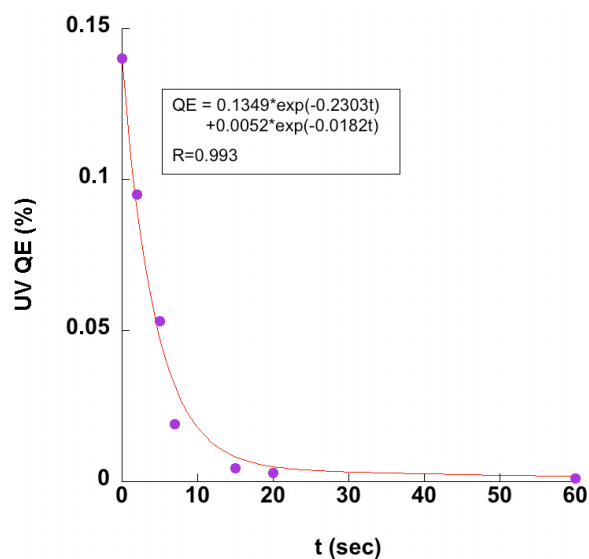


Figure 5.23: QE vs ion beam cleaning duration, Cs:Ag

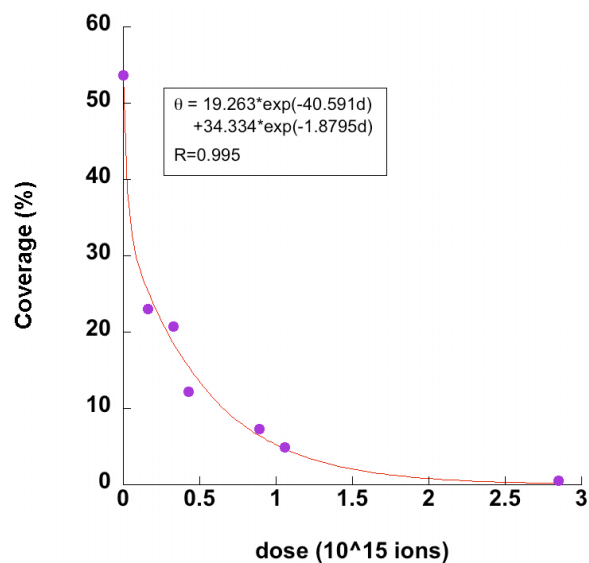


Figure 5.24: Coverage vs ion dose, Cs:Ag

A double exponential fit was used since at high coverage cesium bonds less strongly to the substrate (assumedly why it might sputter more quickly). We can estimate sputtering yield by noting cesium has a covalent radius of 2.44 Å whereas silver has an FCC lattice constant of 4.09 Å. Assuming then that there are four silver atoms under each cesium atom on the [100] face, defining 100% coverage, then for a monolayer coating on a 1" diameter silver cathode there are 1.5×10^{14} cesium atoms per square centimeter (1.2×10^{17} cesium atoms in total), each spaced by twice the lattice constant of silver. 50% coverage sputtering yield is, simply reading from the slope of the graph and converting from coverage to number of cesium atoms as above, roughly 200 adatoms per Ar^+ ion, and 5% coverage, roughly 3 adatoms per Ar^+ ion. The high coverage sputtering yield is an upper bound, since evaporative effects are non-negligible there. It is also likely that the impact of a 6.5 keV argon ion sputters a large number of substrate atoms at the same time as the adsorbed cesium atoms. Copper, for example, has an argon sputtering yield at just 3 keV of about 10 [106]. With the cascading impact comes heating and desorption of a large number of cesium atoms (each of which is known to have an adsorption energy on the order of only an eV). This effect might be more pronounced with silver, which has one of the highest sputtering yields of any common metal (as high as 23 atoms/ion with Ar at 10 keV [107]), than with, say, the refractory metals like tungsten where sputtering yields can be an order of magnitude less. And in general, such numbers should be approached with caution since even in literature it is well known that the same material, ion species and energy can exhibit variability in yield of several hundred percent due to differences in material preparation, composition, and experimental conditions [106]. Suffice it to say that a few minutes' ion cleaning with the apparatus in this work

($\sim 0.1 \text{ mA/cm}^2$, 6.5 keV) is sufficient to completely remove an adsorbed monolayer of cesium.

Additional sputtering of the substrate will occur at the same time, though with lower yield.

Chapter 6: QE of Sub-monolayer Coated Metals

6.1 Theoretical Basis

6.1.1 Introduction

Many of the experiments and theoretical comparisons detailed in this work concern adsorbed partial monolayers of atoms on metallic surfaces, as these surfaces are precisely those of concern to dispenser photocathodes. The physics of these surfaces and particularly of photoemission from them is the subject of this chapter section.

Photoemission on a conceptual basis is described by Spicer's well-known three-step model as follows. First, the incident light penetrates the surface to some depth and the photon energy is absorbed, contributing to the kinetic energy of an electron in the material. Second, that photoexcited electron, able to propagate within the material, proceeds to travel ballistically and to scatter off of other electrons (electron-electron scattering) or off of the material lattice structure (electron-phonon scattering). In metals, the former scattering process dominates; in semiconductors, the latter. If and when the electron reaches the material-vacuum boundary, it encounters the third step, that of overcoming the emission barrier given sufficient energy compared to the barrier height or given a tunneling probability made sufficiently large through a narrowing of the barrier width, the latter being possible via the application of high electric field and Schottky barrier lowering. Let us consider the third step first, and then return to transport/scattering and photon absorption. We here consider the case of metals, which have a largely filled conduction band, a barrier height characterized by the work function, and a Fermi level which is positive with respect to the bottom of the conduction band. A later chapter shall contrast the case of semiconduc-

tors, which have a largely vacant conduction band, a barrier height characterized by the electron affinity and the band gap, and a Fermi level which is doping-dependent and negative with respect to the bottom of the conduction band.

6.1.2 Effect of Adsorbates on Electron Emission

The height of the emission barrier (in the case of a metal, the work function), is what is modified by adsorbates on the material. This effect of adsorbate coverage on work function has been studied since the initial work of DuBridge in 1933 [108] and more significantly Langmuir's seminal work in that same year [51]. Langmuir's detailed investigations proposed that the work function as it depended on coverage should also experience variation with temperature and of course adsorbate vapor pressure. The resulting theory was not valid for more than low coverage. A more advanced theory would take three decades to develop, and would be proposed by Gyftopoulos and Levine in Ref. [109], whose 1962 treatise is hereafter referred to as the GL theory. A further modification and refinement of the GL theory, describing the effect on the emission barrier of an adsorbed partial monolayer of highly electronegative atoms on a metallic substrate, is described by Jensen et al. in Ref. [66]. Jensen's particular contributions which appear in this formulation as well are threefold: to redefine as needed for emphasis on parameters which compare across various sets of experimental data, to include updated values for any empirical parameters since the GL theory was published, and to reduce the number of parameters to a minimal set.

Following Gyftopoulos and Levine who did away with Langmuir's temperature dependence and assuming zero vapor pressure of the adsorbate, energetically the barrier to emission is described by an electronegativity component $W(\theta)$ and a dipole component $d(\theta)$ (derived from a dipole moment $M(\theta)$) which are solely functions of θ , which in turn represents the fractional surface coverage and varies from 0 (no coverage) to 1 (monolayer coverage). We define an effective work function:

$$(6.1) \phi_e(\theta) = W(\theta) + d(\theta)$$

The two components of this effective work function will now be examined in turn. The electronegativity component is first discussed. Electronegativity refers to the energy input requisite to separate one electron from its neutral parent atom or molecule, ionizing that parent. For example, cesium as an atom has an electronegativity of 0.79 on the Pauling scale and tungsten, 2.36. Thus it takes less energy to remove an electron from cesium than from tungsten. This has important implications for the theory of photoemission, as GL theory postulated when looking at the emission barrier's electronegativity term.

Boundary conditions are placed on the functional form of the function $W(\theta)$, i.e. the electronegativity of the surface with respect to the vacuum, by the required values of the function and its derivative (differentiating with respect to number of adatoms, or equivalently by the coverage θ) at the extreme cases of zero and monolayer coverage.

$$(6.2) W(0) = \phi_m, W(1) = \phi_f, \left(\frac{dW}{d\theta} \right)_{\theta=0,1} = 0$$

where ϕ is the material work function and subscript m and f refer to the metal and adsorbate film.

GL theory, in a nod to Occam's razor, postulates that the simplest possible polynomial dependence on coverage should be used which simultaneously satisfies the four boundary conditions above. That polynomial is:

$$(6.3) W(\theta) = \phi_f + (\phi_m - \phi_f)(1 + 2\theta)(1 - \theta)^2$$

or, simplifying,

$$(6.4) W(\theta) = \phi_f + (\phi_m - \phi_f)H(\theta)$$

where $H(\theta) = 1 - 3\theta^2 + 2\theta^3$. Note that $H(0) = 1$ and $H(1) = 0$ as required by the boundary conditions.

We turn now to the more involved case of the dipole term of the effective work function, $M(\theta)$. The crux of GL theory as it concerns the dipole component of the emission barrier is to consider an adatom and its substrate lattice site as a Pauling molecular dipole. For a single adatom the dipole moment is therefore proportional to the difference in electronegativities of the unadsorbed and adsorbed states $M_0 \propto W(0) - W(1)$. In aggregate the combination across the

surface of some occupied and some unoccupied states results in a coverage dependence

$M(\theta) \propto W(\theta) - W(1)$. Now we take the ratio of these proportionalities to create an equality:

$$(6.5) \frac{M(\theta)}{M_0} = \frac{W(\theta) - W(1)}{W(0) - W(1)} = \frac{H(\theta) - H(1)}{H(0) - H(1)} = H(\theta)$$

where we have simplified using Eq. (6.4) and the values of the polynomial at the boundaries of zero and monolayer coverage. We therefore obtain the coverage dependence of the dipole moment as:

$$(6.6) M(\theta) = M_0 H(\theta)$$

We postpone the discussion of the constant term in order to note the foregoing discussion neglects dipole-to-dipole interactions, which at high coverage tend to reduce the overall moment as individual dipoles begin to cancel each other out. Thus there is an effective dipole moment therefore which is defined as:

$$(6.7) M_e(\theta) = M(\theta) - \alpha E(\theta)$$

where there is a depolarizing electric field on any individual dipole induced by neighboring dipoles, and the polarizability α will be discussed later. As discussed by Topping in Ref. [110], this field is obtained from the effective dipole moment per adsorbate $M_e(\theta)$ and the number of adsorbate atoms per unit area $(f/(2r_f)^2)$, where f is a dimensionless parameter indicative of the fact that the atoms of a monolayer coating will not, in practice, have exactly the hard sphere sep-

aration $2r_f$ (or alternatively, a monolayer coating covers a fraction of the surface due to polycrystalline-, contamination-, or roughness-related effects), via:

$$(6.8) E(\theta) = \frac{9(f/(2r_f)^2)^{3/2} \theta^{3/2} M_e(\theta)}{4\pi\epsilon_0}$$

We can now solve the preceding three equations for the effective dipole moment:

$$(6.9) M_e(\theta) = \frac{M_0 H(\theta)}{1 + 9\alpha(f/(2r_f)^2)^{3/2} \theta^{3/2} / 4\pi\epsilon_0}$$

Following Jensen in his book, Electron Emission Physics [5], since this is the effective dipole moment per adsorbate, we wish to multiply by the number of adsorbates per unit area $(f/(2r_f)^2)\theta$ and calculate the dipole term in the effective work function as:

$$(6.10) d(\theta) = -M_e(\theta)(f/(2r_f)^2)\theta/\epsilon_0 = -\frac{M_0 H(\theta)(f/(2r_f)^2)\theta}{\epsilon_0 + 9\alpha(f/(2r_f)^2)^{3/2} \theta^{3/2} / 4\pi}$$

We now turn to the values of M_0 and α , the single-adatom dipole moment and polarizability. The polarizability, again following Jensen, is approximated by:

$$(6.11) \alpha = 4\pi\epsilon_0 n r_f^3$$

where r_f is the covalent radius of the adsorbate (film) atom, and n is a factor which accounts for the effect of electronic shell structure on the polarizability. If the adatom is alkali metal, there is only one valence electron, and n is 1. If the adatom is an alkaline-earth metal then there are two

valence electrons, and n is 1.65. The reduction from 2 is because of the partial shielding of one valence electron by the other by a factor 0.35 [33].

For M_0 , the approach of GL theory is a geometric one, a hard sphere model. The larger adsorbate, in this case an alkali metal like cesium, is located on top of the lattice of the substrate. Tungsten and silver, the substrates experimentally used in this work, have BCC and FCC lattices respectively. And so without loss of applicability to the data herein reported, we consider an adsorbate alkali atom centered on top of four smaller metallic substrate atoms, forming a tetrahedral structure. Each substrate atom can be considered to have its own Pauling dipole M_{fm} with the adsorbate atom, and the reason to do this is to then incorporate a depolarization effect between the four substrate atoms in the tetrahedral structure which is best approximated, according to Ref. [111], by

$$(6.12) M_{fm} = \frac{K(\phi_m - \phi_f)}{1 + \alpha/(4\pi\epsilon_0 R^3)}$$

As Jensen derives in Ref. [66], the constant K is given by $\epsilon_0 r_0^2$ where r_0 is the constant radius parameter (4.3652 Å in the case of cesium on tungsten), a composite of factors relating electronegativities and molecular dipole moments. The work functions of the bare metal ϕ_m and the monolayer-coated metal ϕ_f have empirical values reported in the literature. The constant R is the sum of the atomic radii of the adsorbate and substrate, and the polarizability is as defined previously.

With this tetrahedrally clustered single-substrate-atom dipole moment in hand, we now sum the contribution of all four substrate atoms, taking the vector component along the surface normal,

$$(6.13) M_0 = 4M_{jm} \cos(\beta)$$

where the tetrahedral angle is defined by the hard-sphere center-to-center separations by

$$(6.14) \sin^2 \beta = \frac{2}{w} \left(\frac{r_m}{R} \right)^2$$

The adjustable parameter w , analogously to f for the adsorbate, is used to account for the substrate atoms not being in a close-packed square lattice, such that $w/(2r_m)^2$ is the number of substrate atoms per unit area. The factor w is hence dimensionless and is equal to 1 if the substrate atoms are arranged with a cell size defined by the square of the hard-sphere radius. We therefore combine the preceding four equations to obtain:

$$(6.15) M_0 = 4 \frac{\varepsilon_0 r_0^2 (\phi_m - \phi_f)}{1 + nr_f^3/R^3} \left(1 - \frac{2}{w} \left(\frac{r_m}{R} \right)^2 \right)^{1/2}$$

Then from Eq. (6.10) we have

$$(6.16) d(\theta) = - \frac{4r_0^2 (\phi_m - \phi_f) H(\theta) (f/(2r_f)^2) \left(1 - \frac{2}{w} \left(\frac{r_m}{R} \right)^2 \right)^{1/2} \theta}{(1 + nr_f^3/R^3) (1 + 9nf^{3/2}\theta^{3/2}/8)}$$

Now, combining this result with Eqs. (6.1) and (6.4), we finally have an expression for the effective work function of the substrate-adsorbate surface with functional dependence on θ , parameterized by the dimensionless w and f which describe the departure from an ideal hard-sphere square lattice surface density for the substrate and adsorbate respectively. The atomic radii are taken as the empirically obtained covalent radii reported in literature. After simplifying,

$$(6.17) \phi_e = \phi_f + (\phi_m - \phi_f) H(\theta) \left(1 - \frac{4r_0^2 (fl(2r_f)^2) \left(1 - \frac{2}{w} \left(\frac{r_m}{R} \right)^2 \right)^{1/2} \theta}{(1 + nr_f^3/R^3)(1 + 9nf^{3/2}\theta^{3/2}/8)} \right)$$

Jensen modifies the GL theory by reducing the number of parameters one further, noting that the relative sizes of the substrate and adsorbate atoms can define a relationship between the substrate and adsorbate atomic densities per unit area. We here define that relationship as a monolayer surface density ratio

$$(6.18) \zeta_{mf} = \frac{\sigma_m}{\sigma_f} = \frac{wl(2r_m)^2}{fl(2r_f)^2} = \frac{wr_f^2}{fr_m^2}$$

This ratio describes the number of substrate atoms per unit cell compared to the monolayer number of adsorbate (film) atoms per unit cell. Because the energetically favorable adsorption sites are spaced by the dimensions of the substrate lattice, the monolayer surface density ratio can be an integer value; for example, Jensen takes $\zeta_{mf} = 4$ for cesium on tungsten, while this value is closer to 2 for alkaline earths such as barium on various metals. The monolayer surface density ratio is crystal-face dependent and atomic species dependent. With this modification and additio-

nal simplification, recalling the polynomial $H(\theta) = 1 - 3\theta^2 + 2\theta^3$ to make the dependence on percent monolayer coverage explicit, the form of the effective work function is

$$(6.19) \phi_e = \phi_f + (\phi_m - \phi_f)(1 - 3\theta^2 + 2\theta^3) \left(1 - \frac{f \left(\frac{r_o^2}{r_f^2} \right) \left(1 - \frac{2}{\zeta_{mf} f} \left(\frac{r_f}{R} \right)^2 \right)^{1/2} \theta}{\left(1 + n \left(\frac{r_f}{R} \right)^3 \right) \left(1 + \frac{9n}{8} (f\theta)^{3/2} \right)} \right)$$

Notice the functional dependence on fractional monolayer coverage θ is only parameterized by f : n is fixed by whether the adsorbate is alkali (1) or alkaline earth (1.65); r_f , r_m , and their sum R are empirical covalent radii from literature; the radius parameter r_o is a constant of the adsorbate and substrate species, fully determined from literature; ζ_{mf} is a constant for a given substrate, adsorbate, and crystal face; and the monolayer work function ϕ_f and bare substrate work function ϕ_m are also empirically fixed or reported in literature.

The Gyftopoulos-Levine coverage-dependent work function for cesium on tungsten is graphed in Fig. 6.1. The initial value is that of uncoated tungsten, and the final value is the monolayer coverage value. There is a minimum in the workfunction at 53% coverage, because as coverage increases further, individual cesium atoms pack close enough to reduce the dipole moment of adjacent cesium atoms.

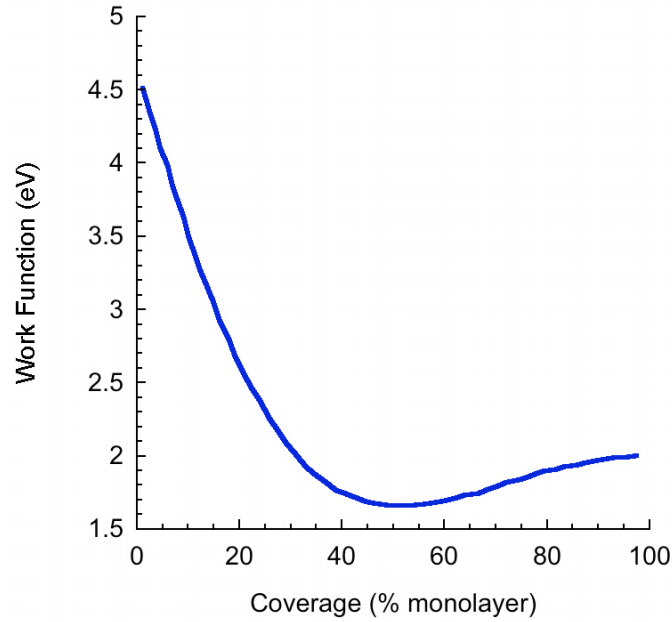
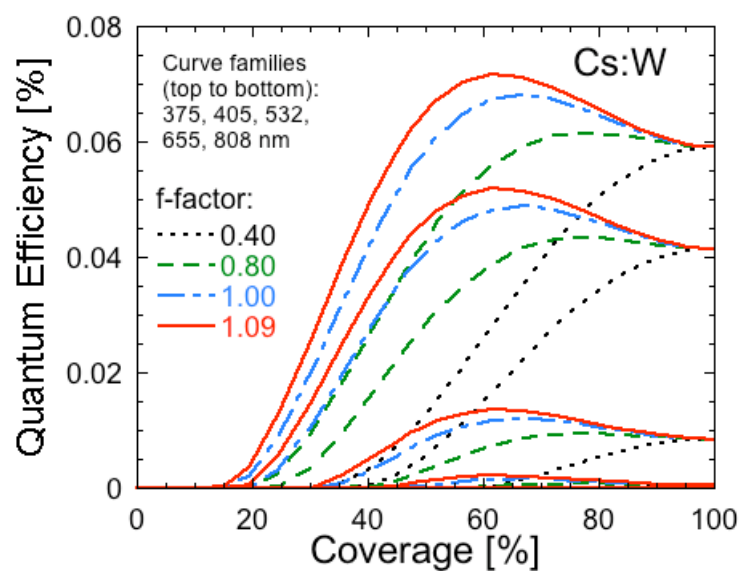
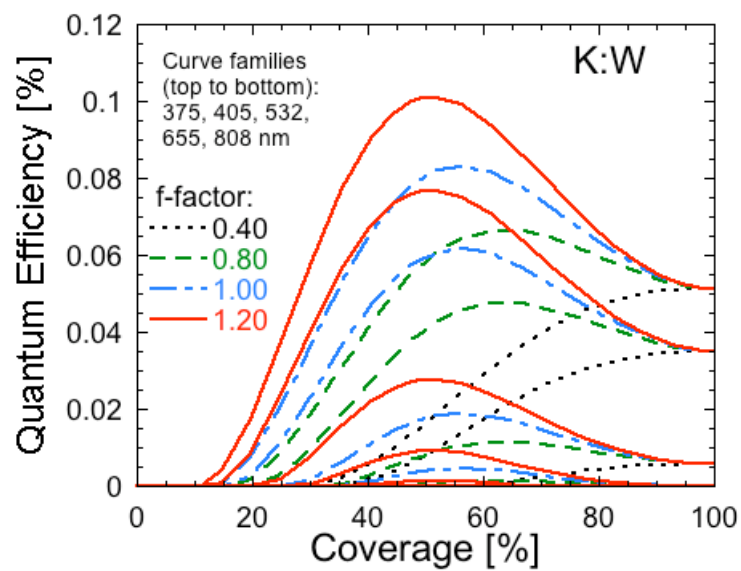


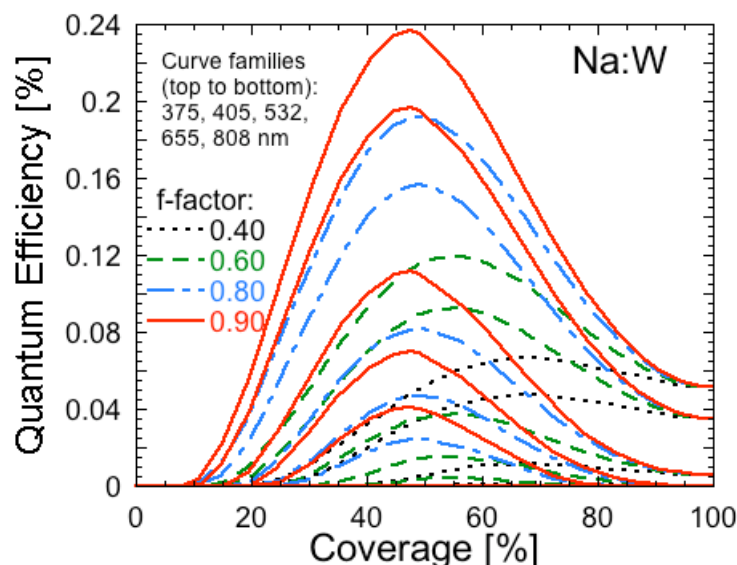
Figure 6.1: GL theory: work function of cesium on tungsten

With the effective work function in hand, the evaluation of (work function dependent) emission terms in the theoretical models for quantum efficiency are now valid for partial monolayer coated surfaces. The lowering of the emission barrier by the adsorbed alkali atoms has now been accounted for. Where the work function is referenced later in the theory, Eq. (6.19) should be used in the case of a coated substrate.

6.1.3 The f-factor

The dependence on the f-factor, f , of the quantum efficiency of an alkali-coated metal surface is of interest. Following Ref. [112], we consider the following figures displaying the theoretical behavior of QE as a function of coverage for various alkali species on tungsten.

Figure 6.2: Cs:W study of f Figure 6.3: K:W study of f

Figure 6.4: Na:W study of f

In each figure, there are five wavelengths modelled, each having a family of four curves corresponding to different f . One should note for Cs:W, the curve families show the effect of *reducing* the f -factor from an already high value, whereas for K:W and Na:W the curve families show the effect of *increasing* the modelled value of the f -factor from the initial low value, so that all three of the curve families have comparable values of f . For very low f , a monotonically increasing function of coverage results, whereas for high f , a pronounced peak at submonolayer coverage appears.

Also as reported in Ref. [112], when evaluating the quantum efficiency of an alkali-coated metal surface using the above work function, the parameter f does not merely describe the

theoretical relationship between adsorbate and substrate surface densities. It also aids in scaling the data from a quartz microbalance mass measurement to a coverage value. This will be detailed in Section 6.2.1.

6.1.4 MFD Formulation of Quantum Efficiency

Introduction

We now turn to the theoretical description of quantum efficiency. As described earlier, the three-step process of photoemission involves photon absorption, electron transport, and electron emission. Formulaically this is simply obtained by defining QE as the ratio of number of emitted electrons to incident photons, which in the steady-state (such as in UMD experiments with CW lasers) or in perfectly prompt emission (where the emitted electron bunch exactly follows the temporal behavior of the incident laser pulse):

$$(6.20) \text{QE} = \left(\frac{hc}{q\lambda} \right) \frac{J_{\lambda}}{I_{\lambda}}$$

where I_{λ} is the incident optical intensity, J_{λ} is the resulting photoemitted current density, and $q\lambda/hc$ converts units of current density and optical intensity to numbers of electrons and photons per unit area, respectively. (Notice the implicit assumption that the emission area and laser spot size are identical. For negligible heating by the laser spot, such as is the case with the experiments herein reported, this is a valid assumption.)

It should be stated at the outset that while the above equation is general, the choice of technique for calculating the photoemitted current density is not. The first technique historically used by UMD's cathode group was the Modified Fowler-Dubridge approach (MFD). This will be discussed here for comparison and because it is perhaps more immediately intuitive, but there are several important inherent assumptions which limit its accuracy and applicability. The second technique, that currently used, is the Moments-based approach. This is a more elegant and powerful technique than MFD but has the disadvantage of being a bit more mathematically opaque. It is hoped that by presenting the basic MFD formulation first and detailing the additional physics incorporated by the Moments-based approach second, a clearer narrative can be established.

The primary attraction, at least visually, of the MFD formulation of QE is that the three steps of photoemission are included explicitly term-by-term in the MFD formulation of photoemitted current density:

$$(6.21) J_{\lambda} = (1 - R(\lambda)) \left(\frac{q\lambda}{\hbar c} \right) I_{\lambda} F_{\lambda} P(\phi, \mu, \lambda, F, T)$$

so that Eq. (6.20) results in

$$(6.22) QE = (1 - R(\lambda)) F_{\lambda} P(\phi, \mu, \lambda, F, T)$$

where R is the optical reflectance of the surface (which in the most general form would depend on incidence angle as well as wavelength, though in practice the incidence angle is usually fixed); F_{λ} is the transport factor accounting for optical absorption depth, electron transport, and

scattering; and $P(\phi, \mu, \lambda, F, T)$ is the emission probability, where for completeness it has been expressed with functional dependence not only on work function, chemical potential and photon energy via wavelength but also on applied electric field and temperature. Thus we see the first term corresponding to absorption, the second, F_λ , corresponding to transport probability to the surface, and the third corresponding to emission probability, which are the three steps of photoemission to which we continue to refer.

Both the preceding equations assume a substrate substantially thicker than the optical penetration depth such that all photons not reflected are absorbed (i.e., zero transmission): this is valid since for metals and semiconductors [23] typically used with photoinjectors, and with visible or near-infrared drive lasers, that depth is on the order of tens of nanometers. (An interesting corollary is that the measurement of thin film thickness with ellipsometry or reflectometry is not feasible above roughly 100 nanometers.)

Emission Probability

Jensen evaluates the emission probability in the MFD approach as a ratio of Fowler functions, giving the probability that an electron has an energy greater than the barrier height, which including the effect of applied field (so as to be completely general) is written as

$$(6.23) P = \frac{U[\beta_r(\hbar c/\lambda - \phi_e(\theta) + \sqrt{4QF})]}{U[\beta_r\mu]}$$

where $4Q = \alpha_{fs} \hbar c$, α_{fs} is the fine structure constant, F is the applied electric field times the electric charge, and β_T is one over the Boltzmann energy $k_B T$. $\phi_e(\theta)$ is of course the (effective) work function which describes the difference between the energy barrier height and the chemical potential. The Fowler functions themselves are defined by

$$(6.24) U(x) = \int_{-\infty}^x \ln(1 + e^y) dy$$

where an approximation valid to within 1% for all values of x is derived by Jensen in Ref. [73]:

$$(6.25) U(x) = \begin{cases} e^x (1 - be^{ax}) & x \leq 0 \\ \frac{1}{2}x^2 + \frac{1}{6}\pi^2 - e^{-x} (1 - be^{-ax}) & x > 0 \end{cases}$$

$$\text{where } a = 12 \left(\frac{\pi^2 - 12 \ln(2)}{12 - \pi^2} \right); b = 1 - \frac{\pi^2}{12}.$$

Since at room temperature the Boltzmann energy is a fortieth of an eV, and since for photon energies appreciably higher than the work function (such as is the case with photoinjector drive lasers) the difference is on the order of an eV, and since the field term can be neglected because in this work applied fields are small (in the experiments in this work, less than 100 kV/m), the argument of the Fowler function in the numerator of Eq. (6.23) is about 40. Turning to Eq. (6.25), the x greater than zero case is used, and the quadratic term dominates, so we can now write the emission probability as approximately

$$(6.26) P \approx \frac{U[\beta_T(hc/\lambda - \phi_e(\theta))]}{U[\beta_T\mu]} \approx \frac{(hc/\lambda - \phi_e(\theta))^2}{\mu^2}$$

In other words, QE is directly proportional to the emission probability, which is in turn quadratically proportional to the difference between photon energy and work function, under the terms of the approximations used above. This quadratic dependence is observed in experiment.

Electron Transport

With the emission probability in hand, we now turn to the next critical component of Eq. (6.22), the transport term f_λ , which is the fraction of excited electrons successfully reaching the cathode surface. There are several considerations here. First, the photons which excite the electrons do so at the depth they are absorbed, and this depth of course varies from case to case. The statistics follow an exponential decay characterized by an optical penetration depth δ (which is in turn derived from the optical constants of the material, namely the imaginary part of the optical index of refraction via $\delta = \lambda/4\pi k$) such that the probability of an electron being excited by a photon at a depth x is:

$$(6.27) p_{abs}(x) \propto \exp(-x/\delta)$$

Second, the electrons which are excited can then travel in any direction, so we must account only for those which have an initial momentum component towards the cathode-vacuum interface. And third, an electron on its way to the surface will undergo scattering - in metals, primarily

electron-electron scattering - and if we approximate the situation such that a single scattering event is sufficient to reduce the electron energy below the work function, we can say that the probability of an excited electron reaching the surface is given by the probability that it *will not* undergo a scattering event during transport. This approximation is harsh, for scattering can not only change an electron's state *unfavorably* for emission; it can also change it *favorably* such that the electron scatters into an energy state which can be emitted. However, since in a metal (for which the MFD theory is intended) electron-electron scattering dominates, and since such scattering events tend to *reduce* the energy of the excited electrons involved, and furthermore since photon energies of interest are only slightly larger than the work function, our assumption of one scattering event precluding emission is in large part justified. We can write this probability of reaching the surface as:

$$(6.28) p_{\text{surface}}(x, \psi) \propto \exp(-r(\psi)/l(k))$$

where ψ is the angle of the excited electron's path relative to the surface normal, $r(\psi)$ is the distance along that path to reach the surface, and $l(k)$ is the mean free path of the electron as a function of momentum, and which incorporates the appropriate scattering factors.

Before we can write a complete expression for the total probability of an excited electron reaching the surface, we must also define a supply function which describes the distribution of electrons having a given momentum along the surface normal. This 1D supply function is obtained by integrating over all transverse components of the Fermi-Dirac distribution characterizing the electron energies, and is given by

$$(6.29) f(k) = \left(\frac{m}{\pi \beta_T \hbar^2} \right) \ln[1 + \exp(\beta(\mu - E(k)))]$$

where μ is the chemical potential, β_T is one over the Boltzmann energy $k_B T$, k is the electron momentum, m is the electron mass, and $E(k) = \hbar^2 k^2 / 2m$.

Now, with the supply function, probability of absorption, and probability of reaching the surface, we can combine factors and integrate over all possible absorption depths, electron propagation angles, and electron momenta, normalizing to the population of all excited electrons regardless of whether they propagate towards the surface or whether they scatter on the way there:

$$(6.30) F_\lambda = \frac{\int_0^\infty k^2 f(k) \int_0^{\pi/2} \exp[-r(\psi)/l(k)] \sin \psi d\psi dk \int_0^\infty \exp[-x/\delta] dx}{\int_0^\infty k^2 f(k) dk \int_0^\pi \sin \psi d\psi \int_0^\infty \exp[-x/\delta] dx}$$

Note that we need not write out the integrals over azimuthal angle, since they are normalized out in the end. Also note the limits of integration for the angle from the surface normal: in the numerator, $\pi/2$, and in the denominator, π . This reflects the fact that only half the electrons ever have a chance of reaching the surface; half propagate away from the surface and deeper into the material. Lastly note that again the assumption of an infinitely thick absorber is made, which is valid for typical experiments herein reported where optical penetration depths are tens of nanometers.

Several simplifications may be made in order to permit more ready evaluation of the scattering factor above. First, only electrons with energies permitting emission need be considered. Second, the momentum integrations in the numerator and denominator cancel if the mean free path, which in general is momentum-dependent, is considered a constant of $k = \sqrt{2m(\mu + \phi)/\hbar^2}$, which is to say that most electrons in metals which can be emitted have energies very nearly that of the barrier to their emission.

Evaluation of the integrals then gives, first over the depth x where the photon is absorbed and electron initially excited,

$$(6.31) \frac{\int_0^\infty \exp\left[-\frac{r(\psi)}{l(k)} - \frac{x}{\delta}\right] dx}{\int_0^\infty \exp\left[-\frac{x}{\delta}\right] dx} = \frac{\int_0^\infty \exp\left[-\frac{x}{l(k)\cos\psi} - \frac{x}{\delta}\right] dx}{\int_0^\infty \exp\left[-\frac{x}{\delta}\right] dx} = \frac{\cos\psi}{\cos\psi + \frac{\delta}{l(k)}} \equiv f_\lambda$$

and next over the angle with respect to the surface normal,

$$(6.32) F_\lambda = \frac{1}{2} \int_0^{\pi/2} \frac{\cos\psi}{\cos\psi + \frac{\delta}{l(k)}} \sin\psi d\psi = \frac{1}{2} \left\{ 1 + \frac{\delta}{l(k)} \ln\left[\frac{\delta}{\delta + l(k)}\right] \right\}$$

where it is worth repeating that we have assumed $k = \sqrt{2m(\mu + \phi)/\hbar^2}$. We note that the integration in Eq. (6.32) is here performed in the MFD approach but will be delayed in the Mo-

ments-based approach, discussed in the subsequent section, until transport and emission are integrated simultaneously.

The one term left undefined thus far for the transport probability is the mean free path of an electron. Since we have heretofore expressed everything in terms of the electron wavenumber k , we need merely write the momentum as $\hbar k$, so the velocity is $\hbar k/m$, and therefore defining relaxation time τ as the time required to travel one mean free path at a given velocity allows expression of the mean free path in terms of momentum and such relaxation time:

$$(6.33) l(k) = \frac{\hbar k}{m} \tau$$

The relaxation time is a function of both the energy of the photoexcited electron and the energy of the scatterer. As such, it is also temperature-dependent. In metals the relaxation time is dominated by elastic electron-electron scattering. In general, if the electrons which are photoexcited are not photoemitted, their energy is dissipated via inelastic electron-phonon scattering with the lattice over time, re-equilibrating the cathode temperature after every laser pulse. If heat builds up this will impact the scattering via the relaxation time, hence the quantum efficiency. Such effects can be highly temporal in nature and Jensen's models account for such time-dependence. However, with low power lasers such as the diodes in this work, such heating is negligible.

It is, nevertheless, critical to identify the appropriate relaxation time to use in Eq. (6.33). We have already alluded to the two scattering mechanisms present in the electron gas model:

electron-electron and electron-phonon scattering. Each has a characteristic relaxation time (in other words, a characteristic mean free path the electrons would experience if that scattering mechanism were the only one in effect). To combine the two relaxation times we make use of Matthiessen's Law

$$(6.34) \frac{1}{\tau} = \frac{1}{\tau_{ee}(T_e)} + \frac{1}{\tau_{ep}(T_i)}$$

where τ_{ee} and τ_{ep} are the electron-electron and electron-phonon relaxation times, respectively, and T_e and T_i are the electron and ion (lattice) temperatures. To give an idea of the magnitude of these terms, Jensen quotes in Ref. [66] the two relaxation times for tungsten at 300°C at the Fermi level. For electron-electron scattering the value is 5.26 fs and for electron-phonon scattering the value is 0.948 fs. For copper at the same temperature the values are 75.29 fs and 9.383 fs respectively. Using Matthiessen's Law results in an electron-phonon dominated relaxation time at 300°C at the Fermi level. With decreasing temperature the electron-phonon scattering also wins out. This is because the relaxation times scale with temperature as $\tau_{ee}(T_e) \propto 1/T_e^2$ and $\tau_{ep}(T_i) \propto 1/T_i$ [113; 114]. But again, this is for an electron with an energy at or about the Fermi level. For photoexcited electrons well above the Fermi level the electron-electron scattering increases rapidly and the associated relaxation time drops precipitously, because well above the Fermi level there is no scarcity of initial and final states to scatter through. This is discussed in Ref. [21], which updates the work in Ref. [66]. Since electron-phonon scattering does not have such strong dependence on energy above the Fermi level, and remains near its Fermi level value

even while the electron-electron relaxation time drops rapidly, for photoexcited electrons in general the electron-electron relaxation time will dominate in metals. (In semiconductors, the low number of electrons in the conduction band and also the bandgap-disallowed states mean a return to electron-phonon dominated scattering.)

Optical Considerations

The last and perhaps simplest term in the MFD formulation of QE given by Eq. (6.22) is the reflectance term. We have already assumed all photons which are not reflected are absorbed (zero transmission), but since metals, for example, have reflectances of perhaps 50% or more, this is a non-negligible detractor from the QE attainable by a given cathode. A non-normal incidence affects the reflectance. In practice, for photoinjectors utilizing a front-illuminated reflection mode photocathode (not a back-illuminated transmission mode photocathode) there is always a non-normal incidence angle, since the photoemitted electron beam itself must be extracted along the surface normal, hence the drive laser beam and any associated mirrors or optics cannot use the same path.

6.1.5 The Moments-Based Approach

The above formulation of the quantum efficiency [74] used the Modified Fowler-Dubridge (MFD) approach. This is an inherently 1D formulation which ignores the surface-transverse momentum of the electrons in transport and at the emission barrier. It therefore loses validity in cathodes utilizing a low work function coating, when the work function is much less

than the chemical potential or photon energy, as discussed in Refs. [66] and [21]. More recently a moments-based approach to the transport and scattering problem has been developed, which includes a 3D momentum formulation and an energy-dependent scattering term with quantum mechanically correct formulations incorporating the initial energy distribution of the electrons [21].

The Moments-based approach modifies the way the photoemission current density is calculated in Eq. (6.22). It is based on the idea that the transport and emission steps are not separable. Instead, one can combine both steps in one integral over momentum. Intuitively this makes sense: the scattering rate is energy dependent and should be considered as such after the electron is photoexcited, and then a sum over all electrons satisfying the conditions for emission should be performed.

In the Moments-based approach, this sum is performed by integrating in momentum space over all electrons propagating towards the surface, with the probabilities of absorption, initial state occupation, final state non-occupation, transport, and emission lumped into a total distribution function. Such an integral is recognized as a type of moment, hence the term "Moments-based". For current density which is required in the calculation of QE, the appropriate integral is the first moment of the surface-normal component of momentum, $k_z = k \cos \psi = \sqrt{2mE/\hbar^2} \cos \psi$, where we continue to use ψ to define the angle of electron propagation with respect to the surface normal in preference to the more conventional θ in order to avoid any notational degeneracy with the monolayer coverage factor θ used extensively in this work. We define

$$(6.35) M_1(k_z) = 2(2\pi)^{-3} \int_{V/2} \int \int k_z P_{total}(E, \psi) k^2 \sin \psi dk d\psi d\phi$$

where we have used spherical coordinates to integrate over momentum space. We are counting all electron states, so the factor of 2 in front does the double counting for electron spin. The factor of $(2\pi)^{-3}$ is just normalization to the volume in momentum space of one electron state. $V/2$ represents the half-sphere of allowed electron vectors which point towards the surface, defined by the polar angle varying from 0 degrees (surface normal) to 90 degrees (surface parallel). This assumes that only electrons initially directed towards the surface escape; in reality, a small number of electrons likely begin directed away from the surface, scatter without loss of sufficient energy to preclude emission, and are redirected towards the surface. We do not consider such a correction to our simplifying assumptions here, although a Monte Carlo simulation could address the accuracy of these assumptions if desired.

A transformation to an energy integral via $k = \sqrt{2mE/\hbar^2}$ gives

$$(6.36) M_1(k_z) = 2(2\pi)^{-3} (2\pi) \frac{1}{2} \left(\frac{2m}{\hbar^2} \right)^{3/2} \int_0^{\pi/2} \int_0^\infty k_z E^{1/2} P_{total}(E, \psi) \sin \psi dE d\psi$$

and further inserting the definition of the surface-normal component of momentum

$$k_z = k \cos \psi = \sqrt{2mE/\hbar^2} \cos \psi \text{ leads to}$$

$$(6.37) M_1(k_z) = \frac{m^2}{\pi^2 \hbar^4} \int_0^{\pi/2} \int_0^\infty EP_{total}(E, \psi) \sin \psi \cos \psi dE d\psi$$

Since we want photoemission current density to use in Eq. (6.20) to find QE, we must multiply the first moment (having units of the fourth power of k) by the appropriate constants in order to obtain current density:

$$(6.38) J = -\frac{q\hbar}{m} M_1(k_z)$$

We can express this in the form Jensen uses in Ref. [5] by substituting the Richardson-Laue-Dushman constant and Boltzmann constant as appropriate:

$$(6.39) J = -2 \frac{A_{RLD}}{k_B^2} \int_0^{\pi/2} \int_0^\infty EP_{total}(E, \psi) \sin \psi \cos \psi dE d\psi$$

where $A_{RLD} = \frac{mqk_B^2}{2\pi^2 \hbar^3}$.

We turn now to the evaluation of the total emission probability. As stated previously, this term includes four multiplicative factors: transport probability without scattering, initial and final occupation probabilities, and emission probability. Within the transport probability we continue to assume one scattering event is sufficient to preclude emission, which is of course an oversimplification of the problem but a valuable one in the search for an analytic emission solution. The occupation probabilities are Fermi-Dirac functions. The transmission probability is energy de-

pendent as before in the MFD approach, but under MFD it was assumed the entire energy of the photon was funneled into the surface-normal momentum: an overly optimistic assumption which only works well when in, for example, metals where the photon energy is typically comparable to the work function. We wish to go beyond the range of applicability of MFD (metals) to low work function surfaces and semiconductors, and so it is critical that we make the transmission probability functionally dependent now on the total excited electron energy times an appropriate angular factor which takes only the surface-normal component of momentum. Expanding, we write out the factors:

$$(6.40) P_{total}(E, \psi) = f_{\lambda}(E + \hbar\omega, \psi) f_{FD}(E) [1 - f_{FD}(E + \hbar\omega)] T((E + \hbar\omega) \cos^2 \psi)$$

Upon noting photocathodes in this study undergo low-field, near room temperature operation, which is effectively the zero temperature zero field case, not only do the Fermi-Dirac distributions become step functions in energy, but the emission probability itself becomes a step function since the Schottky barrier lowering due to applied field is negligible at experimentally applied fields of $\sim 10 \text{ kV/m}$ herein reported, and any tunneling effects are minimal, so all that is required for emission is for the normal component of energy to exceed the barrier height. (Although, as an aside, at 1 MV/m fields typical of thermionic dispenser operation, the lowering is 0.04 eV which has a nontrivial impact on emission.) This leaves only the transport probability as a function of electron energy and propagation angle, which was derived previously in Eq. (6.31) as

$$(6.41) f_{\lambda}(E, \psi) = \frac{\cos \psi}{\cos \psi + \Sigma(E)}$$

where $\Sigma(E)$ is the ratio of the optical penetration depth to the mean free path of an electron; the latter was defined in Eq. (6.33), but we here write explicitly the energy dependence:

$$(6.42) \Sigma(E) = \frac{\delta}{l(E)} = \frac{m\delta}{\hbar k(E)\tau(E)}$$

Looking at these two equations, one would naively think that the smaller the optical penetration depth, the better the chance of transport without scattering and hence the higher the QE, and that one could force this by making the cathode thinner. However, recall the earlier assumption which still applies here that all photons not reflected are absorbed. This only holds for cathodes appreciably thicker than the optical penetration depth. If a thinner cathode were to be considered the theory would need to be revisited on the basis of the thick cathode assumption.

Now, rewriting the total probability of emission with the changes detailed above, we obtain

$$(6.43) P_{\text{total}}(E, \psi) = \frac{\cos \psi}{\cos \psi + \Sigma(E + \hbar\omega)} \times [1 - \Theta(E - \mu)] \Theta(E + \hbar\omega - \mu - \phi) \Theta((E + \hbar\omega)\cos^2 \psi - \mu - \phi)$$

with the initial state Fermi-Dirac step function turning off above the chemical potential, the final state turning off below the barrier by the amount of the photon energy (below which a photon

could not excite an electron enough to escape), and the transmission probability turning on at the barrier height. In the integral of Eq. (6.39), then, these step functions set the limits of integration:

$$(6.44) J = -2 \frac{A_{RLD}}{k_B^2} \int_{\arccos[\varphi(E)]}^{\pi/2} \int_{\mu + \phi - \hbar\omega}^{\mu} E \frac{\cos \psi}{\cos \psi + \Sigma(E + \hbar\omega)} \sin \psi \cos \psi dE d\psi$$

where we have defined $\varphi(E)$ as the energy ratio $\sqrt{(\mu + \phi)/(E + \hbar\omega)}$, which for photoemission is always less than 1. (This ratio comes from solving the step function corresponding to transmission for ψ , and gives the cosine of the maximum angle from surface normal for which an electron can still escape, often termed the "escape cone" of the electron.) We may additionally make the variable substitution $x = \cos \psi$ to get

$$(6.45) J = 2 \frac{A_{RLD}}{k_B^2} \int_{\mu + \phi - \hbar\omega}^{\mu} E \int_{\varphi(E)}^1 \frac{x^2}{x + \Sigma(E + \hbar\omega)} dx dE$$

As Jensen notes in Ref. [5], the angular integral may be approximated for $\varphi \approx 1$ (where the photon energy is just enough to initiate photoemission over the barrier as is often the case for metals) using

$$(6.46) \int_{1-\delta}^1 \frac{x^2}{x + \Sigma} dx = -\Sigma^2 \ln \left[1 - \frac{\delta}{1 + \Sigma} \right] + (1 - \Sigma)\delta - \frac{1}{2}\delta^2 \approx \frac{\delta}{1 + \Sigma} + O(\delta^2)$$

so the current density is

$$(6.47) J = 2 \frac{A_{RLD}}{k_B^2} \int_{\mu + \phi - \hbar\omega}^{\mu} E \frac{1 - \varphi(E)^3}{1 + \Sigma(E + \hbar\omega)} dE$$

which Jensen approximates to leading order as

$$(6.48) J = 2 \frac{A_{RLD}}{k_B^2} \left\{ \frac{(\hbar\omega - \phi)^2 (2\mu + \phi - \hbar\omega)}{12(\mu + \phi)[1 + \Sigma(\mu + \hbar\omega)]} \right\}$$

The dominant quadratic dependence on the photon energy less the work function (or more precisely, the barrier height above the chemical potential), which was noted previously in the MFD approach, is seen here again.

Since we are operating under the thick cathode assumption where every photon not reflected excites an electron, we may restate the formulation of QE in Eq. (6.22) such that the transport and emission probability terms are expressed as a current density ratio: the emitted current to a theoretical "maximum" current defined as containing every photoexcited electron regardless of directional or energetic considerations. This gives the proportion of absorbed photons that result in emission of an electron; the optical reflection term gives the proportion of total photons which are absorbed.

$$(6.49) QE = (1 - R) \frac{J(\hbar\omega, \phi, \mu)}{J_{\max}}$$

where the maximum current density covers the entire energy range of excited electrons (still assuming zero temperature) and neither transport losses nor the emission barrier are included (refer

to Eq. (6.45) and note that the transport term of Eq. (6.41) is removed and the limits of the energy integration are changed to allow escape of all excited electrons, and that the angular integration is doubled to account for electrons propagating away from the surface as well as towards it):

$$(6.50) J_{\max} = 2 \frac{A_{\text{RLD}}}{k_B^2} \int_{\mu - \hbar\omega}^{\mu} E \int_0^1 2x dx dE = \frac{A_{\text{RLD}}}{k_B^2} \hbar\omega (2\mu - \hbar\omega)$$

QE in the low field, low temperature, thick absorber photocathode is therefore approximated by the analytic expression:

$$(6.51) \text{QE} = (1 - R) \frac{(\hbar\omega - \phi)^2 (2\mu + \phi - \hbar\omega)}{6(\mu + \phi)[1 + \Sigma(\mu + \hbar\omega)]\hbar\omega(2\mu - \hbar\omega)}$$

In the above expression or in the numeric evaluation of the Moments-based approach, for a coated low work function surface the barrier factor ϕ should of course be replaced by the effective work function calculated under GL theory with its dependence on fractional monolayer coverage θ .

6.2 Experimental Results

6.2.1 Comparison to Theory

With the foregoing theory in hand it is possible to not only compare to the experimental results for cesiated tungsten, but also for potassium on tungsten and sodium on tungsten as different alkali sub-monolayer coatings, and for potassium on silver as a substrate with a different

lattice constant (the significance of which will become clear shortly). This will serve to illustrate not only the correspondence of theory and experiment but also to show the effect of f-factor on the comparison, which primarily comes to light through the potassium and sodium data because, as will be seen, f is nearly unity for cesium on tungsten.

When comparing theoretical predictions to experimental data where in the data the amount of alkali on the surface is given in effective thickness (Å) as read by the deposition monitor, it is necessary to re-scale from effective thickness to percent monolayer coverage. There is a linear proportionality between the two. Previously [115] this scaling was done by first centering the peak QE of experiment with the GL peak, and then scaling the measured coating thickness by the bond length of the bulk adsorbate (twice the covalent radius). However, this ignores the true meaning of f-factor as a way of describing any departure of the actual surface density at monolayer coverage from the idealized close-packed hard-sphere value:

$$(6.52) L_{\text{monolayer}} = \frac{\sigma_{\text{actual}}}{\rho} = \frac{f \cdot \sigma_{\text{hard-sphere}}}{\rho} = f \frac{1/(2R_c)^2}{1/(2R_c)^3} = 2fR_c$$

where $L_{\text{monolayer}}$ represents the effective thickness of a monolayer (as would be reported from the deposition monitor in experiment), σ_{actual} is the actual surface density of the adsorbate, $\sigma_{\text{hard-sphere}}$ is the idealized close-packed hard-sphere surface density (a square lattice spaced by the covalent diameter), ρ is the bulk density of the adsorbate, and of course R_c is the covalent radius.

Therefore it is necessary to modify the previous approach and use the scaling relationship in Eq. (6.53) when converting from effective thickness to percent monolayer coverage:

$$(6.53) \theta = \theta_0 + 100\% \cdot L / (f \cdot 2R_c)$$

where L is the effective thickness measured in experiment, f is defined in Eq. (6.52) and was previously discussed when introducing Eq. 6.8, R_c is the covalent radius of the (alkali) adsorbate, and θ_0 is an offset factor accounting for any nonzero initial L in the data set (an artifact of the time between zeroing the deposition monitor and having the sources reach evaporation temperature) and for the actual work function of the surface prior to an experiment (which may differ slightly from the ideal bare metal value).

Comparison using the above scaling relationship was simply to find the appropriate f -factor by matching the slope of the low-coverage side of the QE peak to theory using the scaling relation on the data set, with the electronic work function at monolayer coverage set by the value reported in literature, if available, or by best fit (in the case of Na:W). Each trial value of f results in adjustments to both the shape of the theoretical curve (Section 6.1.3) and to the scaling of the data. On each of the following plots the f -factor so determined is given as well as the literature values of covalent radius and work function and the coverage offset factor.

Fig. 6.5 shows the comparison for cesiated tungsten, plotting QE vs coverage. Note the f -factor is nearly unity, which is why previous work overlooked the importance of f as a data

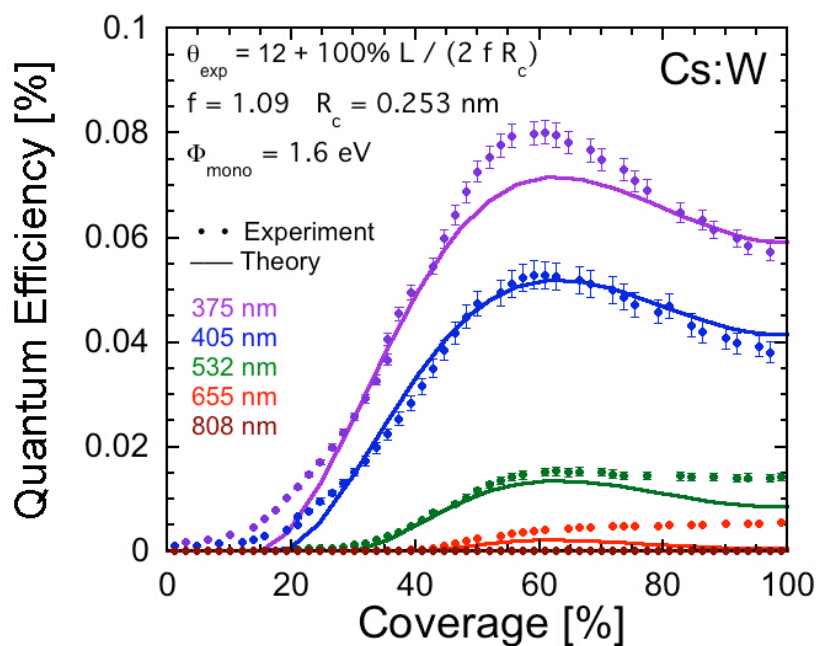


Figure 6.5: Theory vs experiment: cesium on sintered tungsten

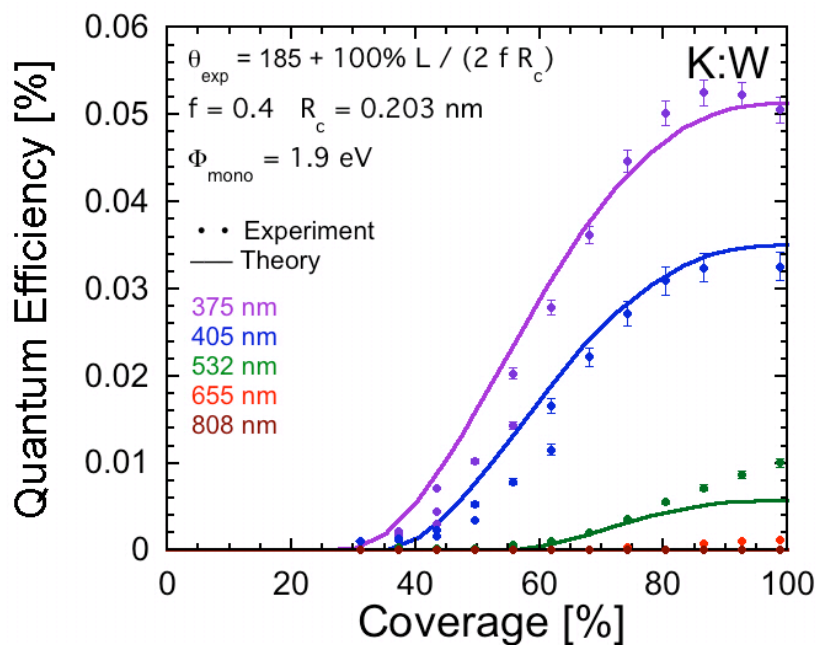


Figure 6.6: Theory vs experiment: potassium on sintered tungsten

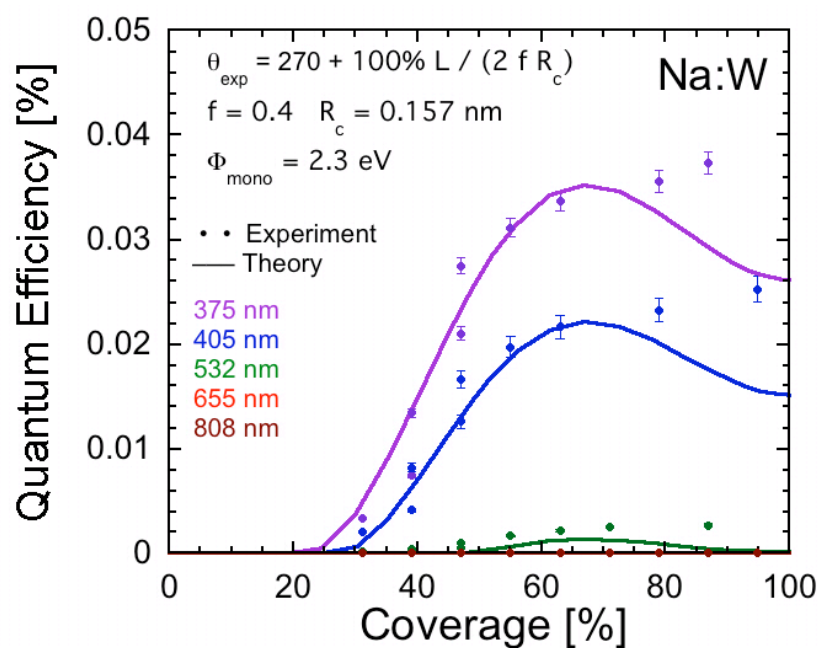


Figure 6.7: Theory vs experiment: sodium on sintered tungsten

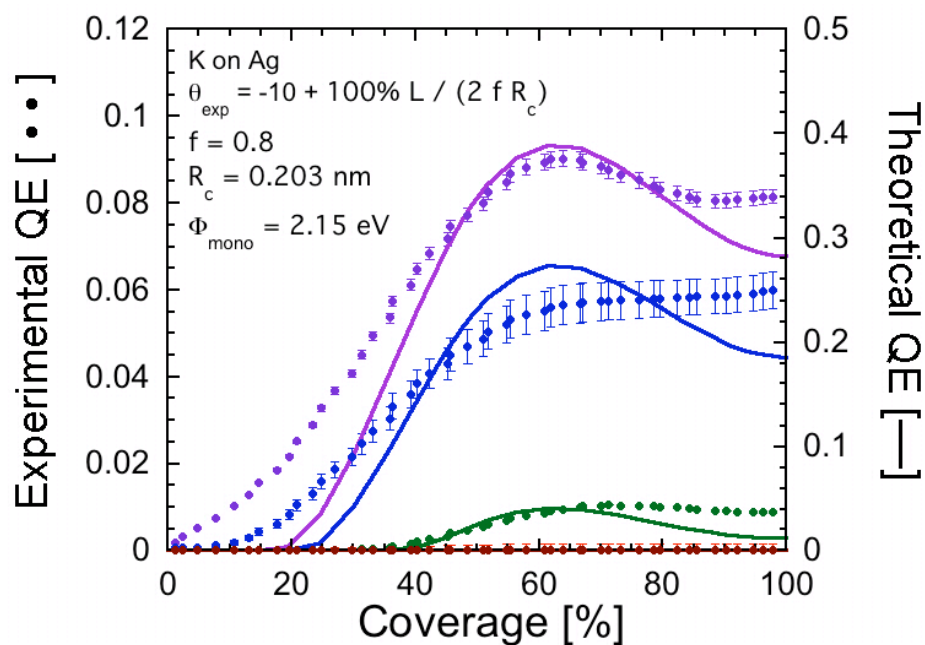


Figure 6.8: Theory vs experiment: potassium on silver

scaling factor. The QE peak of 0.08% in the data is somewhat lower than expected, since peaks of 0.11% have been seen for ion-cleaned tungsten, but the f-factor allows for any surface contamination to also be accounted for in an effective lowering of cesium surface density and allows a more accurate comparison to theory. In Fig. 6.6 the departure of the f-factor from unity is clear with the K:W system, the same substrate as for the Cs:W test. This lower f-factor be attributed to the way the potassium adatoms are arranged on the tungsten surface. Whereas cesium atoms have a covalent diameter of 5.06 Å, significantly larger than the 3.14 Å BCC lattice constant of tungsten (refer to Fig. 6.10 to see how this results in a 4:1 ratio of surface number density of tungsten to that of cesium on the [100] face), potassium atoms have a covalent diameter of only 4.06 Å. Therefore they can occupy the same lattice sites as cesium, but being smaller hence farther apart, have a much weaker dipole-dipole interaction -- and the more sparse coverage at a monolayer is of course the definition of a lower f-factor. Now in Fig. 6.7 for the Na:W system, the covalent diameter of sodium is 3.14 Å, so they can have a surface number density equal to that of tungsten and therefore exhibit the close-packing interaction with QE peak similar to cesium. The last example takes another look at potassium, but this time for a silver substrate. Silver is FCC but has a lattice constant of 4.09 Å which allows closer packing of the potassium atoms (surface number density still 4:1 with that silver) and a stronger dipole-dipole interaction, which in turn manifests itself in the higher f-factor for the K:Ag system of 0.8 compared to 0.4 for K:W. In all tungsten cases the magnitude of the theory compares very well with experiment -- within 12.5% at the QE peaks. For silver the magnitude of the theory compares with experiment within a scale factor of 4.2 at the QE peak.

6.2.2 Discussion of Peak QE Variation between Deposition and Desorption

Some depositions show a QE peak during deposition which is somewhat lower than the desorption peak during heating of the substrate afterward. Such a case is seen in the data set illustrated in Fig. 6.9 for cesium on 70% dense sintered tungsten.

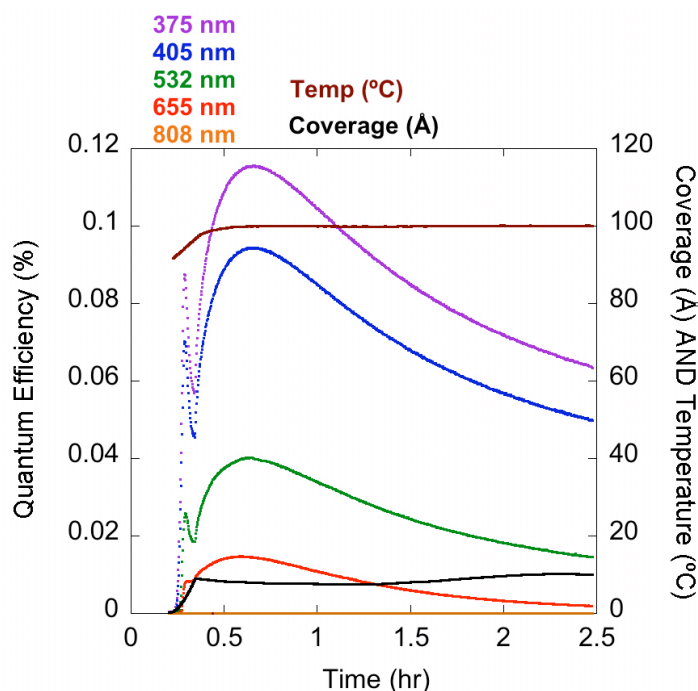


Figure 6.9: Peak QE discrepancy: deposition vs desorption, Cs:W

In order to explain the apparent discrepancy between the initial and final QE peaks in cesium tests like that shown in Fig. 6.9 (hereafter termed the deposition and desorption peaks, respectively) we turn to a discussion of the adsorption of submonolayers of cesium on tungsten. There are three arguments for peak QE variation: local random cesium adsorption, local substrate

nonuniformity including contamination, and global deposition nonuniformity. Each will be considered in turn and the implications discussed.

For the random cesium adsorption argument we use the hard-sphere model to visualize what is happening on the atomic scale. Tungsten has a BCC lattice with a lattice constant very nearly equal to the radius of a cesium atom, such that cesium atoms in the hard-sphere model sit on four substrate tungsten atoms. A monolayer of cesium on the [100] face of tungsten is shown in Fig. 6.10.

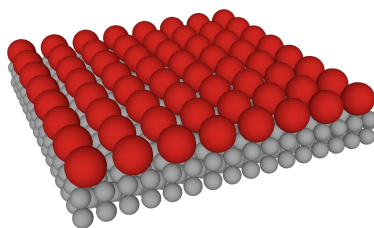


Figure 6.10: Cs:W, hypothetical 100% uniform coverage, hard sphere model (to scale)

An ideal, evenly spaced half-monolayer simply has half the number of cesium atoms, as shown in Fig. 6.11.

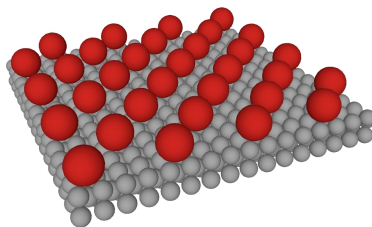


Figure 6.11: Cs:W, hypothetical 50% uniform coverage, hard sphere model (to scale)

And with the adsorption of cesium atoms on the surface during an external evaporative deposition one could imagine coverage of 50% but distributed randomly (where for simplicity we have considered only the original monolayer adsorption sites not intermediate ones) as in Fig. 6.12:

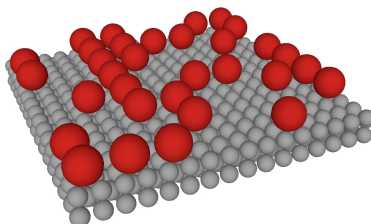


Figure 6.12: Cs:W, hypothetical 50% random coverage, hard sphere model (to scale)

Clearly the QE in the two illustrated cases of 50% coverage would not be the same because of the asymmetric dependence of work function on (local) coverage, which was plotted in Fig. 6.1. The QE of the randomly covered surface, in which most cesium atoms have an adjacent occupied adsorption site (in contrast to the uniformly covered surface where no adjacent adsorption sites are occupied), would be reduced. This is because the dipole lowering of Eq. 6.10 has a maximum effect near 50% coverage (as seen indirectly in Fig. 6.1 as well) and therefore if an individual atom sees adjacent occupied sites this reduces the atomic dipole moment locally, and reduces the QE globally.

The random-adsorption argument relies on cesium atoms remaining stationary throughout the experiment -- frozen on an atomic scale. However, it is known from successful dispenser operation that cesium atoms are diffusively mobile over many hundreds of microns through the tungsten pores and over many microns on the surface at dispenser operating temperatures of ap-

proximately 120 °C and higher. It would be naive to say that at room temperature the cesium atoms are frozen in place and cannot hop locally from adsorption site to adsorption site. A more telling observation is that a properly ion-cleaned sintered tungsten surface can exhibit an identical deposition and desorption peak in QE at room temperature [19]. Since the random-adsorption argument would require that the randomly deposited submonolayer would result in a lower peak QE during deposition than during desorption, and such is not the case in well-controlled experiment, the ability of cesium atoms to diffuse on an atomic scale even at room temperature is indicated.

This is an interesting conclusion to obtain from a space-averaged, time-averaged measurement like QE, but it is supported by the literature on alkali diffusion on refractory metal substrates. The problem of hopping is discussed in detail by Gomer [116] and has been modeled for cesium diffusion [70]. Gomer also notes that adjacent chemisorbed dipoles of Cs on W are almost purely ionic at low coverages and have an interaction energy from dipole-dipole repulsion characterized by $J_{d-d} = p^2/2r^3$, where $p = 2dq$ is the adsorbate dipole moment with charge q a distance d above the surface and image charge $-q$ a distance d below it, and where r is the dipole-dipole separation. For cesium at low coverage $q = e$, e being the (positive) unit of charge, corresponding to a nearly ionic cesium adatom. For cesium at higher coverages it is possible to have $q < 0.5e$, but this still results in a strong dipole-dipole repulsion particularly since the atoms are more densely adsorbed. The dipole-dipole interaction in part mediates the uniformity of coverage obtained by hopping (and may explain some of the strong coverage dependence in the evapora-

tion rate as well). However, although we have explained why it is possible to have an experiment where the deposition and desorption peak are the same, we are now left without an explanation for cases in experiment where the deposition and desorption peak QEs are *different*, so we turn to the remaining arguments of local substrate nonuniformity and global deposition nonuniformity.

Local nonuniformity of substrate is possible due to different crystal faces, roughness, contamination, etc. The effect is to have large patches of the surface exhibit different work functions, different bond strengths with adsorbed cesium, and different QE for the same surface density of adsorbed cesium atoms. The QE varies because the f-factor will vary for the different substrate patches. Thus the ideal coverage is not the same in all areas in order to peak the QE.

If the diffusivity of the cesium were not enough to allow it to move from patch to patch, at room temperature there would be no improvement in peak QE. Heating would allow the cesium to diffuse on the micron scale required to traverse such patches and would allow optimal cesium coverage to be obtained on each patch, thereby maximizing QE. This would be energetically favorable since it would also maximize the bond strength of the cesium atoms. This effect is seen in heat-cleaned (anneal-cleaned) sintered tungsten where the surface still may have patches of contaminants on it. Peak QE during deposition is indeed lower than during desorption.

A final case not yet explained is why an ion-cleaned surface may exhibit different QE peaks from deposition and desorption, because in this case the surface should be atomically clean and so the patch effect with contaminants does not come into play. As previously noted, experiments do in fact normally see identical deposition and desorption peaks for ion-cleaned sub-

strates. The question is then, what is different about the experiments where the QE peaks vary? For this we turn to the global deposition nonuniformity argument.

Suppose that one of the alkali evaporation sources is not pointed directly at the cathode. The rate of deposition is fastest in the center of the evaporant "beam" and falls off from there. If not centered on the cathode a higher deposition rate can occur on one side of the cathode compared to the other, causing it to go through its maximum-QE coverage first. By the time the slow-deposition side of the cathode reaches maximum coverage, the QE of the fast side is already past peak and lowered. The average QE of the cathode overall is thus reduced, and the peak QE is less than that for a uniformly deposited cesium sub-monolayer.

After more than a monolayer is deposited and then heating is performed to initiate fast evaporation, that evaporation has a strong coverage dependent rate (known from thermionic dispensers to be θ^n where n is a very large power law depending on adsorbate and conditions, typically between 10 and 20), tending to result in a faster loss of cesium from the more cesiated portions and a slower loss from the less cesiated portions, evening out the coverage overall and hence a resulting in a higher desorption peak QE compared to the initial deposition peak. (The evaporatively-induced coverage smoothing is also present for an operating dispenser in which diffusion and evaporation are occurring: this may improve the uniformity of emission from a dispenser both globally and locally on the scale of the pore-to-pore spacing. Of course at temperatures with low evaporation, diffusion alone can result in more uniform emission.)

Chapter 7: QE of Semiconductors

7.1 Theoretical Basis

The quantum efficiency of semiconductor photocathodes is a broad topic. The intent here is to provide a useful discussion of why the QE differs so greatly from metals, what physics is behind that, how the QE of select alkali antimonides in particular can be effectively modelled using those physics, and how such understanding can guide future work. This will lead into the presentation of experimental results on the fabrication of alkali antimonide photocathodes and some characterization of their properties.

7.1.1 Introduction and Contrast with Metals

In stark contrast to the limited quantum efficiency of metals (which in the case of copper, for instance, is only 0.014% even at a UV drive laser wavelength of 266 nanometers), the quantum efficiency of semiconductors is quite good: of the order of 1-50%, depending on material choice and drive laser wavelength. Response times are longer than for metals, from 1-10 picoseconds or more. These longer response times can beneficially damp power fluctuations on the drive laser pulse, but if too long, prevent the emission of short, well-defined picosecond bunches of electrons for immediate acceleration in the optimum few degrees of the RF standing wave in the accelerator cavity.

Better QE stems from differences between metals and semiconductors on all fronts: in the optical characteristics of the materials, in their scattering and transport properties, and in the

emission barrier. Each of these will now be discussed in turn with appropriate theoretical support analogous to the successful Moments-based approach used for metals in Chapter 6.

7.1.2 Moments-Based Approach for Semiconductors

We begin by restating the Moments-based approach for calculating current density of Eq. (6.39) and Eq. (6.40) for *metals* and noting that this is yet to be modified for semiconductors:

$$(7.1) J = -2 \frac{A_{RLD}}{k_B^2} \int_0^{\pi/2} \int_0^\infty E P_{total}(E, \psi) \sin \psi \cos \psi dE d\psi$$

$$(7.2) P_{total}(E_{initial}, \psi) = f_\lambda(E + \hbar\omega, \psi) f_{FD}(E) [1 - f_{FD}(E + \hbar\omega)] T((E + \hbar\omega) \cos^2 \psi)$$

where for clarity the energy has been emphasized as the initial electron energy before photoexcitation.

For semiconductors we must incorporate a consistent and appropriate convention for energy given that the bottom of the conduction band (which, as for metals, is taken as our zero) is now at the top of a bandgap, and the initial state for a photoexcited electron is below the bandgap in the valence band. Thus the total photoemission probability as a function of energy and electron propagation angle with respect to surface normal shall be defined with reference to the energy of the *final* state of the electron in the semiconductor, whereas for metals it was with reference to the *initial* state.

$$(7.3) P_{total}(E_{final}, \psi) = f_\lambda(E, \psi) f_{FD}(E - \hbar\omega) [1 - f_{FD}(E)] T(E \cos^2 \psi)$$

As for metals we make the low-temperature approximation which turns the Fermi-Dirac functions into step functions. The transport probability is the same as previously derived. However, the transmission probability as a function of energy must be modified: as Jensen discusses in Refs. [78; 117], this is a triangular barrier described by

$$(7.4) D(E(k)) = \frac{4k\kappa_p}{2k\kappa_p + (\kappa_p^2 + k^2)\exp\left(-\frac{4}{3f}\kappa_p^3\right)}$$

where $k = \sqrt{2mE/\hbar}$, $\kappa_p = [(2m/\hbar^2)^{1/2}(E - E_a)^2 + p^2 f^{4/3}]^{1/4}$, $f = 2mF/\hbar^2$, F is the applied electric field times the electron charge, and $p \approx 2/5$. Under the low field approximation $\kappa_p \approx [2m(E - E_a)/\hbar^2]^{1/2}$. Also under the low field approximation the transmission probability described above is zero below the electron affinity, such that tunneling is neglected, we may make the same step function argument for the turn-on of the transmission probability as for metals, resulting in an escape cone which places limits on the angular moments integration. However, unlike for metals, the transmission probability is not constant with respect to electron energy above the escape cone limit. Therefore we write for semiconductors

$$(7.5) P_{\text{total}}(E, \psi) = f_\lambda(E, \psi) \Theta(E - E_a) [1 - \Theta(E - (\hbar\omega - E_g))] \Theta(E \cos^2 \psi - E_a) D(E \cos^2 \psi)$$

with the transport probability without collision, f_λ , defined by Eqs. (6.41) and (6.42), and where E_a is the electron affinity (defined with reference to the bottom of the conduction band as usual) and E_g is the bandgap.

Now the step function approximations discussed can be used to place the appropriate limits on the angular and energy integrations of Eq. (7.1).

$$(7.6) J = -2 \frac{A_{\text{RLD}}}{k_B^2} \int_{\arccos(\sqrt{E_a/E})}^{\pi/2} \int_{E_a}^{\hbar\omega - E_g} E f_\lambda(E, \psi) D(E \cos^2 \psi) \sin \psi \cos \psi dE d\psi$$

Additionally substituting $x = \cos \psi$ yields

$$(7.7) J = 2 \frac{A_{\text{RLD}}}{k_B^2} \int_{\sqrt{E_a/E}}^1 \int_{E_a}^{\hbar\omega - E_g} E f_\lambda(E, x) D(E x^2) x dE dx$$

with, as for metals,

$$(7.8) f_\lambda(E, x) = \frac{x}{x + \frac{m\delta}{\hbar k(E)\tau(E)}}.$$

The important distinctions between the application of the moments approach to current density for semiconductors and for metals have now been outlined: a careful definition of energies and limits of integration, and a modified transmission probability, now triangular not step-like.

The evaluation of QE proceeds as a numerical integration to obtain current density, followed by, as for metals, the calculation

$$(7.9) QE = (1 - R) \frac{J(\hbar\omega, \phi, \mu)}{J_{\text{max}}}$$

where analogously to the case of metals,

$$(7.10) J_{\max} = 4k_B^{-2} A_{\text{RLD}} \int_0^1 x dx \int_0^{\hbar\omega - E_g} E dE = \frac{A_{\text{RLD}}}{k_B^2} (\hbar\omega - E_g)^2$$

7.1.3 Electron Transport and Scattering

The relaxation time found in the transport probability requires reconsideration for semiconductor materials. The scattering processes emphasized are not the same as for metals. Matthiessen's rule can still be used to sum contributions from all processes, but one must consider polar optical phonons, ionized impurities, and acoustic phonons separately:

$$(7.11) \frac{1}{\tau(E)} \approx \frac{1}{\tau_{\text{po}}(E)} + \frac{1}{\tau_{\text{ii}}(E)} + \frac{1}{\tau_{\text{ac}}(E)}$$

In addition the mass found in the transport probability should be considered the effective mass for semiconductors, which in the "alpha-semiconductor" model [23] is written as

$$(7.12) m = (E_g / R_\infty) m_0$$

where the bandgap, Rydberg energy (13.6 eV), and electron rest mass in vacuum are identified.

In Ref. [78] by Jensen and Montgomery, using cesium antimonide as a representative semiconductor at a drive laser wavelength of 532 nm, the relaxation times for the scattering processes mentioned are calculated and reported under realistic conditions. For a temperature of 300 K and an impurity concentration of 10^{18} per cubic centimeter, polar optical photon scattering

is found to dominate. The relaxation time for polar optical scattering is calculated under the above conditions as 27 femtoseconds. Acoustic phonon scattering is much less strong, at 700 femtoseconds, and ionized impurity scattering is negligibly weak at 4400 femtoseconds. These values will vary with electron energy (hence photon energy), with phonon energy (hence temperature), and with impurity concentration.

7.1.4 Optical Absorption

In Eq. (7.9) the reflectance must be calculated for the semiconductor in question. Again, this equation makes the thick cathode assumption: that the photocathode thickness is much greater than the optical penetration depth so that all light not reflected is absorbed. Just as for metals, the optical constants of the material (n and k , the real and imaginary parts of the refractive index) are used to calculate R , which for normal incidence is simply:

$$(7.13) R = \frac{(n - 1)^2 + k^2}{(n + 1)^2 + k^2}$$

(The extinction coefficient k can also be used to calculate the optical penetration depth via $\delta = \lambda/4\pi k$.) The reflectance for semiconductors tends to be lower than for metals: this is good, since this implies higher absorption and hence higher QE. The optical penetration depth tends to be larger, which along with comparably larger electron escape depth, increases response time compared to metals.

A Lorentz model, fit to literature data, can be used to calculate optical constants if they are not reported explicitly for the photon energies of interest. This process is detailed in Ref. [23] fit to data from Ref. [118] and the resulting curves are shown in Fig. 7.1.

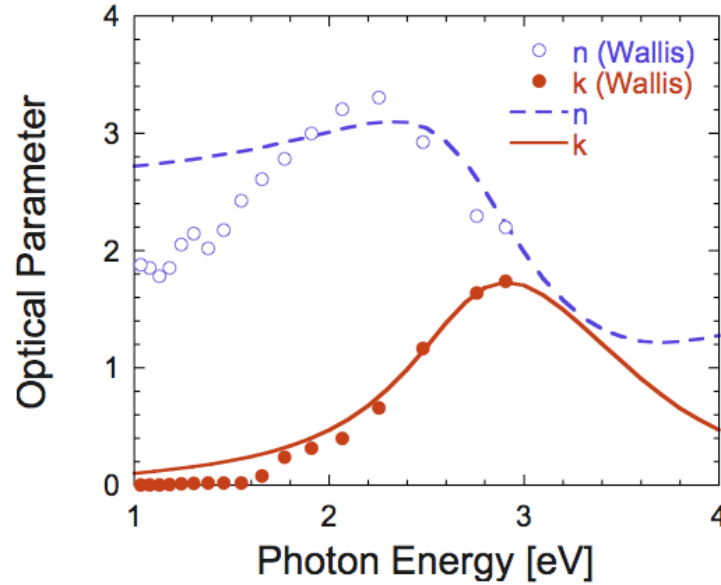


Figure 7.1: Cs3Sb optical parameters

Some experimental variation in these parameters from sample to sample is to be expected, and can cause the resulting reflectance to vary as well, for example in some multialkalis changing R over the range 0.2 to 0.3 for a green drive laser [23]. This should be expected to cause the QE to differ from experiment, solely due to the variation in optical parameters, by of order 10% of its calculated value.

7.1.5 Comparison to Literature

The calculated QE of Cs_3Sb based on the Jensen semiconductor theory is shown in Fig. 7.2. It is compared to data from W. E. Spicer, Ref. [119]. Given that there are no adjustable parameters in the theory, and that some variation in sample properties may be expected in practice as discussed for reflectance, it is remarkable that agreement is within a scale factor of 15%.

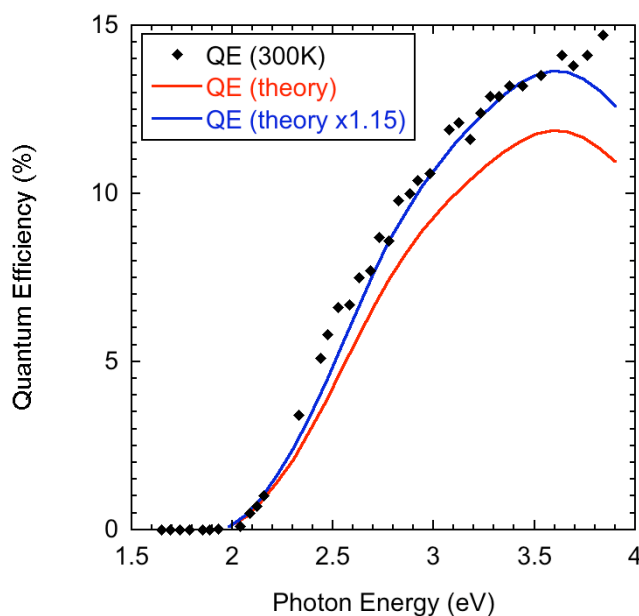


Figure 7.2: Theory vs Literature Data: QE of Cs_3Sb

7.2 Experimental Results: Cs_3Sb

7.2.1 Fabrication

The first alkali antimonide to be discovered as a photocathode material was cesium antimonide. As one of the simpler antimonides to fabricate, it was attractive for this initial line of research, since the variables in the formation process are fewer than, say, for the multialkalis.

The initial experimental tests with cesium antimonide used a thick cathode in order to demonstrate the QE potential of the material. Those results follow. With a thick cathode the substrate presumably contributes little to the optical or transport characteristics of the deposited film.

7.2.2 Measured QE

The fabrication process for cesium antimonide cathodes is shown visually in Fig. 7.3.

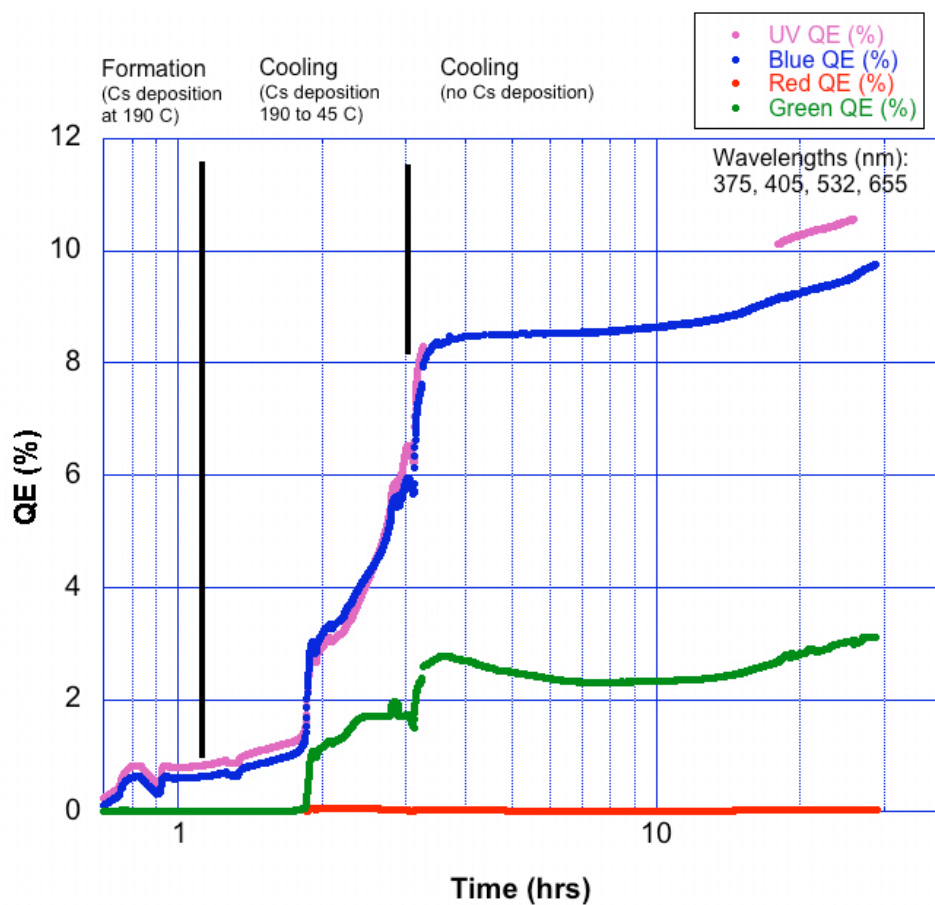


Figure 7.3: QE during fabrication of Cs₃Sb

The data shown is for an initial one hundred Ångström layer of antimony on a sintered tungsten substrate, followed by cesium as required to cause the QE to peak. The final thickness of the cathode after fabrication cannot be measured, nor can it be inferred from the amount of cesium deposited since it is unclear how much cesium actually adsorbs and reacts, and how much evaporates during the process of fabrication. However, the relation between the initial antimony thickness and the final cesium antimonide thickness has been reported to be approximately 1:5.9 [102]. Therefore this implies a final cesium antimonide thickness of approximately 590 Ångströms, which clearly satisfies the thick cathode assumption in the theory comparison which will follow.

During fabrication the continual external evaporation of cesium onto the hot cathode surface must be maintained so that, at a minimum, it exceeds the loss of cesium due to evaporation of cesium from the hot surface. For this reason, when the cathode is cooled, the deposition of cesium is tapered off until a peak in QE is reached. Additional improvement in QE occurs after the end of deposition during final cooling.

Unfortunately the experimental apparatus is not fitted with the ability to perform detailed surface diagnostics which might confirm that the stoichiometry of the cathode is in fact 3:1 Cs:Sb. Variations in stoichiometry have been reported in the literature [120]. The best indication that near-ideal stoichiometry has been achieved in this case is that the QE was carefully peaked prior to cooling the cathode. Further support comes from the comparison in the next section

where experimental data has excellent correspondence to the independently derived theory already summarized.

In Fig. 7.4 the response of the cathode to cooling following initial fabrication and the resulting stabilization in QE are shown. In the UHV conditions of the chamber, with nanotorr vacuum maintained after cooling the sources and cathode and with oxidizing gas partial pressures at least two orders of magnitude below that (in most cases below the measurement resolution of the RGA), the cathode lifetime is excellent.

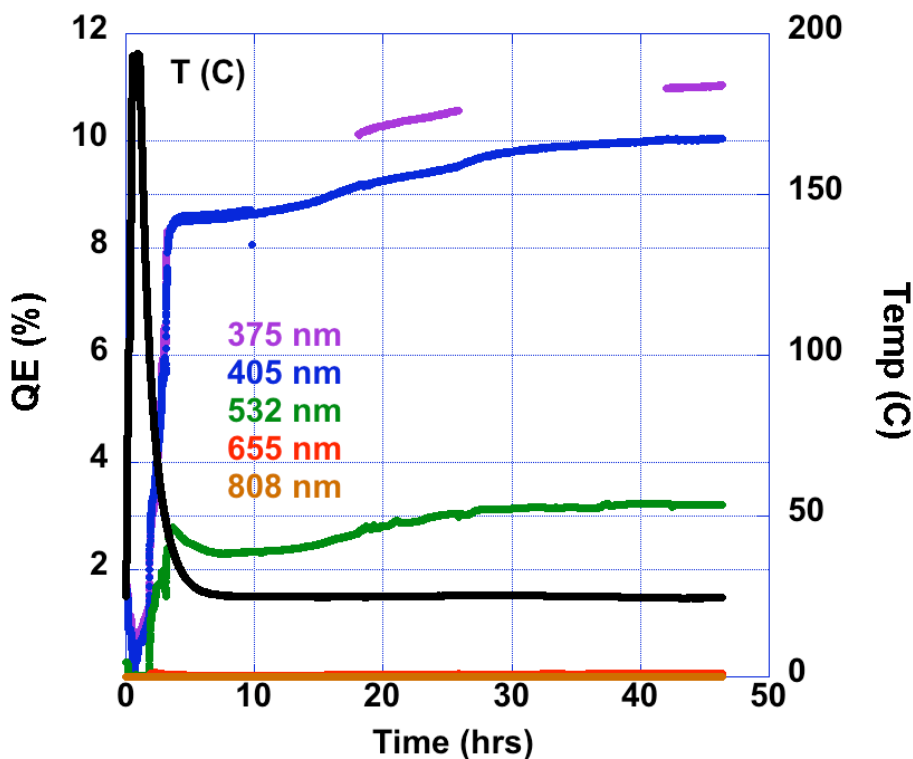


Figure 7.4: QE vs temperature during fabrication and cooling

For all alkali antimonide tests, the higher QE achieved than for metals requires a higher applied field so that the photocurrents resulting from the drive lasers are not space-charge limit-

ed, and remain linear with optical power. This was ensured by increasing the bias voltage of the isolated cathode-anode circuit to achieve up to approximately 30 kV/m, more than required to achieve linearity. (Alternatively neutral density filters could have been used to attenuate the laser power.)

7.2.3 Comparison to Theory

The same theory used to calculate the QE of cesium antimonide in Section 7.1 [23] is compared to the peak QE obtained at the five wavelengths measured in Fig. 7.4. The results are graphed in Fig. 7.5. The theory is not a fit to the data. This is a predictive theoretical curve based on fundamental constants and measured values reported in literature, with no scaling or fitting parameters used.

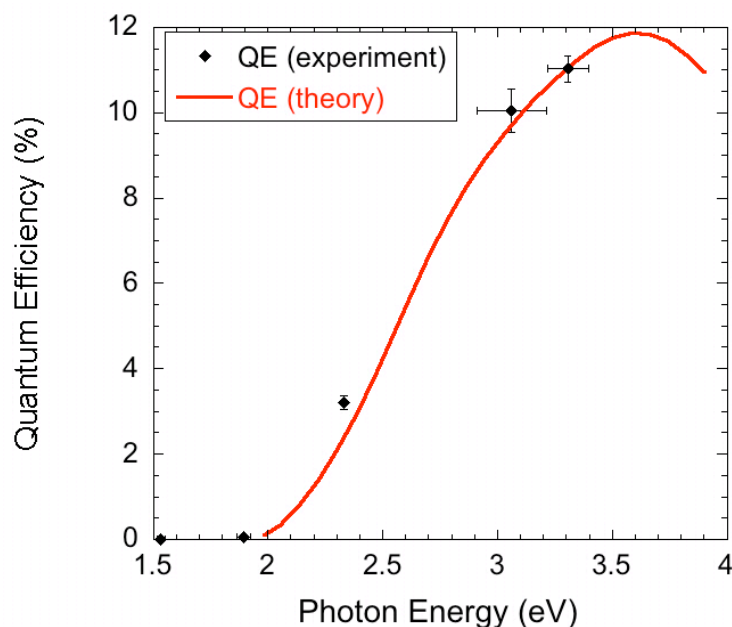


Figure 7.5: QE of Cs₃Sb, experimental results vs predictive theory

While there is no way outside of detailed surface analysis techniques (e.g., x-ray spectroscopy or Auger depth profiling) to probe the exact stoichiometry of the cathodes fabricated at Maryland, it is indicated by literature that optimum QE occurs at the proper stoichiometry, and since we have peaked the QE in experiment, it is reasonable to conclude that the correspondence between data and theory is much more than coincidental. Referring also to Fig. 7.2 it is clear that these results are consistent with experimental data in the literature.

7.3 Experimental Results: $\text{Na}_2\text{KSb}(\text{Cs})$

7.3.1 Fabrication

The trialkali material cesium sodium potassium antimonide, where the bulk is formed by sodium potassium antimonide and the surface layer is cesium-based, has more attractive thermal stability than cesium antimonide. (See Section 8.4.) For this reason it was chosen to follow the cesium antimonide experiments. Fabrication entailed upgrades to the experimental apparatus to allow multiple alkali sources to be used simultaneously or in succession.

As described in Sections 4.8 and 5.4, the cathode test chamber at UMD allows repeated deposition and cathode cleaning while monitoring QE during the fabrication process. Because there is no load-lock on the evaporative source flange, an exchange of evaporative sources necessitates a return to atmosphere and subsequent bakeout of the chamber to achieve ultrahigh vacuum again. Obviously this should be minimized. To that end, most tests extend life of the sources in the chamber by fabricating thinner cathodes than are standard elsewhere -- thinner,

even, than the optical penetration depth in some cases -- allowing repeated experimental runs without quickly depleting the evaporative materials. The QE thereby achieved should not be construed as representative of the maximum achievable. However, the response of the material to heating and contamination and the resulting changes in QE are expected to follow the same behavioral trends as for thicker cathodes, and as such, allow us to obtain insights into the suitability of such materials for dispenser applications even though the films in question are thin.

At the same time, thin cathode structure invalidates the assumption of the 1-R term in the QE calculated by theory, with the potential not only for less absorption in the cathode itself, but also for interaction with the substrate in the form of interference effects or photon penetration into the substrate and subsequent photoexcitation there. These are not addressed by the present form of the theory. Literature data for the trialkali is more difficult to obtain (and in fact because of the fabrication complexity, wide variation in such parameters might be expected), and therefore all these points preclude a comparison of trialkali data to theory such as was performed for cesium antimonide. Nonetheless, the practical outcome of significant QE with the trialkali material on dispenser-type substrates is an important demonstration and may also serve to guide future theoretical development, and is a necessary precursor to future high-QE rejuvenation studies.

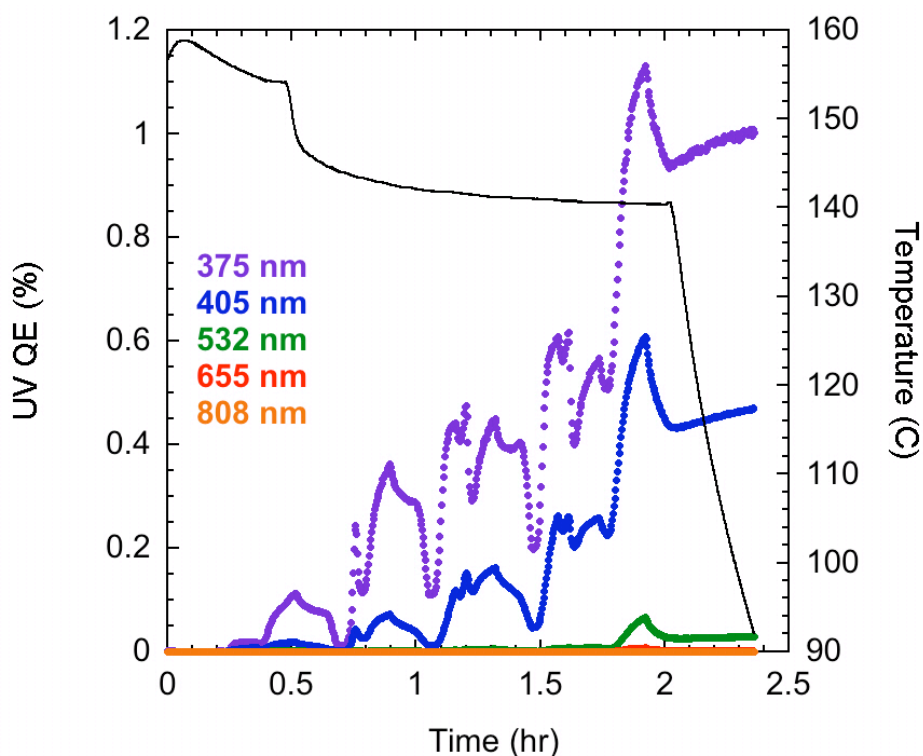
7.3.2 Measured QE

Shown in Fig. 7.6 is the fabrication process for sodium potassium antimonide. Evident in the process is the cyclical deposition of consecutive layers of antimony, sodium, and potassium, and the final application of a cesium surface treatment. The sintered tungsten substrate (60%

dense) was annealed to 700C and then argon ion cleaned for a standard 40 minutes as detailed in the procedures chapter. The deposition of material was done consecutively not simultaneously, and the QE was peaked in each step. The sequence of depositions is shown in Table 7.1. Total material deposited (not all alkali would have remained due to evaporation which would be higher for K than Na and highest for Cs) was 46 Å Sb, 27 Å Na, 38 Å K, and 27 Å Cs.

Material	Thickness deposited (Å)	Temperature (°C)
Sb	12	160-155
Na	15	155
K	10	155-145
Sb	15	145
Na	7	145
K	7	145-140
Sb	10	140
K	6	140
Na	3	140
K	7	140
Sb	9	140
K	8	140
Na	2	140
Cs	27	140

Table 7.1: Trialkali fabrication steps

Figure 7.6: QE during fabrication of $\text{Na}_2\text{KSb}(\text{Cs})$

The prompt response of the QE to the end of cesium evaporation and also to the end of active heating indicates a temperature-sensitive surface equilibrium between the cesium being added by external evaporative deposition and that being lost by temperature-dependent evaporation. As confirmation, note the behavior of the green drive laser. Best QE is obtained at the point in the procedure where the cesium deposition is ended, and intentionally prior to cooling the cathode. This allows a subsequent evaporation of cesium and strongly affects the emission barrier, causing the QE in the green to retreat steeply from its near-percent-level peak. An ideal QE will therefore require a careful application and/or maintenance of the correct amount of cesium on the surface.

Chapter 8: Cesium Loss and Recesiation

8.1 Introduction

The principle of the cesium dispenser photocathode is first, that loss of cesium in that delicate surface coating contributes to the loss of QE over time, and second, that replacing that cesium *in situ* (where cesium is supplied via diffusion from a subsurface reservoir to the surface) will rejuvenate the QE, a process known as recesiation. We will show that cesium lost to heating and evaporation, and the subsequent loss of QE, is reversible by external recesiation (cesium evaporated from an external source onto the cathode surface) as well as by *in situ* recesiation, as discussed in Section 8.3.1. Section 8.3.2 addresses the important question of whether recesiation can reverse the QE lost due to contamination by oxidizing gases which can be found in the vacuum of a photoinjector. Although the focus in contamination and recesiation experiments detailed here is on external recesiation, the results serve to support *in situ* recesiation as well, validating the cesium dispenser photocathode concept.

Before opening experimental results we discuss the mechanisms for cesium loss. We then consider experimental data from cesiated metals and cesium-based semiconductors in turn.

8.2 Cesium Loss Mechanisms

High efficiency photocathodes often rely on a low work function coating (in this case, cesium) which is quite sensitive to vacuum conditions and contamination by background gases present in the environment of the photoinjector. The reduced lifetime of cesium-based cathodes

in operational conditions, as shown in Fig. 1.2, is due in large part to degradation of the delicate low work function surface conditions characteristic of these cathodes. Cesium, as the work function lowering material, is unfortunately lost under several mechanisms, resulting in an increase of the average work function and a reduced QE and lifetime. Investigation of this process is critical in support of cesium dispenser photocathode development. The mechanisms for cesium loss discussed here, in turn, are evaporation, ion back-bombardment, contamination, and dissociation.

8.2.1 Evaporation

Cesium has one of the lowest melting points of any metal at 28.44 °C, second only to mercury. It should be no surprise that it then has high vapor pressures and evaporation rates even at modest temperatures (1 Pa at 144.5 °C). These bulk properties provide an indication that monolayer and sub-monolayer films of cesium should be prone to evaporation, but the evaporation rates of such coatings will differ from the bulk because cesium bonds differently to various substrates. For instance, cesium on anneal-cleaned, polished, polycrystalline tungsten has been measured to have a sub-monolayer evaporation rate of 0.009 Å/s and a multiple-monolayer evaporation rate of approximately 0.214 Å/s at temperatures less than 200 °C [19]. For comparison, bulk cesium's vapor pressure of 7.5×10^{-2} Torr at 195 °C indicates (for a 5 Å monolayer thickness) an evaporation rate of a remarkably fast 375,000 Å/s. Evaporation data from semiconductors has been published [121] and cesium has been reported to have a vapor pressure equivalent to a sub-monolayer evaporation rate from sodium potassium antimonide of approximately 0.02

monolayers/hr at 150 °C, or 0.00003 Å/s assuming (as for coated metals) a monolayer thickness of the covalent diameter of cesium, about 5 Å.

8.2.2 Back-bombardment

Under the extremely strong field gradients which accelerate negatively charged electrons away from the photocathode to high energy, any positive ions present in the vacuum environment near the cathode will find themselves accelerated in the opposite direction, impacting the cathode at high energy. This is not as critical in RF guns where the field cycles at frequencies of approximately a gigahertz, but in DC guns back-bombardment is a limiting factor on cathode lifetime. DC gun photocathode lifetimes are often specified by charge extracted rather than hours, days, or weeks of operation. The cesiated (NEA) GaAs cathodes at Jefferson Lab's DC photoinjector have a lifetime of 2000 C/cm². With an average current of 10 mA this corresponds to a few hundred hours of operation.

8.2.3 Contamination

Historically there have been numerous examples of the sensitivity of cesium-based photocathodes to contamination, particularly to reactive gases. The Boeing/LANL 433 MHz RF gun, achieving world-record 32 mA average current under operation in 1992, was reported as having contamination-limited lifetime of its CsK₂Sb cathodes of, on average, just 2.3 hours. There were elevated levels of water vapor present in the gun which were particularly detrimental. The cesium telluride (Cs₂Te) cathodes used at PITZ in Germany were discovered in 2007 to exhibit un-

naturally low lifetime; subsequent investigations revealed the presence of fluorine contamination from Teflon parts elsewhere in the vacuum chamber [122]. In fact, literature on the whole indicates that the operation of high quantum efficiency photocathodes in RF guns in general has been contamination-limited.

8.2.4 Dissociation

If a high quantum efficiency cathode such as a member of the alkali antimonide family is heated during operation in the photoinjector (whether that be RF heating or laser heating) and the temperature of the cathode rises too high, it is possible for dissociation of the semiconductor compound to occur. Dissociation energies and their corresponding (calculated) temperatures of maximum rate of dissociation are shown in Fig. 8.1 for several alkali antimonides (adapted from Dolizy and Groliere, Ref. [121]).

The thermal compatibility of the antimonides (or lack thereof) with dispenser photocathode technology is of concern in this work. Cesium dispenser operating temperatures are normally in excess of 150 °C, and therefore it is expected from Fig. 8.1 that the more temperature-stable antimonides, such as Na_2KSb , will prove more suitable as a high quantum efficiency dispenser coating. Ref. [121] also notes that the loss of cesium from a monolayer on the bialkali Na_2KSb amounts to 0.02 monolayers per hour at 150 °C. As long as the cesium resupply rate from the dispenser exceeds this (as is indicated by dispenser tests at Maryland), thermal compatibility is promising.

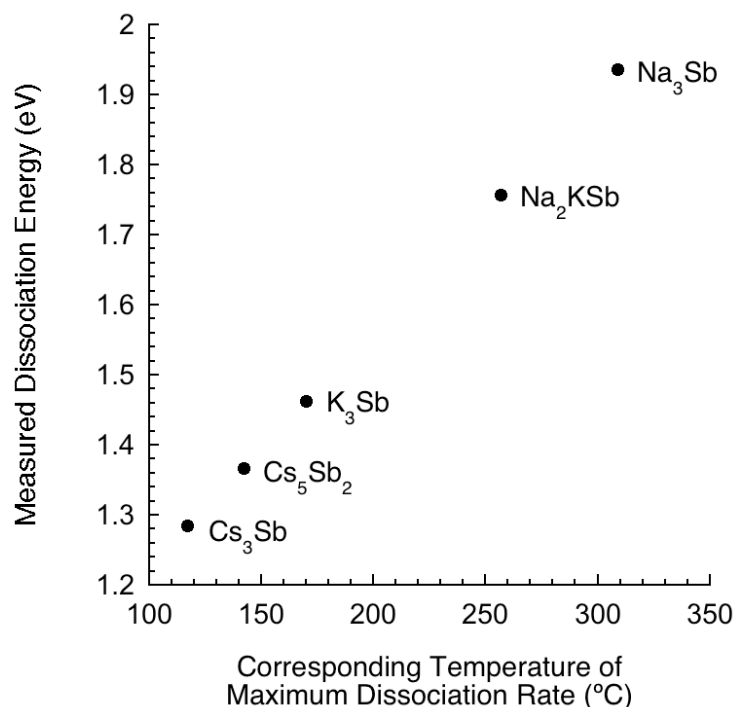


Figure 8.1: Dissociation Energies and Temperatures for Alkali Antimonides

Having introduced the loss mechanisms for cesium, we now turn to a discussion of experimental results for cesiated metals and for cesium antimonide: the loss of QE and its possible recovery via recesiation. Heating and contamination are tested for metals, and heating for cesium antimonide (since the dissociation energies indicate dissociation and subsequent loss of cesium during normal dispenser operation is a possible show-stopper for use of that material with dispenser photocathodes). Back-bombardment is not tested directly, but the use of an argon ion gun of 6.5 keV beam energy to clean the cathode substrate between experiments should indicate that elevated levels of back-bombardment can be extremely detrimental.

8.3 Cesiumated metals

8.3.1 Heating

Following a standard 40-minute, 30 milliCoulomb argon ion beam cleaning at 6.5 keV, cesium was deposited onto a 60% dense porous tungsten substrate from an external evaporative source (Alvatec). The cathode was then heated to observe the evaporative response of the cathode's monolayer cesium coating. This substrate is precisely the type used in the cesium dispenser, and so the response is also the behavior of cesium evaporating from the dispenser, isolated from the effect of any cesium resupply.

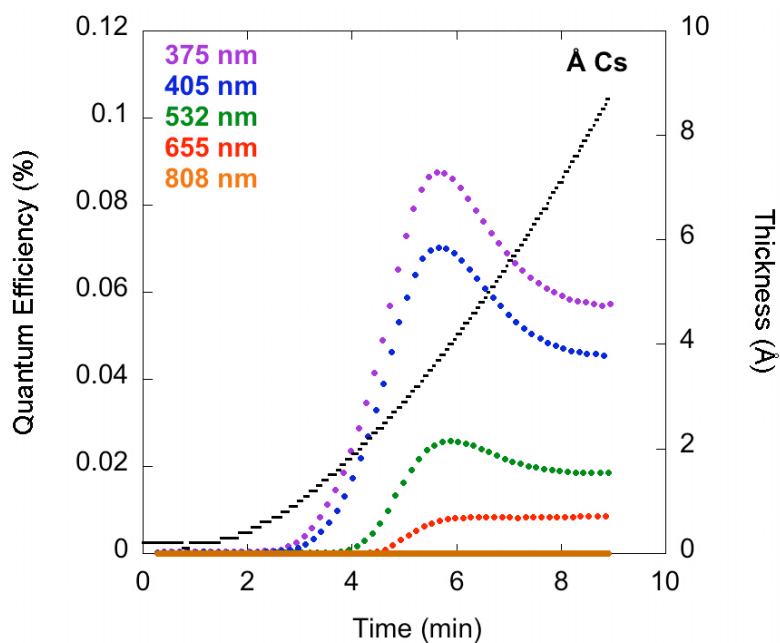


Figure 8.2: Cs:W deposition (100 °C)

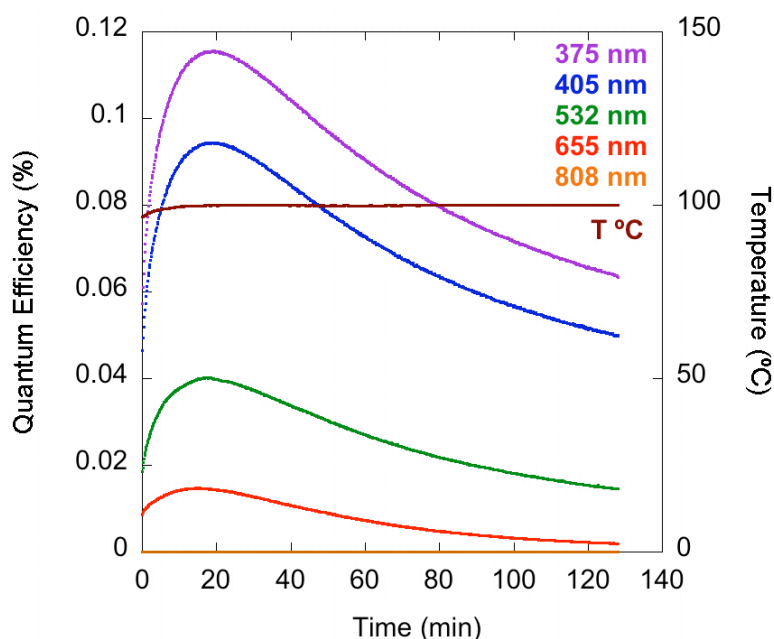


Figure 8.3: Cs:W evaporation

As the cesium evaporates it retraces the submonolayer peak in QE seen in the initial deposition. The early-time behavior is faster than the late-time, low-coverage evaporation, illustrating the strong coverage dependence of the evaporation rate even at submonolayer coverages. The retraced peak QE is higher than the initial deposition peak QE, however. Possible explanations for this, including patchy contamination (unlikely for ion cleaned substrates) or non-uniform deposition across the cathode face (more likely with Alvatec sources than with SAES sources because of narrower alkali emission angle), were discussed at length in Section 6.2.2.

8.3.2 Contamination and Recesiation

For contamination and recesiation tests, a peak-QE submonolayer coating of cesium was applied externally onto a polished, polycrystalline silver substrate. Three contaminant gas

species were tested, based on the fact that oxidizing gases are known to be detrimental to cathode lifetime in the vacuum of typical photoinjectors [57; 123]: carbon dioxide, oxygen, and nitrous oxide. Purity of the gas leak was assured by not permitting background partial pressure $>1\%$ for any oxidizer present other than the one under test. The course of the experiments introduced in Fig. 8.4, are shown in Figs. 8.5, 8.6, and 8.7 [105]. In each case, the initial QE is that of clean silver at 375 nm with an optimal submonolayer coating of cesium. A sharp decrease in QE denotes contamination, and a subsequent increase in QE denotes recesiation. Full rejuvenation of QE was achieved in each case.

The procedure in each case was as follows: first, a controlled gas leak of a selected contaminant gas known to degrade QE was performed on the chamber and an RGA analysis of the gas constituency was done to determine the purity of the gas supply. The chamber was re-evacuated. Next, the 1 inch diameter silver substrate was argon ion cleaned for 30 minutes at 5 kV and 10 mA. An external evaporative source of cesium (Alvatec) was heated gently until the optimal submonolayer coating of cesium was deposited on the silver substrate such that QE was maximized (typically 2-3 Angstroms). A timed exposure to a carefully monitored pressure of the gas from the controlled leak was used to contaminate the cathode and cause QE to fall. Immediately following re-evacuation, the surface was recesiated using the external evaporative source. QE rise was monitored and the recesiation was ended after the QE again peaks. The final QE peak was compared to the initial QE peak to determine if recesiation was effective in rejuvenating the cathode.

CO₂ tests were conducted using a background gas composition of 75% CO₂ and the remainder residual levels of cathode-inert gases (H₂, N₂, Ar). N₂O tests, due to limitations in the gas supply system, were conducted under a background gas composition of 10.2% N₂O and the

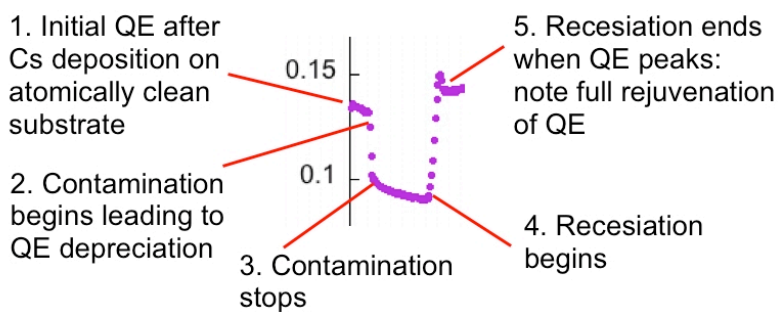


Figure 8.4: Contamination and recesiation procedure (QE vs time)

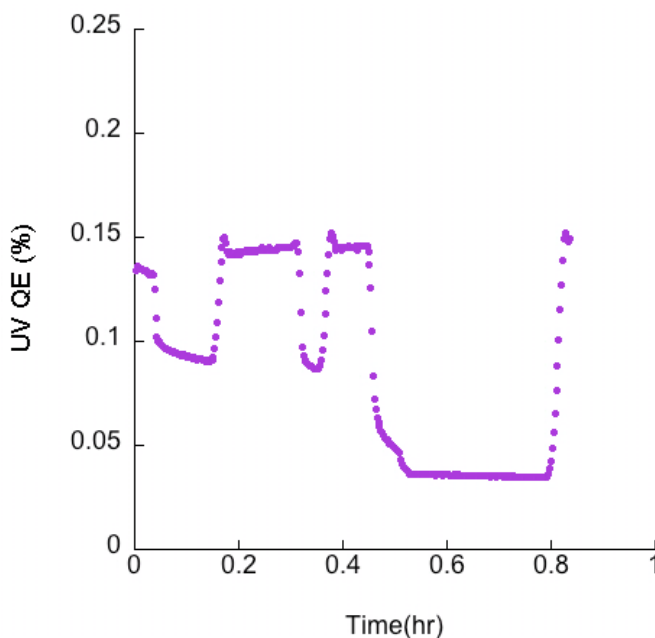


Figure 8.5: Recesiation of Cs:Ag after CO₂ contamination

remainder again cathode-inert gases to the 1% level. O_2 tests were conducted with background gas composition of 15% O_2 and the remainder cathode-inert gases.

For the case of CO_2 , repeatability of rejuvenation is shown in Fig. 8.5 after various levels of contamination. It is clear that full rejuvenation is possible via recesiation. The small peaks at the end of each rise in QE are due to slight overcesiation of the surface (past the optimum QE); this is the standard way to ensure that the QE maximum has in fact been reached.

The O_2 test in Fig. 8.6 shows a marked QE enhancement over the initial QE level, but enhancement of QE in the case of O_2 is a known effect seen in, for example, an S-1 photocathode [16]. The continued decay of QE after recesiation is due to residual levels of oxygen which

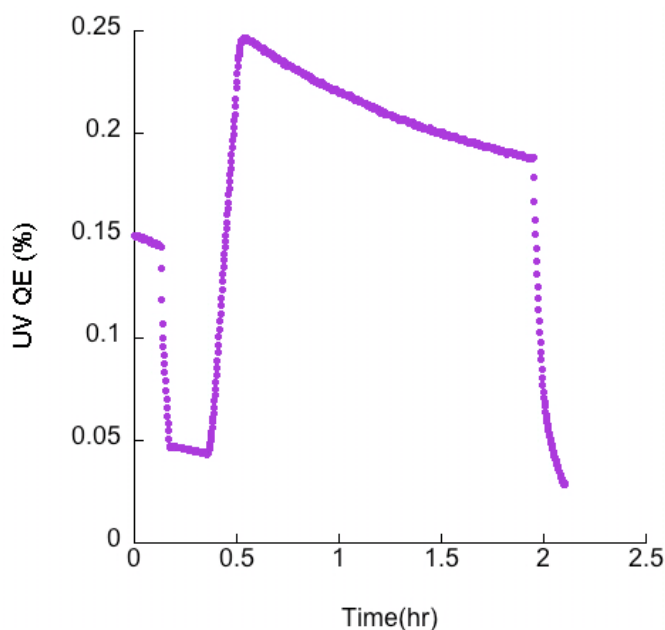


Figure 8.6: Recesiation of Cs:Ag after O_2 contamination

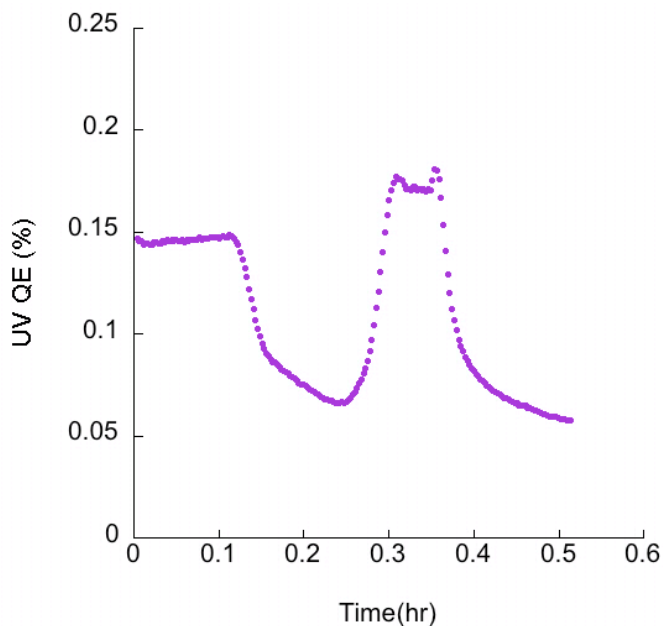


Figure 8.7: Recesiation of Cs:Ag after N_2O contamination

were slow to turbopump out of the vacuum chamber.

The N_2O test in Fig. 8.7 likewise displays full rejuvenation. Note the pronounced small QE peak both ending the first recesiation and beginning the second contamination. This behavior is a particularly strong indication that it is cesium loss and not adsorption of contaminants which is affecting the QE. This is because the peak is characteristic of the dipole interference effects between adjacent cesium atoms as discussed in depth in Section 6.1.2 and such effects would not be seen if cesium adsorption sites were being filled by contaminating atoms.

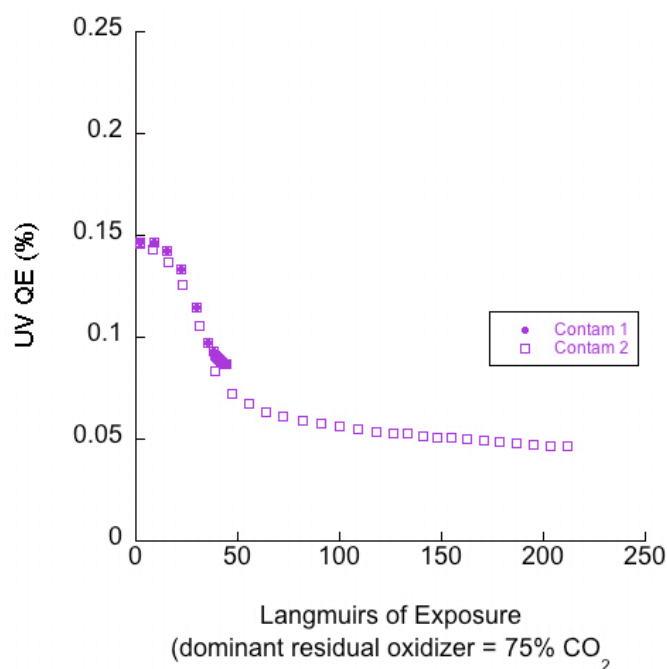
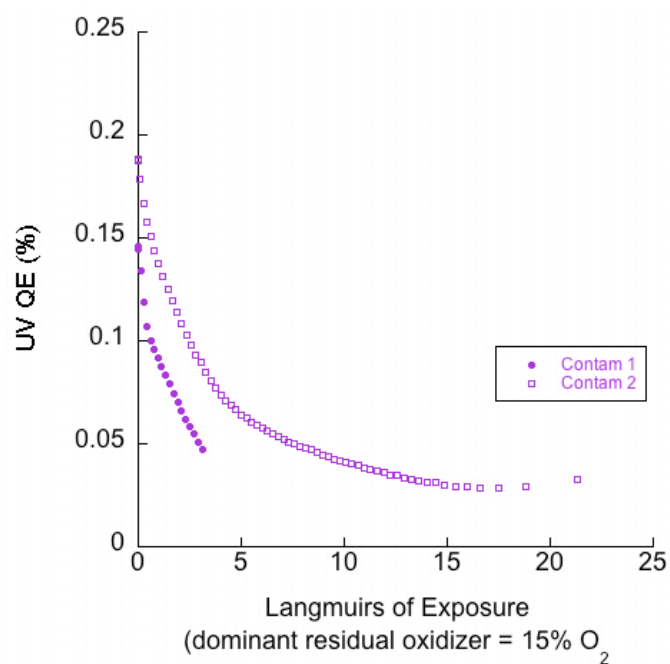
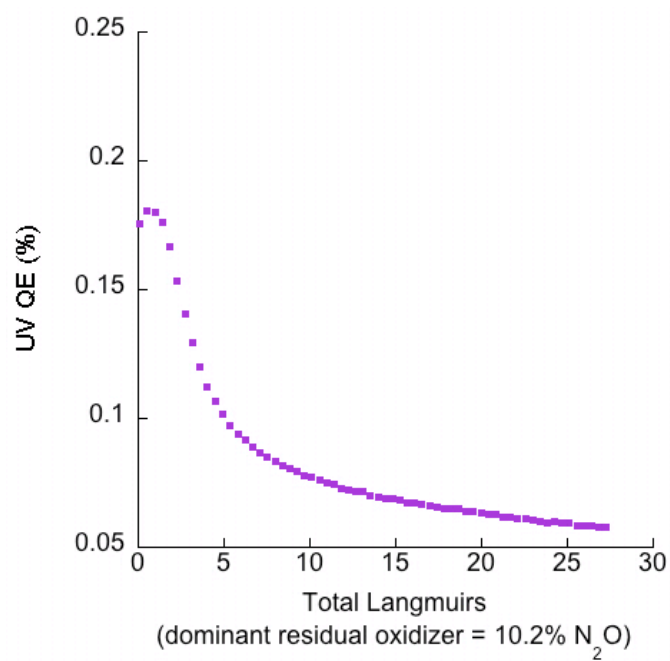


Figure 8.8: QE of Cs:Ag vs Langmuirs of exposure to CO₂

In Figs. 8.8, 8.9, and 8.10 the contamination of cesiated silver as a function of exposure is quantified. Units of Langmuirs are used, where one Langmuir is defined as the exposure to 1×10^{-6} Torr of the contaminant gas for 1 second. Results are particularly repeatable for the higher purity CO₂ experiments, as would be expected. The two experimental runs in Fig. 8.8 were run with different contamination rates, showing it is not the rate of contamination but the integrated exposure to contaminants which is important to QE loss.

The effect of recesiation is likewise quantified in Figs. 8.11, 8.12, and 8.13. QE is plotted as a function of deposited cesium thickness as compared to the initial cesium deposition required to reach peak QE on a clean silver substrate. It is important to note for CO₂ and N₂O that the amount of cesium required to rejuvenate is very comparable to that required to initially cesiate a

Figure 8.9: QE of Cs:Ag vs Langmuirs of exposure to O₂Figure 8.10: QE of Cs:Ag vs Langmuirs of exposure to N₂O

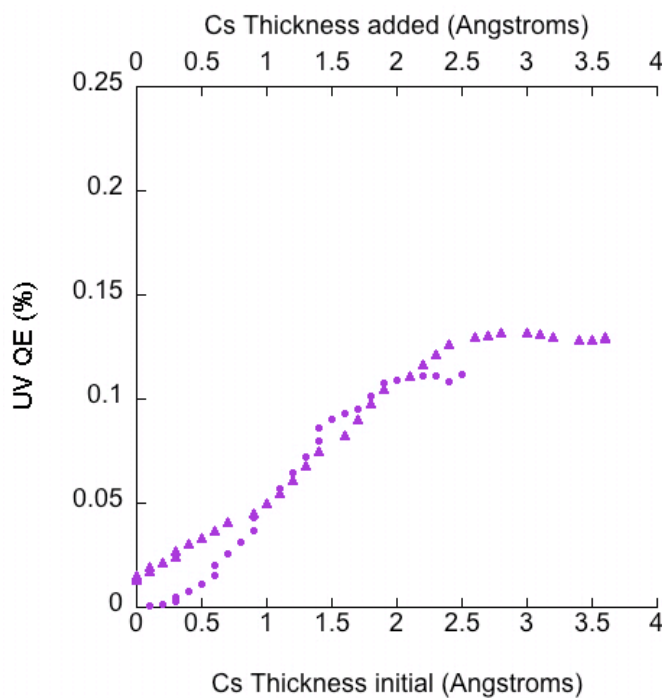
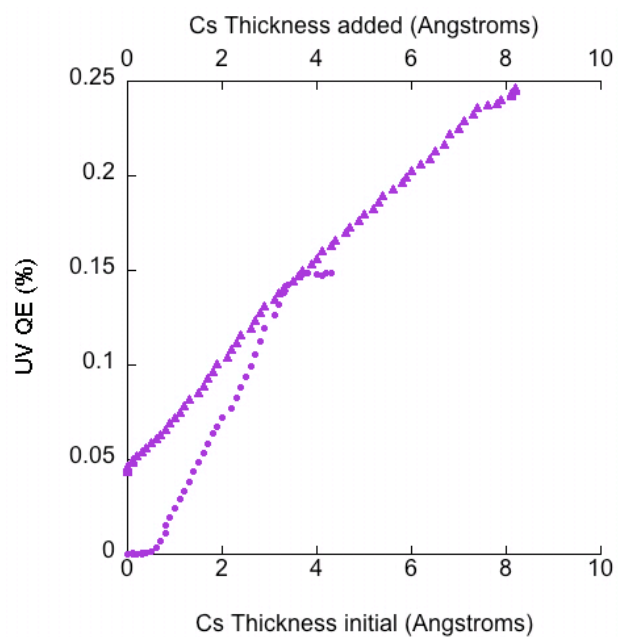
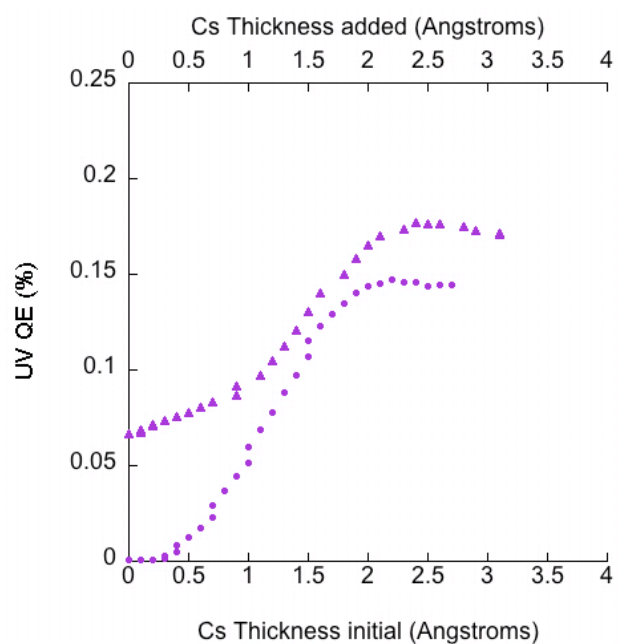


Figure 8.11: QE of Cs:Ag vs deposition, pre- and post-CO₂ contamination

clean surface. Again, this is strong indication that the process of recesiation is reversing loss of QE, not overlaying cesium on adsorbed contaminants.

The known interaction with O₂ is also noted [59; 124-126], where in that specific case the amount of cesium in recesiation exceeds the initial submonolayer application by a factor of 2.

Figure 8.12: QE of Cs:Ag vs deposition, pre- and post-O₂ contaminationFigure 8.13: QE of Cs:Ag vs deposition, pre- and post-N₂O contamination

8.4 Semiconductors

8.4.1 Heating

A cesium-antimony cathode was fabricated in-situ on an activated cesium dispenser (porous tungsten substrate) as described in Section 9.4 with an initial 100 Å Sb layer. The cathode formed was stable in UHV at room temperature over several hours with no observed reduction in QE, as shown in Fig. 8.14. The low QE (of order 1% compared to expectations of 10%) indicates the cathode, while exhibiting better QE than, say, bare antimony, was not able to achieve optimal 3:1 stoichiometry of Cs_3Sb . It is assumed that the cathode was Sb-rich following the in-situ fabrication process.

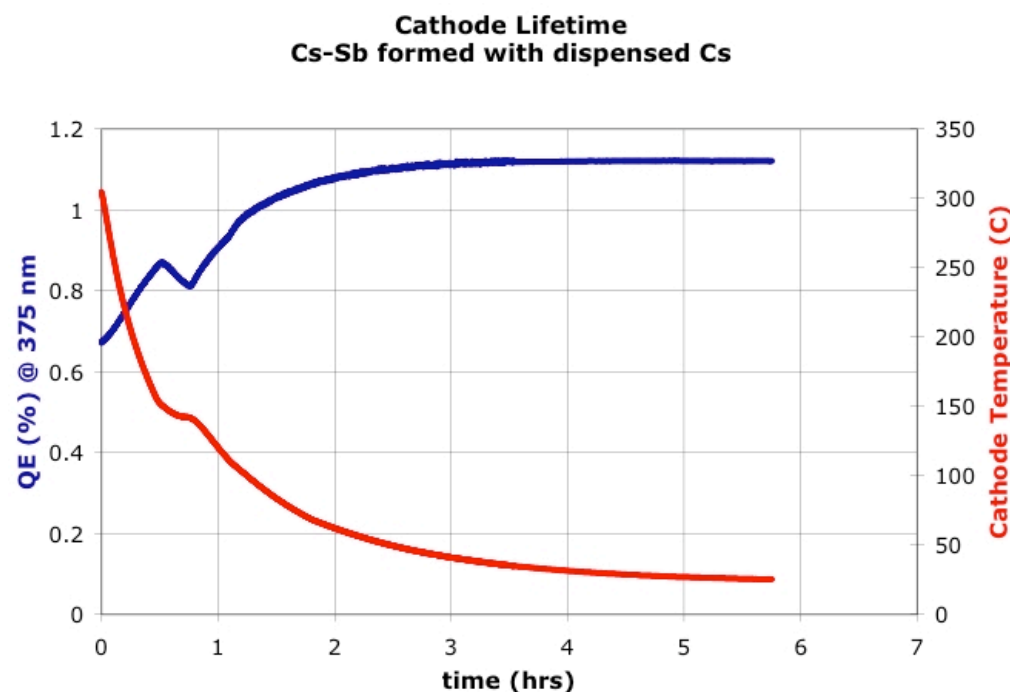


Figure 8.14: Initial cooling and stability of Cs-Sb cathode formed in-situ on dispenser

The cathode was then subjected to stepwise temperature increases and a return to room temperature in order to determine whether QE was irreversibly lost and whether significant dissociative or evaporative cesium loss could be inferred. The results of this experiment are shown in Fig. 8.15. When the cathode is heated and then cooled, the QE does not return to its initial level. Cesium loss is indicated. The cesium antimonide system appears to be incompatible with operating temperatures of cesium dispenser photocathodes.

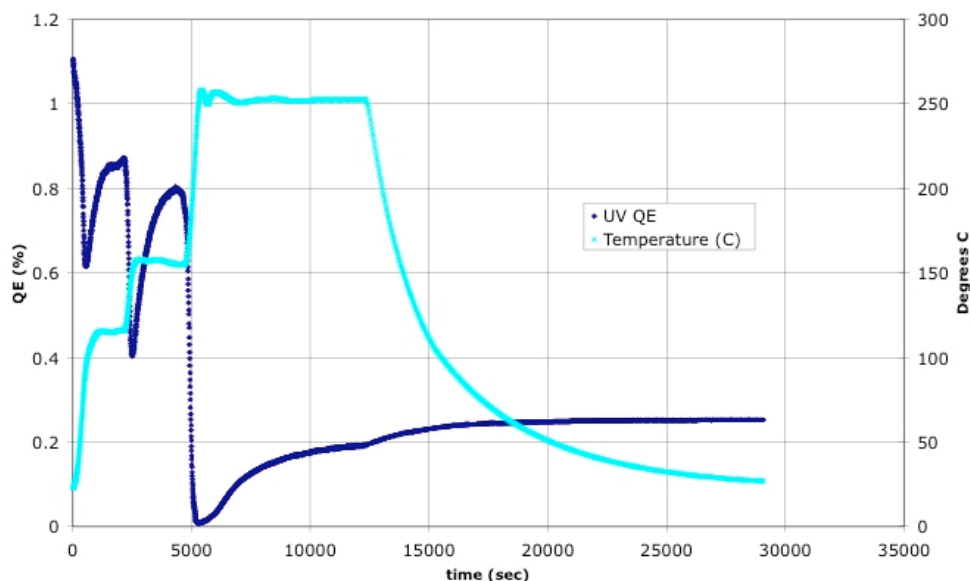


Figure 8.15: Re-heating and irreversible QE loss of Cs-Sb cathode despite active dispenser

The results of this test instigated a search for more thermally stable high QE cesium-based cathodes. In the next section we discuss the resulting survey of the temperature stability of various alkali antimonides based on literature data.

8.4.2 Survey of Alkali Antimonide Temperature Stability

Antimony by itself is quite temperature stable. The melting point of antimony is 630 °C. Vapor pressures of antimony at elevated dispenser operating points in excess of 200 °C are negligibly low. However, the alkali antimonides have non-negligible vapor pressures for the alkali metals over the bulk material at temperatures comparable to dispenser operating conditions. This should be no surprise given the melting points of cesium, potassium, and sodium are 28.44 °C, 63.65 °C, and 97.72 °C, respectively.

A literature survey revealed an excellent paper by Dolizy and Groliere in 1986 investigating the vapor pressures of the alkalis over various antimonides [121]. The data shown in Fig. 8.16 is adapted from their work. The reported vapor pressures are exponential with temperature; endpoint markers have been added for emphasis. With the vertical scale being logarithmic the exponential relation is shown as straight lines. Equivalent evaporation rates have been shown for the given partial pressures of the alkalis. These are calculated using the definition of the Langmuir unit of gas exposure: a monolayer of evaporation per second is equivalent to 1×10^{-6} Torr of pressure. The approximate operating range of the cesium dispenser is shown. Compatibility between dispenser and antimonide is inferred where the equivalent evaporation rate is less than one monolayer per hour within the dispenser operating range, since it is known the dispenser can supply a monolayer per hour to the surface without difficulty. Among cesium-based antimonides this points clearly to the trialkali $\text{Na}_2\text{KSb}(\text{Cs})$ as the best candidate.

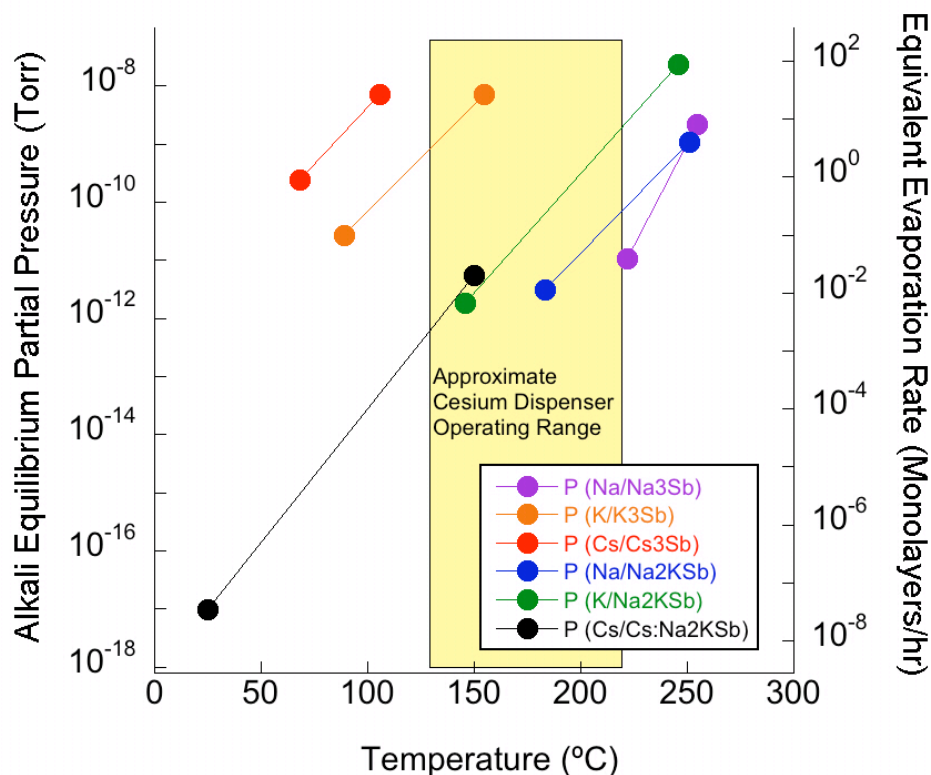


Figure 8.16: Vapor Pressures of Alkalis over Selected Antimonides

The results of this analysis combined with the unsatisfactory cesium antimonide (Cs_3Sb) test results at dispenser operating temperatures motivated fabrication of the trialkali $\text{Na}_2\text{KSb}(\text{Cs})$, due to its expected improved thermal stability compared to Cs_3Sb . The fabrication of and QE measurement of the trialkali material was detailed in Section 7.3 when discussing the QE of semiconductors.

Chapter 9: Cesium Dispenser Photocathode

9.1 Design and Fabrication

9.1.1 Introduction

Thermionic dispenser cathode technology is well established after five decades of research, as discussed in Section 2.3.2. These dispensers are, however, designed to operate at temperatures of order 1000 °C. Their work functions are lowered by surface coatings of barium, calcium, etc. which are not as effective as cesium coatings. But cesium, with its low melting point, is incompatible with operating temperatures for thermionic emission. Even though they are not traditionally used as photoemitters, QE of commercial thermionic dispensers can be measured, and varies with type (from highest to lowest: M-type, scandate, and B-type), but is about 0.1% at 266 nm and less than 0.01% at 532 nm. A commercial dispenser is shown in Fig. 9.1.



Figure 9.1: Commercial dispenser (thermionic cathode)

The prototype Maryland cesium dispenser photocathode design is shown in Fig. 9.2. It is comprised of a stainless steel cylinder, nickel-brazed for a hermetic seal to a porous sintered tungsten disk which fits inside one end of the cylinder, and with a stainless steel cap laser-welded onto the other end after the source material has been inserted. The laser weld is used in preference to a braze to keep the temperature of the cathode low enough during the weld process to avoid activation of the cesium source inside the cylinder.

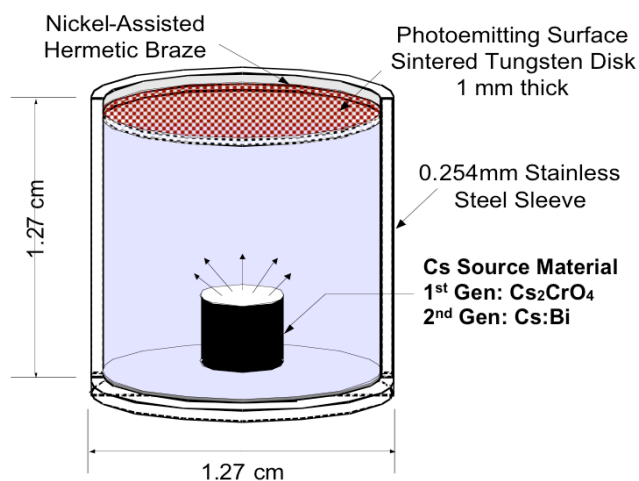


Figure 9.2: Prototype dispenser from UMD

9.1.2 Canister

The canister of choice is stainless steel. Readily available for machining, stainless steel also has the added benefit of low thermal conductivity which makes it ideal for laser welding. The rear face of the cathode can be laser welded after insertion of the cesium source into the can-

ister, and the heat transfer to the unactivated cesium source during atmospheric exposure is minimized in this way. Heat-induced activation of the cesium source would result in cesium release and cesium oxide formation at atmosphere, rendering the dispenser inoperable.



Figure 9.3: First cesium dispenser cell

The first generation cesium dispenser cell was designed in 2006 by then-UMD doctoral student Nathan Moody. Fabrication of this and subsequent cathodes have been performed to spec by B. Vancil of E-beam Incorporated. In the first cell shown there is some excess braze material: it was unknown how much would be required to get a hermetic seal. The braze joint in subsequent cathodes has been much cleaner. Nevertheless, all that is required is that the center, laser-illuminated area of the cathode be free of braze material and able to freely diffuse cesium. The dispenser is mounted in the QE test chamber in a copper clamp. Copper transfers heat well from the heater assembly to the dispenser reservoir.



Figure 9.4: Dispenser in copper clamp

9.1.3 Sintered Tungsten

The porous front face of the cathode, made from sintered tungsten, has certain design constraints. The porosity of the tungsten is lower-bounded at 60% density by the manufacturing process used at Spectra-Mat, the supplier. Less dense tungsten is available but has a "spongy" appearance and does not have a suitably flat surface for photoemission experiments. The tungsten can be sintered and machined in various thicknesses. A sub-mm thin disc is not a problem during manufacturing but can cause other difficulties. Initially a 40-mil (1 mm) thick, 70% dense sintered tungsten disc was used which had been well polished. Later a 20-mil (0.5 mm) thick, 60% dense polished sintered tungsten disc was used. It was found that brazing of the 40-mil thick disc could be done reliably, but that the geometry of the joint (where the only mated surfaces were the edges of the disc with the inside walls of the cylinder) made brazing of the 20-mil disc difficult. A hermetic seal (assured via bubble testing) was achieved only one out of four attempts with the thinner disc. Future iterations of the design will likely contain a braze onto the face of the tungsten disc instead of onto the edge, which is not a problem as long as sufficient

area in the dispenser center is clean of braze material to allow the active area to exceed the laser spot size.

The tungsten substrate/diffusion barrier itself has been characterized in Section 5.6. Optical and electron microscopy were performed and pore structure was analyzed using focused ion beam milling. The effect of varying porosity and thickness will be introduced in Section 9.2.

9.1.4 Cesium Reservoir Materials

Initially the reservoir material of choice for the prototype dispenser, as designed by Moody, was a cesium chromate and titanium powder. They were mixed 5:1 by weight and pressed by hand into small pellets. At a measured activation temperature of 425 °C the chromate reacted with the titanium, leaving free cesium in the reservoir. Subsequent gentler heating was all that was necessary to initiate cesium flow to the surface of the cathode through the porous tungsten substrate. The problem with the chromate source is that the release is not as pure as with the alternative: the proprietary cesium-bismuth intermetallic compound available from Alvatec, an Austrian company. This material also has a lower activation temperature of 273 °C. Because the compound is not air-stable, it is indium-sealed in an argon atmosphere prior to transfer to the dispenser. Indium melts at 157 °C, exposing the intermetallic compound and resulting in a momentary release of argon gas. This is followed by activation and sublimation of cesium around the 350 °C mark. Once cesium has been released into the reservoir, as in the case of chromate-based material, a gentle heating is all that is needed to initiate cesium flow.



Figure 9.5: Custom Cs:Bi reservoir cartridge from Alvatec: (left) indium seal, (right) rear seal



Figure 9.6: Cs:Bi reservoir cartridge and cathode for scale

The cesium cartridge shown in Figs. 9.5 and 9.6 is custom-fabricated by Alvatec for the UMD dispensers with their highest concentration intermetallic compound (65% Cs by weight). It contains approximately 525 milligrams of cesium in an 800 milligram fill of Cs:Bi. The indium seal is visible in the unused cartridge shown. The cartridge is air-tight, and to further ensure purity and extend shelf life it is argon-packed until needed for installation in the dispenser. Following fabrication the dispenser containing the cartridge was installed under vacuum within a few days.

9.2 Installation and Activation

9.2.1 Cathode mount

For a dispenser the anode arm is extended from the heater assembly so that there is room to install the cathode clamp and dispenser and retain cm-scale spacing between anode and cathode, so that applied voltages result in the same applied field as in the case of (silver or tungsten) disc cathode tests. This ensures that the dispenser QE tests will be below the space charge limit using the same voltage supply as for the disc cathodes. The arrangement is shown in Fig. 9.7.



Figure 9.7: Cathode mounted behind annular anode

9.2.2 Activation

Prior to activation the dispenser must be outgassed through a slow, gradual heating. The standard bakeout of the chamber in excess of 150 °C served this purpose in preparation for the activation to be performed. The activation process allows for measurement of QE throughout. This experiment is illustrated in Fig. 9.8. The comparison of activation temperature in the first

and second generation dispensers (cesium-chromate-titanium pellets versus Alvatec cesium-bismuth intermetallic compounds) is deferred to Section 9.5.1. In the activation process shown, cesium begins to sublime shortly before 273 °C where the first cesium diffuses to the surface to affect the QE, then equilibrates. At about 333 °C thermionic emission begins to significantly augment photocurrent.

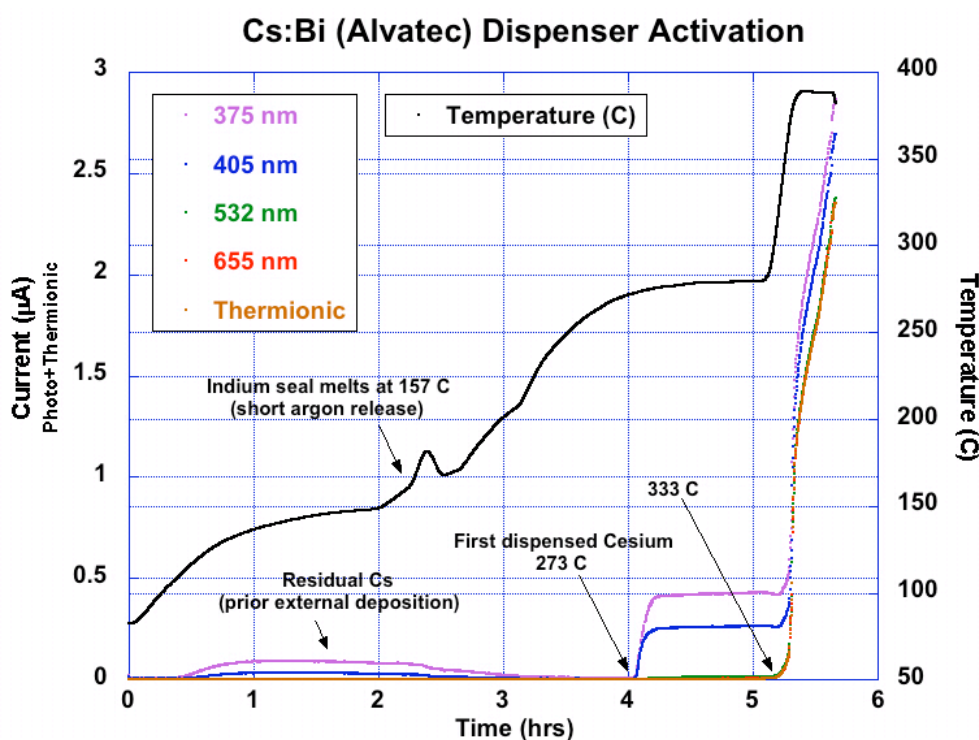


Figure 9.8: Activation of 2nd gen. cathode with Alvatec Cs:Bi reservoir

The outgassing corresponding to the activation process described above is shown in Fig. 9.9. There is an initial argon release following the melt of the indium seal, and a high-temperature argon release of argon trapped in the Cs:Bi compound itself. There is an initial outgassing of the material which is quickly ameliorated as the free cesium begins to act as a getter material.

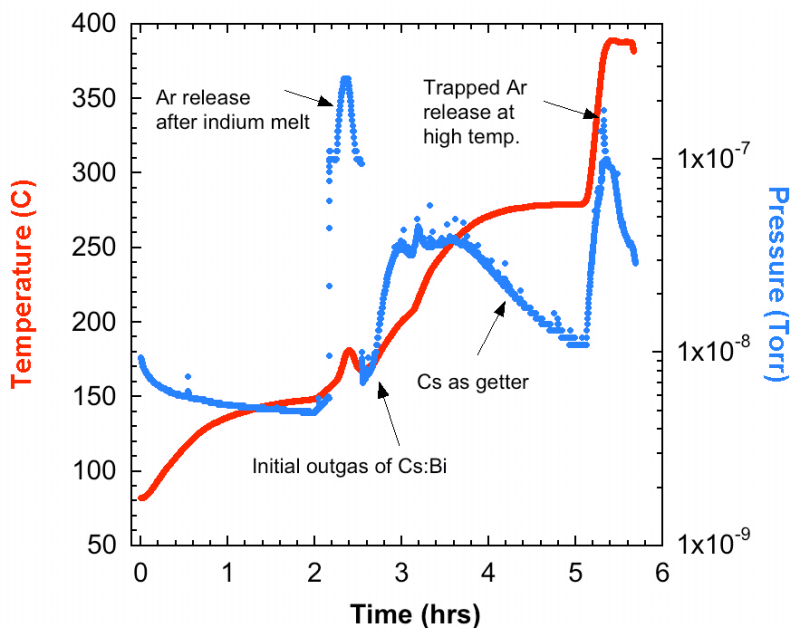


Figure 9.9: Pressure and temperature of 2nd gen. cathode activation

It should be noted that there is a switch to ion pumping following the initial argon release. This is to keep the vacuum pressure as low as possible during the activation. Ion pumps do not pump noble gases well, so although the argon release at high temp appears comparable to the initial one, it is actually much lower since it occurred during the ion pumping phase and the first release was during the turbopumping phase. (The break in the pressure data after the first argon release is due to the switch between pumping systems.)

In Fig. 9.10 the activation (heating) of a second-generation dispenser containing an indium-sealed, argon-packed Cs:Bi compound in the reservoir is compared to an identically designed but smaller, standard cesium source from Alvatec GmbH. The behavior in both cases is consistent with the release of argon immediately following the indium melt (In has a melting point of 157

°C), a rapid pressure rise as the argon release temporarily overwhelms the pumping system, and then a gradual drop in pressure as the source is kept hot. The vacuum further improves upon cooling the source or cathode. Note that CO and N₂ both have 28 amu and are indistinguishable within the resolution of the RGA (a software analysis which assigns a partial pressure or percentage to each can give completely different results the next scan). The current through the Alvasource is given since a direct temperature measurement is not made, but the thermocouple in the dispenser heater assembly allows direct reporting of temperature there. The pumping is specified since ion pumps and turbopumps will have a different pumping speed and hence base partial

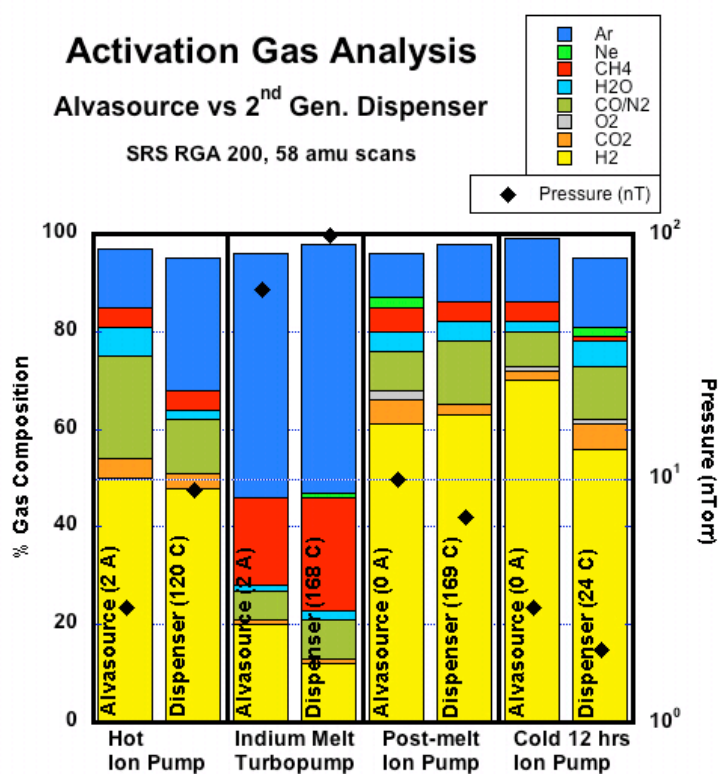


Figure 9.10: Vacuum RGA analysis during activation of 2nd gen. cathode vs Cs Alvasource

pressure for a given gas species. The need for multiple systems, as already mentioned, is to deal with argon release post-indium melt.

9.3 Rejuvenation

The cathode operated without external coatings simply dispenses cesium to the surface, coating the sintered tungsten with a submonolayer of cesium and drastically improving the QE. This process can be repeated if cesium is lost to any of the mechanisms discussed in Chapter 8. The results of a rejuvenation, after having removed all cesium from the room-temperature dispenser by an ion cleaning, are shown in Fig. 9.11. Uniform coverage is indicated by achieving comparable quantum efficiency to the peak seen in previous, externally cesiated sintered tung-

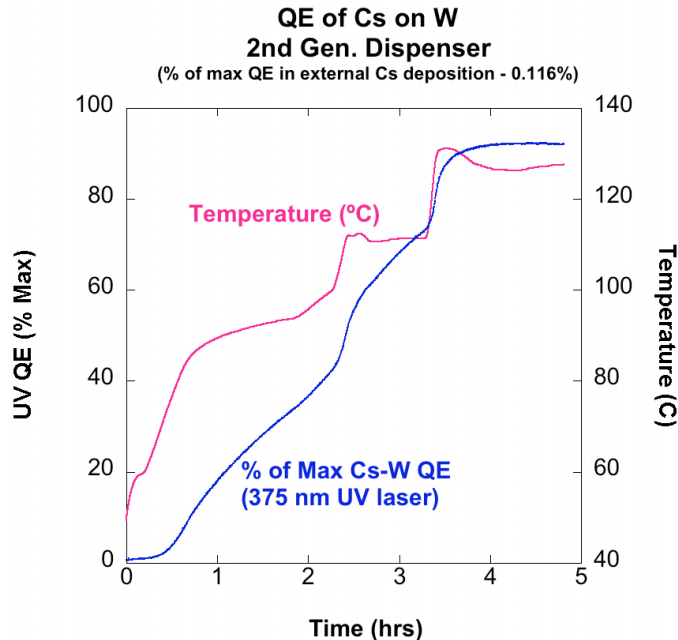


Figure 9.11: Rejuvenation of 2nd gen. cathode with 60% dense 20-mil thick tungsten disc

sten experiments. It is interesting that QE in the dispenser does not exceed this value - evaporation increases significantly at higher temperatures and coverages, such that the QE levels off. The fact that it levels near the ideal coverage for maximum QE is not coincidental: when the cesium atoms have a dipole moment largely unreduced by other nearby atoms, the adsorption to the surface is likewise largely unaffected, as indicated also by the highly coverage-dependent evaporation rates left of the peak QE of Fig. 8.3.

The 5-hour rejuvenation test is intentionally run at lower temperature than could be used, to allow QE to level off at a minimum operating point. Faster response is easily achieved by increasing the operating temperature. Chamber pressure with a hot dispenser was only 4×10^{-9} Torr.

9.4 In-situ Cs-Sb Fabrication on Dispenser

In order to probe the interaction of a cesium-based semiconductor on an activated dispenser, an antimony layer was deposited on an ion-cleaned, though activated, dispenser surface. The experiment was to try to release as much cesium as possible into the antimony and then cool immediately to achieve minimal cesium loss and maximum QE. Unfortunately the test apparatus is not equipped with active cooling, so the dispenser takes on the order of an hour to cool below dissociation temperatures for cesium antimonide: ample opportunity for a cesium-poor material to result as shown in Fig. 9.12. A correct stoichiometry for a cathode of this initial antimony thickness would be expected to have at least 10% QE (Section 7.2); here only 1.1% is achieved.

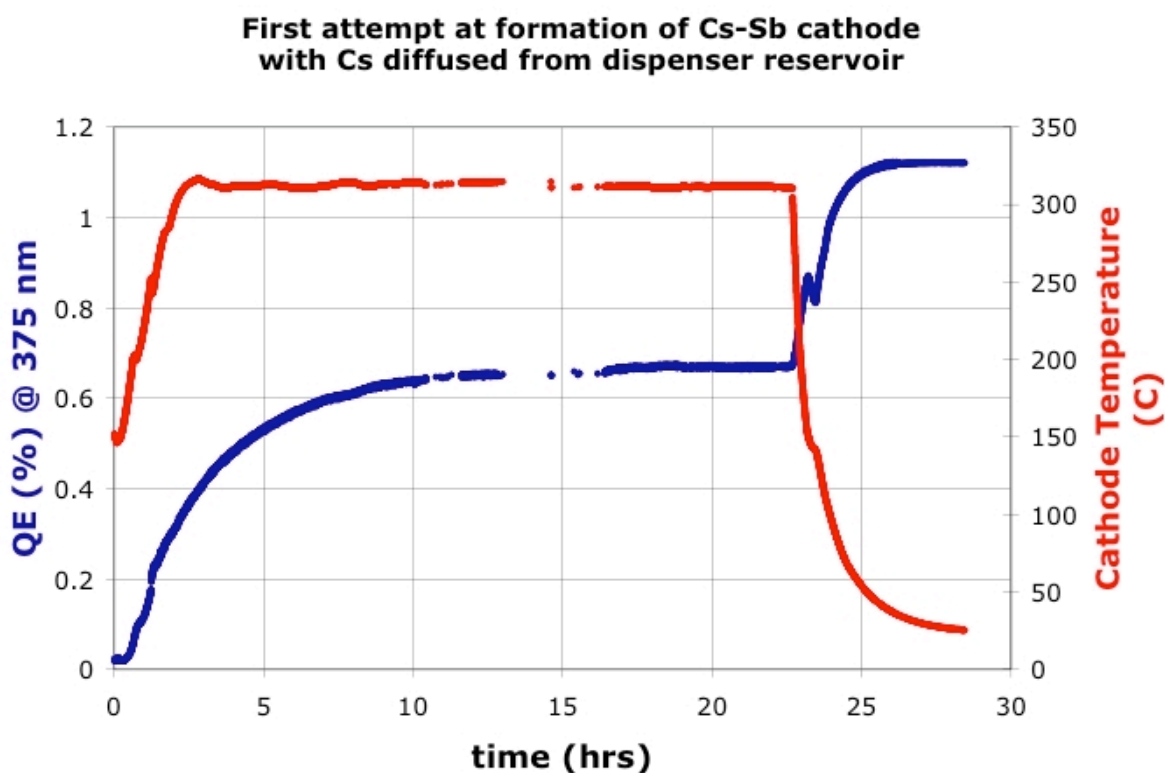


Figure 9.12: Dispensed-cesium Cs₃Sb fabrication attempt

The success of the in-situ cesium-antimony trial is that cesium was shown to diffuse through the antimony layer from within the dispenser. The challenge was the thermal instability of the cesium antimonide itself, which has been discussed at length in Section 8.4.2. One anomaly in the graph is the small downtick in QE during cooling, at the 150 °C mark. The heater here was turned back on with the initial intent to stabilize the temperature and try to improve QE. However, the response of the cathode was nearly immediate and quite detrimental to QE, so the heater was turned off. Such a fast response cannot be due to a change in bulk stoichiometry, and therefore points toward a surface layer with a very temperature-sensitive interplay between cesium being dispensed and evaporated, with cesium diffusing from more highly concentrated re-

gions in the bulk to the surface, and which is constantly losing cesium to evaporation at those temperatures. Any increase of the surface temperature hence the evaporation rate would immediately upset this balance and would impact the emission barrier via the electron affinity.

9.5 Dispenser Comparison and Discussion

9.5.1 Comparison

In Table 9.1 are compared the design and operation for the first and second generation cesium dispenser cathodes, the former having been reported by Moody in Refs. [11; 19] and the latter described in this work.

Gen.	ID	Activation	Rejuvenate Turn-On	Normal Operation	Tungsten Density	Substrate Thickness	Reservoir: Cs mass, material
1	D01	425 °C +	~50 °C	175 °C	70%	1.0 mm	200 mg, CrCs ₂ O ₄ :Ti
2	D04	273 °C +	<80 °C	150 °C	60%	0.5 mm	500 mg, Cs:Bi

Table 9.1: Comparison of Cesium Dispenser Cathodes

The difference in activation energy is due to the replacement of the chromate with the Al-vatec compound. The difference in rejuvenation turn-on temperature subsequent to activation between the two dispensers is due in part to the fact that the first test used a slow, hour-long initial heating profile to reach 50 °C and the onset of steeply increasing photoemission, whereas the second test used a more rapid initial heating profile, reaching 80 °C in twenty minutes where the on-

set of photoemission was observed. The difference in normal operation temperature is enabled by the thinner substrate.

9.5.2 Discussion of Future Design Directions

The changes made to the second generation dispenser were a thinner, less dense tungsten diffusion barrier and a lower activation temperature, cleaner-release cesium reservoir source. Future cesium dispenser cathodes will continue to refine these two areas. The diffusion barrier need not be made of porous tungsten; controlled porosity dispenser (CPD) technology already exists for thermionic dispensers and could be adapted to the cesium dispenser photocathode. Advantages would be increased cesium diffusion uniformity and more design flexibility. The reservoir need not be located directly beneath the diffusion barrier; recent work by Moody at LANL has investigated the use of a separately heated ampoule of elemental cesium attached to the rear cathode face via tube. Advantages are separate thermal control of the cathode and reservoir, which results in the ability to control cesium diffusion rates via concentration gradients separately from the substrate temperature. Future cesium dispenser cathodes intended for in-gun tests will require an updated mechanical design as well. The current prototype at Maryland with its projecting stainless steel lip at the edge of the cathode would be problematic in-gun due to field emission. A redesign with the dispenser diffusion barrier forming the entire front face of the cathode, as is the case for the commercial dispenser in Fig. 9.1, would be straightforward.

The cesium dispenser even in its current configuration has shown good promise for in-situ rejuvenation of cesium-based photocathodes. The incorporation of a high QE coating with a

dispenser in order to extend lifetime of the high QE material, particularly under adverse conditions such as contamination or heating, is a natural next step. Appropriate design considerations based on lessons learned from this work would include pore size and spacing (controlled or sintered), substrate coating (bare substrate or metalized with, say, gold for better thermal and electrical conductivity and possibly better QE), and most importantly, careful thermal design and choice of a temperature-stable high QE material so that operation of the dispenser would be possible without causing uncontrolled and unrecoverable loss of cesium, and would allow full and repeatable rejuvenation of the high QE cathode.

Chapter 10: Conclusion and Outlook

10.1 Summary of Work

The four Expeditions introduced in Chapter 3 and detailed in the body of this dissertation have advanced the cause of basic photocathode science and have led to improved theory and to practical demonstration of improved cesium dispenser prototypes. These four journeys of inquiry are summarized in the following pages: cesium-coated metal photocathodes, cesium-based semiconductor photocathodes, cesium loss and recesiation studies, and cesium dispenser photocathode development.

10.1.1 Cesium-Coated Metal Photocathodes

Utilizing and expanding upon the versatile experimental apparatus for photocathode research at UMD, the heart of which was designed and built under a previous program [19], investigations were continued into coated metal quantum efficiency to further refine sorely-needed theoretical models of photoemission.

Starting from the substrate itself, an effort was described in Chapter 5 to characterize both the pore structure of sintered tungsten and the effect on that material produced by ion beam cleaning. Surface variation across multiple grains in polished sintered tungsten was on the scale of microns. Variations in polishing effectiveness were observed on the front and rear faces of the tungsten disc and possible impact on the density of pores was noted. Where pore sparsity was observed, hydrogen peroxide etching revealed significant subsurface porosity in line with specification of 70% density. Pores tracked beneath the cathode surface using focused ion beam milling

were discovered to narrow markedly, angle irregularly and end abruptly. Significant diffusion of cesium along grain boundaries rather than solely through pores was posited as the mechanism for which uniform cesium coverage is obtained in the cesium dispenser.

Ion beam cleaning using argon ions was studied since it is used in preference to less effective anneal cleaning. Surface roughness induced on sintered tungsten was observed but the effects were small from grain to grain. However, visible evidence of significant sputtering of the tungsten was found. The effectiveness of ion cleaning of coated metal substrates was quantified. Cleanings of cesiated silver with 0.1 mA/cm^2 , 6.5 keV argon beams for just one to two minutes were sufficient to reduce quantum efficiency to negligible levels, indicating full adsorbate removal, and in line with previous work on cesiated tungsten.

Theory of QE for coated metals was presented, correlating QE with coverage (maximally 0.11% with 63% coverage of Cs:W at 375 nm). An updated, Moments-based approach was detailed with a full 3D momentum formulation and an energy-dependent scattering term. The theory was based on fundamental constants and literature values, and as such was not a fit to data, but was rather of predictive utility. Comparing the predictions of this theory to experiments with alkali-coated metals resulted both in validation of the theory and refinement of certain coverage factors in properly comparing to measured data. Since experiments were in the low-field low-intensity regime, many of the damage mechanisms which had complicated such comparison in the past were eliminated, and agreement of the peak QE of each of the alkalis on tungsten was within 15%. The insights provided by theory allowed discussion of peaks in curves of quantum efficiency versus surface coverage. Good indications of cesium diffusion at room temperature on the

atomic scale were found, and the importance of both atomic surface cleanliness and deposition uniformity were re-emphasized based on the interpretation of experimental results.

10.1.2 Cesium-Based Semiconductor Photocathodes

Theory of quantum efficiency for semiconductor photocathodes was detailed and the Moments-based approach for coated metals was adapted for this case. Special emphasis was placed on the origin of improved quantum efficiency of semiconductors over metals: electron transport and scattering processes were discussed and the dominance of polar optical phonon scattering was presented as opposed to the dominance of electron-electron scattering in metals. Optical constants were shown for the representative case of cesium antimonide and with absorption, transport, and emission barrier described, predictions of the quantum efficiency of cesium antimonide were compared to literature and to experiment with excellent results. Agreement with experiment was within 20% across the photon energy range from IR to UV.

Experimentally, the fabrication of cesium antimonide was reported and discussed, and of particular interest was the tapering deposition of cesium during cooling required to obtain good quantum efficiency. With an external cesium source this is straightforward. With an *in-situ* source like a dispenser where cathode temperature and cesium supply are not independently variable, this is potentially problematic. Nevertheless, quantum efficiencies in excess of 10% in the UV and 3% in the green were demonstrated. The fabrication of the more thermally stable trialkali, cesium sodium potassium antimonide, was also reported, enabled by upgraded experimental capabilities. Despite a thin-film deposition, QE in excess of 1.1% in the UV was shown, and

stabilization of QE post-deposition occurred at much higher temperatures than for cesium antimonide: a promising signal for dispenser compatibility.

10.1.3 Cesium Loss and Recesiation Studies

Four mechanisms for cesium loss in photoinjector operating environments were introduced: evaporation, back-bombardment, contamination, and dissociation. Evaporation rates for sub-monolayers were emphasized as orders of magnitude less than for bulk cesium or even for multiple monolayer coatings of cesium on tungsten. Back-bombardment was described as a limiting factor in DC photoinjector cathodes. Contamination was discussed as the limiting factor on RF photoinjector cathode lifetime. Dissociation was introduced as a way for alkalis to escape (and subsequently evaporate) from the bulk of semiconductor compounds, with serious implications for QE lifetime.

Experimental results were presented for evaporation of cesium coatings from heated tungsten. Strongly coverage-dependent evaporation for sub-monolayer coatings was indicated. Contamination and recesiation tests for alkali-coated silver were shown. Remarkably, repeatable recovery of full QE after contamination was demonstrated, providing strong support for the cesium dispenser concept as a means of extending the lifetime of contamination limited cathodes in RF photoinjector environments. Experiments with the heating of cesium antimonide semiconductor cathodes confirmed earlier suspicions of the temperature sensitivity of that material and definitively eliminated it as a candidate coating for reservoir-type cesium dispenser cathode with an embedded heater. Irreversible loss of QE was shown in conjunction with the heat cycling of

an operating dispenser. A survey of more thermally-stable alkali antimonides was performed and cesium sodium potassium antimonide was identified as a cesium-based candidate material.

10.1.4 Cesium Dispenser Photocathode Development

The design and fabrication of the prototype UMD cesium dispenser photocathode was discussed. Specific modifications to the design, both in sintered tungsten porosity and thickness were discussed. Reduced temperature operating points at which cesium was readily diffused were demonstrated with the thinner and more porous diffusion barriers. With regard to the choice of reservoir material, formerly used cesium chromate and titanium pellets were replaced by cesium-bismuth intermetallic compounds in custom-fabricated cartridges, and significantly reduced temperature activation (initial release of cesium once the risk of atmospheric contamination is gone and ultrahigh vacuum is obtained) was shown with very pure cesium release. Activation temperature dropped drastically from 425 °C to 273 °C. Rejuvenation of the QE of the second generation dispenser was demonstrated with QE in excess of 90% of the theoretical maximum. An in-situ fabrication attempt for cesium antimonide using deposited antimony but dispensed cesium was reported, and although 1% QE was obtained in the UV, this was an order of magnitude less than should be achievable for a cathode of that thickness, and so was in line with previously reported results on the temperature instability of the cesium antimonide semiconductor. These results reinforced the need to further research the trialkali material as a candidate high QE cesium dispenser cathode coating.

10.2 Future Directions

The Irish novelist Joyce Cary wrote, "To sum up complex problems for action is an act of creative imagination." While each data point and theoretical premise within this work is examined on scientific principle, answering the question "Where do we explore from here?" seems at times a creative, an imaginative, indeed an almost prophetic act. Newton well understood the underpinnings of this farsightedness when he said, "If I have seen further than others, it is by standing upon the shoulders of giants." From Thompson, Hertz and von Lenard's observations of an unknown phenomenon in the late nineteenth century to Einstein's Nobel-winning explanation of photoemission in the early twentieth; from Taylor and Langmuir's studies of cesium on tungsten in the early thirties to the high quantum efficiency photocathode discoveries of Spicer, Sommer, and so many others in the decades since; from Los Alamos' first photoinjector in 1985, to 14.3 kW average power at 1.6 microns by Jefferson Lab in 2006, to first light at 1.5 Å by Stanford's LCLS in 2009, Newton's words ring truer than ever. And so as photocathode explorers we do pose the question, "Where next does this expedition lead?" Several possible research directions are outlined in the following pages and an effort has been made to order them appropriately for a continued, careful, incremental study of the advancement of cesium dispenser photocathodes.

10.2.1 High QE Semiconductor Contamination and Recesiation

With the success of contamination testing and recesiation for cesiated silver comes a natural experimental continuation. First cesiated tungsten should be tested and compared to the sil-

ver results. Following that, the higher QE semiconductors are of great interest as well. With controlled contamination comes the ability to quantify the response of alkali antimonide QE to exposure to various background gases. Since these materials have contamination-limited lifetimes such results would benefit the larger photoinjector community immediately. It also remains to be seen whether external recession of a semiconductor results in the same reversibly rejuvenable QE as for cesiated metals, which is an important indicator for the dispenser cathode's effectiveness with high QE coatings.

10.2.2 High QE Semiconductor Rejuvenation

Just as the external and *in-situ* rejuvenation of cesiated metal photocathodes has been demonstrated at QEs of 0.1% with resulting significantly extended photocathode lifetime, so should experiments be conducted with the trialkali and possibly bialkali antimonides to demonstrate rejuvenation at the 1-10% QE level and to probe the increased lifetime which results. The demonstration of extended lifetime of a high QE coating on a dispenser photocathode is a crucial milestone along the future developmental trajectory of the technology.

10.2.3 Theory of Cesium Diffusion and Evaporation in Dispensers

The dynamics of cesium in a dispenser are complex. Optimization of a dispenser diffusion barrier will require a deeper understanding of those dynamics. Specifically a comprehensive time-dependent theory of cesium diffusion through the porous bulk material and across the surface, with the inclusion of evaporative effects and their proper functional dependence upon

coverage, will serve to strongly support the development of better dispensers with more uniform emission and more ideal operating temperatures.

10.2.4 Alternate Dispenser Diffusion Barrier Designs

Investigations into sintered tungsten of different porosities and thicknesses should be prioritized. Milling of the back side of the diffusion barrier can allow the mechanical integrity of a thicker disc to be preserved while testing the diffusion characteristics of a much thinner barrier. If the desired operating characteristics and emission uniformity cannot be obtained with sintered tungsten, alternative materials can certainly be considered. One such option is controlled porosity via laser drilling, ion beam milling, or deep reactive ion etching. The diameter, spacing, and geometrical arrangement of pores on the surface could then be precisely specified and fabricated, and with theory as a guide could be optimized for a given operating temperature range.

The possibility of depositing a metallic coating on a different substrate opens new possibilities for QE and for controlled porosity. Vapor deposition of copper or gold firstly allows use of insulating substrates like silicon (with the well-developed photolithography techniques it offers), and secondly allows potentially higher QE with the use of metals other than tungsten as the cesiated surface while maintaining the porosity of the diffusion barrier on which it is deposited.

10.2.5 Alternate Dispenser Reservoir Designs

So far two dispenser reservoir designs have been tested at UMD: the cesium chromate and cesium-bismuth systems. Other ways of releasing elemental cesium into the vacuum envi-

ronment of the dispenser reservoir are certainly possible. It might be possible to fabricate an indium-sealed canister like the one for cesium-bismuth but containing elemental cesium. It is certainly possible to procure glass ampoules commercially containing cesium in elemental form. Ampoules must be broken by mechanical means however, and so involve more complexity in reservoir design than a simple heat-activated release mechanism like an indium seal. Alternatively, the source of cesium can be separated from the dispenser diffusion barrier altogether and connected only by a long tube. Thermal isolation of the two parts of the dispenser allows independent thermal control of substrate reaction temperature and cesium reservoir diffusion temperature. The external cesium source in ampoule form can additionally be shock-shattered in-vacuum without the need for complex mechanical breaking techniques.

10.2.6 Enhanced Experimental Capabilities

Quantification of the evaporation of cesium from an operating dispenser is a critical step prior to inclusion of such a cathode in an in-gun test. Such a test could be done using a cathode-facing deposition monitor in tandem with a residual gas analyzer.

Improved systems for the controlled introduction of ultrapure contaminant gas into the cathode chamber would allow more detailed analyses of the contamination-limited lifetime of both coated metal and semiconductor cathodes.

For coated metal experiments, single-crystal metal substrates could be procured in place of polycrystalline materials used thus far to allow definitive measurements of crystal-face dependent QE, diffusion, ion cleaning effects, and the like. An even more rigorous comparison to theo-

ry of the QE of coated metals would result. A statistical combination of various crystal faces would then be enabled as a descriptor for polycrystalline substrates.

Inclusion of a cold finger or liquid nitrogen or helium circulation through a redesigned cathode stalk would enable QE tests at cryogenic temperatures such as those encountered in SRF guns. Cesium tungsten is predicted to increase in QE by about factor of 2 (depending on wavelength) at 77K compared to 300K [94]. Cesium antimonide and cesium telluride, on the other hand, have shown indications of reduced QE under cryogenic conditions [44; 45] and the application of appropriate theory can explain this and inform further research. Reduced cesium loss would also be expected under cryogenic conditions and any changes in contamination susceptibility or lifetime compared to room temperature would benefit cathode design for SRF photoinjectors.

Studies of fabrication of alkali antimonides could benefit from measurement of film resistivity, which has been indicated in literature [127; 128] to have strong dependence on stoichiometry of the cathode and in fact to exhibit sharp peaks at integer ratios of the alkali and antimony constituents. Much more precise fabrication of cathode stoichiometry might be enabled without the significant expense of more complex surface analysis tools such as x-ray diffraction or Auger electron spectroscopy.

10.3 Closing Thoughts

Let us end with the beginning in mind. The themes explored in this work were motivated by the demands of free electron lasers, which rely on laser-switched high brightness photocathodes. Free electron lasers offer high brightness in regions of the electromagnetic spectrum where conventional sources are limited or do not even exist, from x-ray to terahertz and beyond. Future high average power free electron lasers demand cathodes with extended lifetime, high quantum efficiency, and fast response time that are not simultaneously found in any existing combination of gun and cathode, DC or RF, photo, field, or thermionic. Long-lived photocathodes with excellent quantum efficiency to answer this need are promised by cesium dispenser cathode technology. But optimization of cesium dispenser cathodes necessitates a working understanding of the fundamental physics of these devices in order to form a predictive theory both of quantum efficiency and of the function of cesium in operational photocathodes. The theory presented herein is well-developed and already finds application in particle-in-cell beam code with a view towards end-to-end free electron laser simulations. The experimental work presented herein has informed that theory, has provided excellent comparisons with its predictions, has confirmed the tenets of recesiation in support of the cesium dispenser concept, has demonstrated an advancing cesium dispenser design, and has cast new light on the compatibility of high quantum efficiency alkali antimonides with operational dispenser photocathodes. Ahead, the outlook is bright; may the expedition advance!

References

1. P. G. O'Shea and H. G. Freund. "Free-Electron Lasers: Status and Applications." *Science*, **292**, 1853 (2001).
2. C. A. Brau. *Free Electron Lasers* (Academic Press, Boston, 1990).
3. T. C. Katsouleas et al. *Scientific Assessment of High-power Free-electron Laser Technology* (National Research Council, 2009).
4. M. Reiser. *Theory and Design of Charged Particle Beams* (Wiley, New York, 1994).
5. K. L. Jensen. *Electron Emission Physics* (Academic Press, 2007).
6. B. E. Carlsten. "New photoelectric injector design for the Los Alamos National Laboratory XUV FEL accelerator." *Nucl. Instrum. Methods Phys. Res. A*, **275**, 313 (1989).
7. L. Serafini and J. B. Rosenzweig. "Envelope analysis of intense relativistic quasilaminar beams in rf photoinjectors: a theory of emittance compensation." *Phys. Rev. E*, **55(6)**, 7565 (1997).
8. D. Dowell et al. "First Operation of a Photocathode Radio Frequency Gun Injector At High Duty Factor." *Appl. Phys. Lett.*, **63(15)**, 2035 (1993).
9. P. D. Townsend. "Photocathodes--past performance and future potential." *Contemporary Physics*, **44(1)**, 17 (2003).
10. G. Suberlucq. "Technological Challenges for High Brightness Photoinjectors." *Proc. 9th Eur. Particle Accel. Conf., Lucerne, Switzerland*, (2004).
11. N. A. Moody, K. L. Jensen, D. W. Feldman, P. G. O'Shea and E. J. Montgomery. "Prototype Dispenser Photocathode: Demonstration and Comparison to Theory." *Appl. Phys. Lett.*, **90(11)**, 114108 (2007).
12. L. Monaco et al. "High QE Photocathodes Performance During Operation At FLASH/PITZ Photoinjectors." *Proc. PAC 2007*, **THPMN025**, (2007).
13. T. Siggins et al. "Performance of a DC GaAs photocathode gun for the Jefferson lab FEL." *Nucl. Instrum. Methods Phys. Res. A*, **475(1-3)**, 549 (2001).
14. S. H. Kong, J. Kinross-Wright, D. C. Nguyen and R. L. Sheffield. "Photocathodes for free electron lasers." *Nucl. Instrum. Methods Phys. Res. A*, **358(1-3)**, 272 (1995).
15. T. Srinivasan-Rao, J. Fischer and T. Tsang. "Photoemission studies on metals using picosecond ultraviolet laser pulses." *J. Appl. Phys.*, **69(5)**, 3291 (1991).
16. C.-S. Wang. "High photoemission efficiency of submonolayer cesium-covered surfaces." *J. Appl. Phys.*, **48(4)**, 1477 (1977).
17. M. D. Van Loy, A. T. Young and K. N. Leung. "Measurements of barium photocathode quantum yields at four excimer laser wavelengths." *Appl. Phys. Lett.*, **63(4)**, 476 (1993).
18. R. Calabrese et al. "Performance of a GaAs electron source." *Nucl. Instrum. Methods Phys. Res. A*, **340(1)**, 109 (1994).

19. N. A. Moody. "Fabrication and Measurement of Regenerable Low Work Function Dispenser Photocathodes." Doctor of Philosophy, Department of Electrical and Computer Engineering, University of Maryland (2006).
20. Sommer, A. H. *Photoemissive Materials* (Wiley, New York, 1969).
21. K. L. Jensen. "General formulation of thermal, field, and photoinduced electron emission." *J. Appl. Phys.*, **102**(2), 024911 (2007).
22. P. Townsend, D., R. Downey, S. Harmer, W., Y. Wang, A. Cormack, R. Mcalpine and T. Bauer. "Designs for waveguide and structured photocathodes with high quantum efficiency." *J. Phys. D: Appl. Phys.*, **39**(8), 1525 (2006).
23. K. L. Jensen, B. L. Jensen, E. J. Montgomery, D. W. Feldman, P. G. O'Shea and N. Moody. "Theory of photoemission from cesium antimonide using an alpha-semiconductor model." *J. Appl. Phys.*, **104**(4), 044907 (2008).
24. P. Michelato, L. Monaco, D. Sertore and S. Bettoni. "Optical Properties of Cesium Telluride." *Proc. 8th Eur. Particle Accel. Conf., Paris, France*, (2002).
25. S. Benson et al. "First Lasing of the Jefferson Lab IR Demo FEL." *Nucl. Instrum. Methods Phys. Res. A*, **429**(1), 27 (1999).
26. "4GLS Conceptual Design Report." (2006).
27. T. Rao et al. "Photocathodes for the energy recovery linacs." *Nucl. Instrum. Methods Phys. Res. A*, **557**(1), 124 (2006).
28. C. Sinclair. "DC photoemission guns as ERL sources." *Nucl. Instrum. Methods Phys. Res. A*, **557**, 69 (2006).
29. H. Hertz. "Über einen Einfluss der ultravioletten Lichtes auf die elektrische Entladung." *Ann. Physik*, **31**, 983 (1887).
30. P. Lenard. "Erzeugung von Kathodenstrahlen durch ultraviolettes Licht." *Ann. Physik*, **307**(6), 359 (1900).
31. A. Einstein. "Über einen die Erzeugung und Verwandlung des Lichtes betreffenden heuristischen Gesichtspunkt." *Ann. Physik*, **17**, 132 (1905).
32. L. W. Swanson, R. W. Strayer and F. M. Charbonnier. "The effect of electric field on adsorbed layers of cesium on various refractory metals." *Surf. Sci.*, **2**, 177 (1964).
33. Haas, G. A. and Thomas, R. E. *Techniques of Metals Research* (Wiley, New York, 1972).
34. J. L. Adamski, W. J. Gallagher, R. C. Kennedy, D. R. Shoffstall, E. L. Tyson and A. D. Yeremian. "The Boeing Double Subharmonic Electron Injector - Performance Measurements." *IEEE Trans. Nucl. Sci.*, **32**(5), (1985).
35. P. G. O'Shea and L. Spentzouris. "Particle beam sources." *Proc. 8th Adv. Accel. Con. Wkshp., Baltimore, MD*, (1998).
36. D. Alesini et al. "Status of the SPARC Photoinjector." *Proc. LINAC 2006, Knoxville, TN*, TUP038 (2006).
37. C. Hernandez-Garcia, P. G. O'Shea and M. L. Stutzman. "Electron Sources for Accelerators." *Physics Today*, **61**(2), 44 (2008).

38. S. J. Russell. "Overview of high-brightness, high-average-current photoinjectors for FELs." *Nucl. Instrum. Methods Phys. Res. A*, **507(1-2)**, 304 (2003).
39. J. Fraser and R. Sheffield. "A new high-brightness electron injector for free electron lasers driven by RF linacs." *Nucl. Instrum. Methods Phys. Res. A*, **250**, 71 (1986).
40. D. C. Nguyen. "Development of High-Average-Current RF Injectors." *Proc. 30th Intl. FEL Conf., Gyeongju, Korea, THCAU02* (2008).
41. P. G. O'Shea et al. "Initial results from the Los Alamos photoinjector-driven free-electron laser." *Nucl. Instrum. Methods Phys. Res. A*, **318(1-3)**, 52 (1992).
42. P. G. O'Shea et al. "Ultraviolet free-electron laser driven by a high-brighness 45 MeV electron beam." *Phys. Rev. Lett.*, **71**, 3661 (1993).
43. M. E. Conde and e. al. "The Argonne Wakefield Accelerator Facility: Status and Recent Activities." *Proc. PAC 2005, Knoxville, TN*, (2005).
44. A. Michalke, H. Piel, C. K. Sinclair and P. Michelato. "First Operation of High-Quantum Efficiency Photocathodes Inside Superconducting Cavities." *Euro. Particle Accel. Conf. 1992*, 1014 (1992).
45. D. Janssen et al. "First operation of a superconducting RF-gun." *Nucl. Instrum. Methods Phys. Res. A*, **507(1-2)**, 314 (2003).
46. A. Arnold et al. "Development of a superconducting radio frequency photoelectron injector." *Nucl. Instrum. Methods Phys. Res. A*, **577(3)**, 440 (2007).
47. C. Hernandez-Garcia et al. "A High Average Current DC GaAs Photocathode Gun for ERLs and FELs." *Proc. PAC 2005, Knoxville, TN*, 3117 (2005).
48. C. Travier. "Rf Guns - Bright Injectors for FEL." *Nucl. Instrum. Methods Phys. Res. A*, **304(1-3)**, 285 (1991).
49. T. Srinivasan-Rao et al. "Design, Construction and Status of all Niobium Superconducting Photoinjector at BNL." *Particle Accel. Conf. 2003*, **MOPB010**, 92 (2003).
50. J. Smedley et al. "Photoemission Tests of a Pb/Nb Superconducting Photoinjector." *Proc. PAC 2007*, **TUPMS085**, (2007).
51. J. B. Taylor and I. Langmuir. "The Evaporation of Atoms, Ions and Electrons from Caesium Films on Tungsten." *Phys. Rev.*, **44(6)**, 423 (1933).
52. L. R. Falce. "Dispenser Cathode Technology Review."
53. C. Travier, B. Leblond, M. Bernard, J. N. Cayla, P. Thomas and P. Georges. "CANDELA photo-injector experimental results with a dispenser photocathode." *Proc. PAC 1995*, **2**, 945 (1995).
54. Y.-E. Sun, J. Lewellen and D. Feldman. "Photothermal Cathode Measurements at the Advanced Photon Source." *LINAC Conference, Knoxville, TN*, (2006).
55. D. W. Feldman, P. G. O'Shea, M. Virgo and K. L. Jensen. "Development of Dispenser Photocathodes for Rf Photoinjectors." *Proc. IEEE Particle Accel. Conf.*, **5**, 3323 (2003).
56. K. L. Jensen, D. W. Feldman, M. Virgo and P. G. O'Shea. "Infrared Photoelectron Emission From Scandate Dispenser Cathodes." *Appl. Phys. Lett.*, **83(6)**, 1269 (2003).

57. D. C. Nguyen et al. "Overview of the 100 mA average-current RF photoinjector." *Nucl. Instrum. Methods Phys. Res. A*, **528(1-2)**, 71 (2004).
58. A. H. Sommer. "The element of luck in research - photocathodes 1930 to 1980." *J. Vac. Sci. Tech. A*, **1**, 119 (1983).
59. L. R. Koller. *Phys. Rev.*, **36**, 1639 (1930).
60. N. R. Campbell. *Phil. Mag.*, **12**, 173 (1931).
61. P. Görlich. *Zeitschrift für Physik A Hadrons and Nuclei*, **101**, 335 (1936).
62. A. H. Sommer. "New Photoemissive Cathodes of High Sensitivity." *Rev. Sci. Instr.*, **26**, 725 (1955).
63. K. L. Jensen, D. W. Feldman and P. G. O'Shea. "The Quantum Efficiency of Dispenser Photocathodes: Comparison of Theory to Experiment." *Appl. Phys. Lett.*, **85(22)**, 5448 (2004).
64. N. Moody, D. W. Feldman, P. G. O'Shea and K. L. Jensen. "Fabrication and Measurement of Low Workfunction Cesium Dispenser Photocathodes." *Proceedings of the IEEE Particle Accelerator Conference*, 2953 (2005).
65. N. A. Moody, D. W. Feldman, P. G. O'Shea, K. L. Jensen and A. Balter. "Measurement of Low Workfunction Cesium Metals for Use in Dispenser Photocathodes." *Proc. 27th Intl. FEL Conf., Stanford, CA*, 168 (2005).
66. K. L. Jensen, D. W. Feldman, N. A. Moody and P. G. O'Shea. "A Photoemission Model for Low Work Function Coated Metal Surfaces and Its Experimental Validation." *J. Appl. Phys.*, **99(12)**, 124905 (2006).
67. K. L. Jensen, D. W. Feldman, N. A. Moody and P. G. O'Shea. "Field-enhanced Photoemission From Metals and Coated Materials." *Journal of Vacuum Science & Technology B*, **24(2)**, 863 (2006).
68. N. A. Moody, D. W. Feldman, K. L. Jensen, E. J. Montgomery, A. E. Balter, P. G. O'Shea, J. E. Yater and J. L. Shaw. "Experimental Progress Toward Low Workfunction Controlled Porosity Dispenser Photocathodes." *Proc. 28th Intl. FEL Conf., Berlin, Germany*, THPPH069 (2006).
69. E. J. Montgomery, D. W. Feldman, P. G. O'Shea, Z. Pan, N. A. Moody and K. L. Jensen. "Fabrication and Measurement of Efficient, Robust Cesium Dispenser Photocathodes." *Proceedings of the IEEE Particle Accelerator Conference*, TUPMS010 (2007).
70. E. J. Montgomery, D. W. Feldman, P. G. O'Shea, Z. Pan, N. Sennett, K. L. Jensen and N. A. Moody. "Advances in Cesium Dispenser Photocathodes: Modeling and Experiment." *Journal of Directed Energy*, **3(1)**, 66 (2008).
71. K. L. Jensen, P. G. O'Shea and D. W. Feldman. "Generalized Electron Emission Model for Field, Thermal, and Photoemission." *Appl. Phys. Lett.*, **81(20)**, 3867 (2002).
72. K. L. Jensen. "Electron emission theory and its application: Fowler-Nordheim equation and beyond." *J. Vac. Sci. Tech. B*, **21(4)**, 1528 (2003).

73. K. L. Jensen, D. W. Feldman, M. Virgo and P. G. O'Shea. "Measurement and Analysis of Thermal Photoemission From a Dispenser Cathode." *Phys. Rev. ST Accel. Beams*, **6(8)**, 083501 (2003).
74. K. L. Jensen, D. W. Feldman and P. G. O'Shea. "Time Dependent Models of Field-assisted Photoemission." *Journal of Vacuum Science & Technology B*, **23(2)**, 621 (2005).
75. K. L. Jensen, D. W. Feldman and P. G. O'Shea. "Advanced photocathode simulation and theory." *Nucl. Instrum. Methods Phys. Res. A*, **507**, 238 (2003).
76. K. L. Jensen, P. G. O'Shea, D. W. Feldman and N. A. Moody. "Theoretical Model of the Intrinsic Emittance of a Photocathode." *Appl. Phys. Lett.*, **89(22)**, 224103 (2006).
77. D. H. Dowell and J. F. Schmerge. "Quantum efficiency and thermal emittance of metal photocathodes." *Phys. Rev. ST Accel. Beams*, **12**, 074201 (2009).
78. K. L. Jensen and E. J. Montgomery. "Photoemission Theory and the Development of High Performance Photocathodes." *J. Comp. Th. Nanosci.*, **6(8)**, 1754 (2009).
79. K. L. Jensen, Y. Y. Lau, D. W. Feldman and P. G. O'Shea. "Electron emission contributions to dark current and its relation to microscopic field enhancement and heating in accelerator structures." *Physical Review Special Topics Accelerators and Beams*, **11(8)**, 081001 (2008).
80. K. Jensen, D. Feldman, N. A. Moody and P. G. O'Shea. "Photoemission from Low Work Function Coated Metal Surfaces: A Comparison of Theory to Experiment." *Proc. IEEE Particle Accel. Conf.*, (2005).
81. D. A. Dimitrov, D. I. Bruhwiler, J. r. Cary, P. Messmer, P. Stoltz, K. L. Jensen, D. W. Feldman and P. G. O'Shea. "Development of Advanced Models for 3d Photocathode Pic Simulations." *Proc. IEEE Particle Accel. Conf.*, 2583 (2005).
82. K. L. Jensen, D. W. Feldman, E. J. Montgomery, N. A. Moody and J. Petillo. "A Theoretical Photocathode Emittance Model Including Temperature and Field Effects." *Proc. IEEE Particle Accel. Conf.*, TUPMS091 (2007).
83. J. J. Petillo, D. Panagos, K. L. Jensen and B. Levush. "Detailed Photoemission Modeling Using The 3D Finite-Element PIC Code MICHELLE*." *Proc. IEEE Particle Accel. Conf.*, (2007).
84. K. L. Jensen, P. G. O'Shea and D. Feldman. "A Generalized Current Density Model for Field, Thermal, and Photo-emission." *3rd IEEE Intl. Vac. Electron. Conf.*, 305 (2002).
85. N. A. Moody, K. L. Jensen, D. W. Feldman and P. G. O'Shea. "Experimental Validation of a Photoemission Model for End-to-end Beam Simulations and Custom Photocathode Designs." *IEEE International Vacuum Electronics Conference, 2006 Held Jointly With 2006 IEEE International Vacuum Electron Sources*, 429 (2006).
86. J. E. Yater, J. Shaw, K. L. Jensen, D. W. Feldman, N. Moody and P. G. O'Shea. "Photoelectron Emission and Secondary Electron Emission Characteristics of Cesium P-type GaN." *IEEE International Vacuum Electronics Conference, 2006 Held Jointly With 2006 IEEE International Vacuum Electron Sources*, 433 (2006).

87. J. Petillo, J. DeFord, E. Nelson, K. Jensen and B. Levush. "Application of the Finite-Element MICHELLE Beam Optics Code to RF Gun Modeling." *IEEE International Vacuum Electronics Conference, 2006 Held Jointly With 2006 IEEE International Vacuum Electron Sources*, 83 (2006).
88. E. M. Nelson, J. J. Petillo and K. L. Jensen. "New and Improved Emission Models in the Finite-Element Gun Code MICHELLE." *IEEE International Vacuum Electronics Conference, 2006 Held Jointly With 2006 IEEE International Vacuum Electron Sources*, 501 (2006).
89. K. L. Jensen, D. W. Feldman, N. Moody, D. Demske and P. G. O'Shea. "Thermal and field enhanced photoemission: comparison of theory to experiment." *Proc. 26th Intl. FEL Conf., Trieste, Italy, TUPOS65* (2004).
90. K. L. Jensen, D. W. Feldman, N. A. Moody, P. G. O'Shea and A. Balter. "Photoemission from Coated Surfaces: Comparison of Theory to Experiment." *Proc. 27th Intl. FEL Conf., Stanford, CA*, 355 (2005).
91. K. L. Jensen, N. A. Moody, D. W. Feldman, P. G. O'Shea, J. E. Yater and J. Shaw. "The Development and Application of a Photoemission Model for Cesium Photocathode Surfaces." *Proceedings of FEL 2006, Bessy, Berlin, Germany, THPPH068* (2006).
92. K. L. Jensen, D. W. Feldman and P. G. O'Shea. "Time-dependent Models of Field-assisted Photoemission." *Technical Digest of the 17th International Vacuum Nanoelectronics Conference*, 172 (2004).
93. K. L. Jensen, D. W. Feldman, N. A. Moody, J. Shaw, J. E. Yater and P. G. O'Shea. "Field-enhanced Photoemission From Metals and Coated Materials." *Technical Digest of the 18th International Vacuum Nanoelectronics Conference*, 3 (2005).
94. K. L. Jensen, J. L. Shaw, J. E. Yater, D. W. Feldman, N. A. Moody and P. G. O'Shea. "Photoemission from Cesium Surfaces and Custom-Designed Dispenser Photocathodes: Theory, Experiment, and Model Development." *8th Directed Energy Symposium*, (2005).
95. K. L. Jensen, J. E. Yater, J. L. Shaw, N. A. Moody and P. G. O'Shea. "The Calculated Emittance of a Photocathode." *9th Directed Energy Symposium*, (2006).
96. J. J. Petillo and K. L. Jensen. "Semiconductor Photoemission and Dark Current Modeling in the MICHELLE Code." *11th Directed Energy Symposium*, (2008).
97. J. L. Shaw et al. "Photoemission Images of Prospective Photocathodes." *11th Directed Energy Symposium*, (2008).
98. Bertolini, L. *Accelerator Vacuum Engineering* (2007).
99. R. Smalley and A. Sievers. "The total spherical emissivity of copper." *J. Opt. Soc. Am.*, **68**, 1516 (1978).
100. B. Window and G. Harding. "Thermal emissivity of copper." *J. Opt. Soc. Am.*, **71**, 354 (1981).

101. D. H. Dowell, F. K. King, R. E. Kirby, J. F. Schmerge and J. M. Smedley. "In situ cleaning of metal cathodes using a hydrogen ion beam." *Physical Review Special Topics - Accelerators and Beams Phys. Rev. ST Accel. Beams PRSTAB*, **9(6)**, 063502 (2006).
102. M. Hagino and T. Takahashi. "Thickness of Cs-Sb Films Relative to the Original Sb Films." *J. Appl. Phys.*, **37**, 3741 (1966).
103. A. Balter. "Characterization of Cesium Tungsten Dispenser Photocathodes." *UMD TREND undergraduate research program*, (2006).
104. N. Sennett. "Comparison of Cleaning Techniques to Optimize Cesium Silver Photocathodes." *UMD high school intern program, Montgomery Blair HS, Silver Spring, MD*, (2007).
105. J. Leung. "TREND Report." *UMD TREND undergraduate research program*, (2008).
106. N. Veisfeld and J. D. Geller. "Ion sputtering yield measurements for submicrometer thin films." *J. Vac. Sci. Tech. A*, **6(3)**, 2077 (1988).
107. Y. Okajima. "Estimation of sputtering rate by bombardment with argon gas ions." *J. Appl. Phys.*, **51(1)**, 715 (1980).
108. L. A. DuBridge. "Theory of the Energy Distribution of Photoelectrons." *Phys. Rev.*, **43(9)**, 727 (1933).
109. E. P. Gyftopoulos and J. D. Levine. "Work Function Variation of Metals Coated By Metallic Films." *J. Appl. Phys.*, **33(1)**, 67 (1962).
110. J. Topping. "On the Mutual Potential Energy of a Plane Network of Doublets." *Proceedings of the Royal Society of London Series A*, **114(766)**, 67 (1927).
111. E. S. Ritter. *J. Chem. Phys.*, **19**, 1030 (1951).
112. E. J. Montgomery, D. W. Feldman, P. G. O'Shea, P. Z. Pan, N. Sennett, C. Stortstrom and K. L. Jensen. "Towards a Multialkali Dispenser Photocathode: Experiment and Theory." *Proc. 31st Intl. FEL Conf., Liverpool*, (2009).
113. N. A. Papadogiannis, S. D. Moustazis and J. P. Girardeau-Montaut. "Electron relaxation phenomena on a copper surface via nonlinear ultrashort single-photon photoelectric emission." *J. Phys. D: Appl. Phys.*, **30**, 2389 (1997).
114. N. A. Papadogiannis and S. D. Moustazis. "Ultrashort laser-induced electron photoemission: a method to characterize metallic photocathodes." *J. Phys. D: Appl. Phys.*, **34**, 499 (2001).
115. K. L. Jensen, N. A. Moody, D. W. Feldman, E. J. Montgomery and P. G. O'Shea. "Photoemission from metals and cesiated surfaces." *J. Appl. Phys.*, **102(7)**, 074902 (2007).
116. R. Gomer. "Diffusion of Adsorbates on Metal-surfaces." *Rep. Prog. Phys.*, **53(7)**, 917 (1990).
117. K. L. Jensen. "Electron Emission Theory and Its Application: Fowler-Nordheim Equation and Beyond." *Journal of Vacuum Science & Technology B*, **21(4)**, 1528 (2003).
118. G. Wallis. *Ann. Physik*, **452**, 401 (1956).

119. W. E. Spicer. "Photoemissive, Photoconductive, and Optical Absorption Studies of Alkali-Antimony Compounds." *Phys. Rev.*, **112**, 114 (1958).
120. J. M. Barois, C. Fouassier, M. Onillon and B. Tanguy. "Experimental study of the non stoichiometry of cesium antimonide $\sim \text{Cs}_3\text{Sb}$." *Materials Chemistry and Physics*, **24(1-2)**, 189 (1989).
121. P. Dolizy and F. Groliere. "Dissociation energies of alkali antimonides as thin layers." *J. Phys. D: Appl. Phys.*, **19**, 687 (1986).
122. S. Lederer and e. al. "XPS studies of Cs_2Te photocathodes." *Proc. 29th Intl. FEL Conf., Novosibirsk*, (2007).
123. A. di Bona, F. Sabary, S. Joly, P. Michelato, D. Sertore, C. Pagani and S. Valeri. "Development, operation and analysis of bialkali antimonide photocathodes for high-brightness photo-injectors." *Nucl. Instrum. Methods Phys. Res. A*, **385(3)**, 385 (1997).
124. A. H. Sommer. *Photoemissive materials: preparation, properties, and uses* (Wiley, New York, 1968).
125. J.-L. Desplat and C. A. Papageorgopoulos. "Interaction of cesium and oxygen on W(110) : I. Cesium adsorption on oxygenated and oxidized W(110)." *Surf. Sci.*, **92(1)**, 97 (1980).
126. C. A. Papageorgopoulos and J. L. Desplat. "Interaction of cesium and oxygen on W(110) : II. Codeposition: cesium oxide formation." *Surf. Sci.*, **92(1)**, 119 (1980).
127. K. Miyake. "Formation of Cesium Antimonide. I. Electrical Resistivity of the Film of Cesium-Antimony System." *J. Appl. Phys.*, **31**, 76 (1960).
128. M. Hagino, T. Takahashi and M. Wada. "Composition Dependence of Photoelectric Characteristics of Cs-Sb Compounds." *J. Appl. Phys.*, **35**, 2112 (1964).
129. B. Cordero, V. Gómez, A. E. Platero-Prats, M. Revés, J. Echeverría, E. Cremades, F. Barragán and S. Alvarez. "Covalent Radii Revisited." *Dalton Trans.*, **21**, 2832 (2008).

Appendices

Appendix A: Material Parameters

Element, atomic #	Covalent Radius (Å)	Atomic mass (amu)	Melting point (°C)	Density (@300K, g/cm ³)	Crystal Structure, Lattice Constant (Å)
74, Tungsten (W)	1.62	183.8	3407	19.25	BCC, 3.16
47, Silver (Ag)	1.45	107.9	961	10.49	FCC, 4.09
55, Cesium (Cs)	2.44	132.9	28.44	1.879	BCC
19, Potassium (K)	2.03	39.10	63.38	0.856	BCC
11, Sodium (Na)	1.66	22.99	97.72	0.968	BCC
51, Antimony (Sb)	1.39	121.8	630.9	6.697	Rhomb., 4.51

Covalent radii from Cambridge Structural Database (averages across different compound bonds, polar bonds may differ) [129]